



Norwegian University of  
Science and Technology

# Analysis of the Prestura Rock Slope Failure and Quaternary mapping of Lake Tinnsjø, Telemark

**Hermann Hofseth Berntsen**

Geology

Submission date: May 2018

Supervisor: Reginald Hermanns, IGP

Norwegian University of Science and Technology  
Department of Geoscience and Petroleum





## ABSTRACT

---

This thesis covers an analysis of the Prestura rockslope failure and quaternary mapping of lake Tinnsjø. The analysis of the Prestura rockslope failure involves a structural analysis, kinematic analysis, volume calculations, empirical run-out analysis and semi-empirical displacement wave analysis.

Five different joint sets are identified close to the Prestura failure area by systematic field mapping, confirmed by structural analysis of terrestrial laser scan (TLS) data. The structural data achieved from field mapping were included in the kinematic analysis. The kinematic analysis shows that planar sliding, wedge sliding and direct toppling is feasible at steep slopes dipping over  $60^\circ$ . Thus, only considered as feasible failure modes for small rock volumes. Large scale rock slope failure was only considered feasible by a combination of the over  $60^\circ$  NE dipping exfoliation joint set (J1) and the less than  $20^\circ$  NE dipping foliation (SF), making the complex bi-planar sliding a feasible failure mode.

The volume of the potential failed rock masses is estimated to be 3 – 9 million  $\text{m}^3$ . The volume of the displaced masses was estimated to be 2 – 3 million  $\text{m}^3$ . The difference in volume suggest at least one pre-deglaciation event from the same source that deposited onto the glacier. The volume vs. run-out correlation of Prestura is considered similar to the Randa rockslide (Sartori *et al.*, 2003) classifying the failure of the Prestura rockslope as a rockslide, where the failure lasted over several hours. The semi-empirical displacement wave analysis indicate that Prestura created displacement waves when it failed, however the rockslide is now considered dormant. Thus, this site does not present a high hazard at present.

The structural data and geomorphology of the Prestura rockslide has been compared to the Håkåneset rockslope, in order to understand why the Prestura rockslide failed catastrophically while the Håkåneset rockslope has deformed with low rates over a long time. The structural condition is identical at both slopes thus the steepness of the slope is the only difference that can be mapped out. While Prestura has an average slope inclination of  $46^\circ$  has Håkåneset an average slope inclination of  $38^\circ$ , hence Prestura has more slope sections with a dip where failure become kinematically feasible. This is supported by a general relief analysis showing that Tinnsjø is narrower and deeper at Prestura than at Håkåneset, suggesting stronger glacial slope oversteepening at that place.



Quaternary mapping, based on 2x2m resolution bathymetrical data, reveal landforms such as deltas with dunes, terraces interpreted as kame terraces, landslide scars, landslide deposits, and dead ice terrain at the lake floor. The most frequent mapped landform are landslide scars, with highest concentration along terraces close to the unstable slope of Håkåneset. This is considered as evidence of long-lasting movement of the Håkåneset rockslope. This is further supported by the presence of longitudinal ridges on the terrace surface. These are interpreted to be caused by the Håkåneset rockslide inducing into the terrace and bulldozing the sediments in front of the slide. Despite the high amount of landslide scars, no landslide deposits were mapped at the basin floor. This can be explained by the presence of high velocity currents at the bottom of lake Tinnsjø that can also trigger turbidity currents at the basin floor. Such turbidity currents are considered a potential hazard because they can break subaquatic cables. A larger risk to society might represent potential landslide triggered tsunamis from large subaquatic slope failures. When comparing the volumes of the largest subaquatic failures in lake Tinnsjø with other failures elsewhere in Norway such failures have caused considerable landslide- triggered tsunamis. However, in order to assess the hazard sediment characteristics that control the velocity of failure would have to be studied which is not part of this thesis.

## SAMMENDRAG

---

Denne oppgaven tar for seg en analyse av det forhistoriske Prestura skredet og en kvartærgeologisk kartlegging av Tinnsjø. Analysen av Prestura inneholder: strukturell analyse, kinematisk analyse, volumutregninger, empirisk utløpsanalyse og empirisk flodbølge analyse.

Fem ulike sprekkesett er identifisert i området ved systematisk feltkartlegging og bekreftet ved en strukturell analyse av «terrestrial laser scan» (TLS) data. Den kinematiske analysen ble utført basert på de strukturelle dataene hentet i felt og viser at planer utgliding, kileutgliding og blokktoppling er mulig langs bratte skråninger med helning over 60° og kun antatt som mulige bruddmekanismer for små volum. En kombinasjon av det over 60° NØ hellende sprekkesettet (J1) og den slakere enn 20° NØ fallende foliasjonen (SF), gjør den komplekse bruddmekanismen bi-planer utgliding til en mer sannsynlig bruddmekanisme for Prestura skredet.

Volumet av bruddområdet er estimert til 3 – 9 millioner m<sup>3</sup>, mens skredavsetningene har et estimert volum på 2 – 3 million m<sup>3</sup>. Forskjellen i volum mellom bruddområdet og avsetningene tyder på at minst en hendelse med opprinnelse fra samme område som Prestura, oppsto før isbreen hadde smeltet og ble dermed avsatt oppå isbreen. Den empiriske utløpsanalysen av Prestura er lik det som er blitt observert for Randa skredet (Sartori *et al.*, 2003). Derfor er det antatt at bruddmekanismen for Prestura er lik Randa, hvor skredbevegelsen varte over flere timer.

Strukturanalysen av Prestura er blitt sammenlignet med Håkåneset for å forstå hvorfor Prestura skredet ble utløst, mens Håkåneset har blitt sakte deformert over lengre tid. De strukturelle forholdene er identisk ved begge skråningene. Den eneste kartleggbare ulikheten er helningen på skråningene. Prestura har en snitthelning på 46°, mens Håkåneset har en snitt helning på 38°. Derfor er det antatt at Prestura har flere områder hvor brudd er kinematisk mulig enn Håkåneset. Dette støttes ved at Tinnsjø er smalere og dypere ved Prestura enn Håkåneset, som tyder på kraftigere erosjon av skråningen ved Prestura fra isbreen.

Den kvartærgeologiske kartleggingen var utført basert på et 2x2m oppløselig batymetrisk datasett som viser landformer som, delta med dyner, terrasser tolket som kame terrasser, skredgroper og dødis-terreng langs innsjøbunnen. Den hyppigst kartlagte landformen er skredgroper, med høyest konsentrasjon langs terrassene under Håkåneset. Denne økte

konsentrasjonen av skredgroper er antatt som bevis for bevegelse i fjellpartiet. Dette støttes av tilstedeværelsen av langsgående rygger lokalisert oppå samme terrasse. Disse ryggene er tolket som å ha blitt skapt av at den ustabile fjellskråningen (Håkåneset) har beveget seg ned i terrassen og dyttet sedimentene foran fjellskråningen. Til tross for høy konsentrasjon av skredgroper, er ingen skredavsetninger kartlagt på sjøbunnen, dette skyldes mest sannsynlig strømmer med stor hastighet som beveger seg langs sjøbunnen og frakter med seg sedimenter bort fra skredområdene. Disse strømmene kan også ødelegge undersjøiske kabler. En faktor med større sosiale og økonomiske konsekvenser for området er skredutløste flodbølger. En undersøkelse av undersjøiske skred som har utløst flodbølger i Norge er blitt utført og viser at skred av lignende størrelse som de undersjøiske skredene i Tinnsjø har utløst flodbølger tidligere, men for å kunne evaluere farene for flodbølger i Tinnsjø må sedimentegenskapene som styrer hastigheten til skredene bli videre undersøkt, noe som ikke er en del av denne oppgaven.

# ACKNOWLEDGEMENTS

---

This thesis is a part of my Master degree in geology at the Department of Geoscience and Petroleum at the Norwegian University of Science and Technology (NTNU). The master thesis is written in collaboration with the Geological survey of Norway (NGU). My supervisor has been Reginald Hermanns (head of the Geohazard and Earth Observation team at NGU and professor II at NTNU).

First, I would like to thank my supervisor Reginald Hermanns for discussions, review, feedback and guidance on my thesis. I have really learned a lot! I would also thank Raymond Eilertsen at NGU for helping me with the mapping of quaternary landforms. This was a field of study I had little previous experience with, and your feedbacks helped me a lot.

I would also express my gratitude to the rest of the landslide team at NGU, and in particular Martina Böhme and Ivanna Penna for helping me with software details.

I would also thank my friends Charlotte Siggers and Lars Tollefsrud for reviewing this thesis, your comments were of great importance.

Finally, I would like to thank my family and my girlfriend Kristin Enevoldsen for supporting me through last year, and my classmates at NTNU for filling my years at Trondheim with good memories.

# TABLE OF CONTENTS

---

<b>Abstract</b> .....	<b>iii</b>
<b>Sammendrag</b> .....	<b>v</b>
<b>Acknowledgements</b> .....	<b>vii</b>
<b>Table of Contents</b> .....	<b>viii</b>
<b>1 Introduction</b> .....	<b>1</b>
<b>1.1 Systematic mapping approach of large unstable rock slopes in Norway</b> .....	<b>1</b>
<b>1.2 Aim of the study</b> .....	<b>1</b>
<b>1.3 Available data</b> .....	<b>3</b>
<b>1.4 Previous work</b> .....	<b>3</b>
1.4.1 Master thesis and project assignment .....	3
1.4.2 Tunnel excavation reports: .....	3
<b>2 Geology and topography</b> .....	<b>5</b>
<b>2.1 Rock description</b> .....	<b>5</b>
2.1.1 The Rjukan group .....	6
2.1.2 The Vindeggen group .....	7
2.1.3 The Heddal group .....	7
<b>2.2 Tectonics and structures</b> .....	<b>7</b>
<b>2.3 Topography and Geomorphology</b> .....	<b>9</b>
<b>2.4 Quaternary geology</b> .....	<b>12</b>
<b>2.5 Catchment area and climate</b> .....	<b>16</b>
2.5.1 River catchments and discharge .....	16
2.5.2 Precipitation and temperature .....	19
<b>2.6 Historical events</b> .....	<b>20</b>
<b>3 Theory</b> .....	<b>21</b>

<b>3.1</b>	<b>Landslide terminology and classification .....</b>	<b>21</b>
3.1.1	Fall.....	22
3.1.2	Topple.....	22
3.1.3	Slide.....	23
3.1.4	Spread.....	23
3.1.5	Flow.....	23
<b>3.2</b>	<b>Morphologic evolution of a landslide.....</b>	<b>25</b>
<b>3.3</b>	<b>Sediment structures and landforms in lakes and along their shorelines.....</b>	<b>26</b>
3.3.1	Gravitational deposits.....	26
3.3.2	Bedforms .....	26
3.3.3	Delta .....	27
3.3.4	Dead-ice topography .....	28
<b>4</b>	<b>Method .....</b>	<b>30</b>
<b>4.1</b>	<b>Geologic mapping .....</b>	<b>30</b>
4.1.1	Field work .....	30
4.1.2	Sources of error .....	31
<b>4.2</b>	<b>Kinematic feasibility test.....</b>	<b>31</b>
4.2.1	Planar sliding.....	32
4.2.2	Wedge sliding.....	32
4.2.3	Flexural toppling .....	33
4.2.4	Direct toppling.....	34
<b>4.3</b>	<b>Lidar .....</b>	<b>34</b>
4.3.1	Terrestrial Laser scan (TLS) analysis.....	36
4.3.2	Modell creation (steps 1 – 4).....	36
4.3.3	Structural analysis in Coltop-3D (step 5).....	37
<b>4.4</b>	<b>Ante-rockslide topography (ART) and volume estimation.....</b>	<b>38</b>
4.4.1	Manually construction of ART in Polyworks .....	38

4.4.2	Sloping Local Base level (SLBL) .....	39
4.4.3	Minimum eroded volume .....	41
<b>4.5</b>	<b>Empirical run-out analysis and displacement wave analysis .....</b>	<b>41</b>
4.5.1	Empirical run out analysis using the H/L vs Volume correlation .....	41
4.5.2	Empirical displacement wave analysis.....	42
<b>4.6</b>	<b>Bathymetry .....</b>	<b>43</b>
<b>4.7</b>	<b>Catchment delineation and landform mapping in ArcGis .....</b>	<b>45</b>
4.7.1	Catchment delineation.....	45
4.7.2	Landform mapping .....	45
<b>5</b>	<b>Results .....</b>	<b>46</b>
<b>5.1</b>	<b>Geologic mapping .....</b>	<b>46</b>
5.1.1	Main Structures .....	46
5.1.2	Bedrock description.....	48
5.1.3	Joint Sets .....	49
<b>5.2</b>	<b>TLS.....</b>	<b>59</b>
5.2.1	Structural analysis .....	59
5.2.2	Comparison of data from TLS vs data from fieldwork .....	63
<b>5.3</b>	<b>Kinematic analysis.....</b>	<b>64</b>
5.3.1	Introduction .....	64
5.3.2	Planar Sliding .....	65
5.3.3	Wedge sliding.....	66
5.3.4	Flexural toppling .....	67
5.3.5	Direct toppling.....	68
<b>5.4</b>	<b>Morphology and volume estimation of Prestura .....</b>	<b>69</b>
5.4.1	Morphology of the Prestura failure area .....	69
5.4.2	Morphology of the Prestura deposits .....	73
5.4.3	Volume estimation .....	73

5.4.4	Empirical run out vs Volume correlation .....	75
5.4.5	Displacement wave analysis for the Prestura rockslide .....	76
<b>5.5</b>	<b>Short description of the Håkåneset rockslide .....</b>	<b>77</b>
5.5.1	Slope description, structures and simplified profile (from (Sollie, 2014)) .....	77
5.5.2	Domains and kinematic analysis (from (Sollie, 2014)).....	79
5.5.3	New findings from high resolution (2x2m) bathymetrical data .....	81
<b>5.6</b>	<b>Mapping of lake Tinnsjø .....</b>	<b>83</b>
5.6.1	Marginal slope and bedrock outcrops .....	87
5.6.2	Basin floor area .....	87
5.6.3	Delta .....	89
5.6.4	Terraces .....	97
5.6.5	Landslides.....	99
5.6.6	Ravines, channels and furrows .....	105
5.6.7	Depressions and protuberances .....	105
<b>6</b>	<b>Discussion.....</b>	<b>107</b>
<b>6.1</b>	<b>Subaquatic mapping of lake Tinnsjø .....</b>	<b>107</b>
6.1.1	Lake Tinnsjø – a glacially created lake .....	107
6.1.2	Subaquatic landslides .....	109
<b>6.2</b>	<b>New findings show subaqueous movement of the Håkåneset rockslide .....</b>	<b>111</b>
6.2.1	High landslide scar concentration close to the Håkåneset rockslide.....	111
6.2.2	Longitudinal ridges along terraces indicate movement.....	112
<b>6.3</b>	<b>Analysis of the Prestura rockslide.....</b>	<b>116</b>
6.3.1	One single structural domain.....	116
6.3.2	Bi-planar failure mode most feasible .....	116
6.3.3	Landslide classification .....	117
6.3.4	One or multiple events?.....	119
<b>6.4</b>	<b>Prestura and Håkåneset.....</b>	<b>120</b>



6.4.1	One large unstable complex .....	120
6.4.2	Why Prestura? .....	122
<b>6.5</b>	<b>Landslide threat around lake Tinnsjø .....</b>	<b>122</b>
6.5.1	Threat from displacement wave caused by rockslides moving into a lake Tinnsjø 123	
6.5.2	Threat from subaquatic landslides.....	123
6.5.3	Threat from turbidity currents .....	125
<b>6.6</b>	<b>Recommendations for further investigations.....</b>	<b>125</b>
<b>7</b>	<b>Conclusion .....</b>	<b>126</b>
7.1	Structural analysis of the Prestura rockslide.....	126
<b>8</b>	<b>References .....</b>	<b>128</b>
<b>9</b>	<b>Appendix.....</b>	<b>134</b>
9.1	Appendix A: Stereonet from (Statens Vegvesen, 1989).....	134
9.2	Appendix B: Graphic presentation of structural data and Q-value of the Prestura tunnel. From (Statens Vegvesen, 2013).....	135
9.3	Appendix C: Slope map used during the mapping of lake Tinnsjø. Presented from North to south.....	144
9.4	Appendix D: Schmidt hardnes .....	154
9.5	Appendix E: Map with localities, and map with stereonets of the studied area of the Prestura rockslide .....	158
9.6	Appendix F: Alignment diagram (from (Rowland et al., 2007) .....	160
9.7	Appendix G: Table of all volume calculations of landforms mapped in lake Tinnsjø.....	161

# 1 INTRODUCTION

---

## 1.1 SYSTEMATIC MAPPING APPROACH OF LARGE UNSTABLE ROCK SLOPES IN NORWAY

The Norwegian fjord landscape is internationally acclaimed by its beauty, with two of the fjords Geianrgerfjorden and Nærøyfjorden listed in the UNESCO world heritage list (Amelan, 2005). However, the Norwegian landscape is also hiding a devastating landslide hazard. According to Furseth (2006) over 4000 people have lost their lives due to landslide events the last 400 years. Five of the ten most deadly landslide events are related to rockslides (Hermanns *et al.*, 2012).

To cope with such hazards the Geological Survey of Norway (NGU), has since 2005, carried out a national mapping program of unstable rock slopes in Norway (Oppikofer *et al.*, 2016). This is in cooperation and financially supported by the Norwegian Water and Energy Department (NVE) (Hermanns *et al.*, 2013a).

The national mapping program is performed by combining the qualitative hazard and risk classification presented in Hermanns *et al.* (2012), and the quantitative consequence analysis presented in Oppikofer *et al.* (2016). This thesis cover steps 1 – 5 in the qualitatively hazard and risk classification and steps 1 – 3 of the consequence analysis. These steps involve structural mapping and description of the Prestura rockslide, followed by a kinematic feasibility test, volume estimations, simple run out modelling and simple displacement wave analysis.

The national mapping program is divided into six regions. These regions comprise five high priority counties: Møre og Romsdal, Troms, Sogn og Fjordane, Rogaland, Hordaland and the last region “rest of Norway”. Prestura, Håkånes and Tinnsjø is located in the region “rest of Norway”, which cover mostly well-known hazardous slopes located outside the five high priority counties (Morken, 2017, Krogh, 2017, Sollie, 2014).

## 1.2 AIM OF THE STUDY

The aim of this thesis is to describe the prehistoric rockslope failure at Prestura, compare the results to the unstable Håkåneset slope and try to answer why the Prestura rockslide occurred while the Håkåneset slope has not collapsed. This is followed by quaternary mapping of the of

lake Tinnsjø in order to determine the landslide activity and thus better understand the overall landslide threat in the lake. The main objectives are summarized below:

- Detailed mapping of the Prestura rockslide. Involving discontinuity mapping, lateral surface, backscarp location and basal rupture surface description. This is based both on field observations and TLS processing, and followed by a comparison of the Prestura rockslide and the unstable Håkåneset slope.
- Kinematic feasibility test of the structural data to determine possible failure mechanisms at Prestura.
- Volume estimations of the initial and depositional volume of the Prestura rockslide. Using the Sloping local base level (SLBL), Ante rockslide topography (ART) and “minimum eroded volume” methods.
- Bathymetrical mapping of lake Tinnsjø, involving SLBL and “minimum eroded volume” volume estimations of subaquatic landslides and landslide that are deposited from subaerial sources into the lake. This includes mapping of other landforms and their depositional mechanisms, but with focus on landforms considered related to landslide activity. Because of this was not all landforms mapped with the same level of detail.
- A discussion of the potential displacement waves generated when the prehistoric Prestura rockslide moved into lake Tinnsjø.
- A discussion of the potential hazards of the subaquatic landslides mapped in lake Tinnsjø.

### 1.3 AVAILABLE DATA

The detailed mapping of Prestura is based on a 1x1m resolution digital elevation model (DEM), data collected during field work, carried out by the author and Katrine Moe in late June 2017 and Terrestrial laser scans (TLS) achieved in the same period. The bathymetrical mapping is almost purely based on a 2x2 m resolution bathymetrical map achieved from NGU. Other available data is listed in Table 1:

Table 1: Available site-specific data used in this master thesis.

Available data	Source
Master thesis: <i>The Håkåneset rockslide, Tinnsjø</i>	Sollie (2014)
Project Assignment: <i>Håkåneset, Tinnsjø – Geological investigation of potentially rockslide</i>	Sollie (2013)
Preliminary geological report of the road section Rudsgrend – Mæl, (Hd – 855 A)	Statens Vegvesen (1989)
Reports of the upgrading and restoration of the Jønjljo and Prestura (Lauvik) tunnel done in 2011.	Statens Vegvesen (2013)
1x1m resolution topographic DEM.	Hoydedata.no
2x2m resolution bathymetrical map achieved by Nearshore Survey AS in 2015.	NGU, Nearshore Survey AS
1:250 000 Geological map	NGU

### 1.4 PREVIOUS WORK

#### 1.4.1 Master thesis and project assignment

A master thesis and subsequent project assignment, performed by Inger Lise Sollie in 2013 and 2014 cover a structural analysis and numerical modelling of the unstable slope Håkåneset and are summarized in section 5.5.

#### 1.4.2 Tunnel excavation reports:

A preliminary geological report (Hd – 855 A) was performed before excavating the Jønjljo and Prestura tunnels. This report contains bedrock description, structural mapping of weakness zones and joint sets in the area close to Prestura. The stereoplott of data measured close to Prestura are presented in appendix A.

The second report covers the work done when the tunnels were upgraded in 2011. It consists of a tunnel profile created in the software Novapoint. This represents graphically structural data, weakness zones and Q – values of the rock mass along the tunnel section. The Q – value gives an indication of the condition of the rock mass by giving it a score from 0.001 to 1000. Where a lower Q – value indicate weaker rock mass (NGI, 2015). In this thesis the author used the structural data of this report, but did not look into the Q – value, as those are not part of the Norwegian hazard system of unstable rock slopes. However, the Q – values might be useful for creating a numerical stability model.

## 2 GEOLOGY AND TOPOGRAPHY

---

### 2.1 ROCK DESCRIPTION

Figure 1 shows lake Tinnsjø located in the Telemark block in southern Norway. The Telemark block was created as a product of anorogenic magmatism and sedimentation in the Precambrian era and is a part of the Sveconorwegian orogen (Andersen, 2005) in the southern area of the old Fennoscandian (Baltic) shield (Koykka, 2010). The northern part of the Telemark block close to lake Tinnsjø comprises the Telemark supracrustals (Laajoki *et al.*, 2002), previously divided into four groups, from oldest to youngest: the Rjukan group, Seljord group, Bandak group and Heddal group (Dahlgren, 1993, Dons and Jorde, 1979). However, this division has later been modified by Laajoki *et al.* (2002), Koykka (2010) and Lamminen (2011) and been divided into two main successions. The oldest succession “Vestfjorddalen supergroup” was deposited c.1510 – 1347Ma and consist of the Rjukan group and the Vindeggen group. (Laajoki *et al.*, 2002). The younger succession was deposited c.1170 – 1010 Ma on top of the “Vestfjorddalen supergroup” divided by the sub-Svinsaga unconformity. This succession consists of the previously defined Bandak group (Dons, 1960, Dons and Jorde, 1979, Dahlgren, 1993) in the west, now divided into the Eidsborg formation, the Høydalsmo group and the Oftefjell group (Laajoki *et al.*, 2002). In the east does the succession consist of the Heddal group, Lifjell group and the Brunkeberg formation (Laajoki *et al.*, 2002). The following section will further describe the main lithographical groups surrounding lake Tinnsjø.

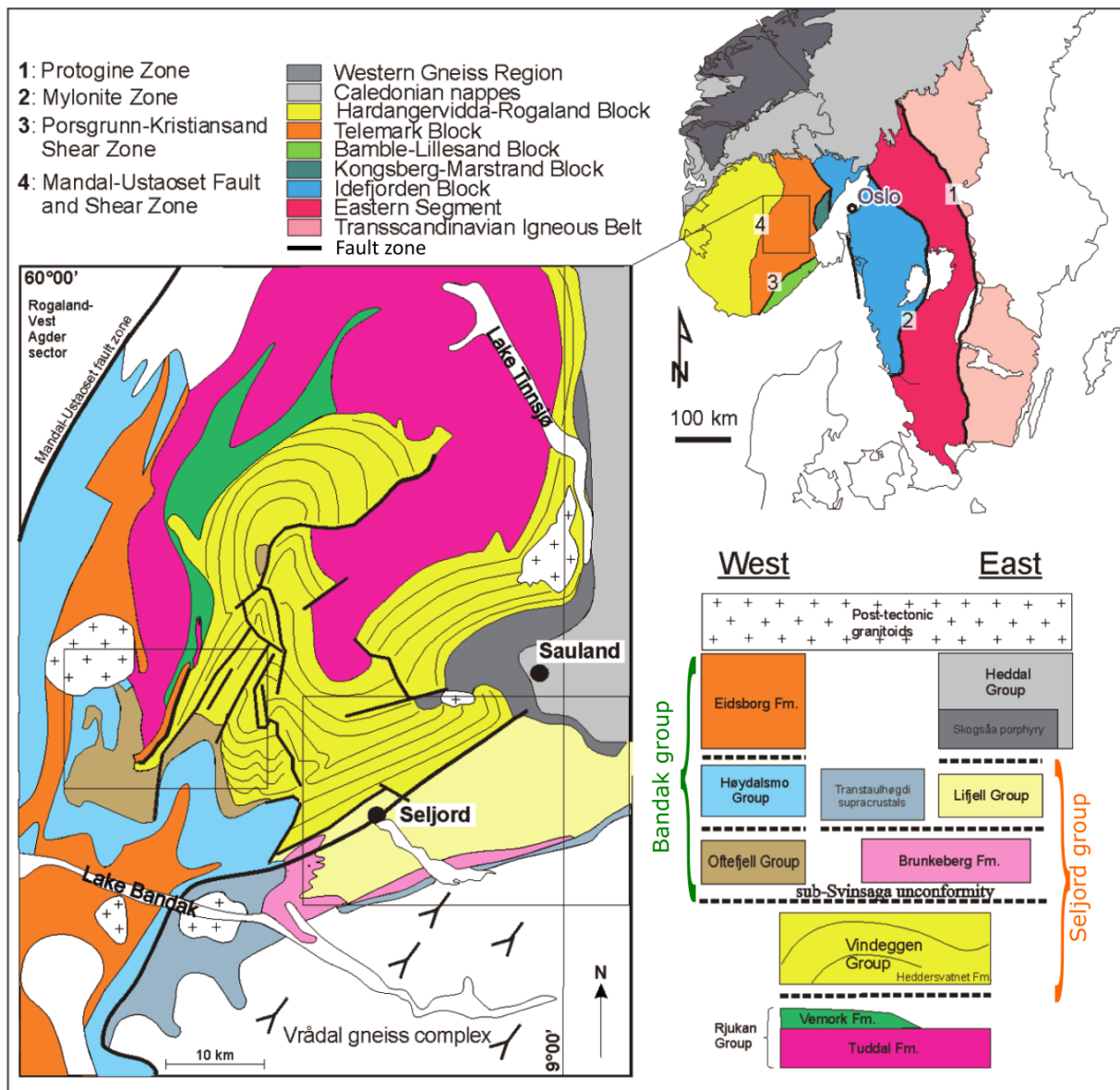


Figure 1: Geological map of central Telemark. The previously defined groups: Bandak group and Seljord group (Dons, 1960, Dons and Jorde, 1979, Dahlgren, 1993) is marked green and orange in the stratigraphic scheme. Modified based on (Lamminen, 2011)

### 2.1.1 The Rjukan group

The Rjukan group consist of the Tuddal formation, dominated by continental felsic rocks (Lamminen, 2011) such as rhyolites and tuffs (volcanic ash) (Dahlgren, 1993). Overlain by the Vemork formation, characterised mainly by mafic volcanic rocks (Lamminen, 2011). As seen from Figure 1, the Tuddal formation covers approximately 60-70% of the area surrounding Lake Tinnsjø. As seen from Figure 2, the Prestura rockslide and the unstable slope at Håkåneset occur inside the Rjukan group.

### **2.1.2 The Vindeggen group**

The Vindeggen group consists of several sandstone and mudstone formations, which are faulted at several locations (Lamminen, 2011). The Vindeggen group is located at the southern area of lake Tinnsjø, covering approximately 30% of the area around the lake.

### **2.1.3 The Heddal group**

The Heddal group consist of feldspar rich sandstones, felsic rocks, conglomerates and a few thin marble layers (Laajoki *et al.*, 2002, Dahlgren, 1993) mapped east of lake Tinnsjø.

## **2.2 TECTONICS AND STRUCTURES**

The area is dominated by big syn – and antiforms with north-north-west (NNW) or north-north-east (NNE) axial orientation in addition to faults and weakness zones mainly having a NE or NW strike. East of Lake Tinnsjø is a Precambrian thrust nappe striking to the NE located (Dons and Jorde, 1979). According to Statens Vegvesen (1989) there are two weakness zones similar to the Precambrian thrust nappe located west of lake Tinnsjø. The most pronounced zone follows the coastline in a NW-SE direction and consist of crushed rock fragments welded together by white hydrothermal quartz and calcite (named regional weakness zone 1 in Figure 2). The other regional weakness zone crosses the Jønjljo tunnel south of Prestura, further named the Jønjljo weakness zone in this thesis. This weakness zone got a thick cover of soil and vegetation, thus a precise description is hard to give (Statens Vegvesen, 1989). Despite the lack of direct observations, it seems that the rock is not as much welded together as the weakness zone along the coast (Statens Vegvesen, 1989).

The sub-Heddersvatnet unconformity, between the Vindeggen group (Seljordgruppen in Figure 2) and Rjukan group (Lamminen, 2011), is located east of the Jønjljo weakness zone.



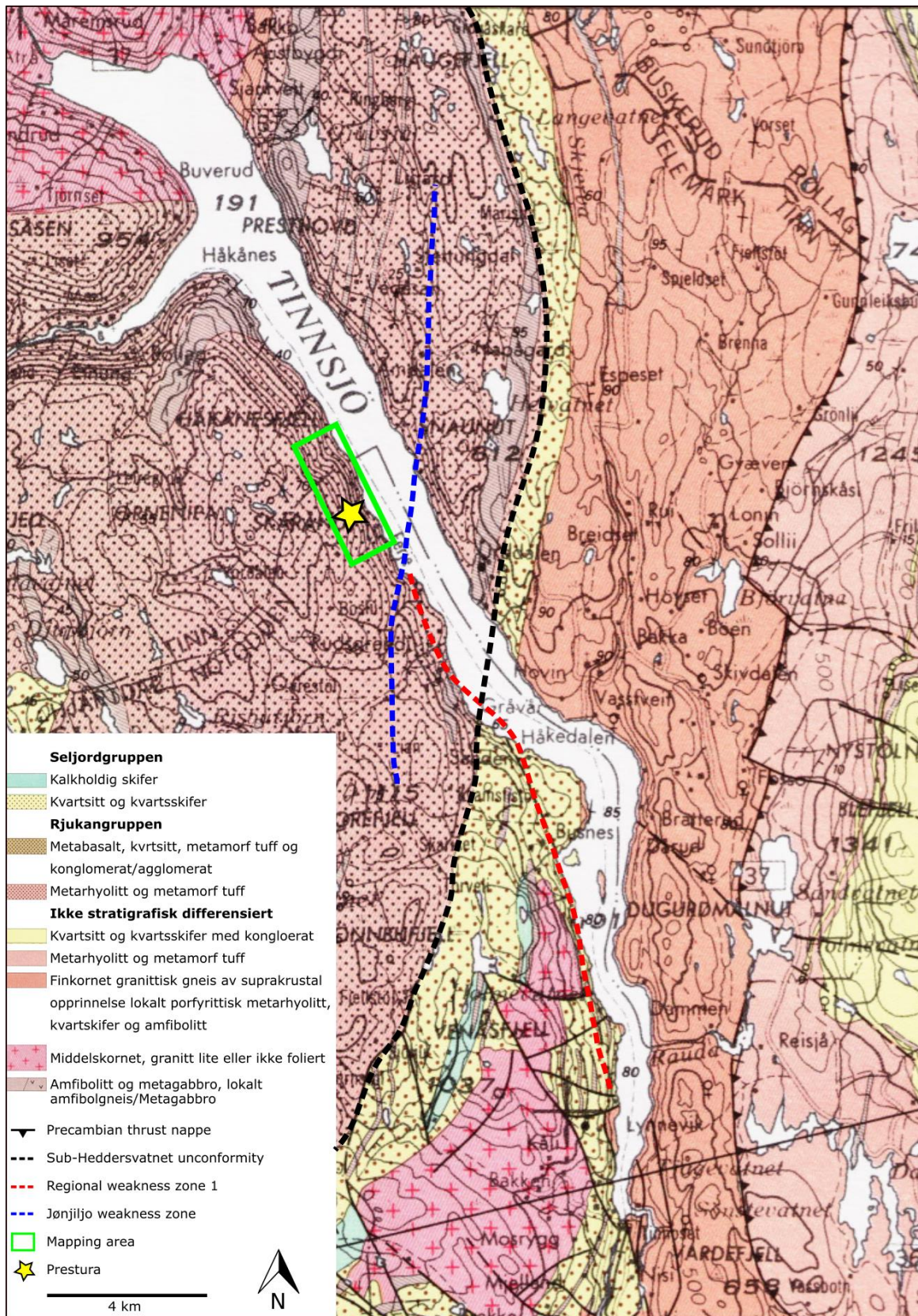


Figure 2: 1:250 000 geological map of areas surrounding lake Tinnsjø. Modified from (Dons and Jorde, 1979), with added regional weakness zones marked by dashed lines collected from (Statens Vegvesen, 1989, Lamminen, 2011).



## 2.3 TOPOGRAPHY AND GEOMORPHOLOGY

Lake Tinnsjø (Figure 3) is located in Tinn and Notoden municipality. The lake covers 51.4 km<sup>2</sup> and is 35 km long, having a water level between 187-191 metres above sea level (m a.s.l.), as a result of regulation of the sea level due to a hydropower plant localized along the river Tinne (Lundbo, 2017). New bathymetrical data (NGU 2015) shows that Lake Tinnsjø has a maximum depth of 440 meters, it is considered the 4<sup>th</sup> deepest lake in Norway (Askheim, 2017).



*Figure 3: Photo of lake Tinnsjø taken from air looking southward. From (Güettler, 2013)*

Several deep valleys and lakes are located in Telemark (Sundal, 2015). These valleys and lakes have been created by ice, eroding the old pelagic surface (Jansen, 1986). The pelagic surface was created during the Mesozoic and early Cenozoic era (Mangerud and Vorren, 2013) by levelling the rests of the Caledonian mountain chain to the sea level, creating a flat surface. Examples of remaining pelagic surfaces in Norway are Finnmarksvidda and Hardangervidda (Mangerud and Vorren, 2013). The latter is located west of lake Tinnsjø and covers parts of the catchment area of the lake.

Along the longitudinal profile of the valleys, several depressions are observed, which result from a local increase in glacial erosion (Jansen, 1986, Sundal, 2015). These depressions have later been filled with water which created the big lakes in the area, such as lake Tinnsjø, lake Bandak and Møsvatn. The common factor between all of the big depressions in the area, is that they are localised downstream of the junction of several valleys (Figure 4). This make it possible for several ice streams to merge and create a thick ice cover,

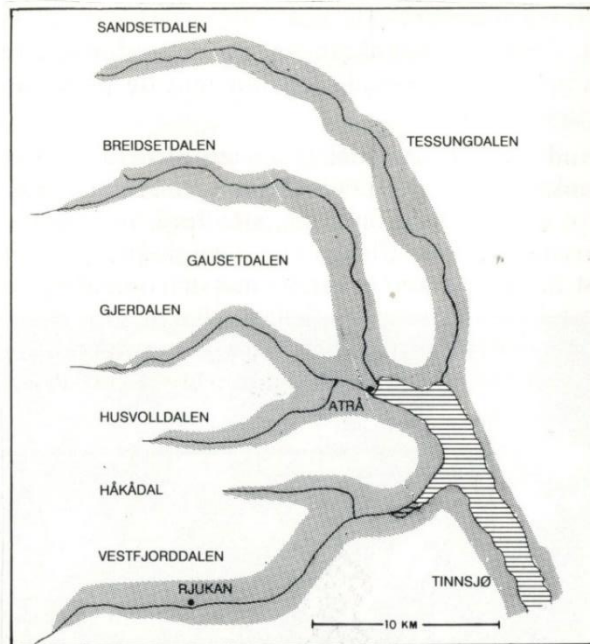


Figure 4: Several valleys merging into the northern parts of Lake Tinnsjø. From (Jansen, 1986)

capable of eroding the landscape. This explains why Lake Tinnsjø is surrounded by steep mountainsides and are much deeper than other lakes in the area (Jansen, 1986), being over 100 meters deeper than the second deepest lake in the area, lake Bandak (Askheim, 2017). Today are the surrounding ice filled valleys substituted with rivers, having catchment areas up to 700 km<sup>2</sup> (NVE, 2018a), eroding the valley and transporting sediments into lake Tinnsjø.

On the western shore of Lake Tinnsjø is the unstable slope Håkåneset localized. Håkåneset is a part of the Norwegian geological survey's (NGU) surveillance program. A potential rock avalanche might create displacement waves with potential hazardous consequences around the lake shore (Sollie, 2014). NGU's mapping program for unstable rockslopes is focusing on defining this hazard. However, preliminary displacement measurements (Sollie, 2014) indicate that deformation rates of today are very low. A similar event, which also might have created displacement waves, is the Prestura rockslope failure, located 2 km south of Håkåneset (Figure 5).



*Figure 5: 3D image of the unstable Håkåneset rockslide to the right and the prehistoric Prestura rockslide to the left. Located at the western margin of lake Tinnsjø. The outline of Håkåneset is defined by Sollie (2014), based on old bathymetrical data. Modified from Google earth.*



## 2.4 QUATERNARY GEOLOGY

Figure 6 shows the extension of the Scandinavian ice cap for the last 110 000 years. The last glacial maximum (LGM) is illustrated in light blue, occurring 18 000 – 25 000 years ago, stretching into Denmark and northern Europe (Mangerud and Vorren, 2013), 3 km thick at its core (Olsen *et al.*, 2013). The maximum altitude of the ice surface is estimated at approximately 2200 m a.s.l. close to Tinnsjø (Sundal, 2015), having a potential thickness of over 2600 meters at the centre of the lake.

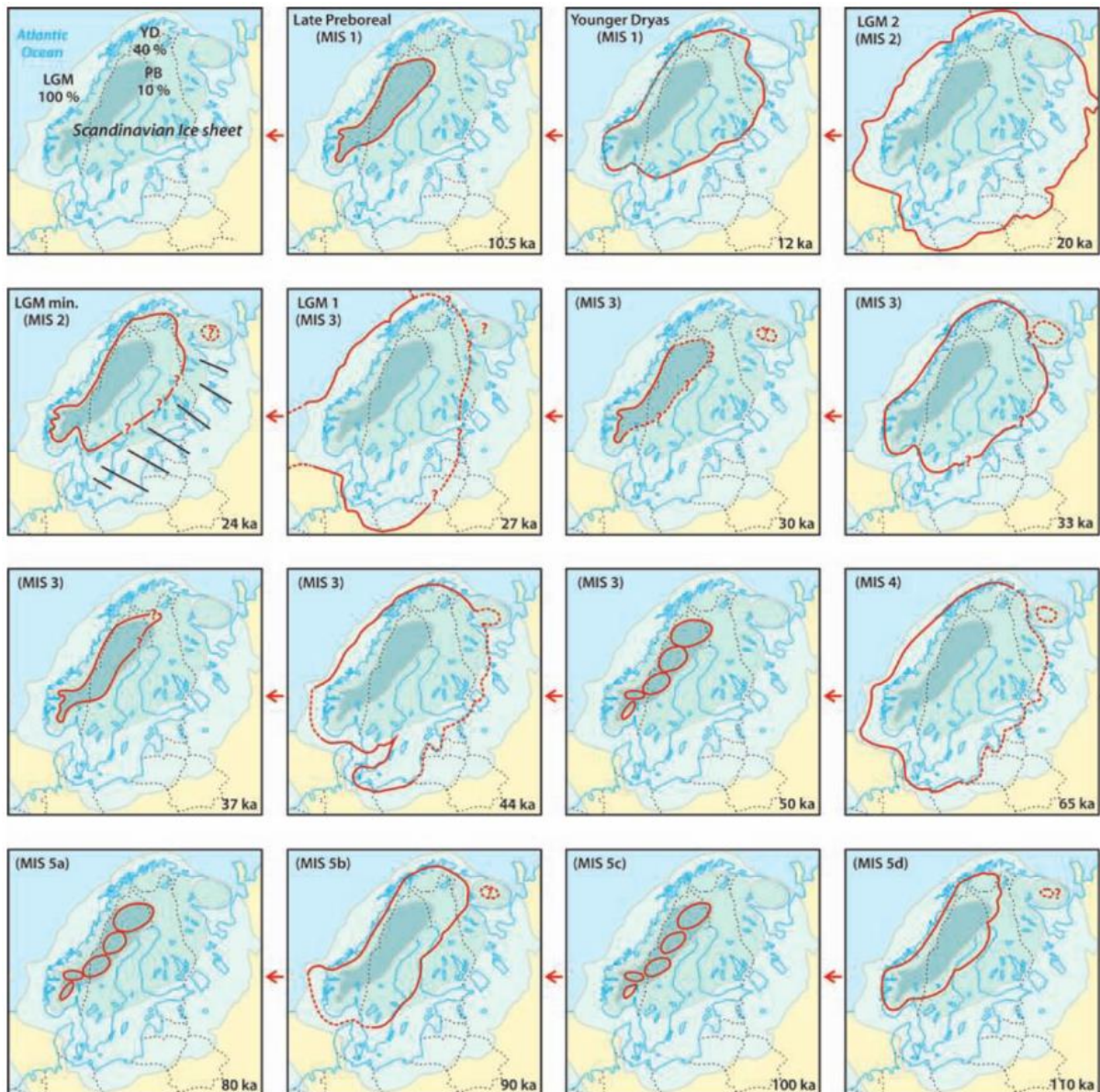


Figure 6: Extension of the Scandinavian ice sheet during the last 110 000 years. The LGM extension is marked light blue on all maps. The younger dryas extension (YD) is marked blue while the Preboreal (PB) is marked dark blue. The red line represents the extension of the different stages trough time. From (Olsen *et al.*, 2013)

The ice divide of the Scandinavian ice sheet was first positioned along the main watershed of Norway (Mangerud and Vorren, 2013) illustrated in Figure 7. Later, it moved south east, covering an area stretching from Gudbrandsdalen in west to the Gulf of

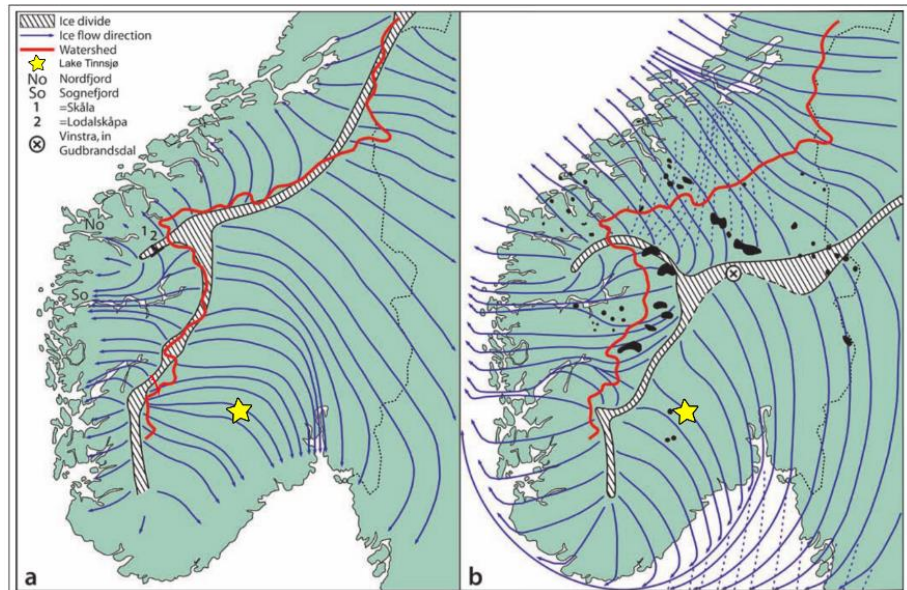


Figure 7: Major ice movement and ice divide in southern Norway during small to moderate ice extension (a) and during the LGM (b). The black spots in map (b) is blockfields. Modified from (Olsen *et al.*, 2013).

Bothina in the east (Mangerud and Vorren, 2013). From the ice divide, the ice flowed in valleys through the mountain range and finally deposited at the continental shelf (Olsen *et al.*, 2013). Lake Tinnsjø is marked by a yellow star in Figure 7, located along the south-eastern ice movement, which is also parallel to the longitudinal axis of lake Tinnsjø.

The terminal moraines observed in Telemark is illustrated in Figure 8, where the oldest Ra moraine occur at Jumfruland in south, while the youngest terminal moraines are found close to Gransherad 5 km south of Tinnsjø (Jansen, 1986). This moraine correspond to Hauersætertrinnet in Romerike (Jansen, 1986), which is deposited by meltwater, creating kame deltas (Mangerud and Vorren, 2013).



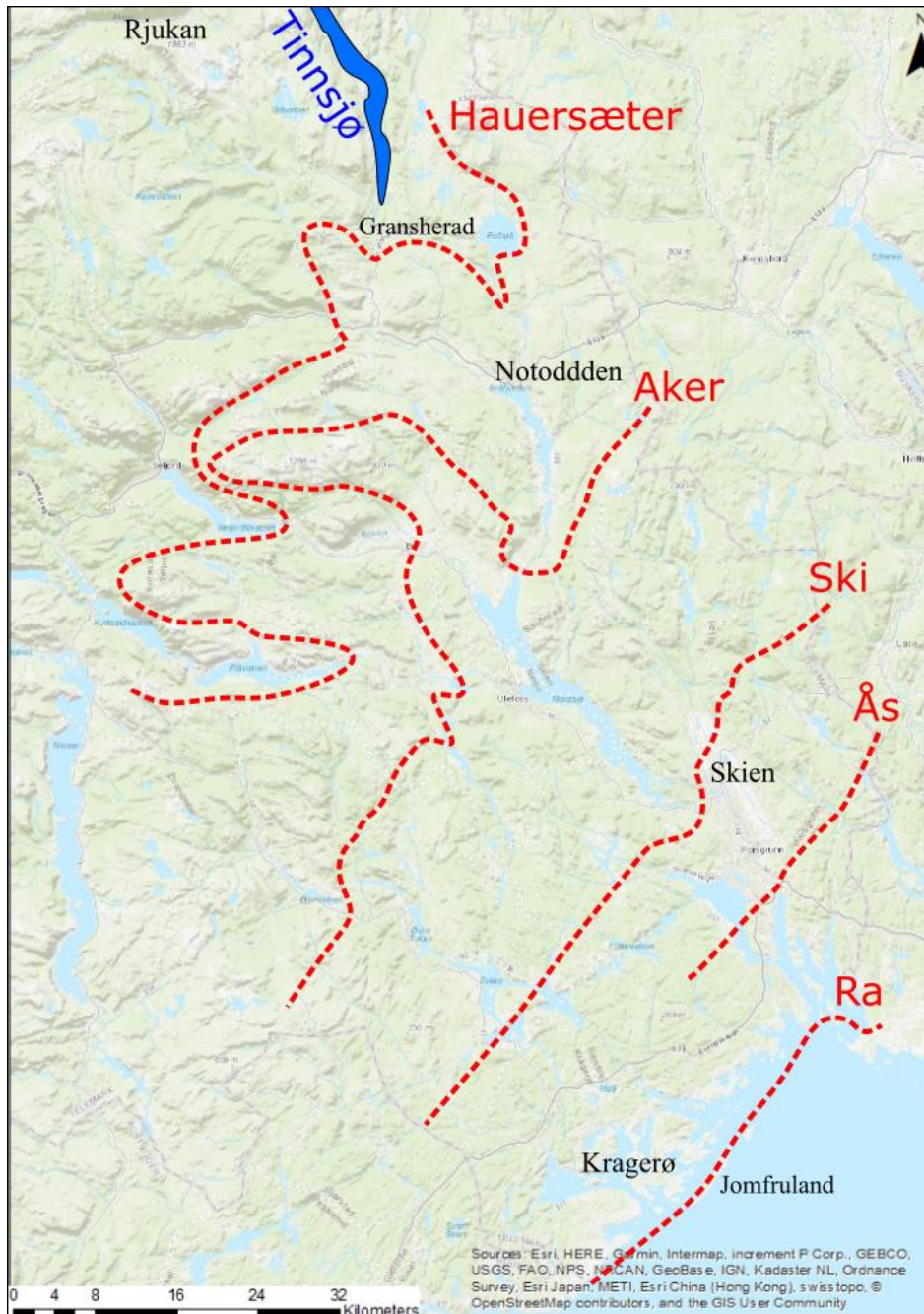


Figure 8: Map of central Telemark with location of terminal moraines marked red, Tinnsjø is highlighted in blue. Modified from (Olsen *et al.*, 2013, Jansen, 1986)

Figure 9 shows that the deposits around Tinnsjø are mainly moraines of various thickness. Exceptions are around the rivers in the north and close to Hovin and Tinnoset in south, where fluvial and glacial deposits can be found. The marine limit in the area is located at 171 m a.s.l. south-east of Gransherad (NGU, 2017), showing that the lake never was a part of a fjord system. This is in contrast with lake Bandak further south (Eilertsen *et al.*, 2016). At the highest mountains, such as Gaustatoppen and Blefjell, blockfields are located. These blockfields have been sources of discussion for the last 100 years (Mangerud, 2004).

Blockfields have been used as evidence for the presence of mountain peaks protruding the ice cover (nunataks) during the LGM (Olsen *et al.*, 2013, Mangerud, 2004). However, according to Sundal (2015), the ice surface is estimated to be at 2200 m a.s.l in the area, which is higher than for both Gaustatoppen (1883 m a.s.l.) and Blefjell (1342 m a.s.l.). Thus, the LGM ice cover did also cover these mountaintops.

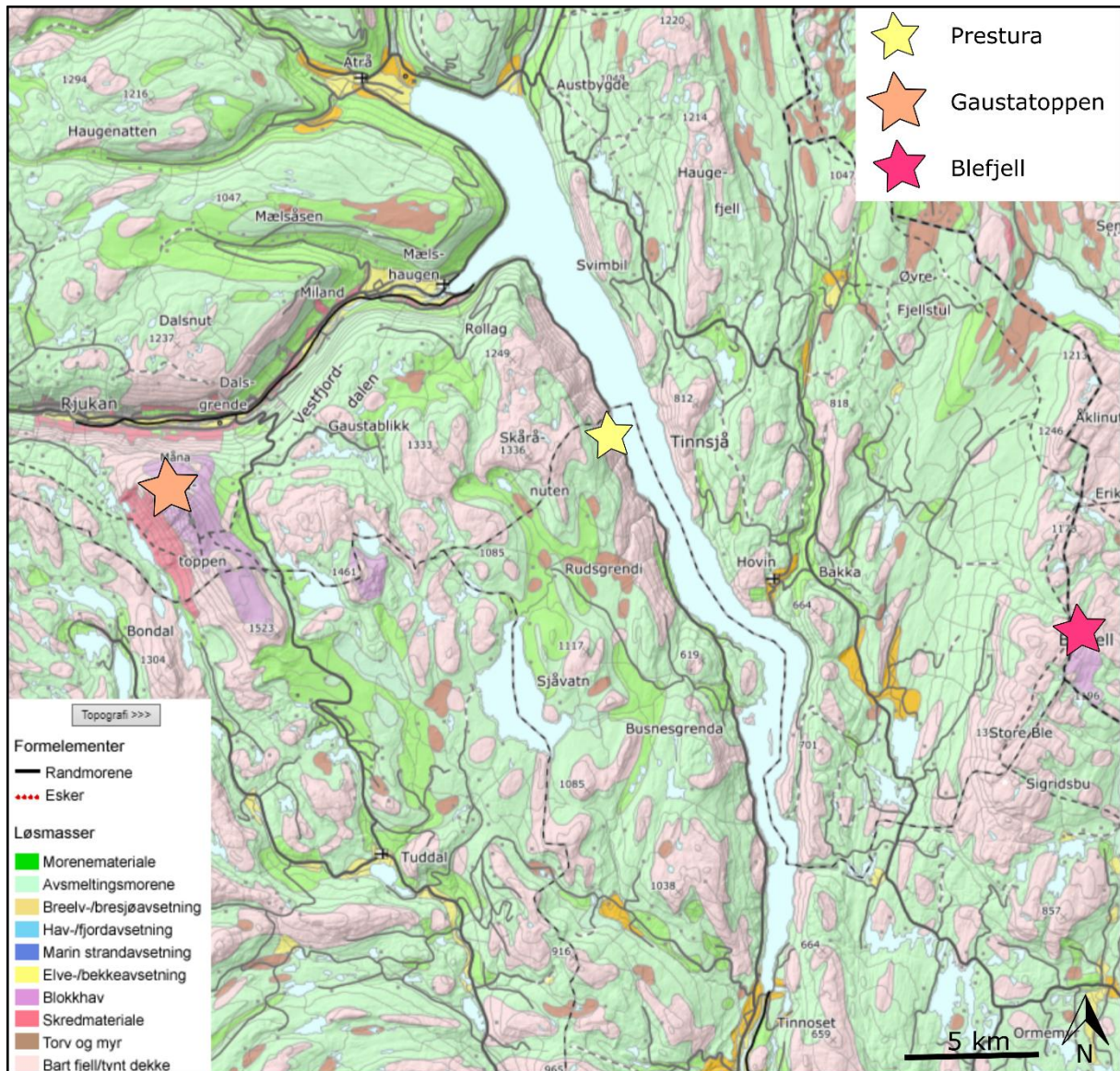


Figure 9: Quaternary deposits around Lake Tinnsjø. Glacifluvial deposits occurs at Tinnoset, Hovin, Austbygde and Åtra. Modified from (NGU, 2017)



## 2.5 CATCHMENT AREA AND CLIMATE

### 2.5.1 River catchments and discharge

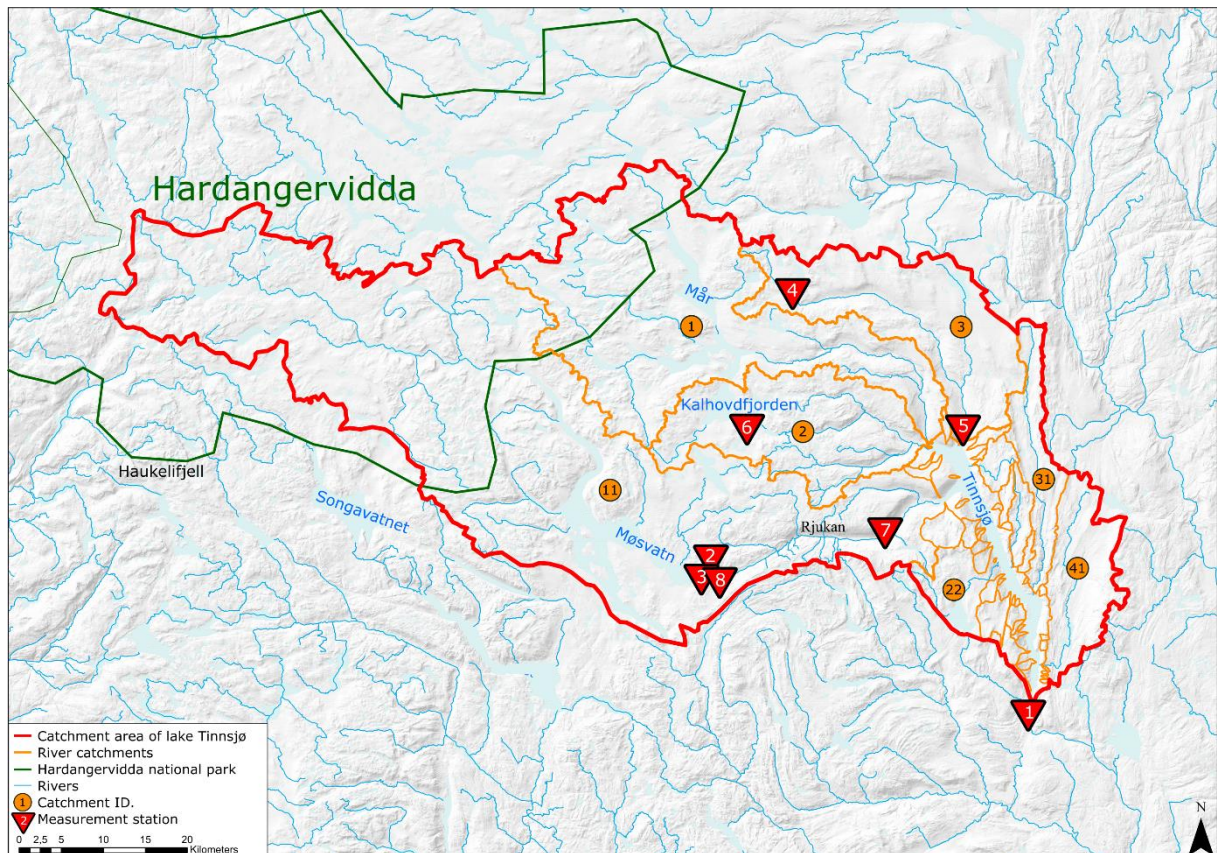


Figure 10: Illustration of the Tinnsjø catchment, covering an area of 3770 km<sup>2</sup>. The 7 largest river catchment is marked with its catchment ID.

The catchment area of Lake Tinnsjø is shown in Figure 10 and covers an area of 3 770 km<sup>2</sup> (NVE, 2018) stretching from Hardangervidda in the west to Tinnsjø in the east. This catchment is part of Skienvassdraget, which is the third largest catchment in southern Norway and covers an area of 10 772 km<sup>2</sup> (NVE, 2018).

The Tinnsjø catchment is further divided into sub-catchments, marked orange in Figure 10 and Figure 11, representing the catchment area of rivers which flows into lake Tinnsjø. The areas of these sub-catchments are presented in Table 2.

The biggest sub-catchments are in the north, being the source of the following major rivers: Månå, Mår, Austbygdåi and Gøyst, covering a combined area of 3190 km<sup>2</sup>. There are also observed several catchments further south with areas over 50 km<sup>2</sup>, but the largest of the southern catchments (Raua) covers less than half the area of the smallest major catchment in the north (Mår).

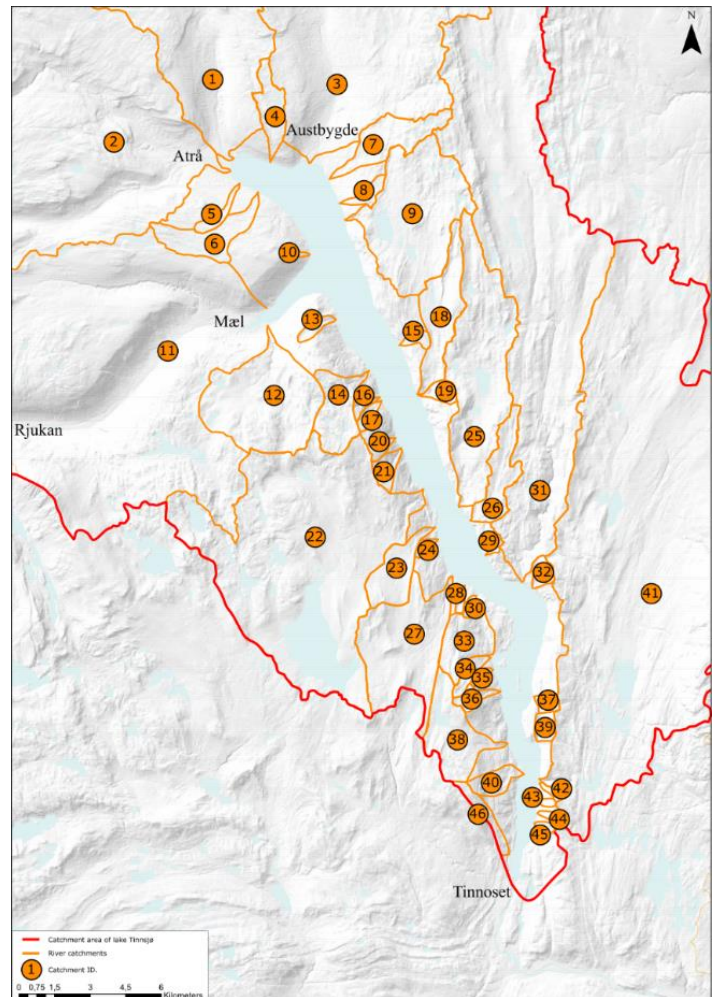


Figure 11: Zoomed image of Tinnosjø, illustrating all river catchments, marked orange.

Table 2: Representation of all rivers flowing into Timmsjø and its calculated catchment area. Data from (NVE, 2018a) and own measurements using the software ArcMap (ESRI, 2017a).

Catchment ID	River name	Catchment area (km <sup>2</sup> )
1	Mår	320.26
2	Gøyst	753.70
3	Austbygdåi	344.42
4	Midtsrandbekken	3.12
5	Spellebekk	0.89
6	Stream 1	4.71
7	Tjyru	5.31
8	Sprettedokkje	0.99
9	Gjuvåi	20.3
10	Stream 2	0.31
11	Månå	1772.43
12	Rollagåe	16.98
13	Kvennebekk	0.76
14	Bjørnebekken	5.12
15	Stream 3	0.68
16	Stream 4	0.45
17	Stream 5	0.56
18	Grasdåle	7.15
19	Holbekk	0.96
20	Prestura stream	0.72
21	Stream 6	1.27
22	Digeråi	64.83
23	Rudsåi	4.37
24	Hovedbekken	0.39
25	Urdalsåi	22.38
26	Stream 7	4.61
27	Haukedalsåi	14.97
28	Stream 8	0.33
29	Stream 9	0.29
30	Bjønnåsbekken	0.41
31	Skirva	103.1
32	Stream 10	0.95
33	Luåa	4.45
34	Fjøshaugbekken	1.12
35	Stream 11	0.34
36	Stream 12	0.93
37	Stream 13	0.59
38	Bergåa	7.13
39	Stream 14	0.98
40	Kyrsbekk	1.75
41	Raua	148.07
42	Stream 15	0.28
43	Stream 16	0.21
44	Stream 17	0.20
45	Stream 18	0.38
46	Stream 19	1.55

## Discharge measurements

The annual discharge from the measurement stations, illustrated in Figure 10 are presented in Table 3. The data was collected from NVE (2018b), representing the mean annual discharge.



The only measurement station available that represents the discharge of a river mouth, is the station located in the Austbygdåi river. The other stations are either located to far upstream or only covering tributary rivers, thus not representing the discharge located at the river mouth.

Table 3: Annual discharge values from measurement stations surrounding lake Tinnsjø. Data from (NVE, 2018b)

ID	Measurement station	Annual discharge (m <sup>3</sup> /s)
1	Kirkoll bru	38367
2	Groset tjern	44.5
3	Møsvatn	1924
4	Viertjern	424
5	Austbygdåi	3003
6	Strengen	5886
7	Mår kraftverk	1727
8	Frøystul kraftverk	19030

### 2.5.2 Precipitation and temperature

Figure 12 shows the mean yearly distribution of precipitation in Norway from 1961 to 2017. Tinnsjø and its catchment area is marked in red. This area has a variation in yearly precipitation from 1000mm to 3000mm, showing significantly lower precipitation rates at the eastern side of lake Tinnsjø than to the west. The mean annual temperature is 2-4 degrees Celsius close to Lake Tinnsjø, while at western end of the catchment area the mean temperature is just below 0 degrees Celsius.

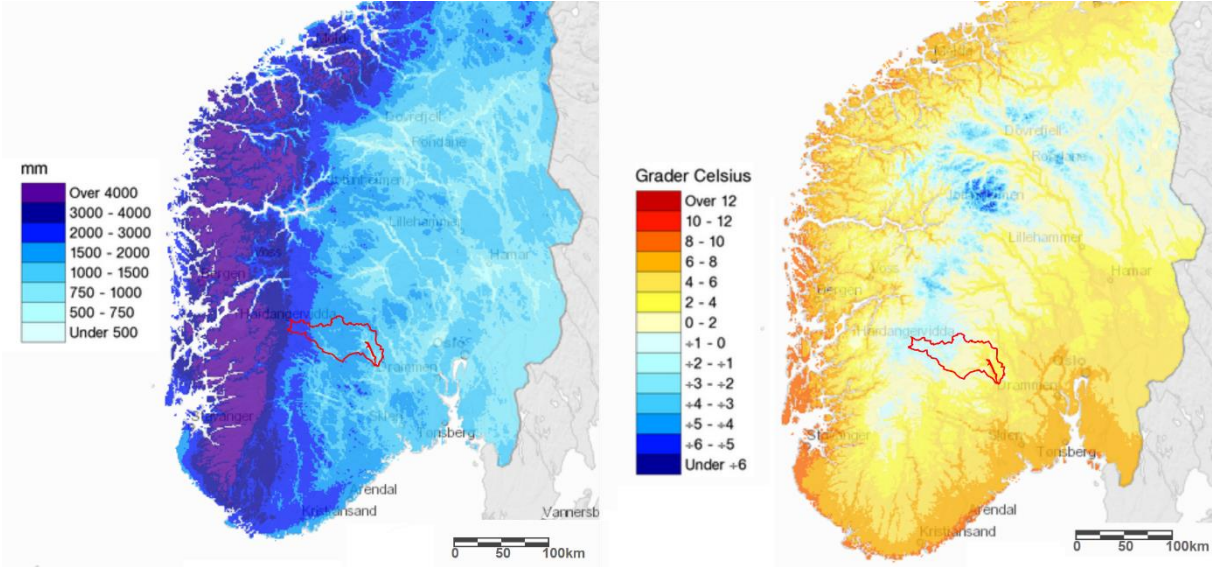


Figure 12: Map of southern Norway showing. Normal annual precipitation (1971-200) to the left. Normal annual temperature (1971-2000) to the right. Modified from (SeNorge.no).

## 2.6 HISTORICAL EVENTS

All data used in this section are collected from the “skredhendelsesdatabase” provided by the Norwegian Water and Energy department (NVE). This database consists of information related to all historically recorded geohazard events in Norway. The major contributors to this database is the national road authorities (Statens Vegvesen), the Norwegian national rail administration (BaneNor), the Geological Survey of Norway (NGU) and the Norwegian Geotechnical Institute (NGI)(NVE, 2018c). In addition, it is also possible for private actors to document events using the web page [www.skredregistrering.no](http://www.skredregistrering.no).

A total of 254 events are recorded along the shore of lake Tinnsjø (Figure 13). 241 events are recorded along the west shore, with highest concentration of events located between the Håkåneset instability in the north and the Jønjljo tunnel in the south (153 events) (NVE, 2018d). The most common type of events in this area is rockfall, with 123 recorded events.

The increasing frequency of events recorded at the west shore compared to the east, can be explained by the construction of Tinnsjøvegen, because of undercutting of the natural slope, but also due to an increased recording of events by the road authorities (Sollie, 2014).

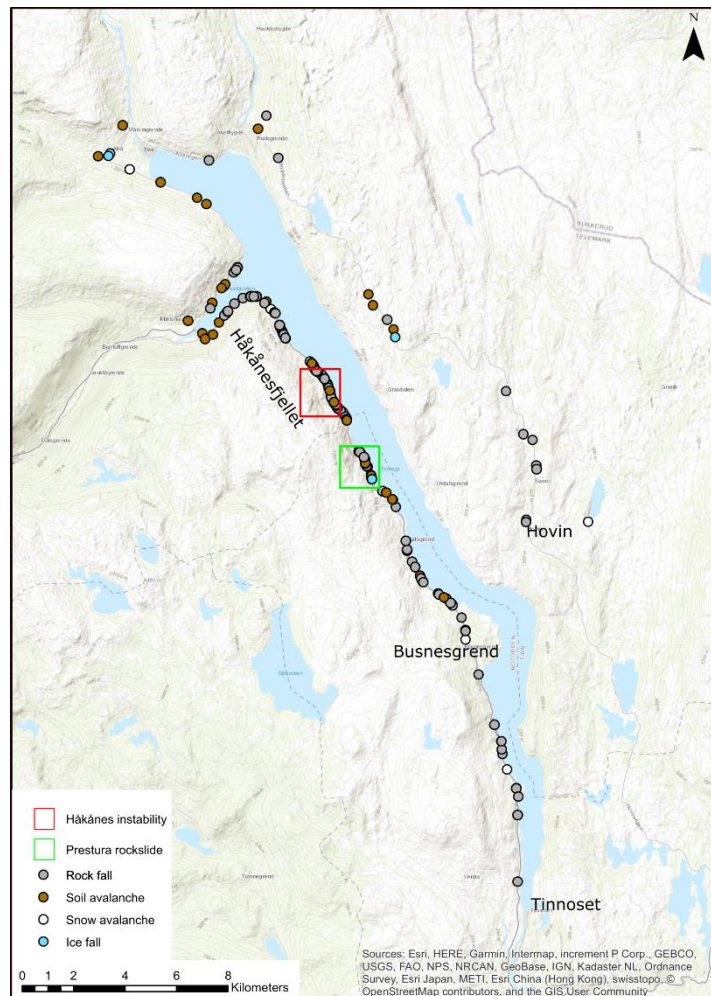


Figure 13: Map of recorded historical landslide and rock fall events along lake Tinnsjø. Data collected from (NVE, 2018d)

## 3 THEORY

---

### 3.1 LANDSLIDE TERMINOLOGY AND CLASSIFICATION

A landslide is the downslope movement of rock, soil or organic material under the effect of gravity and landform that result from this movement, morphologically described in Figure 14 (Highland and Bobrowsky, 2008).

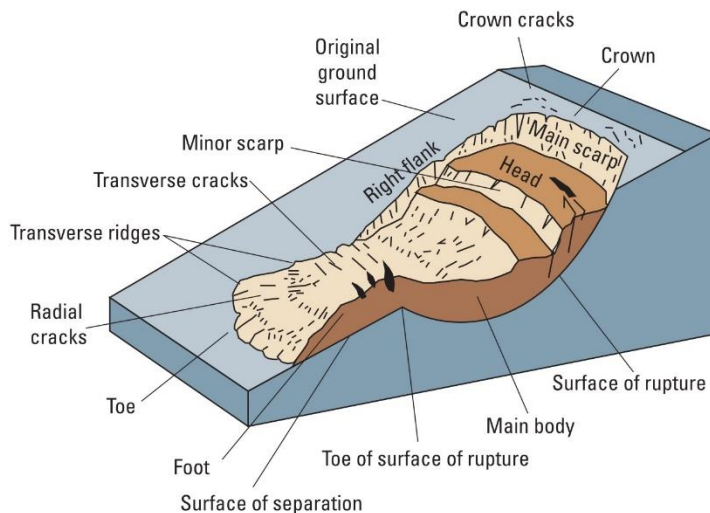


Figure 14: Simple illustration of a rotational slide, with commonly used names of the different parts of the landslide. From (Highland and Bobrowsky, 2008)

Landslides are divided based on its material and movement type. The different materials are usually rock and soil (debris or earth)(Highland and Bobrowsky, 2008). However, in the Norwegian literature the term “skred” (landslide in Norwegian) does also cover snow as a landslide material (Hermanns *et al.*, 2013a). In Norway is the classification of rock slope failure often subdivided into three different types: Rockfall areas, Rockslide areas and Complex fields (Braathen *et al.*, 2004). However, the internationally most common classification of landslides is the Varnes classification (Varnes, 1978) later modified by Hungr *et al.* (2014). This classification system is presented in Table 4, followed by a brief description of the different types of movement.

Table 4: Modified version of the varnes classification system. From (Hungr *et al.*, 2014)

Type of movement	Rock	Soil
Fall	1. Rock/ice fall <sup>a</sup>	2. Boulder/debris/silt fall <sup>a</sup>
Topple	3. Rock block topple <sup>a</sup>	5. Gravel/sand/silt topple <sup>a</sup>
	4. Rock flexural topple	
Slide	6. Rock rotational slide	11. Clay/silt rotational slide
	7. Rock planar slide <sup>a</sup>	12. Clay/silt planar slide
	8. Rock wedge slide <sup>a</sup>	13. Gravel/sand/debris slide <sup>a</sup>
	9. Rock compound slide	14. Clay/silt compound slide
	10. Rock irregular slide <sup>a</sup>	
Spread	15. Rock slope spread	16. Sand/silt liquefaction spread <sup>a</sup>
		17. Sensitive clay spread <sup>a</sup>
Flow	18. Rock/ice avalanche <sup>a</sup>	19. Sand/silt/debris dry flow
		20. Sand/silt/debris flowslide <sup>a</sup>
		21. Sensitive clay flowslide <sup>a</sup>
		22. Debris flow <sup>a</sup>
		23. Mud flow <sup>a</sup>
		24. Debris flood
		25. Debris avalanche <sup>a</sup>
		26. Earthflow
		27. Peat flow
Slope deformation	28. Mountain slope deformation	30. Soil slope deformation
	29. Rock slope deformation	31. Soil creep
		32. Solifluction

### 3.1.1 Fall

Falls are sudden movements of rock, earth or both, that detach from steep cliffs or slopes. The failed material usually collides with the lower slope causing bouncing or rolling further downslope (Highland and Bobrowsky, 2008). According to Domaas and Grimstad (2014) is the material defined as single blocks (usually rocks) with a volume of less than 100m<sup>3</sup> not interacting with each other during the downslope movement.

### 3.1.2 Topple

Toppling is defined by Highland and Bobrowsky (2008) as forward rotation of unstable material out of slope, driven by the change in the centre of gravity in the unstable rock masses downslope.

Toppling are further divided into two different categories (Hungr *et al.*, 2014):

#### 1. Rock block topple:

Rock block topple is the forward rotation of columns, plates or blocks separated by steeply dipping joints oriented into the slope. Rock block topple often occurs when steep joints dipping into the slope is combined with shallow dipping surfaces creating

unstable blocks (Hungr *et al.*, 2014). This failure mechanism is often called direct toppling (Hudson and Harrison, 2000).

## **2. Flexural toppling:**

Flexural toppling occurs in weak rock masses, often in bedded shale or slates where orthogonal joints are not well developed (Wyllie and Mah, 2004). Since the rock mass is weak, the unstable rock mass will start to bend when its centre of gravity is moved instead of creating joints. Resulting in an overturn of the rock mass (Hungr *et al.*, 2014).

### **3.1.3 Slide**

A slide is according to Highland and Bobrowsky (2008) a downslope movement of rock, earth or both, occurring on rupture surfaces or at zones of intense shear strain. The main types of slides are planar/translational, rotational and wedge sliding (Figure 15).

### **3.1.4 Spread**

Spreads occur often at very gentle slopes and is created by the subsidence of fractured rock masses into a weaker underlying material leading to liquefaction or flow in the underlying material (Highland and Bobrowsky, 2008). An example of a spread is quick clay events, with back tilted benches, or horst and graben, where features of intact rock is present (Hungr *et al.*, 2014).

### **3.1.5 Flow**

A flow is a continuous movement of material where shear-surfaces are short lived, closely spaced and often not preserved (Highland and Bobrowsky, 2008). Some examples of flows are: rock avalanche (sturzstrom), debris flows, debris avalanche, earthflow (often quick clay) and creep (Hungr *et al.*, 2014).

If a flow occur under or into a body of water, the failed masses will be suspended, transforming the flow into a turbidity current, which move at high velocities along the basin floor (Kvalstad, 2014). Because of this is subaquatic landslides often associated with turbidity current generation (Schulten *et al.*, 2018, Clare *et al.*, 2016).



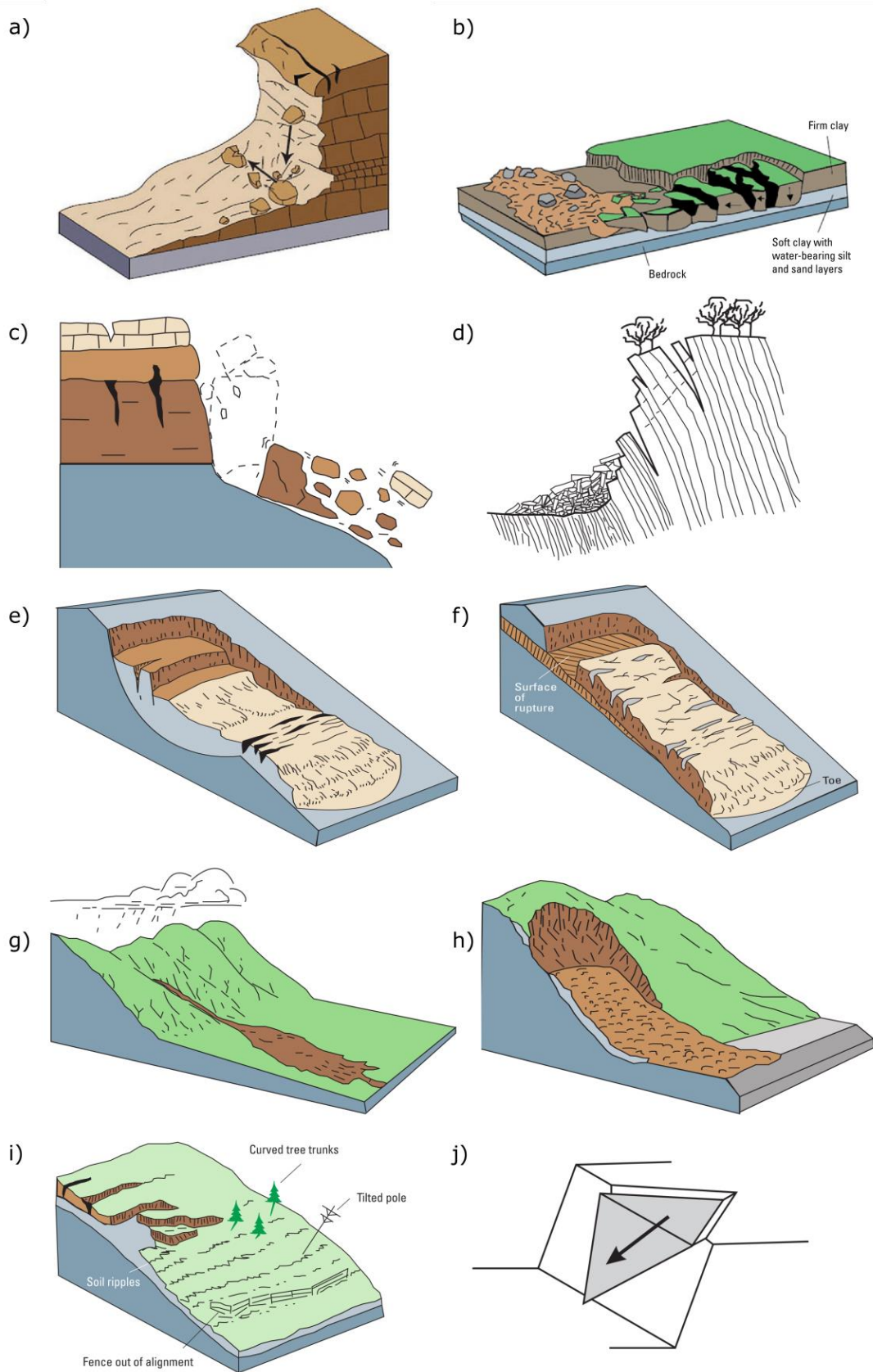


Figure 15: Illustration of different movement types: a) rock fall b) spread c) direct toppling, d) flexural toppling, e) rotational sliding, f) planar sliding, g) debris flow, h) debris avalanche, i) creep, j) wedge sliding. From (Highland and Bobrowsky, 2008, Wyllie and Mah, 2004)

### 3.2 MORPHOLOGIC EVOLUTION OF A LANDSLIDE

A landslide scar changes its morphology with time, gradually from sharp and well defined, to poorly defined almost invisible features. The key features are main scarp, lateral flanks, internal morphology, vegetation cover and toe relationships (Turner and Schuster, 1996). The different morphologic stages are defined from active or recently active to dormant-old and is described in Figure 16.

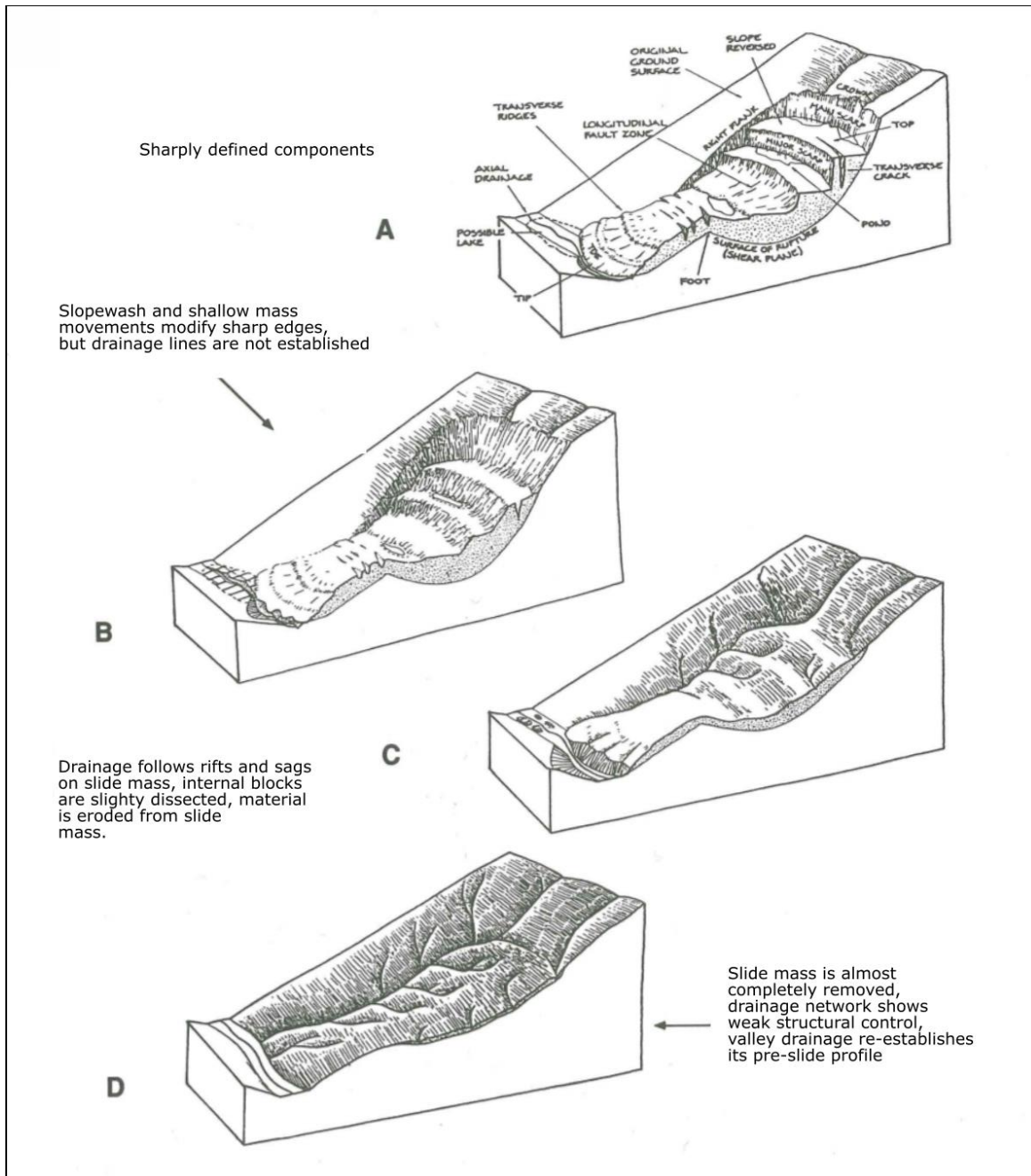


Figure 16: Morphologic changes in time of idealized landslide in arid or semiarid climate. A, active or recently active landslide features are sharply defined and distinct. B, dormant-young landslide features remain clear but are not sharply defined owing to slope wash and shallow mass movements on steep scarps. C, dormant-mature landslide features are modified by surface drainage, internal erosion and deposition, and vegetation. D, dormant-old landslide features are weak and often subtle. Modified from (Turner and Schuster, 1996)

### 3.3 SEDIMENT STRUCTURES AND LANDFORMS IN LAKES AND ALONG THEIR SHORELINES

#### 3.3.1 Gravitational deposits

##### Alluvial fans

Alluvial fans are cone shaped landforms in planar view, often located in the bottom of slopes, with a network of channels or lobes created either by landslides, debris flows or streams. The long profile of an alluvial fan is concave upward towards the slope, while the transverse profile is convex upwards. Alluvial fans can also merge into lakes or oceans and create fan deltas. (Boggs, 2014).

#### 3.3.2 Bedforms

Bedforms occur at the bed of streams, submarine slopes or in aeolian environments (Boggs, 2014). Bedforms are classified based on size and flow velocity. The smallest bedform class is ripples, with lengths from 5 to 20 cm and height of 0.5 to 3 cm. Dunes are similar to ripples but with a significant larger size, with wave lengths ranging from 1 m to over 1 000 m. Both dunes and ripples occur in the lower flow regime defined by a Froude number less than 1 (Boggs, 2014). The Froude number is the relation between the flow velocity and the flow depth and is considered as the relation between the flow velocity and the wave velocity inside the flow (Nichols, 2009). When the flow has a Froude number close to 1, the dunes are destroyed and a plane bed is created, shown in Figure 17. At even higher velocities (Froude number over 1), antidunes are created, which are up to 5 m high symmetrical bedforms. Antidunes migrate upstream, the opposite direction of lower flow regime dunes and ripples (Boggs, 2014).

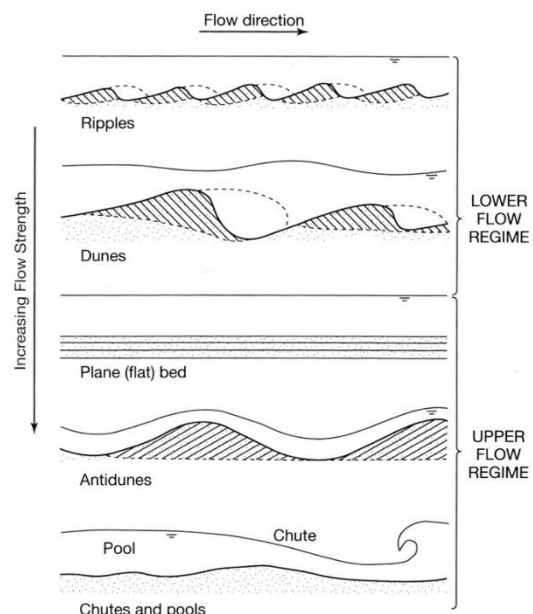


Figure 17: Change in bedform shape with increasing flow velocity. From (Boggs, 2014).

A special type of bedding is cyclic steps. Cyclic steps are both symmetrical and asymmetric bedforms, consisting of a train of upslope migrating bedforms (steps), created by turbidity

currents due to hydraulic jumping (Cartigny *et al.*, 2011). This mechanism is described in Figure 18.

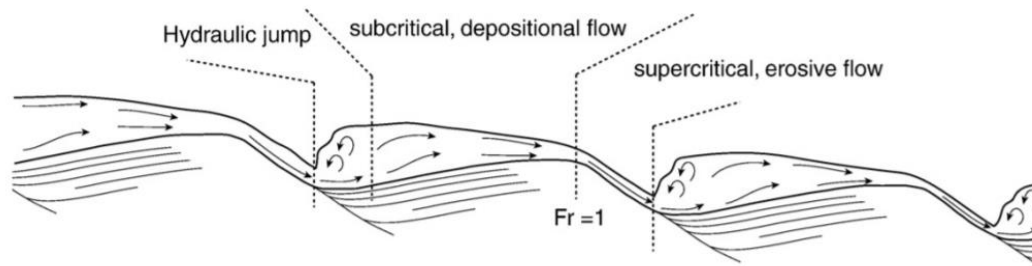


Figure 18: Schematic drawing of a train of downslope asymmetrical cyclic steps, under a Turbidity current. The turbidity current is moving left to right accelerating from a subcritical state at the stoss side of the bedform, reaching the critical Froude number ( $Fr = 1$ ) at the crest of the dune. After reaching the critical Froude number the currents further accelerated down the steep lee side of the bedform, as a supercritical flow. At the toe of the lee side is the fast-moving current colliding with slower moving material creating a hydraulic jump. The high flow depth created by this hydraulic jump leads to low velocity and deposition on the stoss side, while a lower flow depth and high velocity leads to erosion or limited deposition on the lee side. This imbalance between the stoss and lee side generate upstream migration. From (Cartigny *et al.*, 2011)

### 3.3.3 Delta

When a depositional fan merges into a lake or the ocean, it is called a delta (Boggs, 2014).

This landform got its name from the “original” delta at the river mouth of the river Nile which got the shape of the Greek letter  $\Delta$  (delta). (Nichols, 2009).

A special type of delta is the fjord-head delta, which is often created at the output of larger catchments into a fjord or a fjord lake. This delta type is rarely fan shaped. Instead it is visible as a straight delta plain into the fjord confined by the valley walls (Prior and Bornhold, 1990).

#### Delta slope

The delta slope starts at the delta front, where the coarsest material is deposited closest to the shore. As the wave energy is decreasing further away from the front finer material will be deposited. This creates a slope with gradually finer material deposited away from the delta front. This delta slope varies in dip from  $1 - 2^\circ$  in fine grained deltas to over  $30^\circ$  in coarser grained deltas (Nichols, 2009).

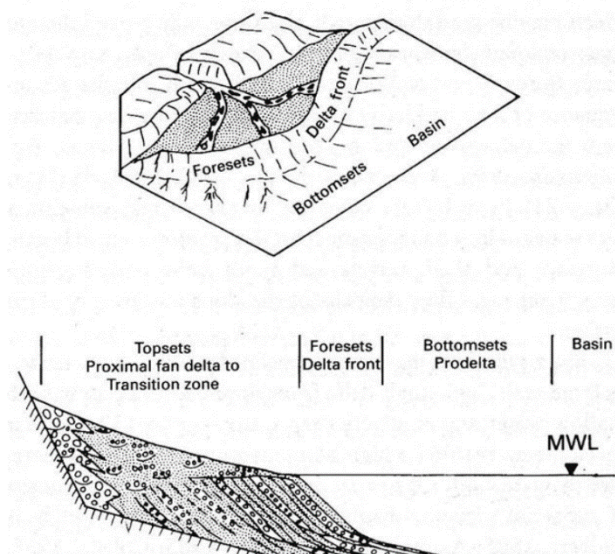


Figure 19: Schematic presentation of a Gilbert-type delta. MWL is mean water level. From (Boggs, 2014).



A special case of delta is the Gilbert-type delta, which is created when river water is entering a waterbody of similar density. A typical Gilbert-type delta is shown in Figure 19 and consists of a topset, foreset and bottomset, as the delta merges toward the basin floor (Boggs, 2014). The topset is sub-aerial with gravels or sands deposited by braided rivers or wave activity. The foreset is located at the front of the topset, with a slope dipping 30° towards the basin floor, created by gravitational processes such as debris flows. The bottomset rest at the bottom of the foreset, containing fine grained sediments deposited by turbidity currents and suspension (Nichols, 2009).

### 3.3.4 Dead-ice topography

Dead-ice activity often creates a hummocky terrain in deglaciated areas, dominated by dead-ice sinks and kettle holes, often divided by eskers or hummocky moraines as illustrated in Figure 20 (Eilertsen *et al.*, 2016). Kettle holes are depressions in the terrain created by former ice-blocks (Brattli, 2015, Eilertsen *et al.*, 2016). Dead ice sinks are similar to kettle hole, but are significantly bigger (Fleisher, 1986).

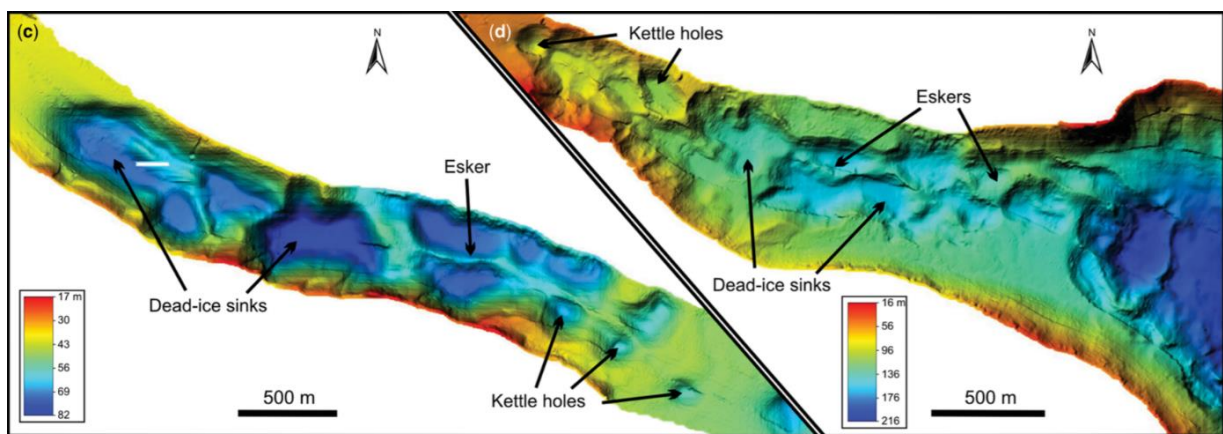


Figure 20: Bathymetric image of lake Bandak, showing kettle holes and dead-ice sinks. from (Eilertsen *et al.* 2016)

### Kame-terrace

Kame-terraces are landforms often related to dead ice and are created by meltwater flowing between the glacier and the hillside, eroding glacial sediments and depositing layered glacial sediments, both on top of the glacier rim and between the glacier and the hillside. When the glacier melts, the deposited glacial sediment will remain, creating a flat terrace shown in Figure 21 (Brattli, 2015).

## Esker

Eskers are long ridges deposited in meltwater channels either under, inside or on top of the ice, during the late melting stages of the glacier (Brattli, 2015, Olsen *et al.*, 2013). Eskers can become up to 15 – 20 meters high and up to several kilometres long (Trømborg, 2006).

## Kame

Kame is piles of sediment, deposited in joints or cavities in the ice during the late melting stages of the glacier (Brattli, 2015).

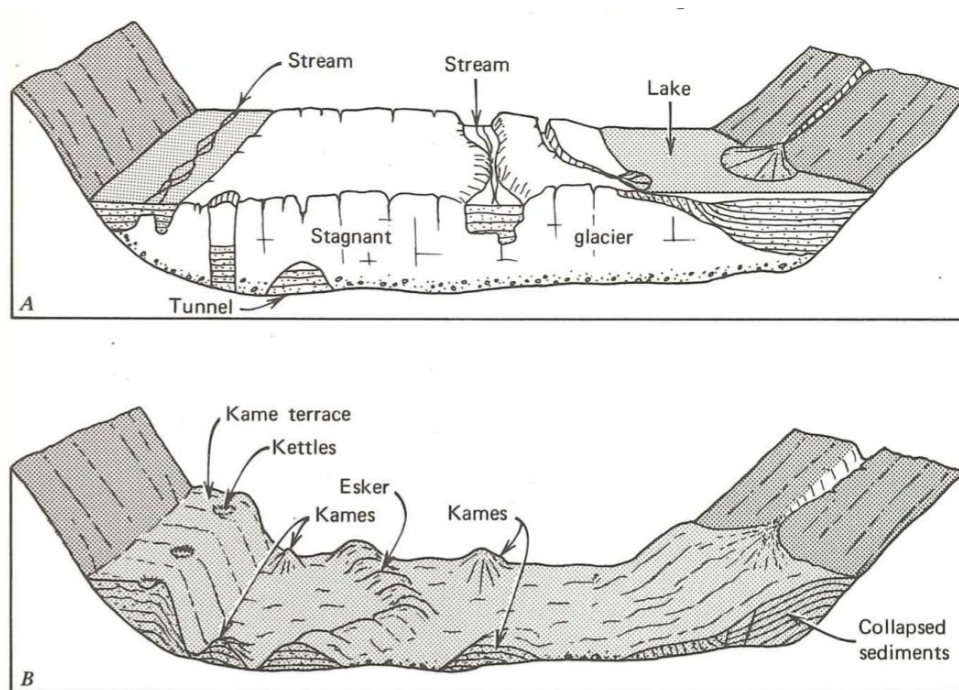


Figure 21: Schematic illustration of landforms created in relation to dead ice: A) The stagnant glacier affords temporary retaining support of the sediments built by streams and lakes. B) When the ice melts, bodies of sediments are deposited. From (Flint, 1971)

# 4 METHOD

## 4.1 GEOLOGIC MAPPING

### 4.1.1 Field work

The field work lasted 5 days, 22<sup>nd</sup> to 26<sup>th</sup> of June 2017, covering the surrounding areas of the prehistoric Prestura rockslope failure, focusing on main characteristics of joints such as orientation, aperture, persistence and roughness. The dip direction/dip was measured using a Clar type compass. Joint characteristics such as aperture, persistence and roughness were not quantitatively measured in field, but are based on visual observations.

For georeferencing the measurements, a “Garmin GPSMAP 60CSx” GPS was used, each GPS point represents a locality, covering an area with up to a 50m radius.

In addition, an estimate of the JCS of the joint sets were performed, using the Barton bandis form, presented in Figure 22. The Schmidt hardness was measured using a Schmidt hammer, while the unit weight of the rock is collected from literature.

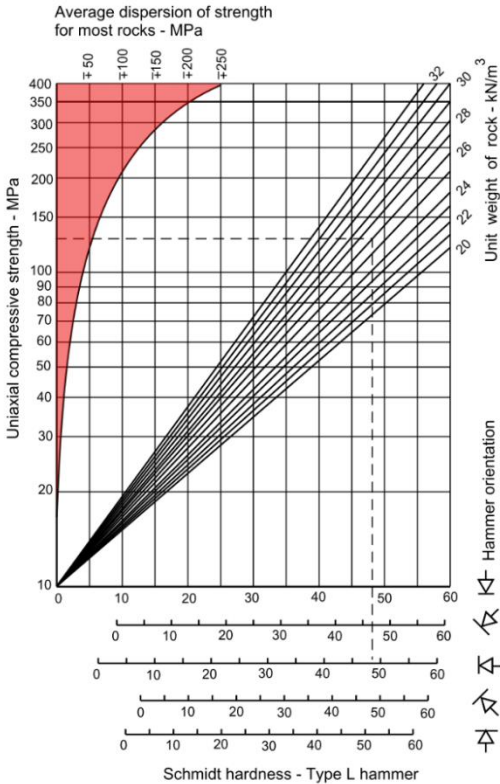


Figure 22: Estimate of JCS from Schmidt hardness. The dashed line shows how the JCS is plotted based on a vertical oriented Schmidt hardness of 47 and a unit weight of 26kn/m<sup>3</sup>. The red area shows the increasing variation in the data with increasing rock strength. Modified from (Hoek, 2007 )

### **4.1.2 Sources of error**

The compass was not adjusted for longitudinal elevation, thus showing an in-correct orientation, with a derivation of one or two degrees. However, the uncertainty when measuring dip direction/dip by hand is considered bigger than the instrumental error. Thus, it is not considered a significant source of error.

Aperture, persistence and joint roughness was mapped based on visual observations, thus having low accuracy. In this thesis, this is considered good enough, but if e.g. a back calculation based on numerical models was performed, a higher demand of the measurements should be required.

The GPS has an error of 3-6m in open terrain. However, since a single GPS point refers to an area with up to 50m radius, is this error not considered significant.

The Schmidt hammer is intended for use on concrete, but may also be used on rock surfaces, however some issues such as hammer type, surface smoothness, weathering and moisture content may underline the reliability of the Schmidt hammer test (Aydin and Basu, 2005). According to Deere and Miller (1966), it has also been observed a high variability in the results for higher strength rocks.

## **4.2 KINEMATIC FEASIBILITY TEST**

A kinematic feasibility test is used to determine the possibility of failure, and which failure mode that most likely occur. The software used in the feasibility test was Dips 7.0 (Rocscience, 2016a), following the recommendations from NGU (Hermanns *et al.*, 2012).

A kinematic feasibility test is done by dividing the structural measurements into potential joint sets, illustrated by a variation cone for each set. In addition to the structural measurements is a daylight envelope, friction cone and lateral limits defined before running the analysis (Hoek and Bray, 1981). The daylight envelope represents the dip of the slope examined. In this study, the slope orientation was measured from a topographic map in the software ArcMap 10.5 (ESRI, 2017a). The friction cone is defined from the angle of friction of the rock mass (Hoek and Bray, 1981), and is illustrated in both pole vector mode (pole friction cone) and dip vector mode (plane friction cone). Hermanns *et al.* (2012) recommends using a conservative friction angle of 20°, when examining large unstable slopes. In this study, a friction angle of 28° was used, based on laboratory test from previous work (Sollie, 2014), assuming that the rock mass close to Prestura is homogenous. The lateral limits



represent the theoretical limits of all potential planes which can daylight. The lateral limits are generally set to 20° (Wyllie and Mah, 2004). In studies of larger failures is the lateral limits often set to 30° or higher, due to the complex structures involved in a large rock slide and the generally more variable slope orientation (Hermanns *et al.*, 2012). In this study was a lateral limit of 30° used for all failure modes.

**4.2.1 Planar sliding**

Planar sliding is possible if the discontinuity both “daylight” and plot outside of the friction cone (Hoek and Bray, 1981) as shown in Figure 23. In other words, is planar sliding possible if the plunge of the discontinuity is less than the dip of the slope, but higher than the angle of friction of the rock mass (Hoek and Bray, 1981).

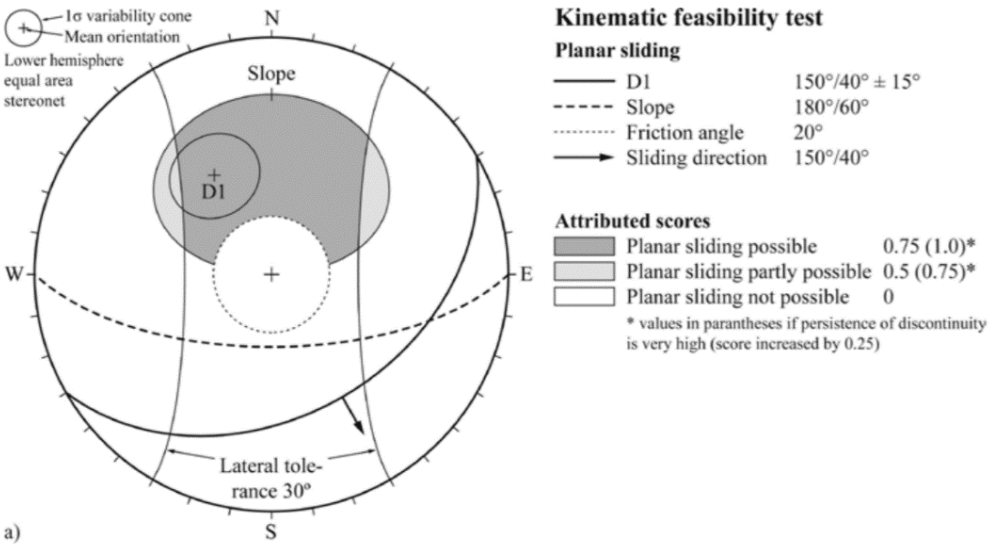


Figure 23: Illustration of planar failure in pole vector mode. From (Hermanns *et al.*, 2012)

**4.2.2 Wedge sliding**

Planar sliding is a special case of wedge failure. Thus, the same requirements apply for both planar sliding and wedge sliding (Hoek and Bray, 1981). The difference is that wedge sliding is represented by the intersection of two discontinuities (Figure 24). Wedge sliding is possible if this intersection has a plunge lower than the dip of the slope, but higher than the angle of friction. Wedge sliding is only plotted in dip vector mode, thus it uses a plane friction cone (Rocscience, 2016b). Both wedge sliding and planar sliding are considered possible if the

difference in sliding direction and slope orientation is less than  $30^\circ$  and is considered partly possible if the difference is larger than  $30^\circ$  (Hermanns *et al.*, 2012).

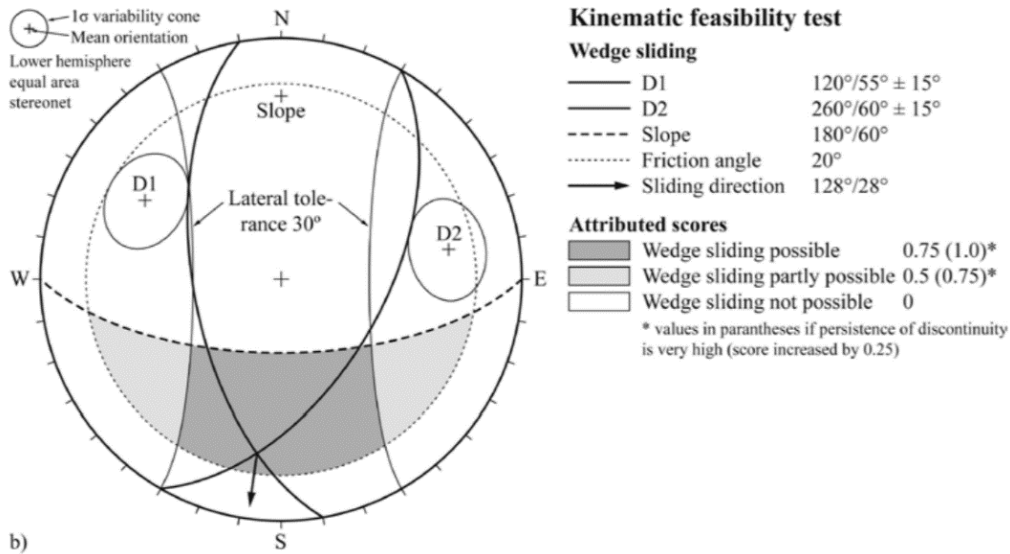


Figure 24: Illustration of wedge failure in dip vector mode. From (Hermanns *et al.*, 2012)

### 4.2.3 Flexural toppling

Flexural toppling is illustrated in Figure 25. Flexural toppling is possible if the discontinuities are dipping into the slope face, with a higher plunge than the angle of friction (Wyllie and Mah, 2004). According to Wyllie and Mah (2004) is toppling failure only possible if the difference in orientation of the discontinuities compared to the slope orientation is less than  $10^\circ$ . However, due to the complexity of large rock slopes is toppling failure considered possible if the difference is less than  $30^\circ$  and partly possible if the difference is less than  $45^\circ$  (Hermanns *et al.*, 2012).

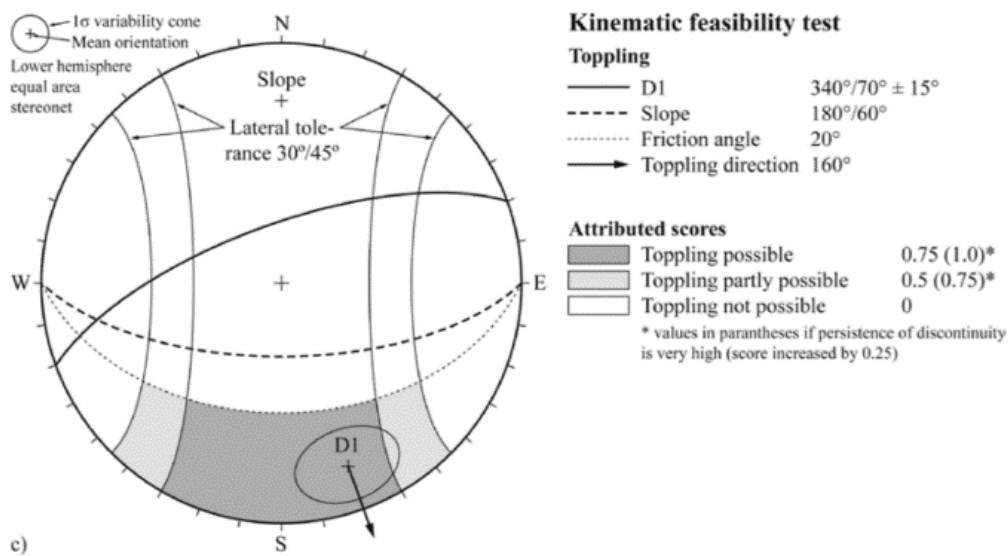


Figure 25: Illustration of flexural toppling. From (Hermanns *et al.*, 2012)

#### 4.2.4 Direct toppling

Direct toppling occurs when the centre of gravity in a block lies outside of the outline of the block, leading to overturning of the block. The possibility of direct toppling is shown in Figure 26, defined by the block geometry and the angle of friction between the block and the surface it is resting on (Hudson and Harrison, 2000). The key elements in a direct toppling test is therefore the intersection of two joint sets, which create block, and the presence of a third joint set which acts as a release surface for the blocks, allowing the blocks to topple or slide (Rocscience, 2016c).

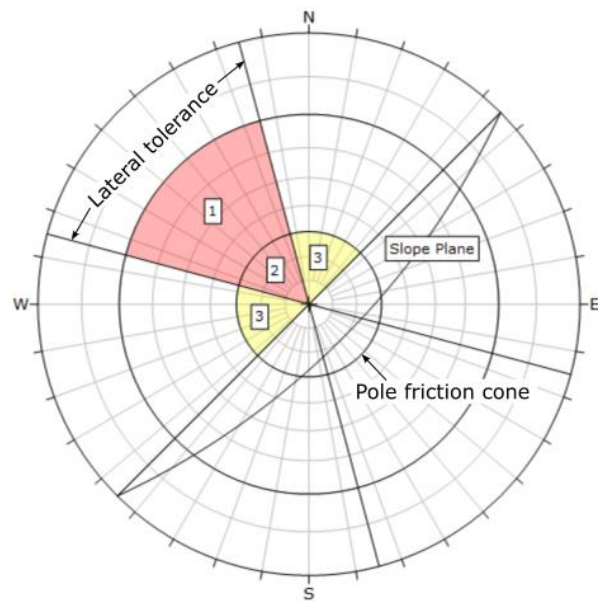


Figure 26: Illustration of direct toppling. Zone 1 and 2 represent the area which it is possible to create blocks, while zone 2 and 3 represent potential release surfaces. Modified from (Rocscience, 2016c)

#### 4.3 LIDAR

LiDAR (Light detection and ranging) or more correctly laser scanning (Jaboyedoff *et al.*, 2012) uses a laser beam to scan the earth surface, stored as a point cloud. After processing, it creates a digital elevation model (DEM) (Clague and Stead, 2012). LiDAR has been developed into two different methods, based on the position of the sensors (Jaboyedoff *et al.*, 2012):

1. ALS (aerial laser system): Airborne based (airplanes and helicopter) and has a point density of 0.5 to 100 pts/m<sup>2</sup>
2. TLS (terrestrial laser system): Ground based (fixed point, car or boat) and has a point density of 50 to 10,000 pts/m<sup>2</sup>.

The mayor principle and construction of the scanners are the same for both ALS and TLS (Clague and Stead, 2012), consisting of a transmitter/receiver of the laser beam and a scanning device. Further, two different methods of range determination are utilized: the phase method and the pulse method. The phase method gives a more accurate range determination, but has limited range, while the pulse method allows a greater range. Because of the greater range the pulse method is usually used in landslide studies (Jaboyedoff *et al.*, 2012) and will be further examined in the following.

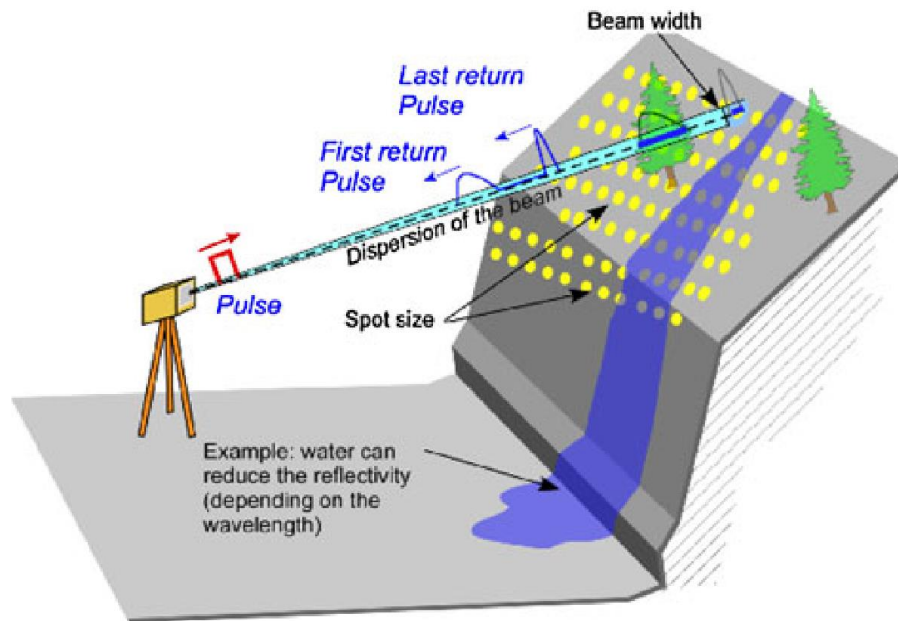


Figure 27: Main principle of LiDAR scan, modified from (Jaboyedoff *et al.*, 2012)

Figure 27 illustrates the main principles of the pulse method. The laser emits laser pulses, and these pulses are reflected when hitting various objects (ground surface, vegetation, constructions etc.). By recording the time ( $\Delta t$ ) it takes for a laser pulse to return to the sensor, it is possible to determine the distance to the object that caused the reflection of the pulse, and by knowing the position and the line of sight (LOS) of the laser scanner. It is possible to determine the position of the reflected surface, represented by x, y and z coordinates (Jaboyedoff *et al.*, 2012).

By using the pulse method, vegetation cover and other objects are possible to distinguish from the surface by only using the last return pulse when creating the point cloud. This is because of the last return pulse, which almost always represents the ground surface. However, when the vegetation cover is too dense, this method is not feasible to use, since the laser beam will not reach the ground surface. When working in dense vegetated areas, this is a significant problem. Thus, creating a DEM based on these data might not be better than a standard resolution DEM (approximately 25m grid size) obtained from topographic maps (Jaboyedoff *et al.*, 2012).

### 4.3.1 Terrestrial Laser scan (TLS) analysis

Terrestrial Laser scan (TLS) is often used by the Norwegian Geological survey (NGU) for structural analysis of unstable rock slopes, especially for mapping of discontinuity orientation, and monitoring of displacement or rockfall activity (Oppikofer *et al.*, 2012).

Figure 28 illustrates the steps in acquisition and treatment of the data followed by NGU.

In this study, TLS data was used for structural analysis and volume estimation, which involve steps 1,2,3,4,5 and 9. Step 1-4 were used to create a 3D model of the slope, step 5 was used to perform a structural analysis in the software Coltop-3D (Terranum, 2014), and step 9 was used in the Ante rockslide topography (ART) volume estimation of the initial volume of the Prestura failure area.

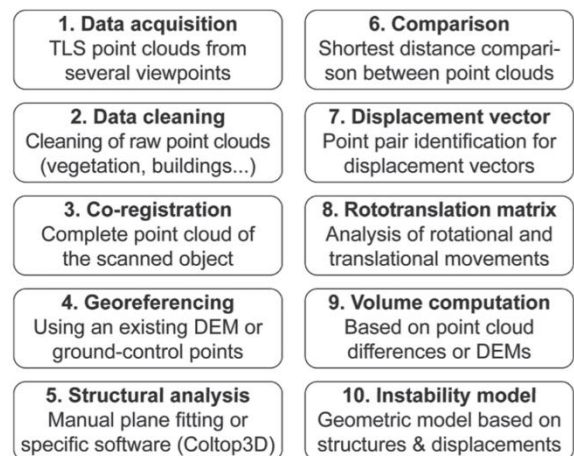


Figure 28: Flowchart for the acquisition, treatment and analysis of TLS data. From (Oppikofer *et al.*, 2012)

### 4.3.2 Modell creation (steps 1 – 4)

The TLS data was obtained (step 1) by performing scans at two different locations in order to get an accurate 3D model (Lato *et al.*, 2010). An Optec ILRIS-LR Terrestrial Laser Scanner, with a wavelength of 1064nm, was used in this study.

Step 2 involves pre-processing of the files. The main objective in pre-processing is to remove noise, such as vegetation or other scattered points (Oppikofer *et al.*, 2012). The pre-processing was done in the software PifEdit (Innovmetric, 2011a).

Step 3 involves alignment of the scans, creating a 3D model of the slope. The alignment followed the recommendations by Oppikofer *et al.* (2009), first manually aligning the scans, by identifying common points and structures in the different point clouds, then automatically align the scans by using a point-to-surface Iterative Closest Point (ICP) algorithm. To get good matching of the datasets when aligning, the overlap of the different scan should be over 20% (Oppikofer *et al.*, 2009). Both manual and automatic alignment were performed in the software Polyworks V12 (Innovmetric, 2011b).

In step 4, the 3D model is georeferenced by aligning the model to a DEM with known coordinates (Oppikofer *et al.*, 2012). In this study, the model was georeferenced using a DEM with a 1x1m resolution. The DEM was downloaded from Hoydedata.no.



### 4.3.3 Structural analysis in Coltop-3D (step 5)

The structural analysis based on TLS was performed in the software Coltop-3D (Terranum, 2014). In Coltop-3D, the orientation of structures is represented by giving the DEM pixels a colour based on their orientation, using the Hue Saturation Intensity (HSI) wheel, shown in Figure 29. The colouring of the DEM cells is based on either the orientation of the pole (normal) of the plane created by 4 neighbouring pixels, or by using Triangulated irregular network (TIN) techniques to colour triangles in the same way as mentioned above (Jaboyedoff *et al.*, 2007). The orientation data collected from Coltop-3D is further exported into Dips 7.0, where mean orientation and standard deviation are determined.

TLS is an efficient tool to perform a rapid structural analysis of a slope, especially when examining areas that are not easily accessible (Jaboyedoff *et al.*, 2007). TLS also collects more data than traditional field mapping, as shown in section 5 in this thesis. Thus, it is more statistical representative and can be used to reduce the uncertainty in data achieved from systematic field mapping.

However, TLS mapping also got biases. According to Jaboyedoff *et al.* (2012), there are two main biases related to the orientation of discontinuities mapped in TLS. These are: a) scale bias, which arise when the discontinuities are smaller than the spatial resolution, and b) orientation bias, such as occlusion, which occur when joints are oriented almost parallel to the scan direction and become shadowed (hidden) and underrepresented in the data (Lato *et al.*, 2009). Because of these biases, one should always perform systematic field mapping to support the findings in a TLS analysis. In this thesis, the TLS structural analysis was used to check if all main joint sets were covered in the systematic field mapping.

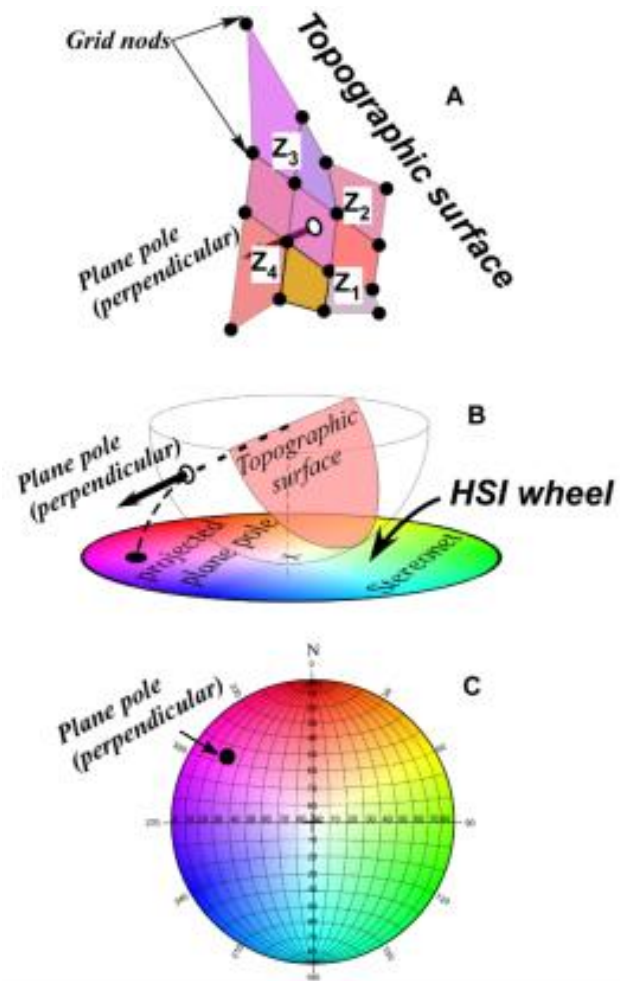


Figure 29: Illustration of the principle of the Coltop-3D colour scheme. A) orientation is based on 4 nearest neighbours or by 3 points of each triangle in a TIN. B) Relationship between a Schmidt projection and the HSL wheel. C) The HSL wheel plotted on a stereonet. Modified from (Jaboyedoff *et al.*, 2007)

#### **4.4 ANTE-ROCKSLIDE TOPOGRAPHY (ART) AND VOLUME ESTIMATION**

To estimate the volume of a landslide, it is required to reconstruct the pre-failure topography, which is called Ante-rockslide topography (ART) (Oppikofer, 2009). This can be achieved by several methods (Oppikofer, 2009):

- a. By using topographic maps and aerial photographs created before the event. Usually available for events younger than 75 years.
- b. Continuity analysis between the present-day topography outside the landslide and within the landslide area. This method uses contour lines or interpolation methods such as inverse distance weighting and kriging.
- c. 3D reconstruction, by using a DEM
- d. By using the Sloping Local Base Level (SLBL) method.

In this thesis, the ART of the landslides were reconstructed using 3D reconstruction in the software Polyworks (method c), as well as the SLBL method (method d). Pre-failure topographic map (method a) was not used, since no pre-failure maps are available for either the Prestura event or the seafloor of lake Tinnsjø. A continuity analysis using contour lines (method b) was considered too time consuming to cover all landslides of interest.

The volume was estimated based on the ART by using three different methods:

1. Spatial analysis in ArcGIS, based on ART created in Polyworks
2. SLBL
3. “Minimum eroded volume”

##### **4.4.1 Manually construction of ART in Polyworks**

The ART is possible to recreate in Polyworks (Oppikofer *et al.*, 2016) by following the two methods presented in Figure 30.

In this thesis, both methods were used. Method 1 was used to determine the maximum initial volume, while method 2 was used to adjust the model to potential post failure erosion.

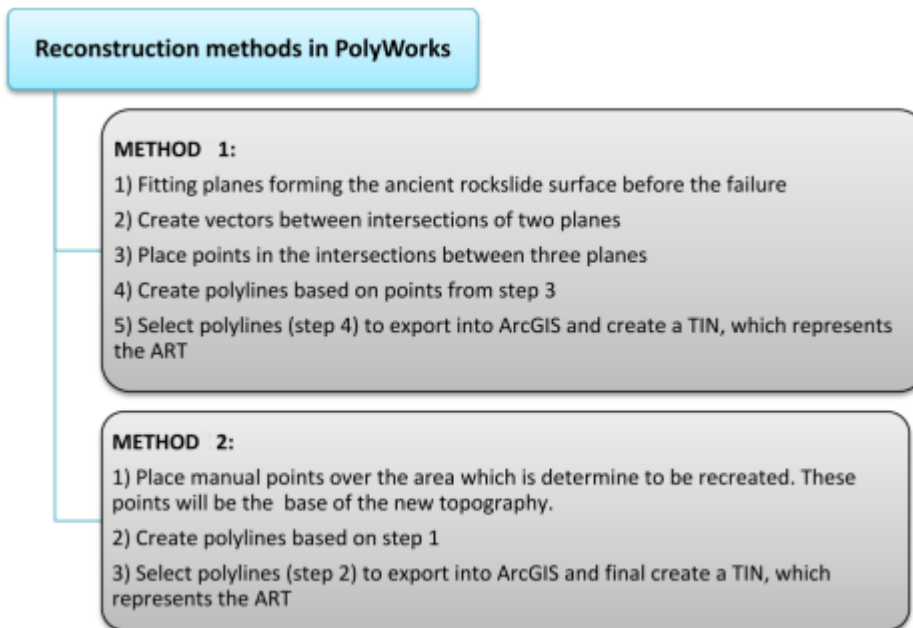


Figure 30: Overview of two manual reconstruction methods applied in Polyworks. Modified from (Sandøy, 2012).

The volume was estimated by converting the TIN to a DEM, followed by using the spatial analyst tool, RasterCalculator in ArcMap, to measure the difference between the created DEM and a 1x1m resolution DEM of the present topography.

#### 4.4.2 Sloping Local Base level (SLBL)

Sloping local base level (SLBL) is based on the principle of the base level concept. It was first defined by J. W. Powell in the 19<sup>th</sup> century, as the lower level that can be affected by erosional processes (Jaboyedoff *et al.*, 2005). On a regional scale, the base level is defined by the sea level, while the base level is defined by a lake or a river on a local scale. This traditionally defined base level is considered horizontal and represents the original peneplane. The peneplane is created by all erosional processes (not just landslides) over a timescale much longer than the scope of a landslide event. Therefore, the base level concept is not applicable for examining landslides. Instead the SLBL is defined, which is not horizontal and assumes that only a limited vertical

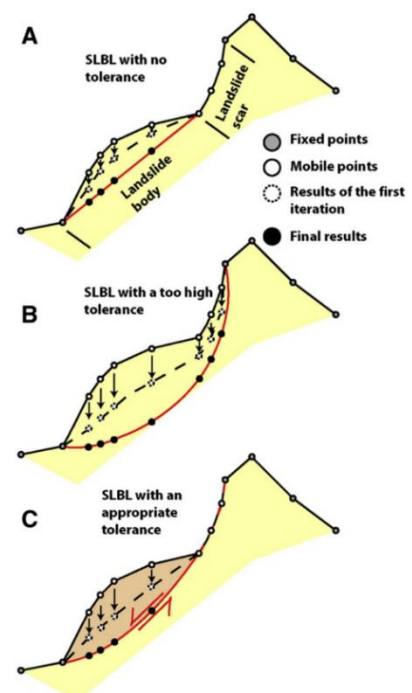


Figure 31: Illustration of SLBL curvature tolerance lines. A) Minimum SLBL  $C=0$ , B) Maximum SLBL  $C=C_{max}$ , C) Most likely SLBL  $C=C_{inter}$ . From (Travelletti *et al.*, 2010)



thickness of a slope is affected by erosion from landslide processes (Jaboyedoff *et al.*, 2004, Travelletti *et al.*, 2010).

The SLBL method calculates a minimum ( $V_{\min}$ ), maximum ( $V_{\max}$ ) and the most likely volume ( $V_{\text{inter}}$ ) of a landslide, based on the curvature tolerance ( $C$ ) of the potential base level. For  $V_{\min}$ , the base level is considered as a straight line with a tolerance  $C = 0$  (Figure 31A). The curvature tolerance  $C$  used in estimating  $V_{\max}$  and  $V_{\text{inter}}$  is represented by a second-degree curve (Figure 31B,C) (Travelletti *et al.*, 2010).

This thesis follows the guidelines in NGUs workflow for the consequence assessment for unstable slopes (Oppikofer *et al.*, 2016) to calculate the curvature tolerance  $C$ . According to Oppikofer *et al.* (2016) is the curvature tolerance ( $C_{\max}$ ) for  $V_{\max}$  calculated based on the height difference between the highest and lowest point of the scenario ( $h$ ), the horizontal length of the scenario ( $l$ ) and the DEM resolution (cellsize  $\Delta x$ ). Shown in Equation 1.

$$C_{\max} = 4 * (1 - \sqrt{2}) * h * \left(\frac{\Delta x}{l}\right)^2 \quad (1)$$

When calculating the curvature tolerance ( $C_{\text{inter}}$ ) of  $V_{\text{inter}}$ , is the angle along the scarp ( $\gamma$ ) and at the toe ( $\beta$ ) added to the calculation. These parameters are defined by field measurements or by detailed DEM mapping (Oppikofer *et al.*, 2016). In this thesis was an elevation map based on 2 m contour lines (appendix C), used to determine the  $\gamma$  and  $\beta$ .

The calculation of  $C_{\min}$ ,  $C_{\text{inter}}$  and  $C_{\max}$  was done using an Excel spreadsheet developed by NGU. After calculating the curvature tolerance, it is possible to perform the volume calculation using the ArcMap script SlopingLocalBaseLevel(Beta2) developed at NGU, with input parameters as follows: 1) 3D polygon representing the ART, 2) a raster (DEM) representing the present topography and 3) the curvature tolerance  $C$ . This ArcMap script is based on the use of the software Conefall (Quanterra, 2003) to recreate the SLBL. Further description of the Conefall method is given in (Oppikofer *et al.*, 2016)

A 5x5m resolution DEM and 3D polygons drawn in the software ArcScene (ESRI, 2017b) were used in this study, along with the calculated curvature values when calculating the volume of landslides.

### 4.4.3 Minimum eroded volume

Minimum eroded volume was done in the software ArcMap, based on the workflow by (Cooley, 2015). The general workflow follows these steps:

1. Define the rim (draw polygon covering the landform)
2. Convert polygon to points
3. Extract elevation to points (elevation from DEM)
4. Create a TIN from the points
5. Convert TIN to raster
6. Clip raster (using the polygon created in step 1 as clipping geometry)
7. Subtract the present-day topography from the clipped raster
8. Calculate volume (number of pixels times the DEM resolution)

The method uses the 3D polygons representing the local base level, such as SLBL, but has not the ability of adding a curvature tolerance. Thus, it only gives a calculation of  $V_{\min}$ . This method has a higher accuracy than the SLBL, since it can use higher resolution DEMs without crashing the computer (max resolution of SLBL = 5x5m, “Minimum eroded volume” could easily use a 1x1m DEM). This method was used on approximately 50-60% of the estimated volumes to check if the values from SLBL seemed reasonable.

## 4.5 EMPIRICAL RUN-OUT ANALYSIS AND DISPLACEMENT WAVE ANALYSIS

### 4.5.1 Empirical run out analysis using the H/L vs Volume correlation

The total horizontal run out of a rockslide is measured from the backscarp to the toe of the landslide deposits, marked as  $L$  in Figure 32, while  $H$  represent the vertical height difference between the backscarp and the toe (Nicoletti and Sorriso-Valvo, 1991, Scheidegger, 1973). The run-out angle ( $\alpha$ ) is the angle between these points illustrated in Figure 32 (Scheidegger, 1973).

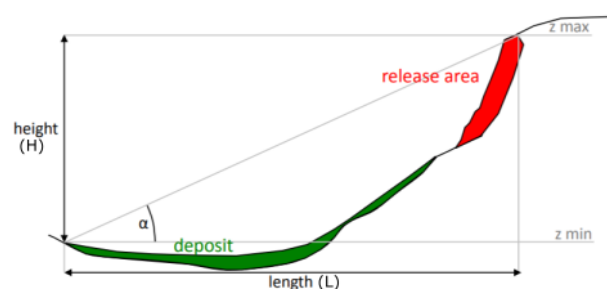


Figure 32: Illustration of the run-out length ( $L$ ), height ( $H$ ) and angle ( $\alpha$ ). Modified from (Romstad et al., 2009)

The relationship between the run-out distance ( $L$ ) and the volume of the landslide was first introduced by Scheidegger (1973), later adjusted to cover smaller landslide volumes by

Corominas (1996) and compared to Norwegian events (Blikra *et al.*, 2002, Hermanns *et al.*, 2012). The H/L vs Volume correlation is represented in Figure 33.

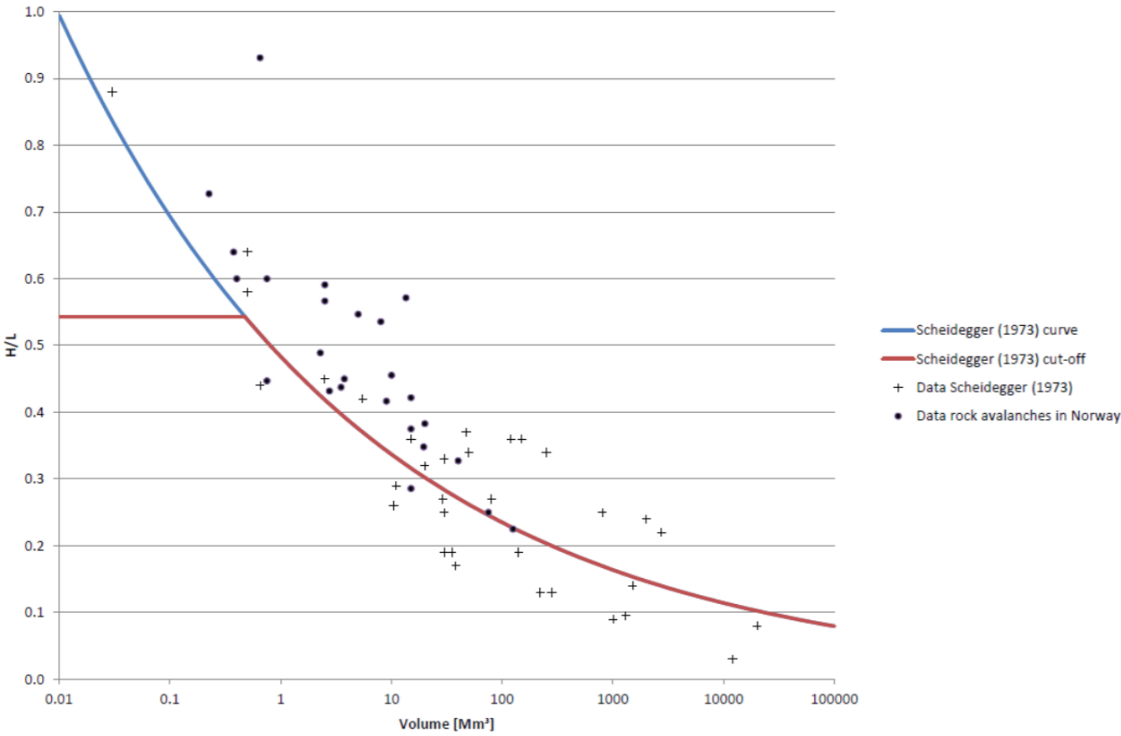


Figure 33: H/L vs landslide volume correlation diagram. From (Hermanns *et al.*, 2012).

**4.5.2 Empirical displacement wave analysis**

A displacement wave analysis corresponds to stage 3 of the quantitative consequence analysis presented in Oppikofer *et al.* (2016) and involves three different methods, ranked from a to c with increasing level of detail.

- a. Semi-empirical prediction of landslide-generated displacement wave run-up height (SPLASH)
- b. Displacement wave prediction based on generally applicable equations from laboratory tests (VAW – model)
- c. Numerical analysis

Method b) and c) were considered too time consuming and need more data such as width, length and velocity at impact. Thus, only a semi-empirical prediction of displacement wave run-up method (method a) was performed in this thesis.

The semi-empirical prediction of displacement wave run-up is based on the Splash equation shown in Equation 2 with best fitted parameters  $a = 18.093$ ,  $b = 0.57110$  and  $c = -0.74189$ .

$$R = aV^b x^c \quad (2)$$

R = run-up height

V = volume of landslide

x = distance from landslide impact

The analysis was performed using an Excel spreadsheet developed at NGU. The input volume (V) of the landslide is defined as the average estimated volume from the SLBL and ART analyses. The distance from impact (x) was measured using ArcMap. Additional parameters are correction factors, such as change in wave direction propagation and decreases in basin depth and width (shallow waters, bays, head of fjords).

It is important to note that this method is considered very conservative, lacking the precision required for detailed quantitative risk analyses, and should only be used in creating susceptibility maps, which shows the maximum possible extent of displacement waves (Oppikofer *et al.*, 2016).

This method is also only applicable for subaerial landslides moving into a body of water. Thus, only used for the Prestura rockslide, not the partly subaquatic Håkåneset rockslide or other subaquatic landslides in lake Tinnsjø.

## 4.6 BATHYMETRY

Bathymetry is the study of underwater depth of lakes, rivers or the ocean floor. A bathymetric map illustrates the land that lies underwater, the same way as a topographic map represent the relief of the overland terrain (NOAA, 2017).

The use of acoustic sensors is the most common tool in bathymetric mapping. The main principle of acoustic range is similar to the pulse method used in LiDAR. A sound pulse (laser pulse in LiDAR) is emitted from a sensor transmitter towards the seafloor. When hitting the seafloor, the sound pulse is reflected and moves back to the sensor. The time the pulse uses to move back and forth is recorded, and if the speed of sound in the water is known, the range (distance) can be computed (Ånonsen, 2010).

This method has further been evolved into four different branches in echo sounding based on its applications. These are (Wille, 2005):

- **The Multibeam or Fan Echosounder**, used in imaging the sea floor relief and other objects.
- **The Sidescan Echosounder**, used in imaging the small-scale morphology of the sea floor and the shape of structures.
- **The Sediment Penetrating Echosounder** used in imaging the internal structure of layers and to detect buried objects.
- **The acoustic Doppler current profiler** used to monitor ocean currents.

The bathymetric mapping of lake Tinnsjø was performed by Nearshore Survey AS in 2015, using a multibeam echo sounder. This is the successor of the single beam echo sounder, which measures the depth to a single point, usually directly below the vehicle. Instead of only measuring one single point at a time, the multibeam echo sounder measures the depth in a fan of points underneath the vehicle, by sending several hundreds of beams. Thus, it covers larger areas underneath the vehicle than a single beam echosounder, illustrated in Figure 34 (Ånonsen, 2010).

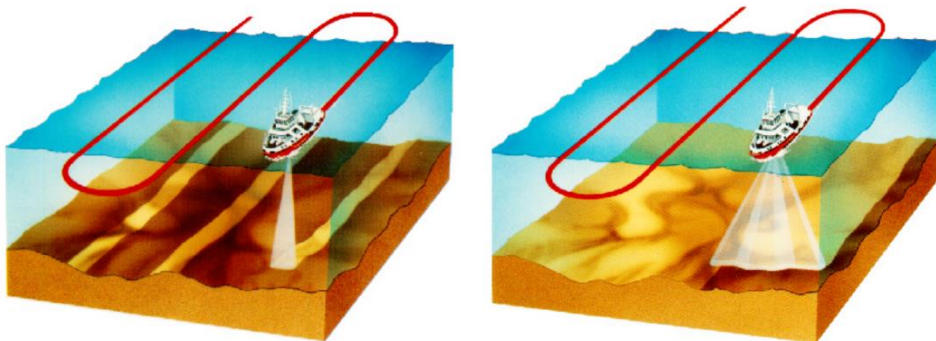


Figure 34: Schematic illustration of the difference in coverage between single beam echo sounder (left) and multi beam echo sounder (right). From (Ånonsen, 2010).

## **4.7 CATCHMENT DELINEATION AND LANDFORM MAPPING IN ARCGIS**

### **4.7.1 Catchment delineation**

According to Dingman (2015) a catchment (also called drainage basin, river basin or watershed) is “the area that topographically appears to contribute all the water that passes through a specified cross section of a stream (the outlet)”. Thus, it is assumed that most of the water passing through the watershed outlet originates as precipitation somewhere inside the watershed boundary. Therefore the characteristics of a watershed control the paths and rate of movement of water in a stream network (Dingman, 2015), which in turn control the erosional and depositional processes at the watershed outflow (Boggs, 2014).

The delineation was performed using a topographic map and contour lines. The watershed was drawn into ArcMap as a polygon, further adjusted to shapefiles achieved from NVE (2018a) when possible.

### **4.7.2 Landform mapping**

The subaqueous landform mapping was performed by drawing lines or polygons in ArcMap, which represents different landform types. The representation of the different landforms follows a similar classification as presented in Hansen *et al.* (2016).

Detailed description of landforms was performed by measuring the height, length, width and slope. The length and width were measured using the measurement tool in ArcMap. The height was determined by using contour lines (up to 1m resolution) and topographic profiles of the landforms. The slope was defined using topographic profiles or Triangular irregular networks (TINs) created from 2m contour, representing the slope dip (see appendix C).

# 5 RESULTS

---

## 5.1 GEOLOGIC MAPPING

### 5.1.1 Main Structures

The rock mass surrounding Prestura is dominated by three sets of major weakness zones:

1. Strike NNW – SSE, following the coastline of Lake Tinnsjø, marked turquoise in Figure 35. These weakness zones are clearly seen in the topography, with a very high persistence (up to several km). Since one of the weakness zone is crossing the back scarp of the Prestura rock slope failure. There are reasons to believe that these weakness zones have big impacts on the stability of the area.
2. Strike ENE – WSW, almost orthogonal on the longitudinal direction of Lake Tinnsjø, marked violet in Figure 35. These do not have as long persistence as the NW – SE striking weakness zones, but they are possible to follow over a distance of 1km on the DEM, thus having a very high persistence. The aperture is observed up to 5m, as shown in Figure 36. Some of the ENE – WSW striking weakness zones are interpreted by Statens Vegvesen (1989) as sills of mafic igneous rock like dolerite (diabas), basalt or gabbro marked as a yellow line in Figure 35.
3. Strike NNE – SSW, marked orange. These weakness zones have the same persistence as the ENE – WSW striking ones, but they are less visible in the terrain with a maximum aperture up to 5m.

Further south of Prestura is a possible lithologic border, marked with a green line in Figure 35. This border divides rhyolittic rock in the north from mafic plutonic rocks in the south and might be the reason why a big depression is located south of Prestura. This border was not observed during fieldwork and are based on previous work done by Statens Vegvesen (1989) only.

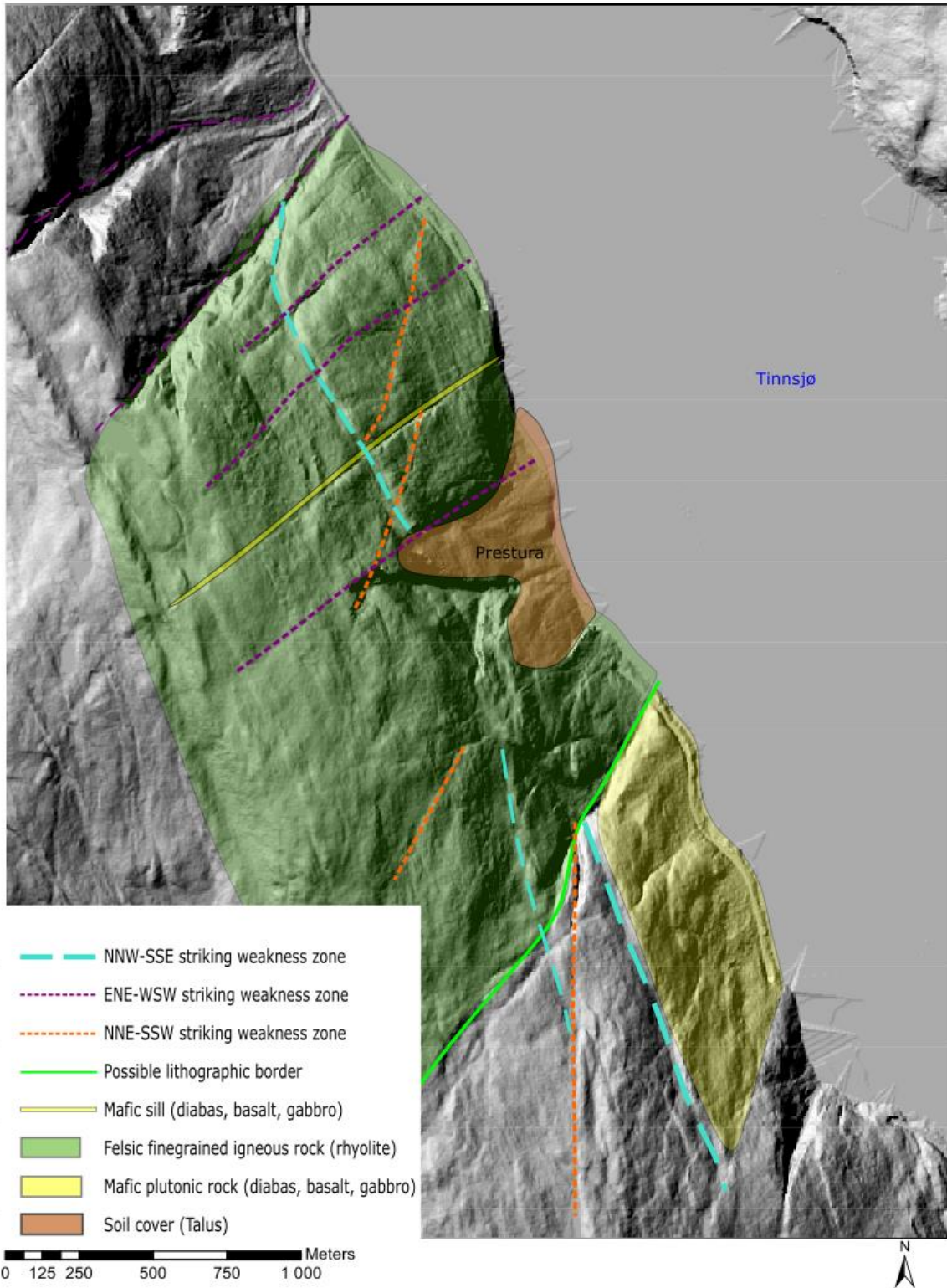


Figure 35: DEM of the area covered in systematic field mapping, showing two different rocks: rhyolite marked green and mafic plutonic rocks marked yellow, three different sets of weakness zones and a possible lithographic border marked green. Data from systematic field mapping and (Statens Vegvesen, 1989), DEM from hoydedata.no.





Figure 36: Photo of ENE-WSW striking weakness zone, with an aperture of 3m. Filled with vegetation and soil. Joint set 2 (J2) is dipping steep towards North.

### 5.1.2 Bedrock description

The dominating bedrock in the area is interpreted as rhyolite (Dons and Jorde, 1979, Statens Vegvesen, 1989), characterized as a dark grey/brown fine grained rock with up to 1 cm diameter white mineralizations. These mineralizations are interpreted as phenocryst (Sollie, 2014, Statens Vegvesen, 1989) and consist of light minerals like feldspar, quartz and calcite. At several locations it is possible to observe exfoliation structures in the bedrock, dipping 60-80° parallel to the slope, towards east, as shown in Figure 37.

It is also, according to Statens Vegvesen (1989), possible to observe coarser grained mafic plutonic rocks in the area such as gabbros or amphibolites. However, these rocks were not observed in field and further interpretations are based on previous work by Statens Vegvesen (1989) only.



Figure 37: To the left: East dipping exfoliation, observed close to Prestura.

To the right: Rhyolitic rock, with smooth surfaces and phenocryst up to 1 cm in diameter.

### 5.1.3 Joint Sets

The joint sets were mapped at 20 localities spread over a mapping area of 8 km<sup>2</sup>, shown in Appendix E. 766 measurements were added in the analysis, including 104 measurements achieved from previous work done by Statens Vegvesen (2013) and Statens Vegvesen (1989).

#### Foliation (SF)

The foliation of the bedrock is according to Sollie (2014) dipping almost horizontal towards N-NE and is referred to as schistose foliation (SF). Therefore, all joint sets with a dip less than 10° were mapped as schistose foliation (SF) joints. This joint set is poorly developed, and it was only visible when cutting steep mountain slopes or road cuts. As shown in Figure 38. This makes SF hard to find and few good measurements are recorded compared to the other discontinuities. This creates big variation in the data illustrated by the stereonet in Figure 39. Due to difficulty in localising this joint set is also the surface conditions, persistence, spacing and aperture very uncertain. However, based on observations (Figure 38) it does seem that the surface condition is smooth and undulating, with a persistence at least up to 5m. No Schmidt hammer measurements were performed on these surfaces. The main properties of the foliation is presented in Table 5.



Table 5: Properties of joint set SF.

Joint set	Discontinuity type	Dip direction/dip (1stdv*)	Consistency	Surface condition	Persistence	Spacing (m)	Aperture (m)	JCS (1stdv)
SF	Schistose foliation	<b>269/5 (26,6)</b>	Variable	Hard to map, but often smooth and undulating	0,1 – 5 meters	-	-	-

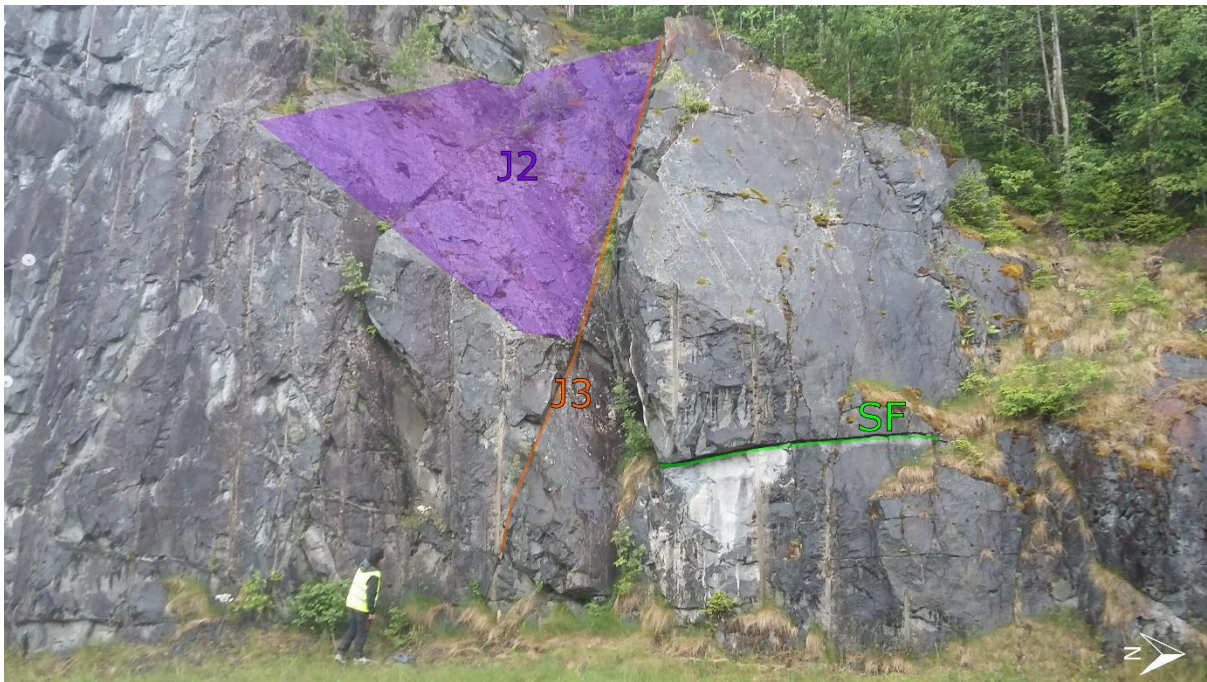


Figure 38: Location D2 (see appendix E) along the roadcut. SF is dipping nearly horizontal into the slope, with an undulating smooth surface. A wedge failure is observed in the middle of the picture, created by the intersection of J2 and J3.

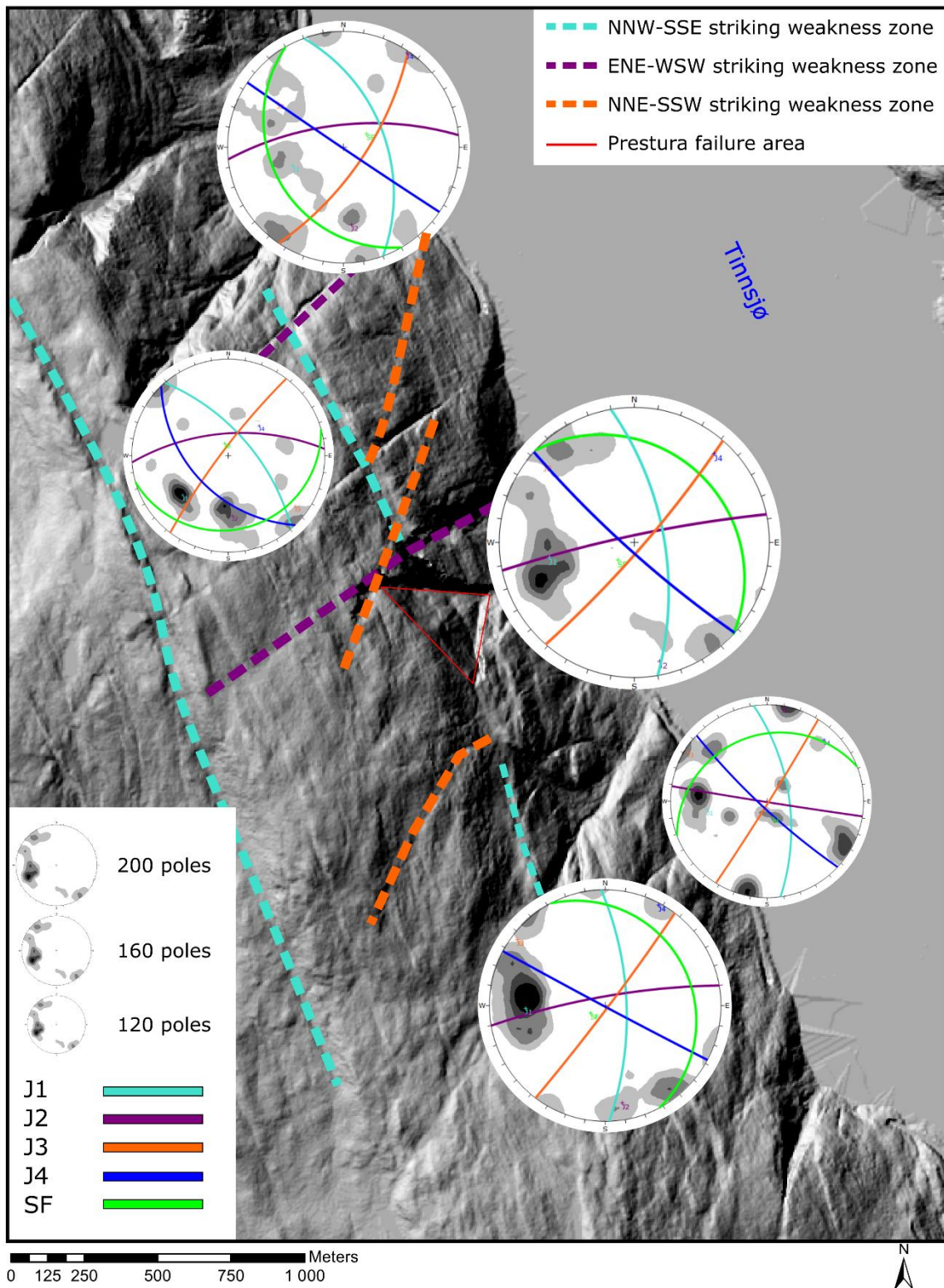


Figure 39: DEM of the mapping area, with the failure area of Prestura in the centre. Weakness zones parallel to the joint set orientations are marked in the same colour as its appurtenant joint set. Structural data were collected by geological mapping. The stereonets are presented with various size based on the number of measurements illustrated in the legend. The stereonets consists of data from north to south of data from localities 1: D1, B1 and B2 (158 measurements), 2: C1, C2, C3, C6, C7 and C8 (124 measurements), 3: A5, C4, C5 and Statens Vegvesen (2013) (209 measurements), 4: D2, D3 and D4 (117 measurements) 5: A1, A2, A3, A4 and A6 (170 measurements). Stereonets of every location can be seen in Appendix E.

In addition to the foliation (SF joints), four joint sets (J1, J2, J3 and J4) were mapped. J1, J2, J3 and J4 are consistent for the entire area and will be described in the following section. Because of the consistency of these joint sets and no distinct regional structures in the area, the entire mapping area is considered as one structural domain.

Table 6 displays the material parameters observed in field, plus data achieved from previous work by Statens Vegvesen (2013) and Statens Vegvesen (1989).

The Schmidt hardness of the joints was obtained from using a schmidt hammer on the different joint sets, then converting the Schmidt hardness to a Joint compressive strength (JCS) value by using the Barton bandis conversion form shown in Figure 22 (JCS is considered the same as Uniaxial compressive strength (UCS) in Figure 22) (Hoek, 2007 ). However, the data achieved from Schmidt hammer was very poor, showing a huge standard deviation (stdv.) in Table 6 and appendix D, and will not be further discussed in this thesis. The other parameters will be further discussed for every joint set in detail, with main focus on dip direction/dip, aperture and persistence.

Table 6: Description of the different joint sets in the mapping area. Aperture, spacing and surface conditions (roughness) are not been measured quantitatively, but are only based on visual observation and previous work by Statens Vegvesen (1989) and Sollie (2013).

\* Only J1 and J3 got a concentration with more than 4%. According to Rocscience (2016b) are joint sets with less than 4% concentration considered insignificant. Unless the joint sets are based on 100s of measurements. Both J2 and J4 have around 100 measurements (112 and 75 poles) and therefore considered significant despite having less than 4% concentration of the total data. To increase the amount of data (72 plots) for SF, is the cluster angle in cluster analysis increased to 35°, therefore increasing the standard deviation (highlighted in the table). A cluster analysis with 30° angle are used for the other joint sets.

Joint set	Discontinuity type	Dip direction/dip (1stdv*)	Consistency	Surface condition	Persistence	Spacing (m)	Aperture (m)	JCS (1stdv)
J1	Exfoliation	084/64 (17,5)	Consistent	Smooth and mostly planar, but some observations are undulating due to weathering.	0,3 – 10s of meters at most localities, up to 100s of meters along weakness zones.	0,2 – 2	0,001 – 0,01	215 (76) MPa
J2	Joint	353/72 (19,3)	Consistent	Smooth and planar	0,2 – 10s of meters	0,2 – 5	0,001 – 0,01 (up to 5 m along ENE – WSW striking weakness zones)	255 (82) MPa
J3	Joint	130/86 (19,0)	Consistent	Smooth and planar	0,2 – 10s of meters	0,2 – 2	0,001 – 0,01	287 (91) MPa
J4	Joint	214/86 (21,5)	Somewhat consistent	Smooth and planar	0,2 – 10s of meters	0,5 – 1	0,001 – 0,01	279 (55) MPa
SF	Schistose foliation	<b>269/5 (26,6)</b>	Variable	Often very undulating and hard to map.	0,1 – 5 meters	-	-	-



## Joint set J1

Joint set J1 has a consistent dip direction/dip of 084/64 for the entire area, except at some localities in the north-western area where the dip direction/dip is roughly 049/64. This is considered as a significant change in orientation. However, data in the north-western area show big variation between localities (shown in Appendix E) making it hard to conclude if this change in orientation is a significant trend in the data or not. Thus, J1 is considered consistent for the entire area.

J1 is oriented parallel to the rock slope dipping towards the lake, interpreted as exfoliation joints. This is supported by the observation of schistosity (Figure 37), interpreted as exfoliation, having the same orientation as the measured J1 joint set. The joints are often covered by a thin, dark material that according to Statens Vegvesen (1989) consists of chlorite minerals, creating a smooth surface. J1 is the dominating joint set in the area and the easiest one to map, thus it is the most measured joint set (248 poles). From Figure 40 it is possible to follow J1 along the entire failure area of the Prestura rockslide, which is interpreted as the surface of rupture. The persistence is observed over 10s of meters and even several kilometres in the NNW-SSE striking weakness zones (Figure 35, Figure 39 and Figure 40), while the aperture of J1 is mostly observed as less than a cm. The properties of J1 are summarized in Table 7.

*Table 7: Properties of joint set J1*

Joint set	Discontinuity type	Dip direction/dip (1stdv*)	Consistency	Surface condition	Persistence	Spacing (m)	Aperture (m)	JCS (1stdv)
J1	Exfoliation	084/64 (17,5)	Consistent	Smooth and mostly planar, but some observations are undulating due to weathering.	0,3 – 10s of meters at most localities, up to 100s of meters along weakness zones.	0,2 – 2	0,001 – 0,01	215 (76) MPa



Figure 40: J1 and the NNW - SSE striking weakness zone oriented along the release surface of the Prestura rock slope failure, seen towards north.

### Joint set J2

J2 is dipping consistently to the north for the entire area. The joint surface is interpreted as smooth and planar with a persistence shown in Figure 36 and Figure 41, often over 4 meters, and over several km along the ENE – WSW striking weakness zones (Figure 35 and Figure 39). The aperture is usually less than a cm, except along the ENE-WSW dipping weakness zones, where it is observed up to 5 meters (Figure 36). The properties of J2 is summarized in Table 8.

Table 8: Properties of joint set J2

Joint set	Discontinuity type	Dip direction/dip (1stdv*)	Consistency	Surface condition	Persistence	Spacing (m)	Aperture (m)	JCS (1stdv)
J2	Joint	353/72 (19,3)	Consistent	Smooth and planar	0,2 – 10s of meters	0,2 – 5	0,001 – 0,01 (up to 5 m along ENE – WSW striking weakness zones)	255 (82) MPa

### Joint set J3

The joint set J3 are consistently dipping towards south-east. The characteristics are similar to J1 and J2, with smooth and planar surfaces, persistence of 0,2 to 10s of meters and aperture usually less than one cm. J3 got also the same orientation as the NNE-SSW striking weakness zones marked orange in Figure 35 and Figure 39. The properties of J3 is summarized in Table 9.

Table 9: Properties of joint set J3

Joint set	Discontinuity type	Dip direction/dip (1stdv*)	Consistency	Surface condition	Persistence	Spacing (m)	Aperture (m)	JCS (1stdv)
J3	Joint	130/86 (19,0)	Consistent	Smooth and planar	0,2 – 10s of meters	0,2 – 2	0,001 – 0,01	287 (91) MPa



Figure 41: Locality C4 (see appendix E) north of the release surface. J1, J2, J3 and SF is evident in the terrain. J2 and J3 is creating small wedge failures along the steepest slopes. While SF is cutting J1 dipping into the slope.



## Joint set J4

J4 is dipping to the south-west, into the slope, as shown in Figure 42. The surface of J4 is considered smooth and planar, with a persistence up to 10s of meters, spacing from 0,5 to 1m and an aperture less than 1 cm. J4 is not as widespread as the other joint sets. It could only be documented at some specific locations (under 2% of the poles at the Prestura locality (stereonet 3) shown in the stereonet in Figure 39). This might be due to its almost vertical dip (almost 90°). Thus, it can be misinterpreted as J2 or J1 on several locations. However, by observing big rock bodies as shown in Figure 42, it is clear that J4 is a significant joint set. The properties of J4 is summarized in Table 10.

Table 10: Properties of joint set J4

Joint set	Discontinuity type	Dip direction/dip (1stdv*)	Consistency	Surface condition	Persistence	Spacing (m)	Aperture (m)	JCS (1stdv)
J4	Joint	214/86 (20,0)	Consistent	Smooth and planar	0,2 – 10s of meters	0,5 – 1	0,001 – 0,01	279 (55) MPa



Figure 42: J4 observed at location D1 dipping into the slope.

## 5.2 TLS

An analysis based on TLS data obtains a lot more measurements for every joint set than what is possible during systematic field mapping. TLS analysis is also collecting data from the entire slope, making it possible to locate new surfaces and joint sets, which is not covered during systematic field mapping. Thus, a TLS analysis was performed to reduce the uncertainty in structural data collected in field and to make sure that every joint set was included in the field observations.

Two laser scans were performed from two different locations and later analysed in the 3D software's Polyworks (Innovmetric, 2011b) and Coltop 3D (Terranum, 2014). A total of 102684 measurements was included in the TLS analysis, which are over 100 times more data than what achieved during systematic field mapping, this creates a more statistical robust analysis compared to systematic field mapping.

### 5.2.1 Structural analysis

The model is based on laser scans performed from two locations at the east side of lake Tinnsjø (marked as 1 and 2 in Figure 43), creating an overlapping image of the two scans. This makes it possible to create a 3D model of the slope. When performing the scans, there were some problems with the battery on the scanner. Thus, the number of scans were limited. The model is therefore only based on 4 different scans of the slope, where especially scan number 4 shows little or no overlap with the other scans. However, the data are still considered good enough to create a 3D model.

The slope is densely vegetated, making it hard to create a 3D model without noise from trees and other vegetation,

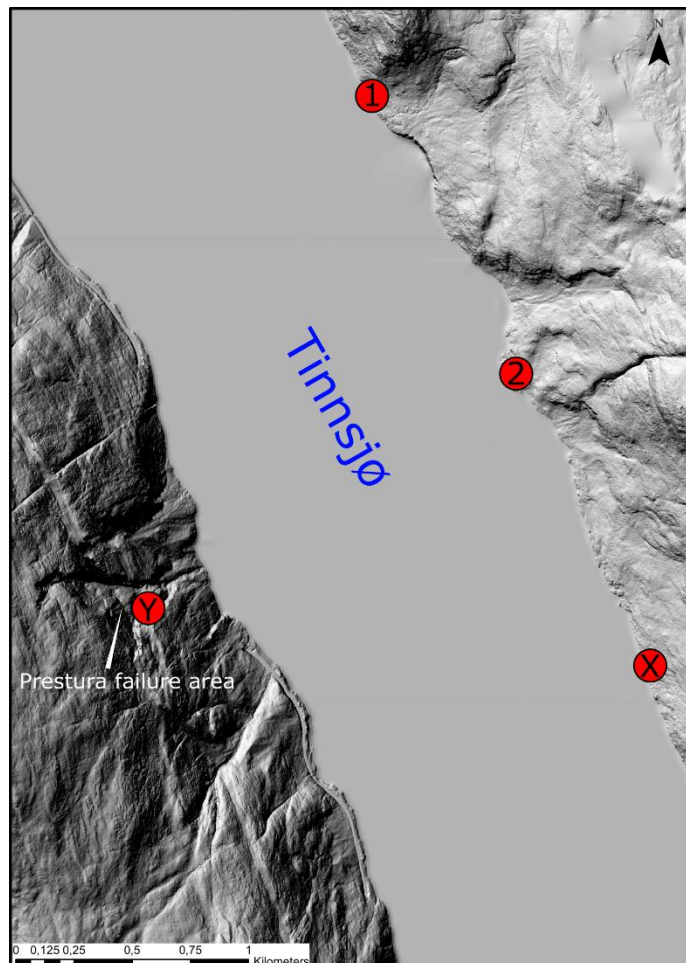


Figure 43: DEM of Prestura showing scanner locations (1 and 2) and suggested positions (X and Y).



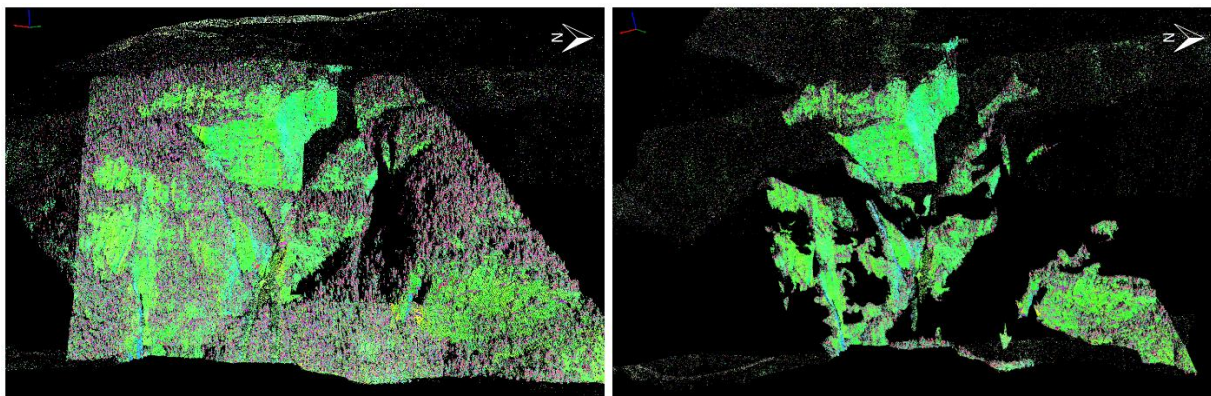
which prevents observations of important structural features. Thus, two 3D models were created of the slope: Model A and model B. Both models are shown in Figure 44.

In model A, a lot of the vegetation was kept, making the overlap between the scans close to 20°, which further makes the creation of an accurate 3D model in Polyworks possible.

However, since the vegetation is included in the model, there is a lot of noise in the data, leading to difficulties distinguishing surfaces from trees in Coltop 3D. Figure 45 and Figure 46 illustrate this problem, where the cloudy pink coloured trees are hard to distinguish from pink joint surfaces.

In model B, the majority of the trees are removed from the model. This creates less noise, but since the dense vegetation covers almost the entire slope, there is not a lot of surfaces left, making it hard to get overlapping scans. Thus, the model is not considered as accurate as model A. As a result, the further work is based on model A, while model B was used as an extra tool to distinguish surfaces from noise in model A.

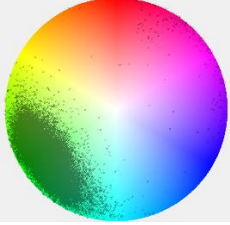
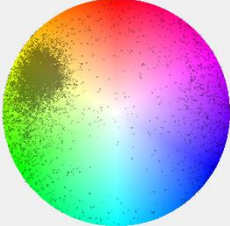
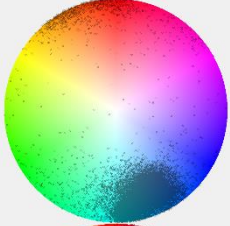
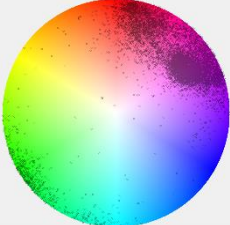
Both model A and model B are georeferenced by aligning the data to a 1x1m resolution DEM of the area, collected from hoydedata.no.



*Figure 44: TLS model of Prestura illustrated in Coltop 3D. To the left model A (vegetation not removed). To the right model B (vegetation is removed).*

Four different distinct orientations were mapped: Green, Yellow, Turquoise and Pink/Red. All data collected are presented in Table 11, and further described in the following.

Table 11: Structural data mapped in Coltop 3D. Illustrated by stereoplots. #point represent the number of dip direction/dip measurements collected for each selection. #surfaces show the number of polygons (surfaces) the data is collected from.

Colour	#surfaces	#points	Dip direction/dip (1stdv)	Observation	Stereonet
Green	6	59 260	059/68 (13,1)	Dominant colour in the area. Oriented along the slope	
Yellow	3	10 931	113/64 (14,1)	Only mappable along the northern lateral flank. Also, visible in small surfaces between green colour.	
Turquoise	6	21 024	344/72 (14,7)	Localized in the southern lateral flanks and in small surfaces inside the green.	
Pink/red	11	11 469	237/66 (14,2)	Only visible in small surfaces distributed across the entire area. Not to be confused with trees.	

The green surfaces are dominating the area, being visible at the release surface. Yellow is almost solely collected at the north lateral flank and is based on few measurements compared to Green and Turquoise (10 931 compared to 59 260 and 21 024). The reason behind this is shown in Figure 45, where approximately 80% of the northern flank is missing in the model. The reason for the missing surface may be because of unfavourable orientation of the scanners, not covering the northern flank. A possible solution of this problem would be to perform an extra scan either further south of the original scans (X in Figure 43) or at the top of the southern flank (Y in Figure 43). However, when moving a scan further south, it would also be moved further away from the slope, decreasing the resolution of the scan. A scan from the top of the southern flank might be possible in theory, but maybe not very smart in terms of



Health, Environment and Safety (HMS) regulations, since carrying the laser up the slope by foot would be the only possible method of transport.

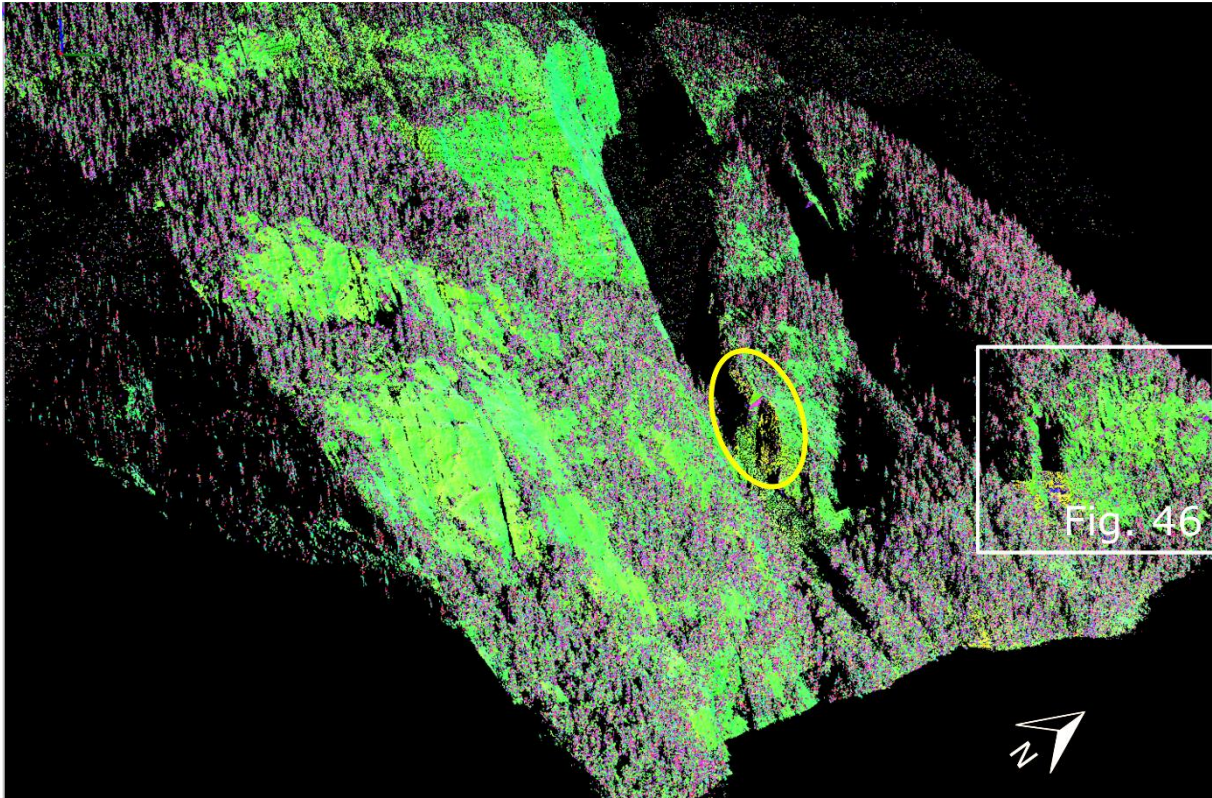


Figure 45: 3D image of failure area of the Prestura rockslide (with vegetation cover). Showing that the data in the northern lateral flanks is missing. The yellow circle represents the entire area of which yellow measurements are found.

The turquoise surfaces are mainly observed at the south lateral surface. Pink/Red surfaces are observed as small surfaces along the entire area and can be hard to separate from vegetation cover (Figure 46). It was considered to divide the Pink/Red surfaces into two different

structures, but since it is possible to see a variation between pink and red at the same surfaces in Figure 46, the Pink/Red surfaces are interpreted as the same joint set.

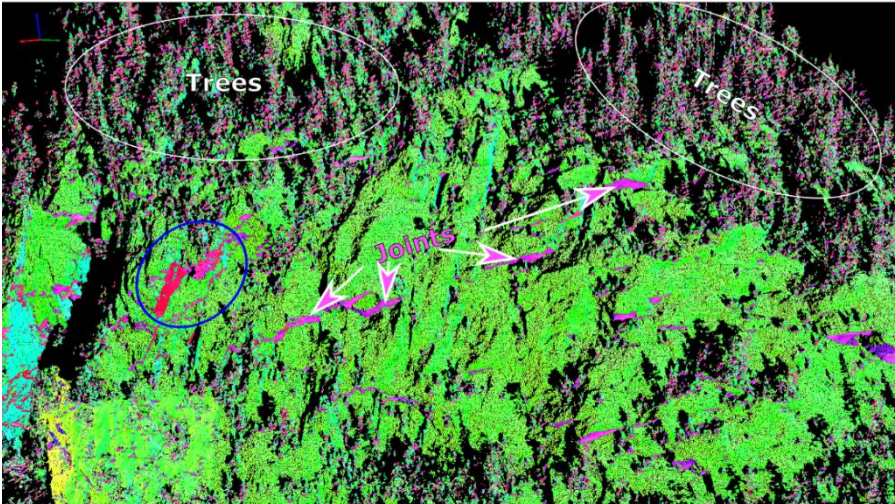


Figure 46: Zoomed 3D image in Coltop 3D. Illustrating the difference between joints and noise in the dataset. The pink surfaces in the centre of the image are more consistent than the trees, thus interpreted as joints. The blue circle show that the pink and red surfaces is occurring together, and may represent the same surface.

## 5.2.2 Comparison of data from TLS vs data from fieldwork

Figure 47 shows data collected from Coltop 3D and the data collected from field mapping in two stereonet, while Figure 48 shows both datasets merged into one single stereonet.

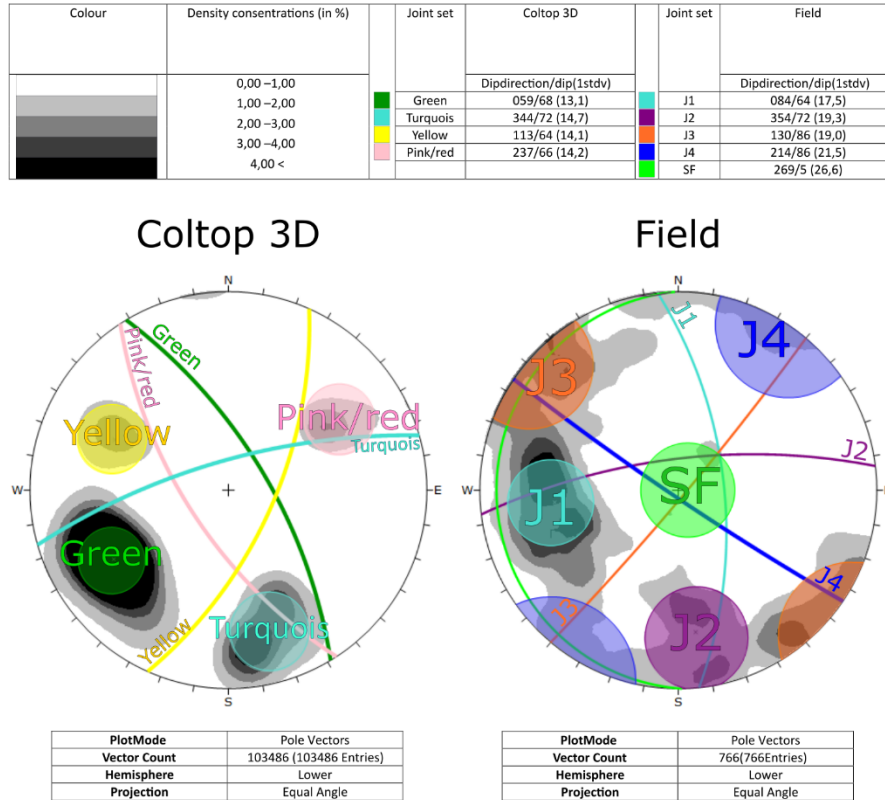


Figure 47: Data from Coltop 3D (left) and data collected during field mapping (right). Plotted in stereonet using the software Dips 7.0.

Based on Figure 47 and Figure 48, the surfaces mapped in Coltop 3D are interpreted as follows:

- Green corresponds to J1
- Turquoise corresponds to J2
- Yellow corresponds to J3. However, Yellow do also plot inside the stdv. interval of J1, thus might also represent J1.
- Pink/red corresponds to J4

No surfaces correspond to SF in the Coltop 3D analysis, due to SF being oriented almost horizontal and will not be visible in the scan due to shadowing

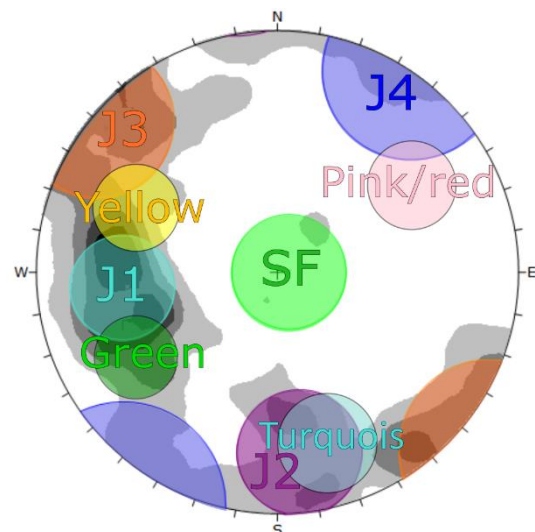


Figure 48: data from both Coltop 3D and field mapping illustrated in one single stereonet (density contours are from field mapping data).

bias (Lato *et al.*, 2009). A feasible solution would be to orient the scanner so it is not parallel to SF. This might be possible if the scanner is placed in position Y in Figure 43.

The mean orientation of all the joint sets in Coltop 3D is deviating 10-30° from the measured data in field. For J1, J2 and J3, this difference is consistent counter clockwise, while for J4, this difference is clockwise oriented. This might be due to an orientation bias described in Sollie (2014) or due to poor alignment when creating the model.

It is also observed that J3 and J4 got roughly 20° less dip in Coltop 3D compared to data obtained in field. For J3, this difference might be because the yellow surfaces were only obtained at very limited locations, thus not representing the orientation of the entire area. The difference in dip between J3 and yellow might also indicate that J3 has been misinterpreted as J1 at surfaces dipping over 60° during field mapping. This is also possible to see in Figure 48, where yellow plots inside the cluster of both J1 and J3.

The difference in dip between J4 and Pink/Red might be due to few measurements of J4 in field (75 measurements). Giving a stdv. over 20° in the data (Table 6, Table 10 and Figure 47). Pink/Red is based on over 10 000 measurements, showing a stdv. of less than 15°. Thus, it gives a better picture of the orientation of J4 than what was mapped in field.

Despite the differences discussed above, Figure 48 show that none of the surfaces mapped in Coltop 3D are significantly different than what was mapped in field. Based on this and that no new joint sets were observed in the model. It is assumed that the field work covered all the main structures. Thus, the data can be used in the following kinematic analysis of Prestura.

## **5.3 KINEMATIC ANALYSIS**

### **5.3.1 Introduction**

Due to the consistency on structures throughout the slope, only one structural domain was defined. Since the release area around Prestura is of highest interest, a kinematic analysis only for the data collected close to Prestura was performed.

Analysis 1 was performed for the area around Prestura, based on data from location A4, C4, C5 and Statens Vegvesen (2013) (see appendix B and appendix E) (209 measurements in total). Orientation is set to 067°, mean slope dip to 46° and maximum slope dip to 70°.

Analysis 2 covers the entire mapping area (766 measurements), having a mean slope orientation of 064°, a mean slope dip of 38° and a maximum dip of 70°.

The failure mechanisms tested are: planar sliding, wedge sliding, flexural toppling and direct toppling. The test was performed with friction angle of  $28^\circ$ , derived from Sollie (2014) and lateral limits of  $30^\circ$ , following recommendations from Hermanns *et al.* (2012). The choice of friction angle of  $28^\circ$  is based on the assumption of a homogeneous rock mass. Thus, a less conservative analysis than the  $20^\circ$  the friction angle recommended by Hermanns *et al.* (2012). Even though it is only a kinematic analysis for these failure mechanisms was performed other more complex failure mechanisms like bi-planar sliding can occur.

### **5.3.2 Planar Sliding**

Figure 49 shows the conditions where planar sliding is possible. The grey area shows the failure envelope at mean slope dip (outlined by a grey daylight envelope), while the pink area shows the failure envelope at maximum dip (outlined by a pink daylight envelope). The variability cone (1stdv) for J1 is plotting inside the failure envelope at maximum dip for both Prestura and the entire area, showing that planar sliding is possible at slopes steeper than  $70^\circ$ . The variability cone for joint set SF is plotting inside the grey area for Prestura, indicating possibilities of planar sliding at slopes gentler than  $20^\circ$ . However, this is only represented by two poles and is therefore considered insignificant. Planar sliding is therefore only considered a feasible failure mechanism at slopes steeper than  $60^\circ$ .



Colour	Density concentrations (in %)	Joint set	Prestura	The entire mapping area
			Dip direction/dip	Dip direction/dip
	0,00 – 1,00	J1	080/65	084/64
	1,00 – 2,00	J2	348/84	353/72
	2,00 – 3,00	J3	131/83	130/86
	3,00 – 4,00	J4	222/83	214/86
	4,00 <	SF	043/20	269/5

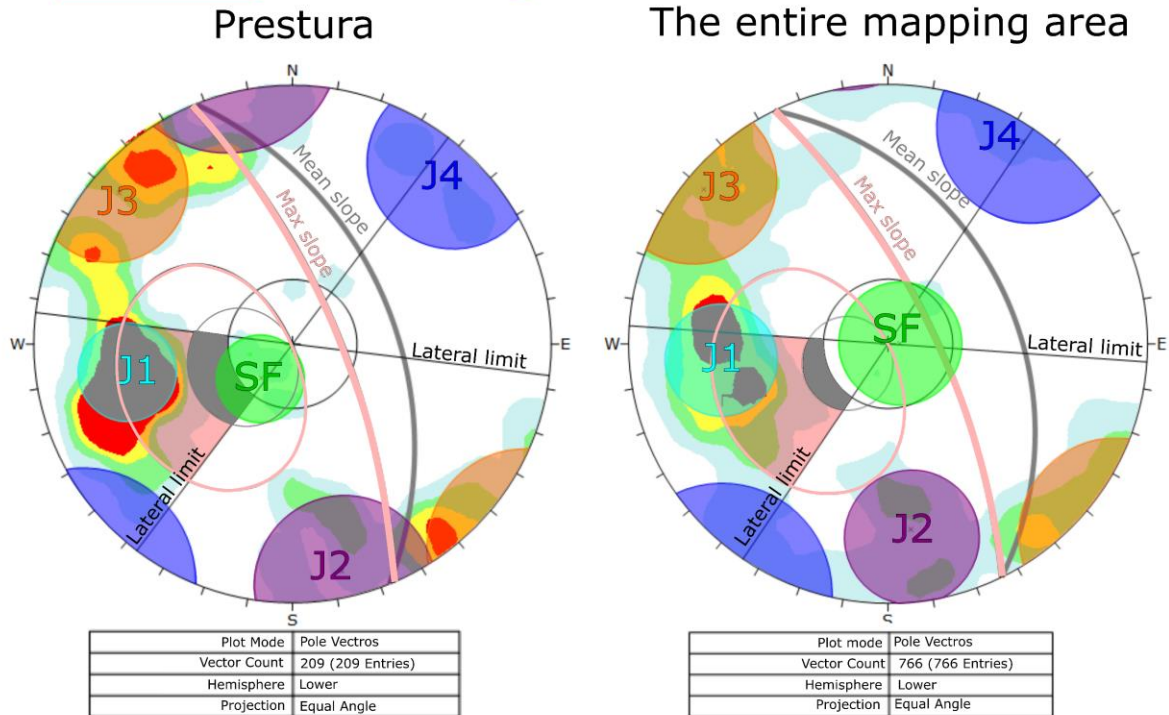


Figure 49: Kinematic feasibility test for planar sliding at Prestura failure area (left) and for the entire mapping area (right), showing variability cones of the poles for the mapped joint sets. Slope orientation, daylight envelope and failure envelopes are coloured pink for maximum slope dip and grey for mean dip.

### 5.3.3 Wedge sliding

Figure 50 shows that wedge sliding is feasible at slopes steeper than  $70^\circ$  along the intersection of J1 and J2, J1 and J3, and J2 and J3 for both the entire mapping area and Prestura. This was also observed at several locations during field mapping (Figure 38 and Figure 41).

Figure 50 shows that J1 is crossing the intersection of J2 and J3 at a gentler slope than this intersection, cutting J2 and J3 before wedge failure is possible, which makes J2 and J3 lateral release surfaces of a J1 oriented failure surface. However, this scenario is interpreted as planar failure and does not show in the wedge failure analysis. It is also worth mentioning that SF (green line in Figure 50) is intersecting both J3 and J2 at the Prestura release area at dips  $5 - 10^\circ$  lower than the failure envelope. This indicates a probability of failure along extreme low friction surfaces (friction angle below  $20^\circ$ ).

Colour	Density concentrations (in %)	Joint set	Prestura	The entire mapping area
			Dip direction/dip	
	0,00 – 1,00	J1	080/65	084/64
	1,00 – 2,00	J2	348/84	353/72
	2,00 – 3,00	J3	131/83	130/86
	3,00 – 4,00	J4	222/83	214/86
	4,00 <	SF	043/20	269/5

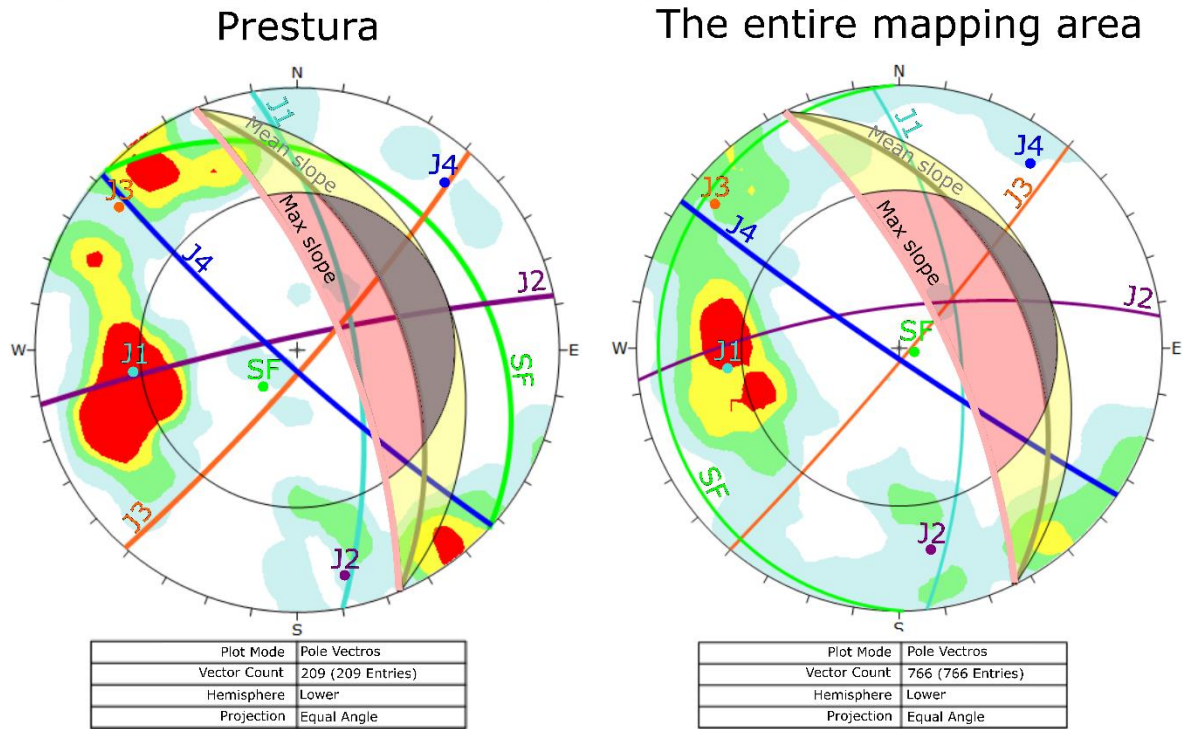


Figure 50: Kinematic feasibility test for wedge sliding at Prestura failure area (left) and for the entire mapping area (right), showing planes of the mapped joint sets. Slope orientation and failure envelopes are coloured pink for maximum slope dip and grey for mean dip.

### 5.3.4 Flexural toppling

Figure 51 shows the variability cone of J4 plotting inside the failure envelope at both Prestura and the entire mapping area. However, it is only considered significant at slopes steeper than 60 – 70°, thus only creating small volume events. Flexural toppling is also only possible at weak rock masses (Hunggr *et al.*, 2014, Wyllie and Mah, 2004, Nichol, S. *et al.*, 2002). The rock mass in the area has a mean UCS of 98 MPa (Sollie, 2014), categorized according to

Brown (1981) as a strong rock mass (grade R4). Therefore, flexural toppling is not considered a possible failure mode.

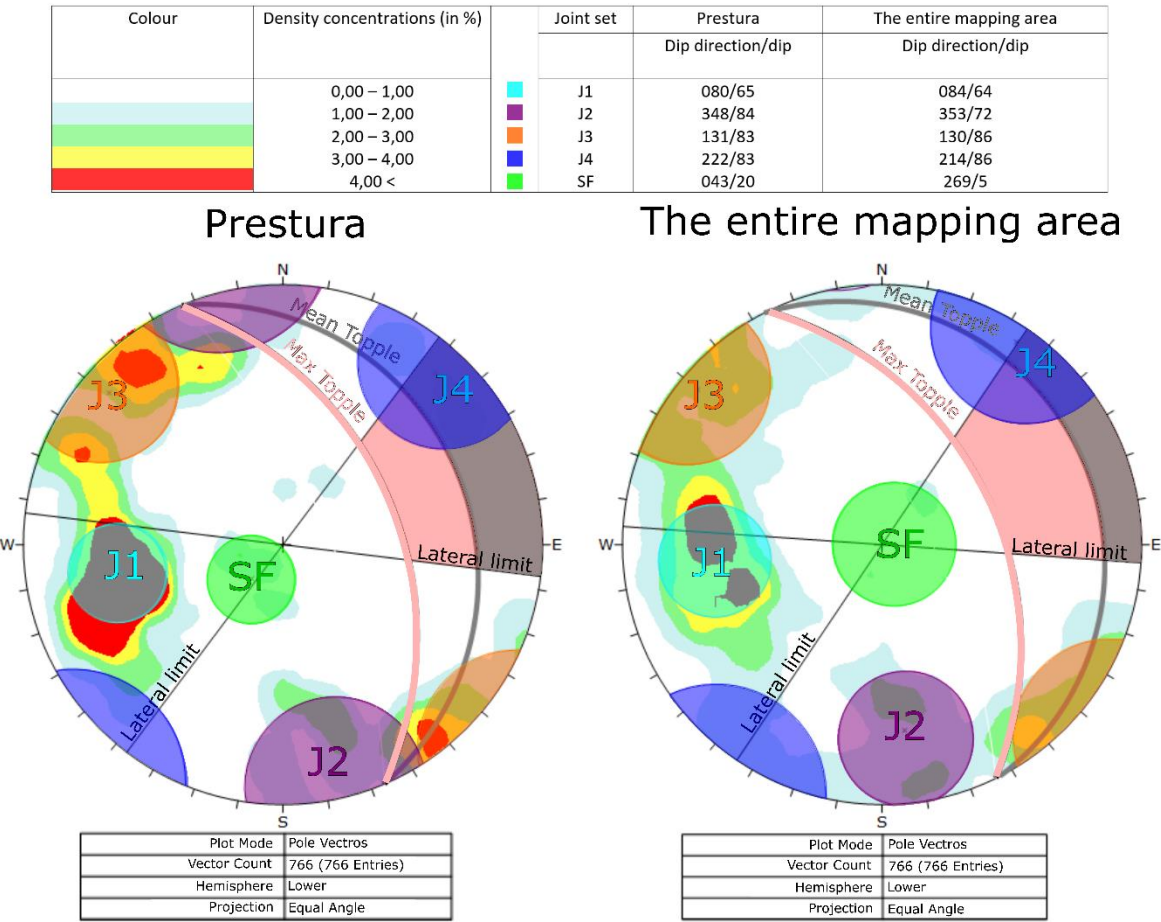


Figure 51: Kinematic feasibility test for flexural toppling at the Prestura failure area (left) and for the entire mapping area (right), showing variability cones of the mapped joint sets. Slope orientation, daylight envelope and failure envelopes are coloured pink for maximum slope dip and grey for mean dip.

**5.3.5 Direct toppling**

Direct toppling is possible in the entire mapping area and at the Prestura release surface, both at max and mean slope (Figure 52). The most critical surfaces are J1 and SF, showing that a combination of these joint sets make failure possible. However, direct toppling rarely causes failure of volumes of the size of Prestura (Nichol, S. *et al.*, 2002). Signs of direct toppling were not observed in the area, but according to Sollie (2013) is rock block toppling observable in smaller rock volumes close to Håkåneset. It is considered as a possible failure mechanism in smaller rock volumes, but assumed less important with respect to the overall slope stability (Sollie, 2013).

Colour	Density concentrations (in %)		Joint set	Prestura	The entire mapping area
				Dip direction/dip	Dip direction/dip
	0,00 – 1,00	■	J1	080/65	084/64
	1,00 – 2,00	■	J2	348/84	353/72
	2,00 – 3,00	■	J3	131/83	130/86
	3,00 – 4,00	■	J4	222/83	214/86
	4,00 <	■	SF	043/20	269/5

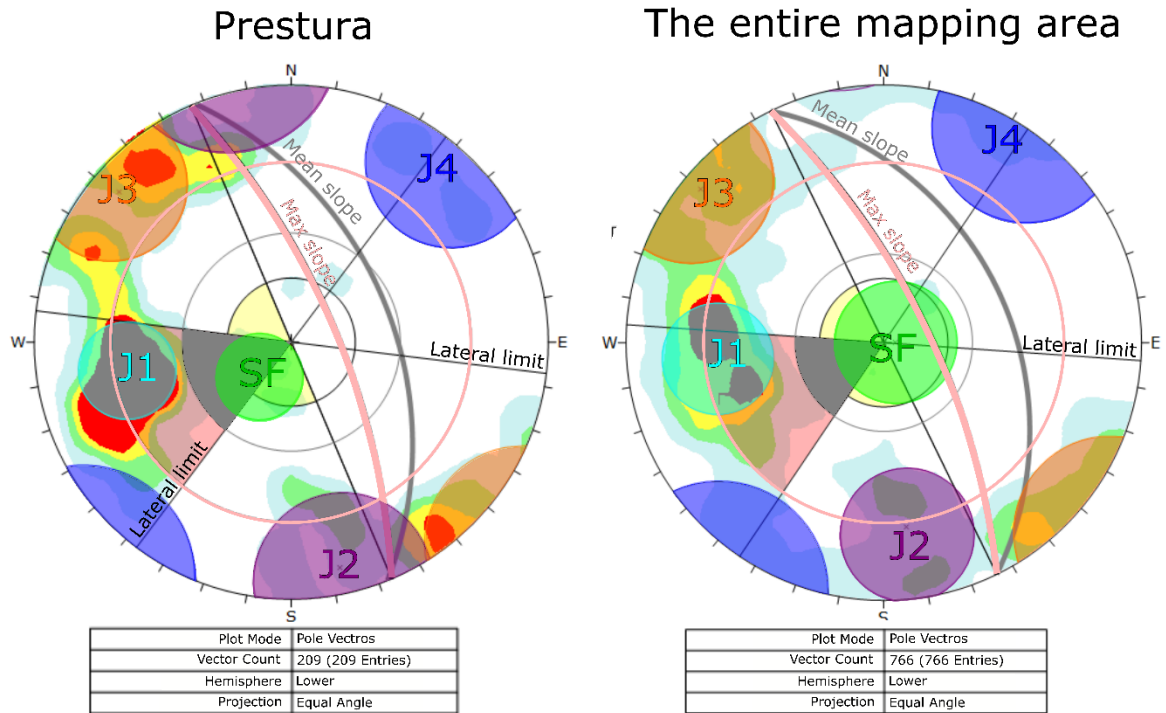


Figure 52: Kinematic feasibility test for direct toppling at Prestura failure area (left) and for the entire mapping area (right), showing variability cones of the mapped joint sets. Slope orientation, pole friction cone and failure envelopes are coloured pink for maximum slope dip and grey for mean dip.

## 5.4 MORPHOLOGY AND VOLUME ESTIMATION OF PRESTURA

In this section is the morphology of the failure area (zone of depletion) and landslide deposits (zone of accumulation) of the Prestura rockslide described, followed by volume estimation, displacement wave analysis and a comparison of the measured run out to the empirical run out estimation based on the H/L vs Volume correlation.

### 5.4.1 Morphology of the Prestura failure area

The morphology of the failure area is done in three stages. Stage one covers a general description of the failure area based on systematic field mapping, and examine orthophotos and DEMs of the failure area. The second stage involves an interpretation of the movement activity including style and distribution of movement. The final stage covers a relative age and state interpretation based on morphologic features seen during systematic field mapping and, examining orthophotos and DEMs.



## General description

The failure area is stretching from the toe of rupture surface at 420m a.s.l. up to the crown at around 800m a.s.l., having an altitude difference of 380 m and a total length of 350m. The main scarp has a dip  $55^\circ$  oriented parallel to the J1 joint set. A southern flank is visible (Figure 53) oriented parallel to joint set J2, while the northern flank is parallel to joint set J3. The failure area has a width of 450 m at the backscarp and less than 30 m at the toe of rupture surface, creating a wedge shape in the terrain. The general morphology of the failure area is shown in Figure 53 with the topographic profile A-A' illustrating the joints set orientations. From profile A-A' in Figure 54, it is shown that the joint sets J1 and SF are creating a possible bi-planar shape by intersecting each other, which supports the interpretation of bi-planar failure being the most likely failure mode from the kinematic analysis.

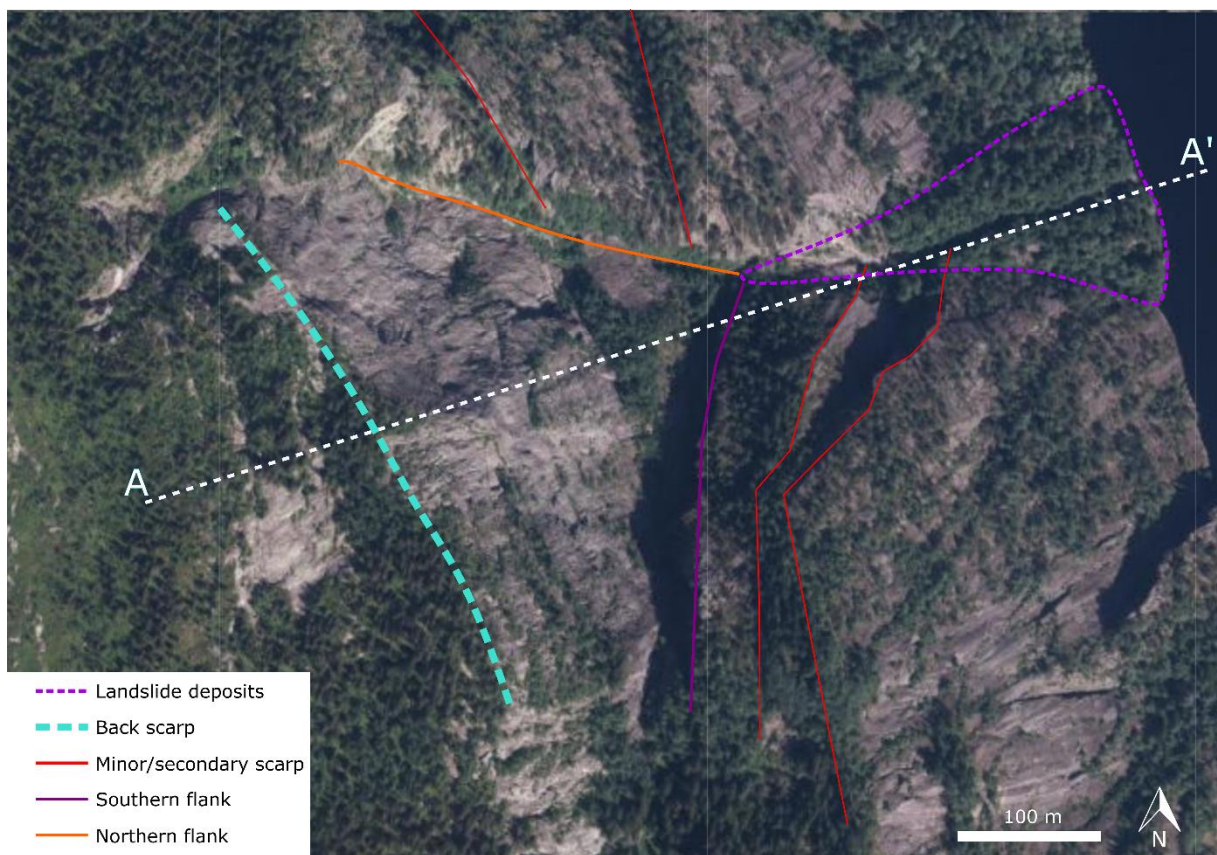


Figure 53: Orthophoto of the Prestura failure area. Showing a 450m wide backscarp oriented parallel to J1 joint sets. The northern and southern flank is parallel to J3 and J2 respectively. The minor scarps show a stepwise structure. The orthophoto is attained from ([www.norgebilder.no](http://www.norgebilder.no), 2018).

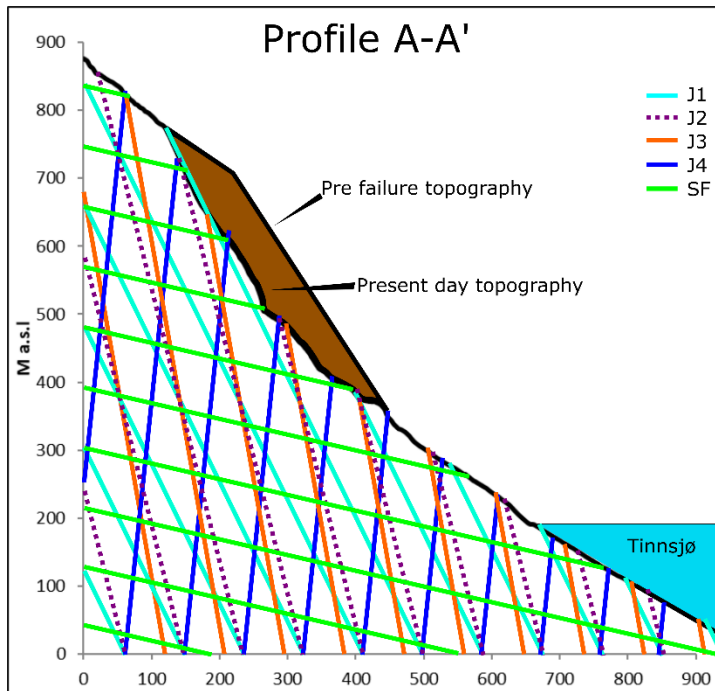


Figure 54: Reconstructed topographic profile of the failure area, showing the different joint sets. J1 is represented by its true dip, while J2, J3, J4 and SF is aligned using an alignment diagram ((Rowland et al., 2007), Appendix E)) The brown part is the most likely ante rockslide topography (ART) (see section 5.4.3) showing a possible slope topography pre-failure.

### Movement direction and distribution

Four NW – SE striking longitudinal topographical depressions occur downslope of the Prestura failure area (Figure 53). These depressions are interpreted as secondary scarps and are distributed in a stepwise structure, interpreted as previously failed rock mass, showing retrogressive distribution of the former instability.

A fan shaped landform occurs below the toe of rupture surface (Figure 53), which stretches into lake Tinnsjø. This landform is interpreted as the displaced mass of the Prestura rockslide, indicating that the failed rock mass was moving eastwards along the surface of failure parallel to the J1 joint sets, passing through the 30m opening at the toe of rupture surface, depositing both subaerially and subaquatic downslope.



## Relative age and state

The main release surface is shown in Figure 40, dipping to the east along J1 with an undulating weathered surface, which is mainly dominated by bedrock with small patches of trees and vegetation occurring at cracks and slopes dipping less than 45°.

At the northern lateral surface of Prestura, a 1 – 2m wide NNE – SSE striking crack occurs with a persistence of 10 meters, illustrated in Figure 55. This is interpreted as evidence of previous movement at the northern flank of Prestura (location C5 in appendix E). However, this crack is filled with considerable amount of soil and vegetation. This indicates that movement is low or completely absent, suggesting a suspended or dormant slope.

Because of the presence of vegetation cover and landslide features such as backscarp and minor scarps is the relative age and state determined to be Young –

Dormant, following the recommendations from Turner and Schuster (1996) illustrated in Figure 16.



Figure 55: Picture showing well developed joint observed at location C.5 (see appendix E). The width is over 1 meter and the bottom is filled with soil and vegetation.

## 5.4.2 Morphology of the Prestura deposits

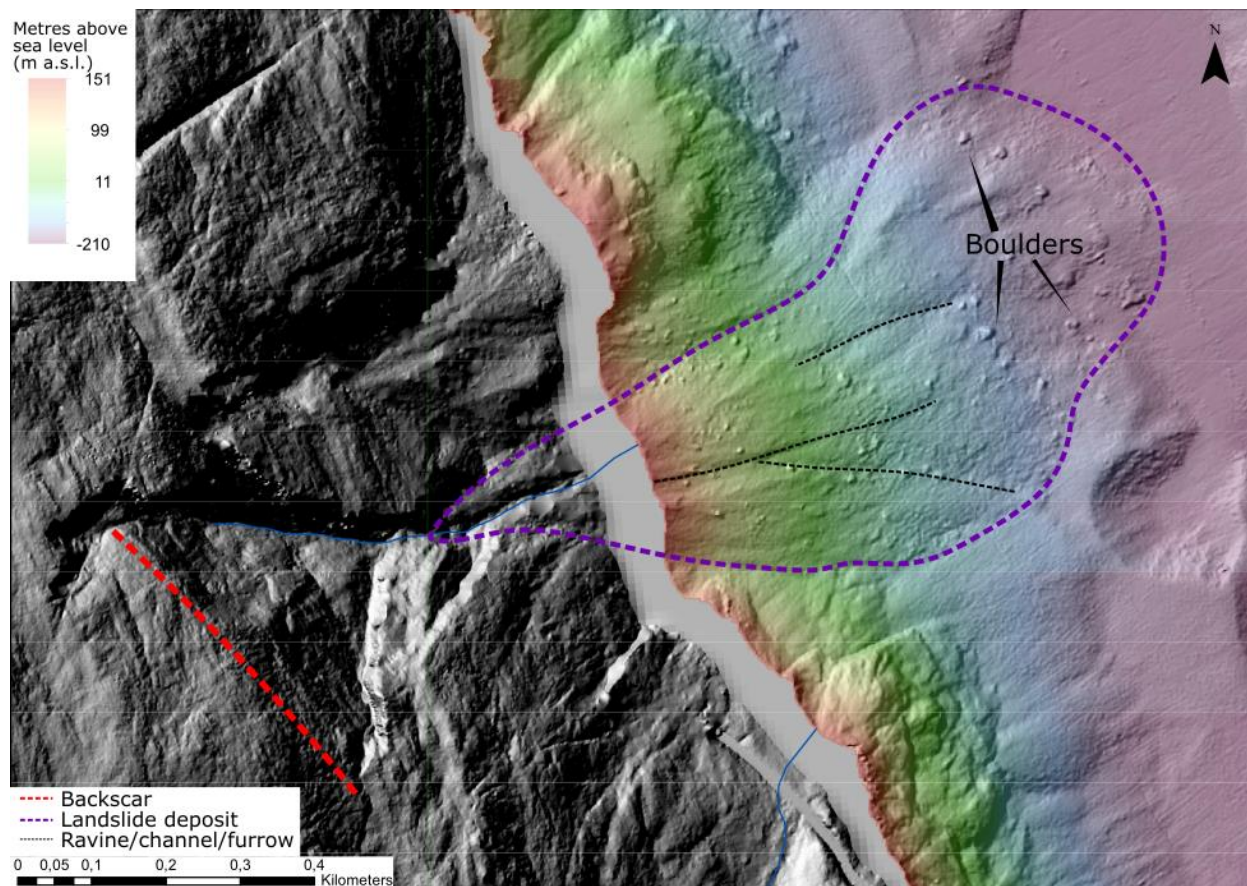


Figure 56: DEM of Prestura (Grey), with a bathymetrical model (coloured) representing the lake floor of Tinnsjø. The Prestura deposit is located east of the Prestura failure area, reaching the basin floor of the lake.

A fan shaped landform occurs east of the failure area reaching the basin floor of lake Tinnsjø at a depth of 360 m (-210 m a.s.l.) (Figure 56). The length of the landform is measured to be 750m, while the width is at its widest over 500m at the toe of the fan. At the toe are angular boulders with a diameter up to 20 m localized. The presence of big boulders at the toe is usually observed in relations to landslide events (Domaas and Grimstad, 2014). Thus, based on the fan shape and the presence of big boulders is the landform interpreted as the deposit of the rock slope failure causing the depletion zone on the slope. The size of the deposit and its location in relation to the Prestura failure area, indicate that this is the displaced mass of the Prestura rockslide, named “Prestura deposit” in the following.

## 5.4.3 Volume estimation

Three different methods were used to estimate the volume of the Prestura rockslide.

1. Spatial analysis in ArcGIS, based on ART. (referred to as “ART method” in the following).
2. SLBL.



### 3. Minimum eroded volume.

All three methods were used to estimate the initial volume of the potential failed mass, while only SLBL and “minimum eroded volume” were used in estimating the displaced volume.

#### **ART reconstruction**

Art reconstruction was performed in the software Ployworks, following the steps presented in Figure 30. The ART achieved from using method 1 is illustrated in Figure 57. This model was considered conservative since the polygon are hovering above the topography, representing an artificially high initial volume. The model was nevertheless included in the results representing the maximum possible failed volume.

Two additional models adjusted to fit the present topography, using method 2 were created (Figure 57). One represents the minimum failed volume, based on an assumption of a high degree of post landslide erosion (model B), while the other (model C) represents the most likely scenario.

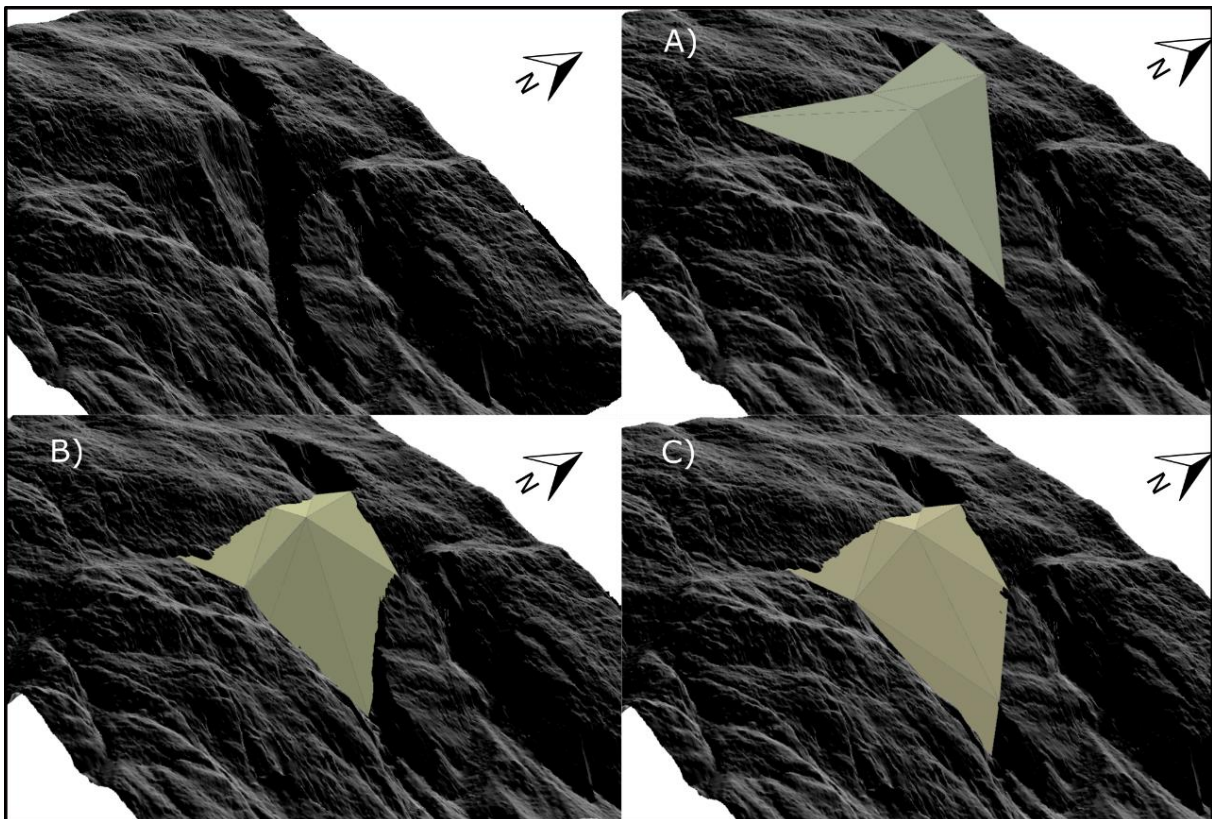


Figure 57: Ante Rockslide Topography (ART) reconstruction of the Prestura rockslide presented in ArcScene (ESRI, 2017b). A), Model a) based on method 1 (maximum volume), hovering above the topography. B), Model b) adjusted to the topography (minimum volume). C), Model c) adjusted to topography (most likely volume). The upper left picture represents the post failure topography.

## Volume results

The estimated volume of failed rock mass and the displaced volume, using the three different methods are presented in Table 12.

Table 12: Result of volume estimation based on the “ART method”, SLBL and “minimum eroded volume”.  $V_{min}$  represent the volume of model b) in the ART method and a curvature value (C) of 0 for the SLBL.  $V_{inter}$  is model c) in ART and  $C = 0.03098$  in SLBL of the failed volume and  $C = -0.0085$  in the SLBL of the displaced volume.  $V_{max}$  is model a) in ART and  $C = 0.14844$  in SLBL of the failed volume and  $C = -0.01606$  in the SLBL of the displaced volume.  $V_{mean}$  is the average volume, based on  $V_{min}$ ,  $V_{inter}$  and  $V_{max}$ .

Method	$V_{min}(Mm^3)$	$V_{inter}(Mm^3)$	$V_{max}(Mm^3)$	$V_{mean}(Mm^3)$	Stdv
Failed Volume					
ART method	4,98	6,44	9,32	6,91	2,41
SLBL	3,54	4,81	8,87	5,74	3,13
Min. eroded volume	3,70	-	-	3,70	-
Displaced Volume					
SLBL	1,41	1,68	3,99	2,36	1,63
Min. eroded volume	2,23	-	-	2,23	-

From Table 12 shows that the “ART method” estimate a 1,2 million  $m^3$  larger mean initial volume than the SLBL method. However, with a standard deviation of 2,41 is this difference is not significant and is considered a good fit. The “minimum eroded volume” method is based on the same principle as the SLBL, with a curvature tolerance (C) set to zero, but used on a higher resolution DEM (1x1m). Thus, it should be similar to the  $V_{min}$  result obtained from SLBL calculation, and should not be part of the determination of the most likely rockslide volume. This similarity between the  $V_{min}$  for SLBL and minimum eroded volume is also evident for the subaquatic landslides mapped in lake Tinnsjø, shown in appendix G.

Based on the results shown in Table 12, the failed volume is considered to be in the order of 3 – 9 million  $m^3$ . While the displaced is in the order of 2 – 3 million  $m^3$ . This indicates that the displaced volume is less than the failed volume.

### 5.4.4 Empirical run out vs Volume correlation

The Prestura rockslide has a run out (L) of 1300m a height difference (H) of 1000 m and a volume of 3 – 9 million  $m^3$ . From Figure 58 it is possible to see Prestura rockslide plotted in a H/L vs Volume diagram.

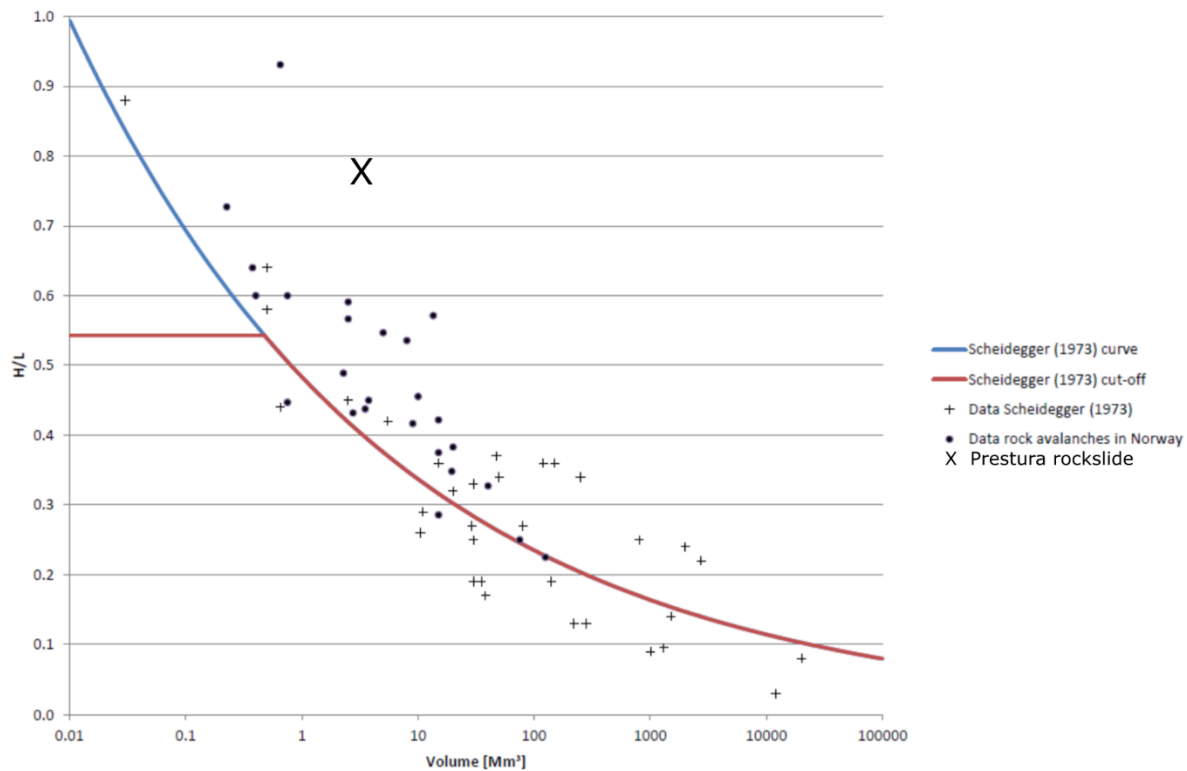


Figure 58:  $H/L$  vs Volume correlation diagram with the volume of the Prestura rockslide marked X. Modified from (Hermanns *et al.*, 2012)

### 5.4.5 Displacement wave analysis for the Prestura rockslide

A displacement wave analysis was performed for the Prestura rockslide, which is based on the SPLASH equation described in (Oppikofer *et al.*, 2016). The input landslide volume is based on the combined average volume of both the SLBL and ART methods, set to 6.33 million  $m^3$ . The analysis was further performed for five denser populated areas localized along the shore of Tinnsjø. Results and correction factors are presented in Table 13.

From Table 13 it is shown that the Prestura rockslide might have created displacement waves of 10 to 19m height at the shore.

Table 13: Run-up height displacement wave created by the Prestura rockslide at densely populated areas along lake Tinnsjø.

Populated area	Distance from Prestura (km)	Number of changes in wave propagation direction			Shoreline type	Run-up height (m)
		45°	60°	90°		
Austbygde	12.18	0	0	0	Bay	16.2
Mæl	10.79	0	0	1	Fjord head	18.7
Åtrå	14.18	1	0	0	Fjord head	18.5
Hovin	8.35	0	1	0	Bay	16.7
Tinnoset	20.48	1	1	0	Fjord head	10.9



## **5.5 SHORT DESCRIPTION OF THE HÅKÅNESET ROCKSLIDE**

This section cover a short description of the Håkåneset hillside based on the work done by Sollie (2014), followed by new findings in the bathymetrical analysis performed in his thesis.

### **5.5.1 Slope description, structures and simplified profile (from (Sollie, 2014))**

The Håkåneset rockslide lies on an ENE-dipping slope with a on average 38° dip. The unstable area ranges from a NNW trending back wall at 530 masl, down to the toe at almost 345-meter depth in Lake Tinnsø.

The bedrock in the area is dominated by two different rocks. One gneissic rock with visible wavy foliation and a dark metaryholitic rock with quartz, calcite and amphibole. The joint sets are presented in Table 14 with its main properties, and a simplified profile of the hillside with the mapped structures are presented in Figure 59.

Table 14: Field descriptions of the identified joint sets at Håkåneset. From (Sollie, 2014).

**Table 6: Field descriptions of the identified joint sets at Håkåneset.**

Joint set	Discontinuity type	Dip direction	Consistency	Surface condition	Spacing	Persistence	Features
J1	Exfoliation	NE	Steeper in Upper-South domain than Lower-South domain	Slightly weathered, planar to undulated, stepped, rough. Brown weathering surface with thin spots of quartz/feldspar	0,1 - 2,6m	0,2 - 3,4 m ( $\pm 0,2$ ), also 10s of meters	Slickensided lineations (trend/plunge: 044/42) Groove marks (trend/plunge: 081/47)
JF2	Tectonic (conjugate)	N	Consistent	Mostly planar and smooth. Brown Fe-mineralization	0,1-10m	1m to more than 10 m	Well developed mineral lineations formed at least partially by muscovite sheets. Subhorizontal (13/279 (trend/plunge)), thus indication strike slip movement.
JF3	Tectonic (conjugate)	SE	Consistent	Undulating to stepped. Mainly rough. Fe-mineralization. Quarts/feldspar mineralization	0,2-2m	0,2-10m	Fault: ~ 1 km
J4	Joint	SW	Dip direction more north in the North domain compared to the south domain	Smooth to rough, angular or planar. Brown Fe-mineralization	0,2-0,5m	0,1 m to more than 10 meter	
SF	Schistose foliation	variable	Difficult to map	-	-	-	-

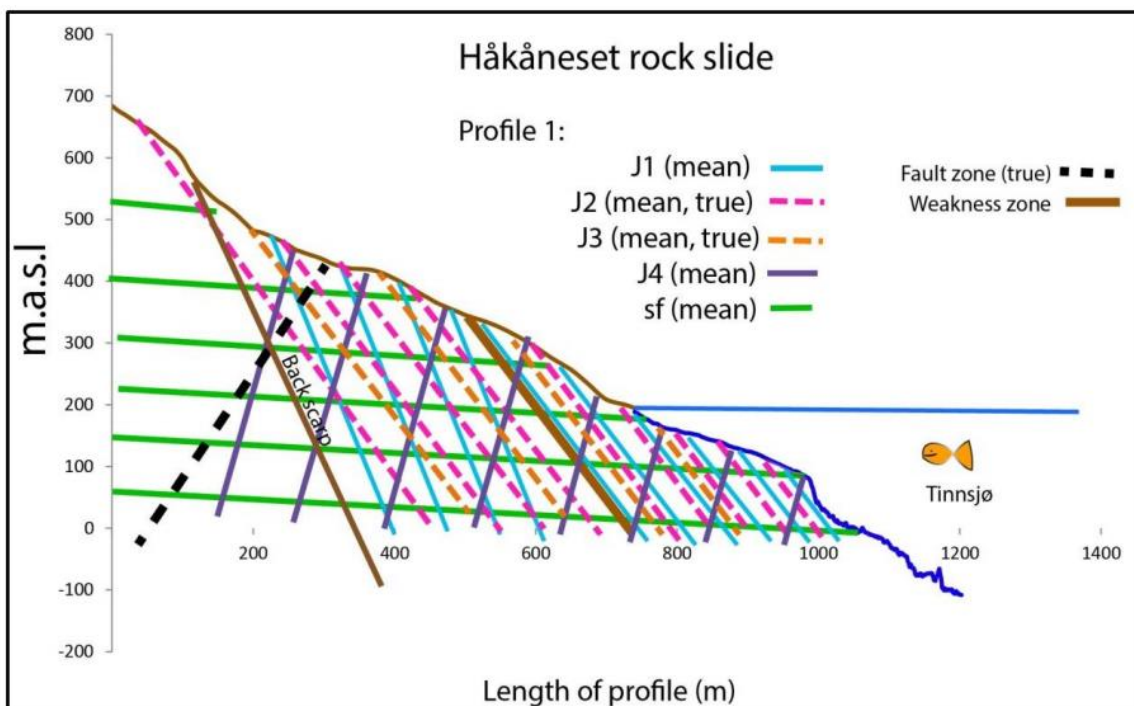


Figure 59: All mapped structures in a SW-NE profile of the Håkåneset rock slide. From (Sollie, 2014).

The lateral limit was defined by Sollie (2014) by a SW – NE striking fault system in the north, while the southern lateral limit does not show a topographic distinct appearance, which is suggested as transitional. The lateral limit was based on limited bathymetrical data (Figure 60). Therefore, the toe area and the NW flank could not have been defined correctly. The new data makes a better definition possible that is outlined in Figure 61. Based on the limited data, only the structural model is described in the following. However, the Geological Survey of Norway is working with a revisited analysis of failure scenarios and related volume.

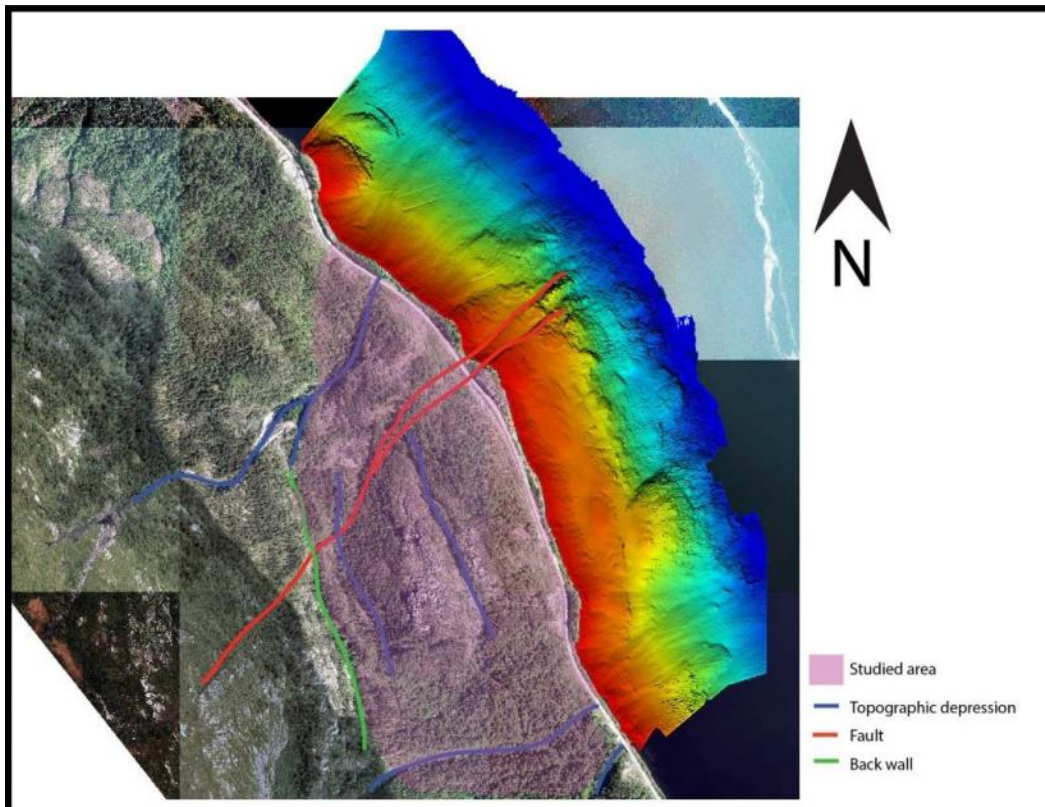


Figure 60: Air photo and bathymetric map of Håkåneset rock slide. Showing the limited bathymetrical data only reaching a depth of 300m. From (Sollie, 2014).

### 5.5.2 Domains and kinematic analysis (from (Sollie, 2014))

The area is divided into three subaerial domains (upper-south, Lower south, and North) and two subaquatic domains (Bathymetry-South and Bathymetry-North). The subaerial domains were divided based on a systematic change in the orientation of joint set J1 and J4 and mapped tectonic features, while the subaquatic domains were divided based on geomorphological features that are visible on bathymetrical images. The kinematic analysis is performed based on the mean and max dip of the slope in the domain and is presented in Table 15.

Table 15: Summary of results from kinematic analysis.

Type of failure	Lower-South domain	Upper-South domain	North domain
Planar	Possible along J1 in the steepest part of the slope. SF has a favorable direction, but might not be steep enough for failure to take place.	Not as dominant as in the Lower-South domain. Not possible along SF.	Possible at the shallowest dipping J1 discontinuities in the steepest part of the slope. SF not possible, due to mainly dipping into the slope.
Wedge	Possible in the steepest part of the slope for intersection between J1 and J2, J1 and J3 and between J2 and J3. J1 is also cutting the intersection of J2 and J3, which might turn J2 and J3 into lateral surfaces in planar sliding.	Possible between J2 and J3.	Possible between J2 and J3 at slopes steeper than 55°.
Toppling	Possible along J4. (Only smaller volumes).	Partly feasible along J4.	Possible for J4.



### 5.5.3 New findings from high resolution (2x2m) bathymetrical data

The bathymetry data used by Sollie (2014) does not cover the entire unstable slope of Håkåneset (Figure 60). By using 2x2m resolution bathymetrical maps of the lake floor, it was possible to find morphologic features that had not previously been mapped.

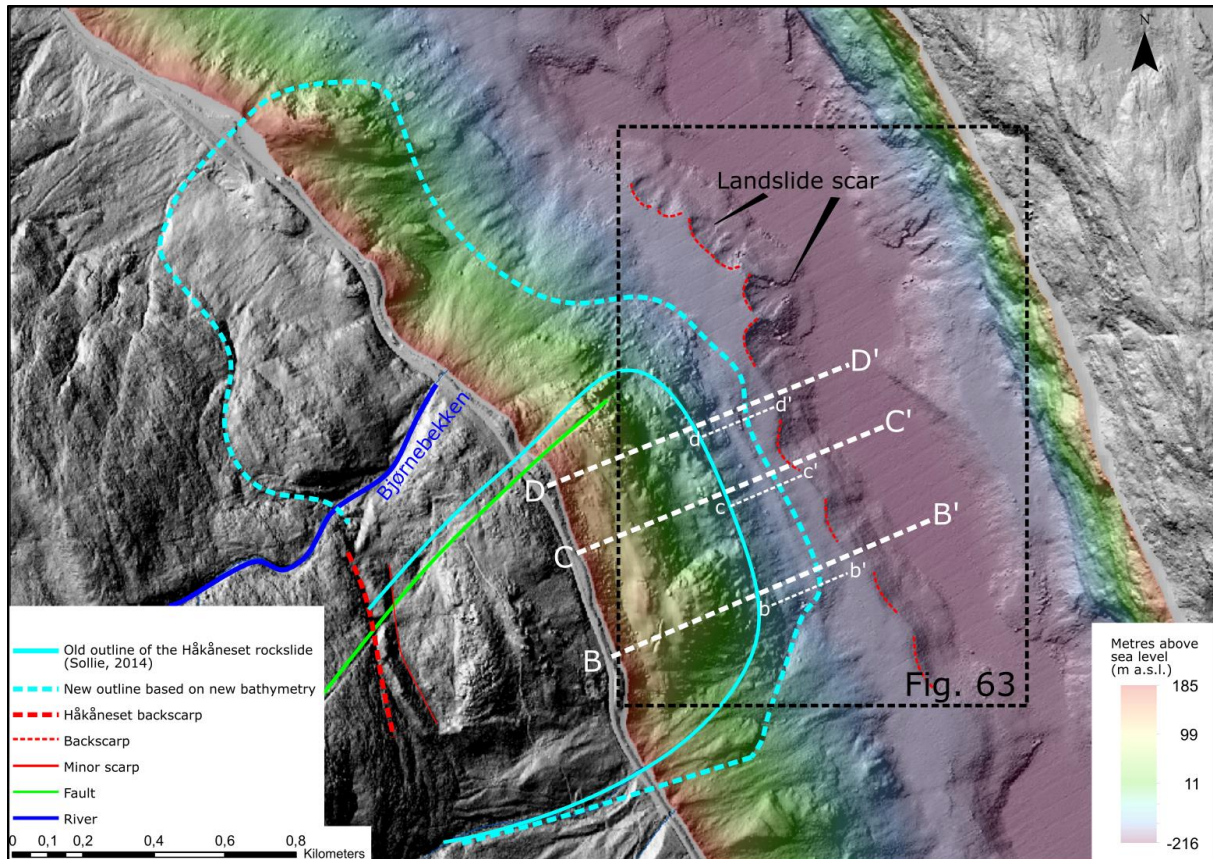


Figure 61: Bathymetrical map of the Håkåneset rockslide, with subaquatic landforms including landslide scars. Profile B-B', C-C' and D-D' depict the slope morphology. The smaller profiles marked b-b', c-c' and d-d' represent zoomed in areas of the main profiles, at the foot of the deformation. The structures occurring at the subaerial slope such as Håkåneset backscarp, minor scarp and fault is attained from (Sollie, 2014).



### Small ridges on subaqueous terraces

At a depth of 345 m (-160 m a.s.l.) it is possible to see two NW – SE oriented ridges (Figure 61 and Figure 62), disturbing the surface of a horizontal landform. These ridges have an average height of 6 – 15m, a width of 33 – 53m and length of 800 – 1000m. These ridges express the movement of the Håkåneset rockslide (Further discussed in section 6.2.).

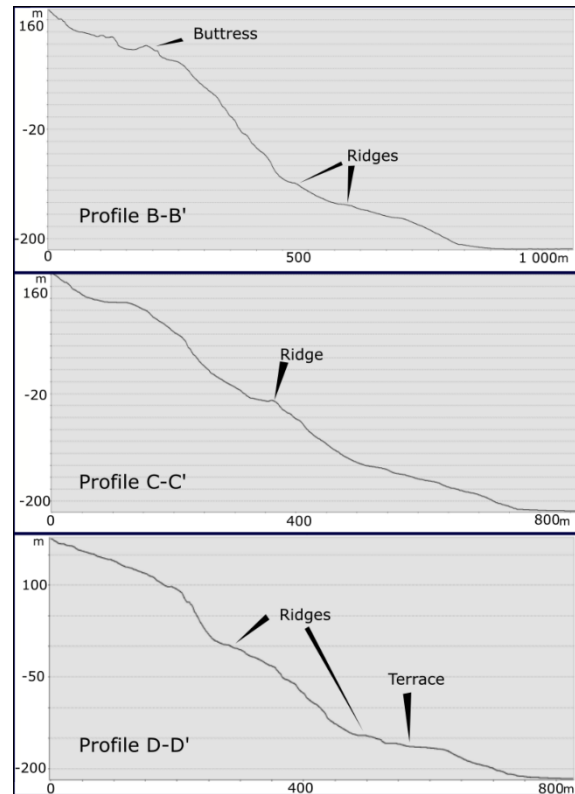


Figure 62: Profiles B-B', C-C', and D-D', showing ridges along the marginal slope close to the Håkåneset rockslide.

### Landslide scars at the terrace rim

At the horizontal landform just below the Håkåneset, occur 10 pear shaped depressions, with rupture surfaces of variable preservation potential. These landforms are interpreted as landslide scars.

The interpreted landslide scars show different relative age based on how sharply defined the landslide features are (such as backscarps and flanks). In Figure 63, the 10 landslide scars are divided into clusters based on its relative age, ranged from 1 to 4 from youngest to oldest. At the youngest landslide scars (numbered 1 in Figure 63), both the backscarp and minor longitudinal scarps are sharply defined in the terrain, indicating an active or recently active landslide. The oldest landslide scars

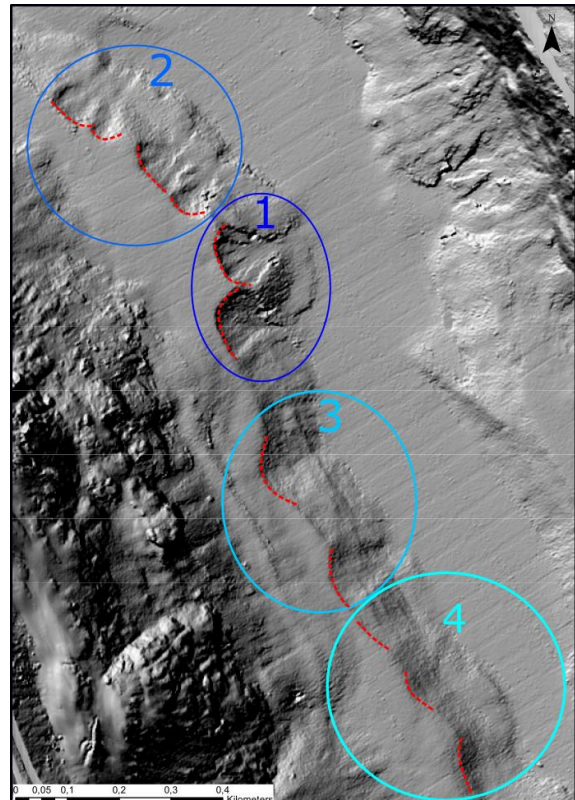


Figure 63: Landslide scars occurring at the terrace rim close to the Håkåneset rockslide. Numbered from 1 - 10 from youngest to oldest.

(numbered 4 in Figure 63) are almost not visible in the terrain, thus, interpreted as dormant-mature or dormant-old. It is also important to note that local erosion and sediment supply are influencing the visibility of landslide features. This is especially evident close to cluster 2 and 4, occurring downstream of streams, which have a larger local sediment supply than the other areas. These sediments cover the landslide features, making the landslide scars seemingly older.

## **5.6 MAPPING OF LAKE TINNSJØ**

In this section, landforms occurring in lake Tinnsjø are presented and described. A map of the interpreted landforms is illustrated from north to south in Figure 64, Figure 65, and Figure 66. Meanwhile the subsections will be covering a description of every landform type present in the lake.

All landforms mapped in the lake are covered in the results of this thesis. However, the entirety of the dataset is considered too big to be covered in detail by one single master thesis. As a result, only the landforms and mechanisms associated with landslides and the stability of Håkåneset and Prestura are further discussed.

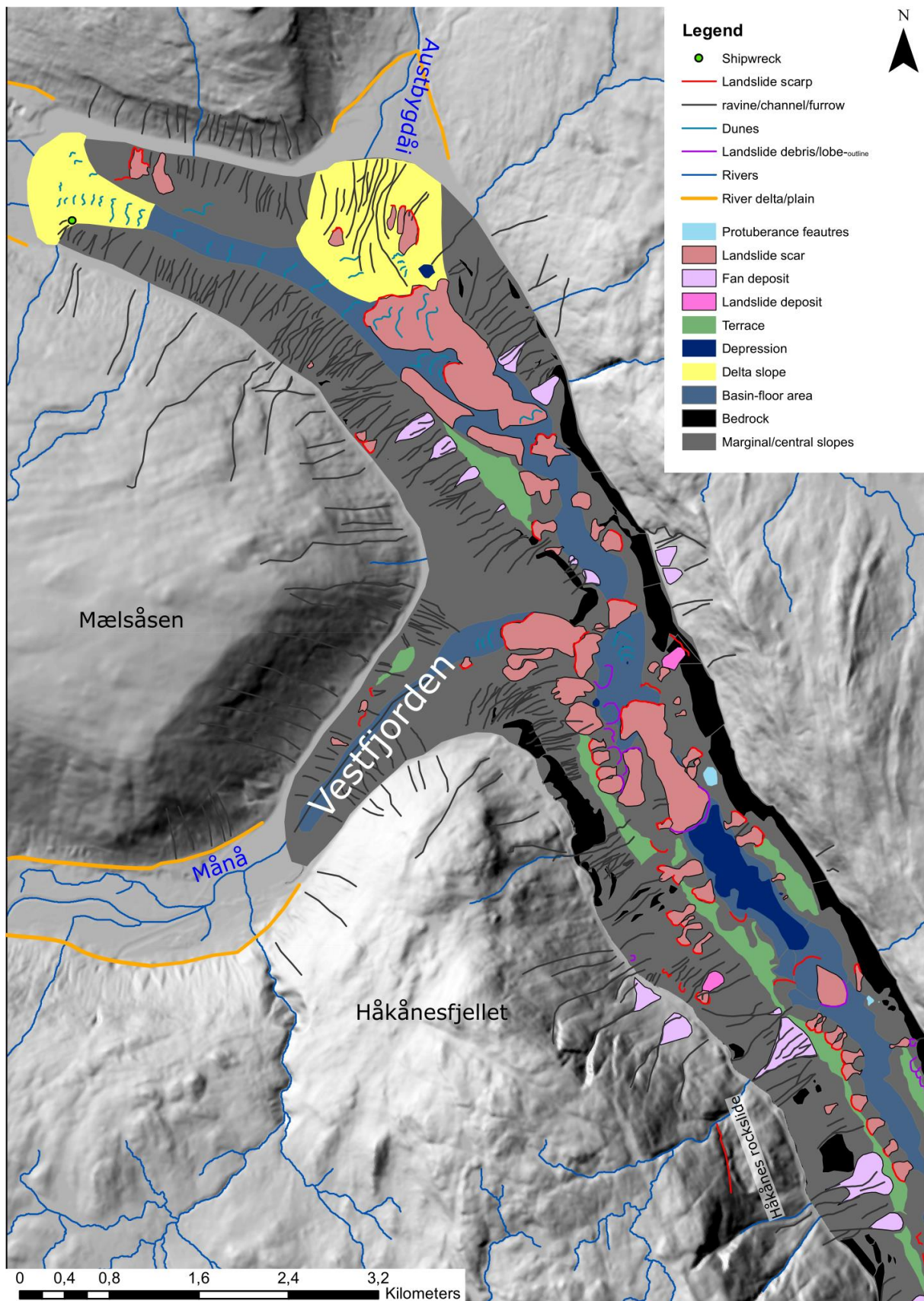


Figure 64: Map over the northern lake Tinnsjø with interpreted bathymetry. Classification is based on Hansen et al. (2016).



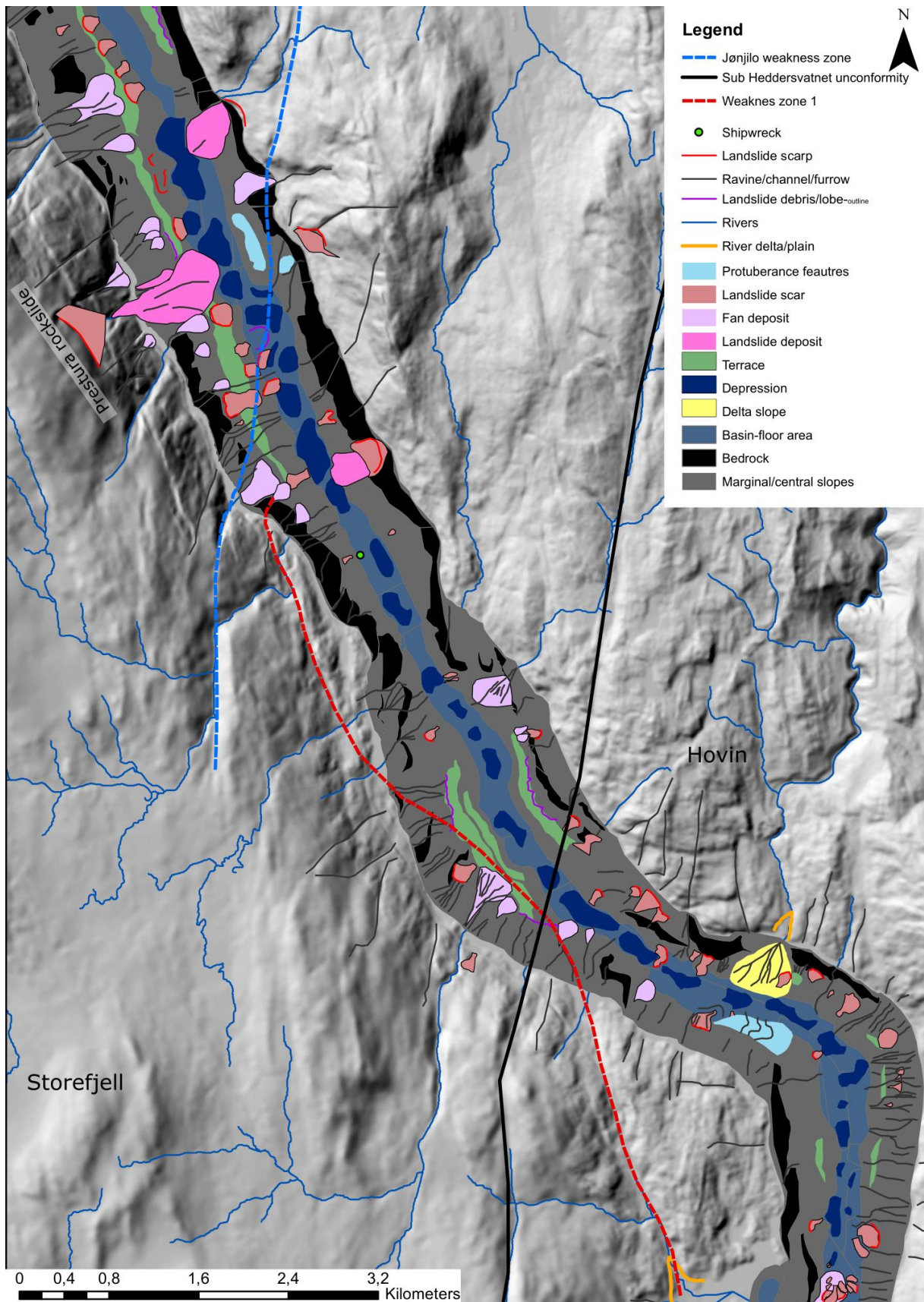


Figure 65: Map over the central area of lake Tinnsjø with interpreted bathymetry. Classification is based on Hansen et al. (2016). "Jønjljo weakness zone" and "weaknes zone 1" is added from Statens Vegvesen (1989). "sub Heddervatnet unconformity" is added from Dons and Jorde (1979).



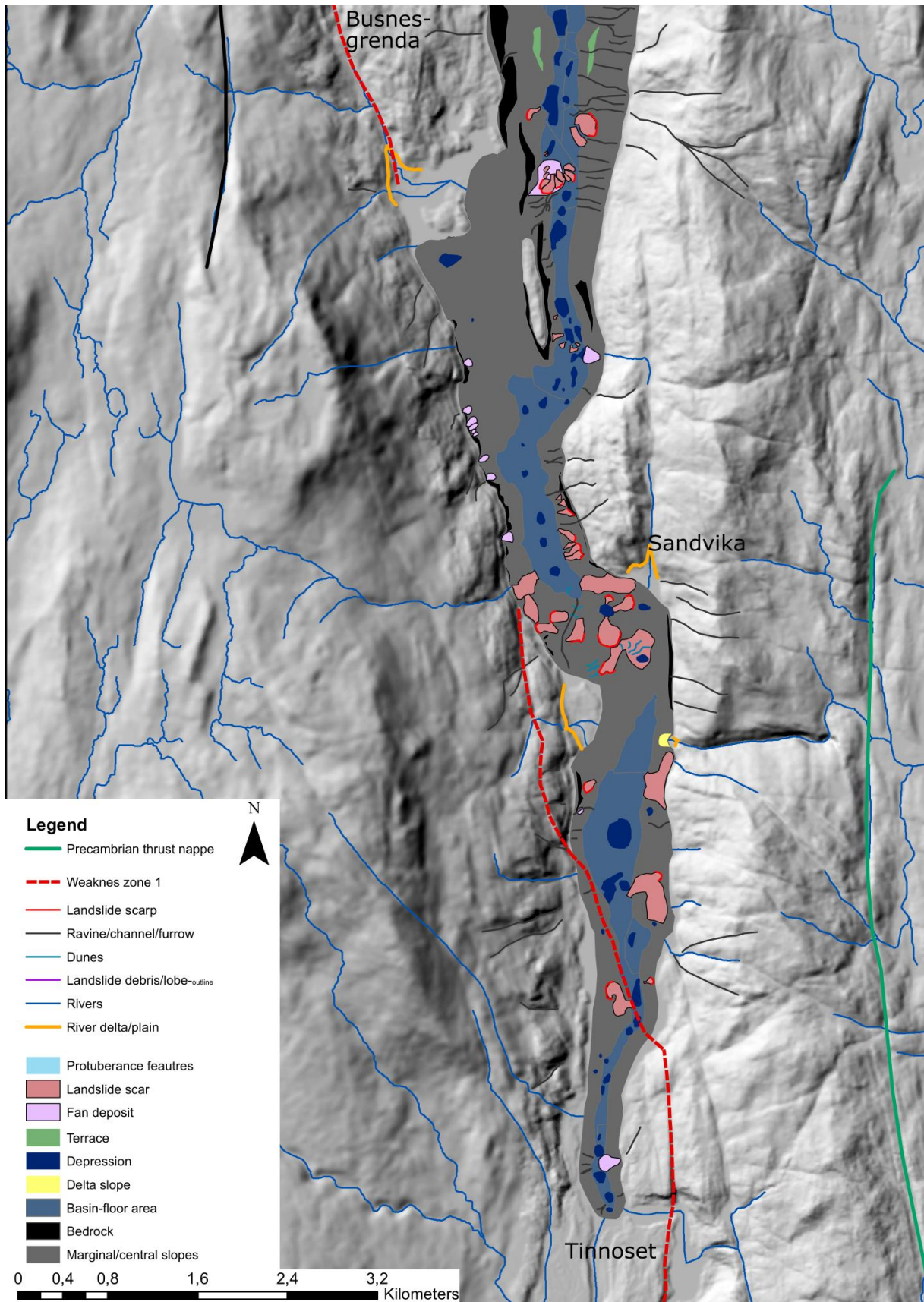


Figure 66: Map over the southern area of lake Tinnsjø with interpreted bathymetry. Classification is based on Hansen et al. (2016). “Weakness zone 1” is added from Statens Vegvesen (1989). “Precambrian thrust nappe” is added from Dons and Jorde (1979).



### 5.6.1 Marginal slope and bedrock outcrops

From the rim of lake Tinnsjø the slope is dipping 10 – 45° towards the basin floor. This is mapped as marginal slopes. The surface of the marginal slope is smooth, indicating the presence of a soil cover, most likely dominated by fine grained sediments and moraines. The surface is also disturbed by less than 1m deep, 5m wide and over 100m of long depressions, interpreted as channels, ravines or furrows.

In slopes with a dip over 45° is the slope surface disturbed by angular high reflective features, interpreted as bedrock outcrops. Soil is usually not stable at slopes steeper than 45°. Thus, the mapping of bedrock outcrops mainly is based on a slope map (appendix C), where slopes dipping over 45° are considered bedrock outcrops. The visual difference between bedrock outcrops and marginal slopes are illustrated in Figure 67

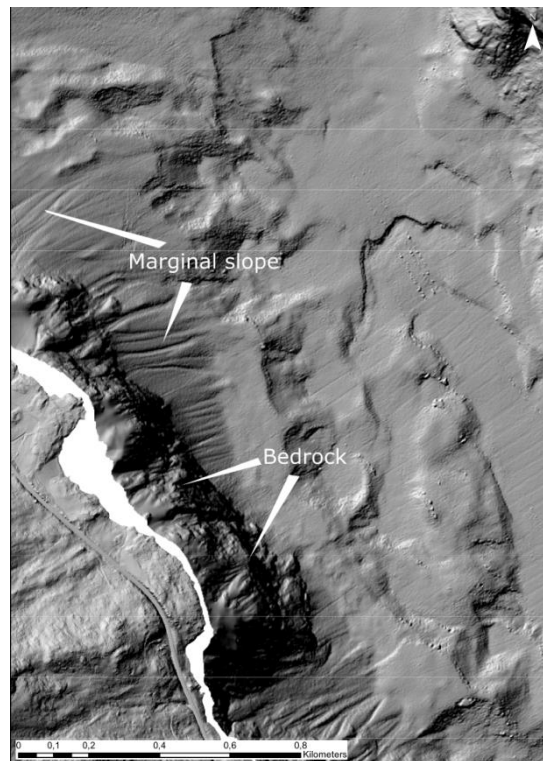


Figure 67: Illustration of marginal slope and bedrock. Marginal slopes are smooth and dim, while the bedrock outcrops is angular and reflective. Location: Just south of Vestfjorden.

### 5.6.2 Basin floor area

The lake basin floor is defined as the central areas of lake Tinnsjø, having an almost horizontal surface (less than 10° dip).

The basin floor area is changing in appearance from north to south. In the north part close to the Gøyst delta, the basin floor is dipping 0-5° to the south and is disturbed by over 5m high undulations. Several large scale arcuate depressions occur from the Austbygdåi delta in the north to the unstable slope at Håkåneset. Further southwards, the basin floor is gradually becoming more undulating due to depressions and protuberance ridges occurring southwards of the Prestura deposits.

The deepest point in lake Tinnsjø is mapped at a depth of 432m (-252 m a.s.l). From this point the basin floor is stepwise rising both towards the south and the north (profile E-E', F-F', and G-G' in Figure 68). Each step is divided by 2 – 10 m high ridges, varying in length from 100m to over 1000m. These ridges are shown in Figure 68 occurring in relation to depressions

at the basin floor. They are interpreted as ridges related to dead ice sinks (for further description of dead ice sinks see section 5.6.7).

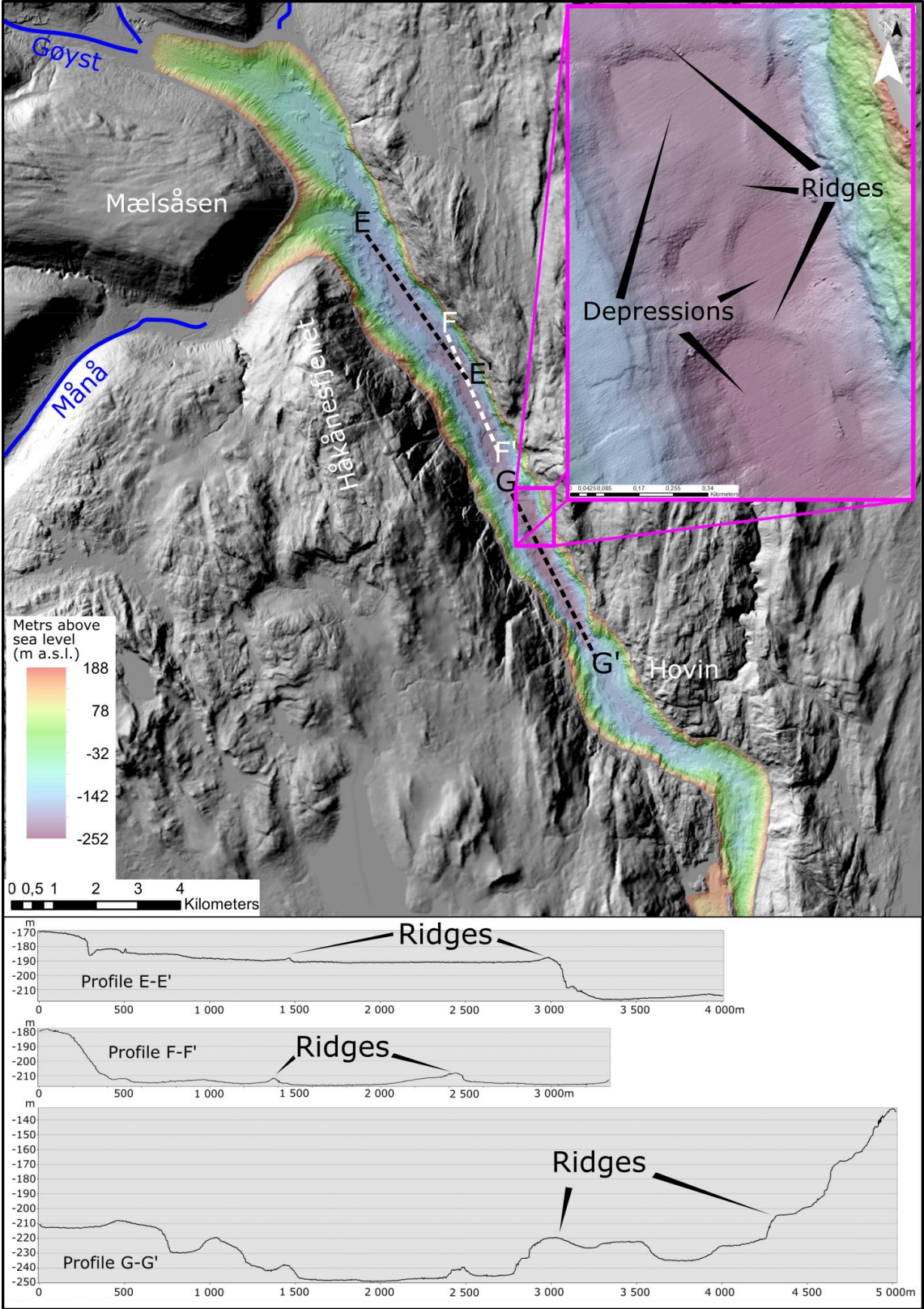


Figure 68: Longitudinal profiles of the basin floor and its locations. Profile E-E', F-F and G-G show a stepwise rising of the basin floor divided by ridges. The ridges occur along depressions seen in the zoomed pink window.



### 5.6.3 Delta

In total eight delta plains are mapped in lake Tinnsjø, named in succession from north to south after their main distributary river: Gøyst delta, Austbygdåi delta, Månå delta, Skirva delta, Luåa delta, Sandvika delta, Kyrsekk delta, and Raua delta.

In the following section, each delta will be described. This will be followed by an interpretation of delta type and sedimentation mechanisms occurring at the delta slope.

#### Gøyst delta

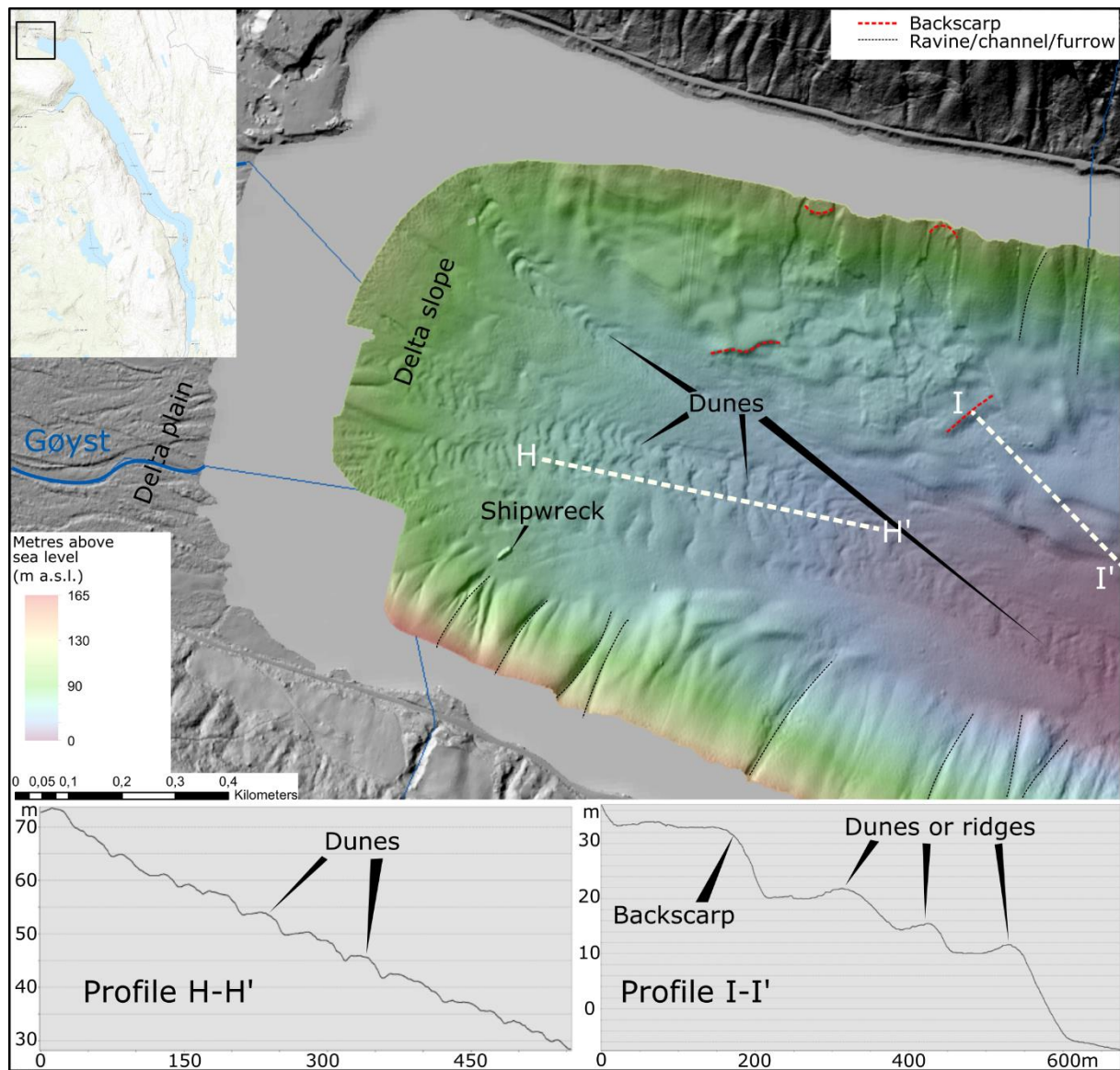


Figure 69: Bathymetry of Gøyst delta, localized at the north-western margin of lake Tinnsjø.

Close to the north-western margin of lake Tinnsjø, there is mapped a subaerial horizontal plain, with a width of 1 200m and a length of 6 000m. The plain stretches from the local valleys into lake Tinnsjø. The plain does not have a typical delta shape, but has a similar

shape as fjord-head deltas discussed in Prior and Bornhold (1990). This being constrained by the surrounding hillsides, creating a long delta plain, relative to its width.

The delta slope occurs further east having an over 20° dipping foreset and a less than 5° dipping bottomset towards the basin floor. The foreset is not fully mappable due to lack of bathymetrical data close to the lake margin, but is assumed to have a length of roughly 1 000m, a height of 140m, and a width of maximum 1 300m, restrained by the surrounding hillsides. The dip of the foreset is measured to be 20°. However, since a delta slope is often steepest close to the topset (Corner, 2006), it is assumed that the maximum dip is steeper than 20°, maybe close to 30°.

Along the foreset and bottomset of the delta slope channels undulating surfaces as wide as 100m occur. These undulations are presented in profile H-H' (Figure 69), having a mean height of 2-3m and a length of 30-40m. They are interpreted as trains of dunes originating from the large rivers Gøyst and Mår. Because of their dimensions and short distance from rivers, the dunes are interpreted as sand dunes. However, it is possible that the material can be finer grained sediments than sand. The dunes show symmetrical features, thus interpreted as cyclic steps. Cyclic steps occur in the upper flow regime (Froude number over 1), created by the imbalance in erosion and deposition due to the presence of hydraulic jumps (Figure 18) and are generated by turbidity currents (Cartigny *et al.*, 2011).

The northern marginal slope close to the Gøyst delta is irregular close to the basin floor, varying in dip between 5° to 35° towards the basin floor. Profile I-I' (Figure 69) show that the irregularities represent different topographic levels with gentle dip (5-10°). At the rim of each level there is a protuberance feature, either representing sand dunes similar to what observed at the river delta slope, or the remains of landslide lobes and backscarps. Thus, they might be considered as a part of the Gøyst delta.

## Austbygdåi delta

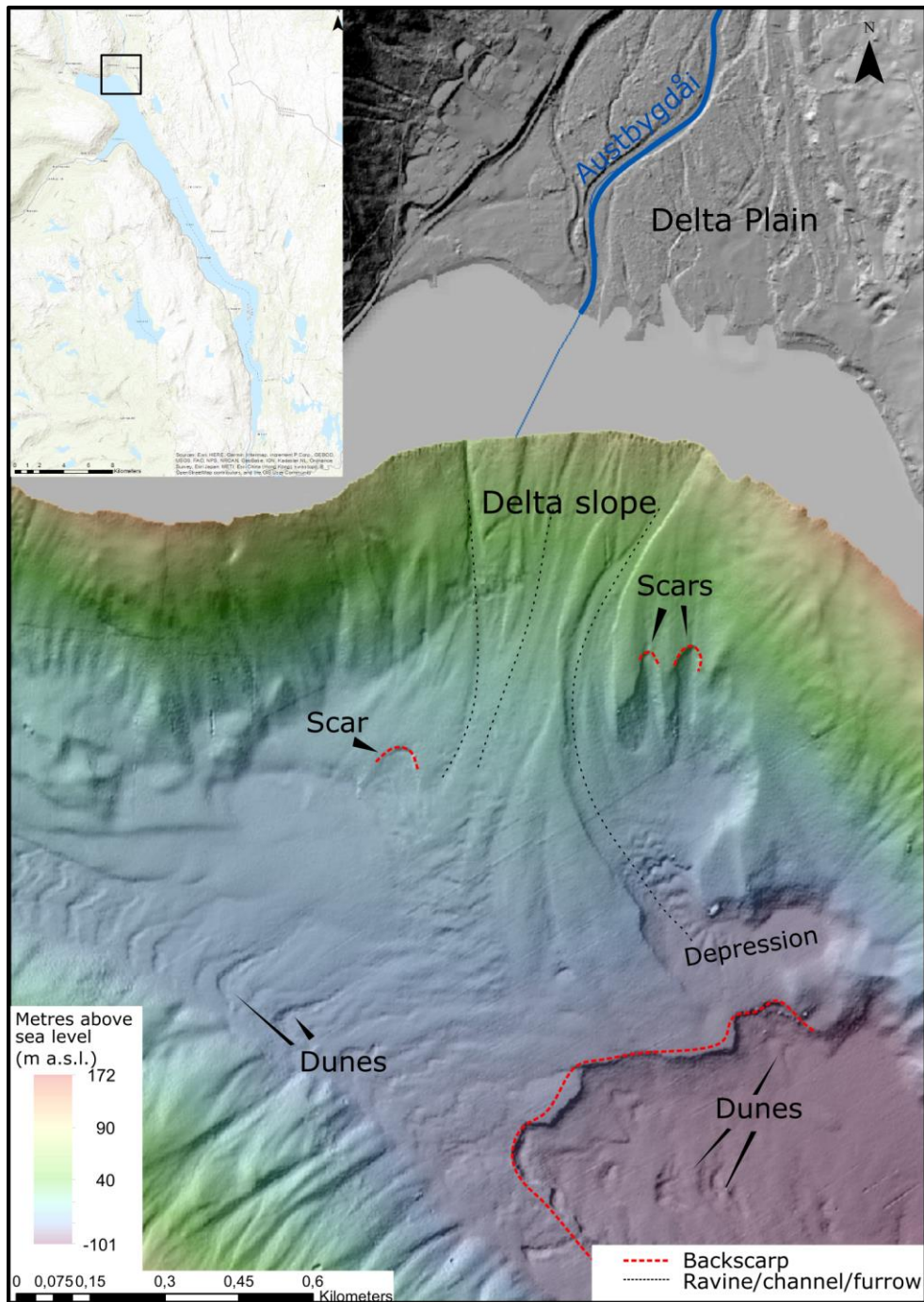


Figure 70: Bathymetry of Austbygdåi delta, localized at the northern margin of lake Tinnsjø.

Close to the northern margin of lake Tinnsjø the river Austbygdåi reaches the lake. A delta has formed, with its maximum width measuring 1 000m, occurring at the river mouth (Figure 70). The delta slope has a similar shape as the Gøyst delta slope, showing delta features such as a 25° dipping foreset and a 5 - 10° dipping bottomset.



The surface of the foreset and bottomset show an undulating geometry, similar to the surface of the Gøyst delta. Thus, they are interpreted as cyclic steps. Both the foreset and bottomset is also disturbed by less than 1m deep elongated landforms, interpreted as chutes originating from the Austbygdåi delta. Four arcuate depressions with visible backscarps, are interpreted as landslide scars. The shape of the backscarps are similar to what usually observed examining clay related landslides (L'Heureux *et al.*, 2011a, Glimsdal *et al.*, 2016, L'Heureux *et al.*, 2011b). This is especially evident when examining the 700m wide backscarp occurring southwest of the delta slope. This landslide scar might resemble a large quick clay slide (L'Heureux *et al.*, 2011a) and are further described in section 5.6.5. The age of this landslide scar is considered relatively young due to the sharply defined backscarp, but despite its young age dunes are occurring at the surface of the landslide scar, indicating high sediment supply in the area.

## Månå delta

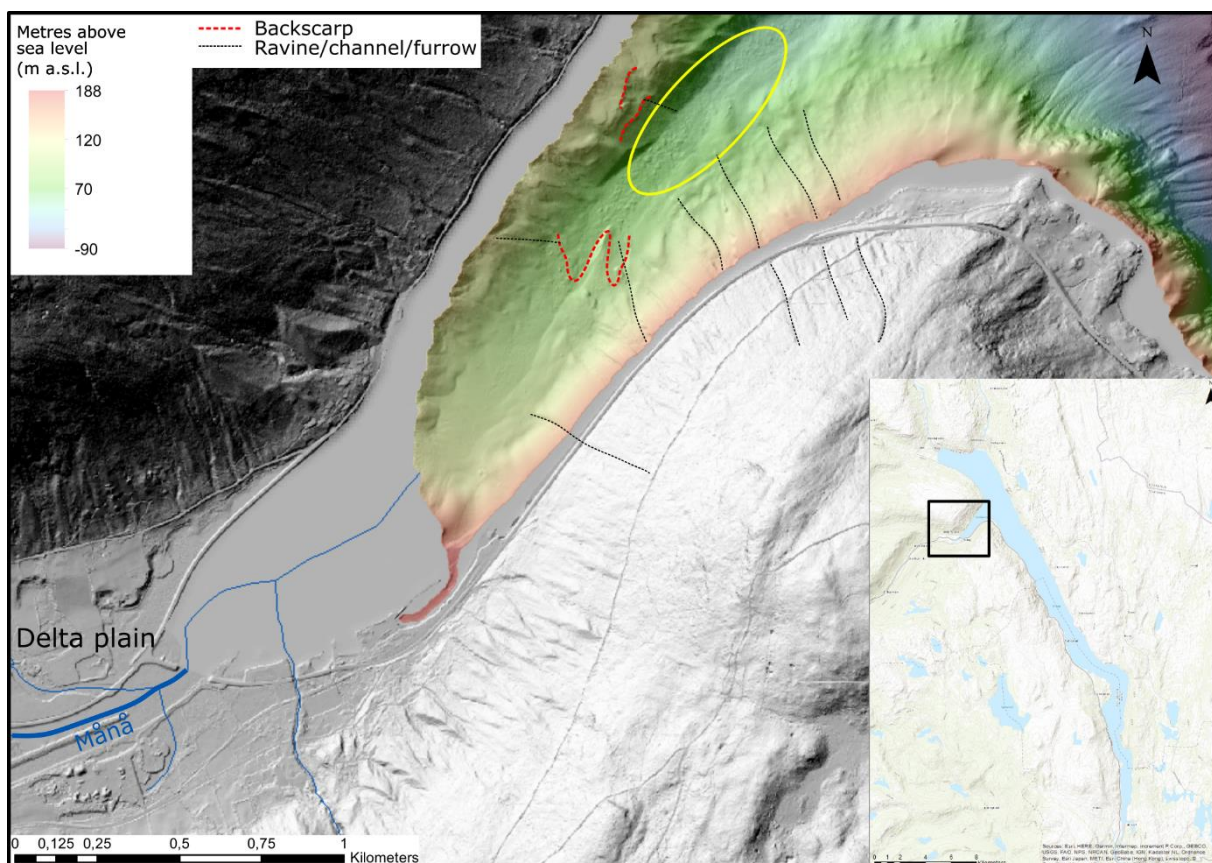


Figure 71: Bathymetry of Månå delta, localized at the western margin of Vestfjorden. The yellow circle represent blocks or hummocky surfaces.

Close to the western margin of Vestfjorden at the mouth of the river Månå a delta occurs with a subaerial plain with a width of 950 m close to shore and a length of 4 000m. Thus, a similar

shape of fjord-head deltas and interpreted as a river delta plain. The foreset of the delta slope is hard to map due to lack of bathymetrical data close to shore. Circular blocks occur at the bottomset roughly 2 000m east of the Månå river mouth marked by a yellow circle in Figure 71. The blocks might originate from a rockslide, but no large failure areas occur in the area and the shape of the blocks are not as angular as the boulders close to the Prestura rockslide (Figure 56). Another explanation is that the blocks originate from rockfall events, however no sign of boulders is visible upslope the marginal slopes. Another more plausible explanation is that the hummocky surface is remains of a large clay or silt slide similar to events described in Rissa (L'Heureux *et al.*, 2011a)

## Skirva delta

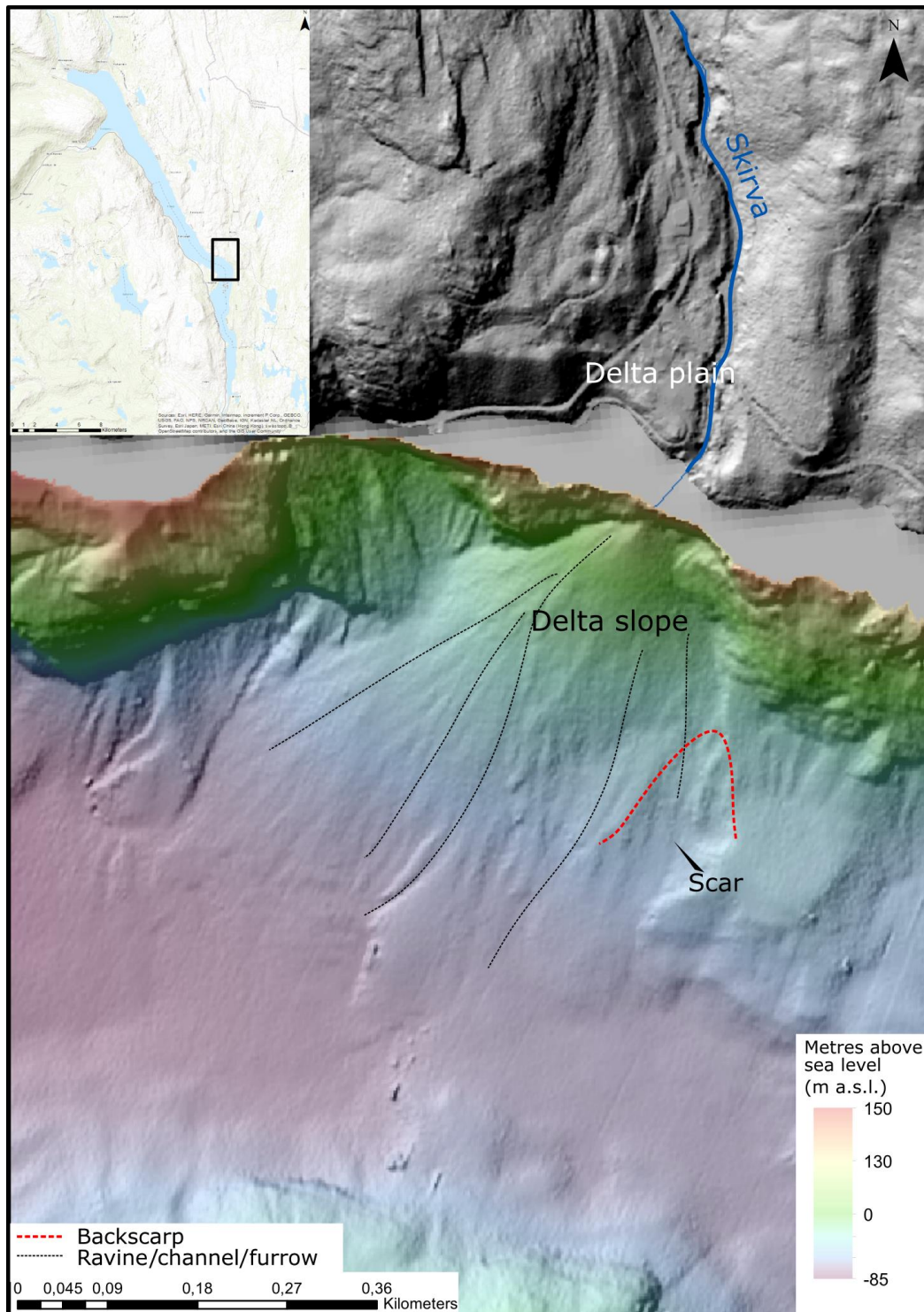


Figure 72: Bathymetry of Skirva delta, localized at the eastern margin of lake Tinnsjø.

Along the river Skirva there occurs a horizontal plain, with a length of 170m and a maximum width of 130m at the river mouth (Figure 72). This is interpreted as a delta plain. The delta slope has a mean dip of  $30^\circ$  towards the basin floor, interpreted as the forest of a Gilbert delta. The foreset has a length of 400m before the slope starts dipping less than  $10^\circ$



towards the basin floor indicating a bottomset. Along the surface of the foreset there occur several 1m deep elongated landforms, interpreted as channels, ravines or furrows. At the eastern slope of the foreset occur an arcuate depression, interpreted as a landslide scar.

It is also noted that a 10 – 15 m high vertical wall is dividing the delta plain and the delta slope. Thus, the delta slope can also be defined as a subaquatic alluvial fan. Similar landforms occur along the marginal slope of Tinnsjø, interpreted as subaquatic alluvial fans, marked as fan deposits in Figure 64, Figure 65, and Figure 66.

### Luåa delta

A subaerial plain occur close to the Luåa river in the south-west of lake Tinnsjø (Figure 73). This plain is interpreted as a delta plain, due to its delta shape. It is measured to have a width of 350m at the river mouth, and a length of 450m. Because of a lack of bathymetrical data close to the shore, the delta slope is not visible in the dataset.

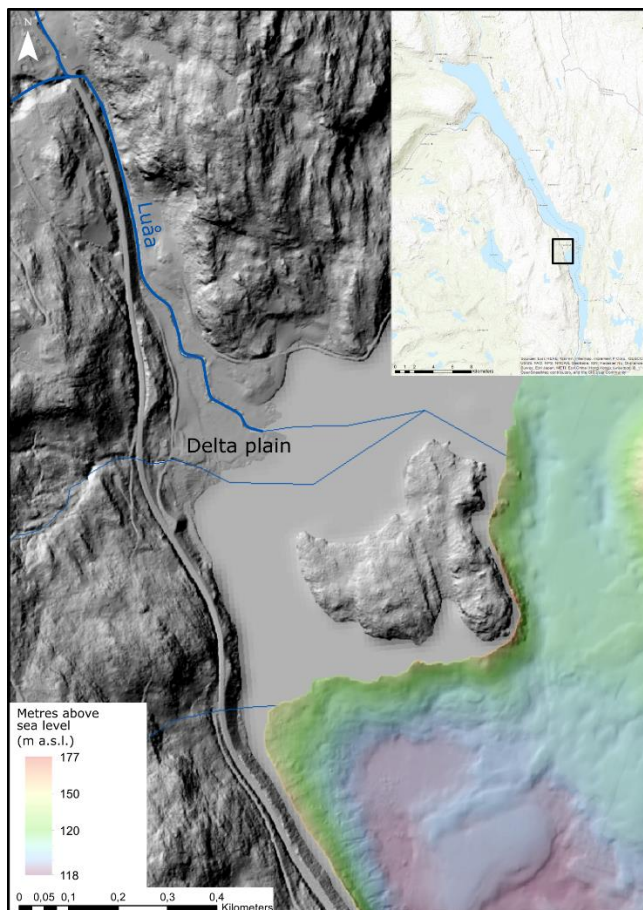


Figure 73: DEM showing of the Luåa delta plain. The delta slope is not visible, due to lack of bathymetrical data.



## Sandvika, Kyrsebekk, and Raua delta

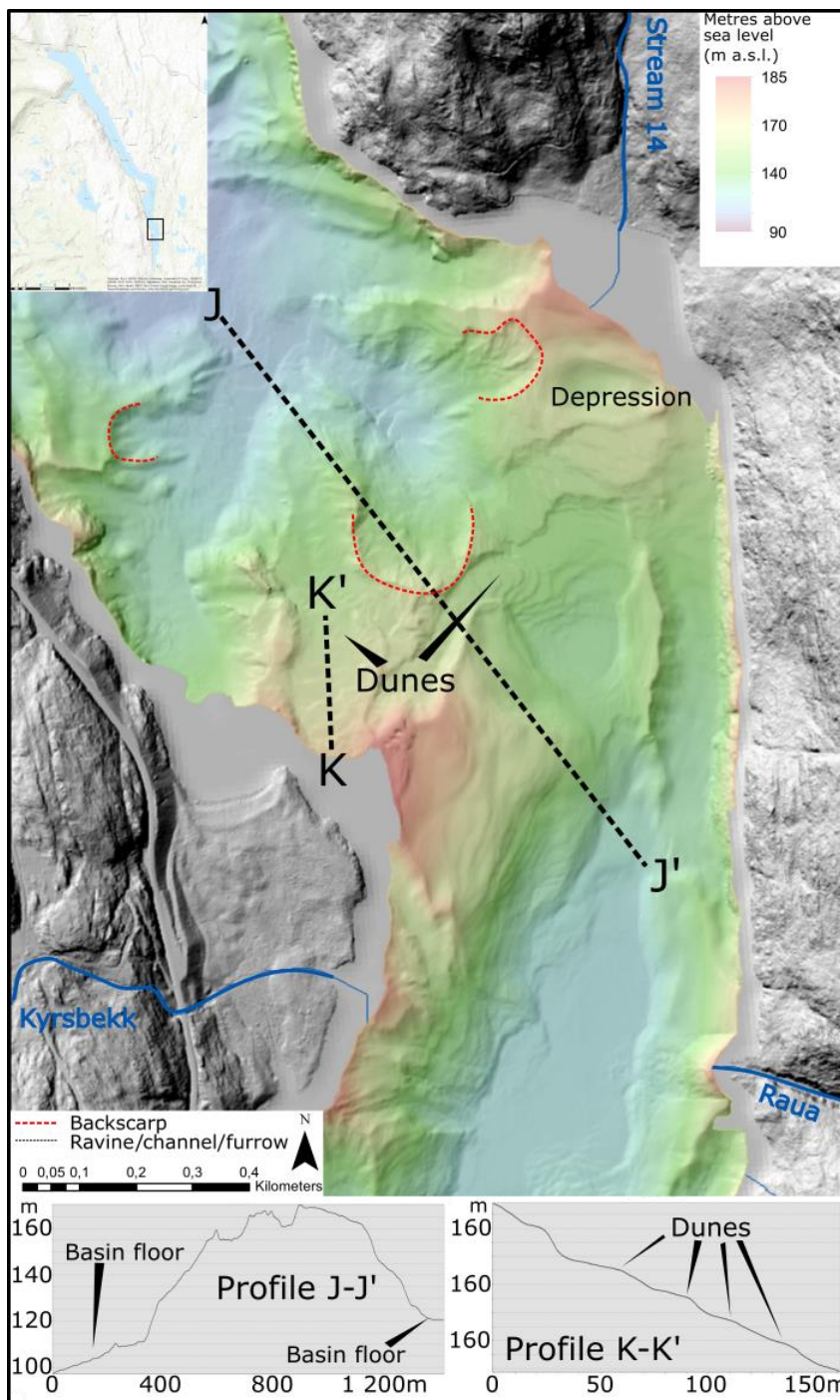


Figure 74: the three delta plains, Sandvika delta, Kyrsebekk delta and Raua delta. localized south in lake Tinnsjø.

The Sandvika delta plain is localized north in Figure 74, connected to stream 14, having a width of 200m at the river mouth and a length of 140m. The corresponding delta slope is hard to see due to lack of data close to the shore, and is disturbed by arcuate depressions similar to the landslide scars occurring further north.

The Kyrsbekk delta plain occur west in Figure 74, having an angular shape and no distinct delta slope is visible.

The Raua delta plain occur in the south-eastern area in Figure 74, with a width of 40m and a length of 60m, connected to a slope dipping  $30^\circ$  towards the basin floor, interpreted as a Gilbert delta. This delta slope has a length of 70m and a width of 100m. Thus, considered significantly smaller than the delta slopes located further north.

#### **5.6.4 Terraces**

Several relatively flat features with elongated surfaces dipping  $0-5^\circ$  towards the basin floor occur in lake Tinnsjø, separating the marginal slope into an upper and lower part. These flat features are interpreted as terraces and occurs at six different areas. These terraces are described from north to south in the following:

- A. Terrace A occurs at 270m depth (-90 m a.s.l.) in the north, east of Mælsåsen (Figure 75A). The terrace has length of 1300m, a width of 100 – 300m and a height of 10-30m above the basin floor. In addition, four landslide scars occur along the terrace rim.
- B. Terrace B occurs at a depth of 90m (90 m a.s.l.) south of Mælsåsen (Figure 75B), having a length of 300m and a width of 150m. The surface of this terrace is undulating, with visible depression at its centre. This terrace has a less elongated and more undulating surface than the others, and might represent a bedrock protuberance. Thus, not included in the following interpretation.
- C. Terrace C occurs at a depth of 300m (-120 m a.s.l.), south of Vestfjorden (Figure 75C). Having a length of 1300m and a width of 50 – 150m. Five landslide scars occur along the rim of the terrace.
- D. Terrace D occurs at a depth of 350m (-170 m a.s.l.), covering the area between the Håkåneset rockslide and the Prestura deposits (Figure 75D). The terrace occurs both at the west and east marginal slope of lake Tinnsjø, having a length over 7 000 m and a width varying from 250m north of Håkåneset to less than 20m close to the Håkåneset rockslide. 10 closely spaced landslide scars occur just below Håkåneset (described in section 5.5.). Below the Prestura failure area lay the Prestura deposits covering the entire terrace (further discussed in section 6.3).
- E. Terrace E occurs at a depth of 300m (-120 m a.s.l.) close to Hovin (Figure 75E). With a length of 1 000m and width of 100 – 150m located at both the eastern and western slope. This terrace occurs at the same depth as terrace C. Thus, it might have been

deposited at the same time. There also is a smaller terrace occurring at a depth of 350m (– 170 m a.s.l.) in the area, having a length of 1 000 m and width of 50 m. This terrace might be correlated to terrace D.

F. Terrace F occurs at a depth of 210m (– 30 m a.s.l.) south of Sandvika (Figure 75F), having a length of 1 300m and width of 40 – 70m, located both at the western and eastern marginal slope.

Figure 75 show that the terraces often occur in relation to depressions mapped on the basin floor, interpreted as dead ice sinks (see section 5.6.8). Because of the close relation to dead ice sinks and the almost horizontal terrace surface these terraces are interpreted as kame terraces.

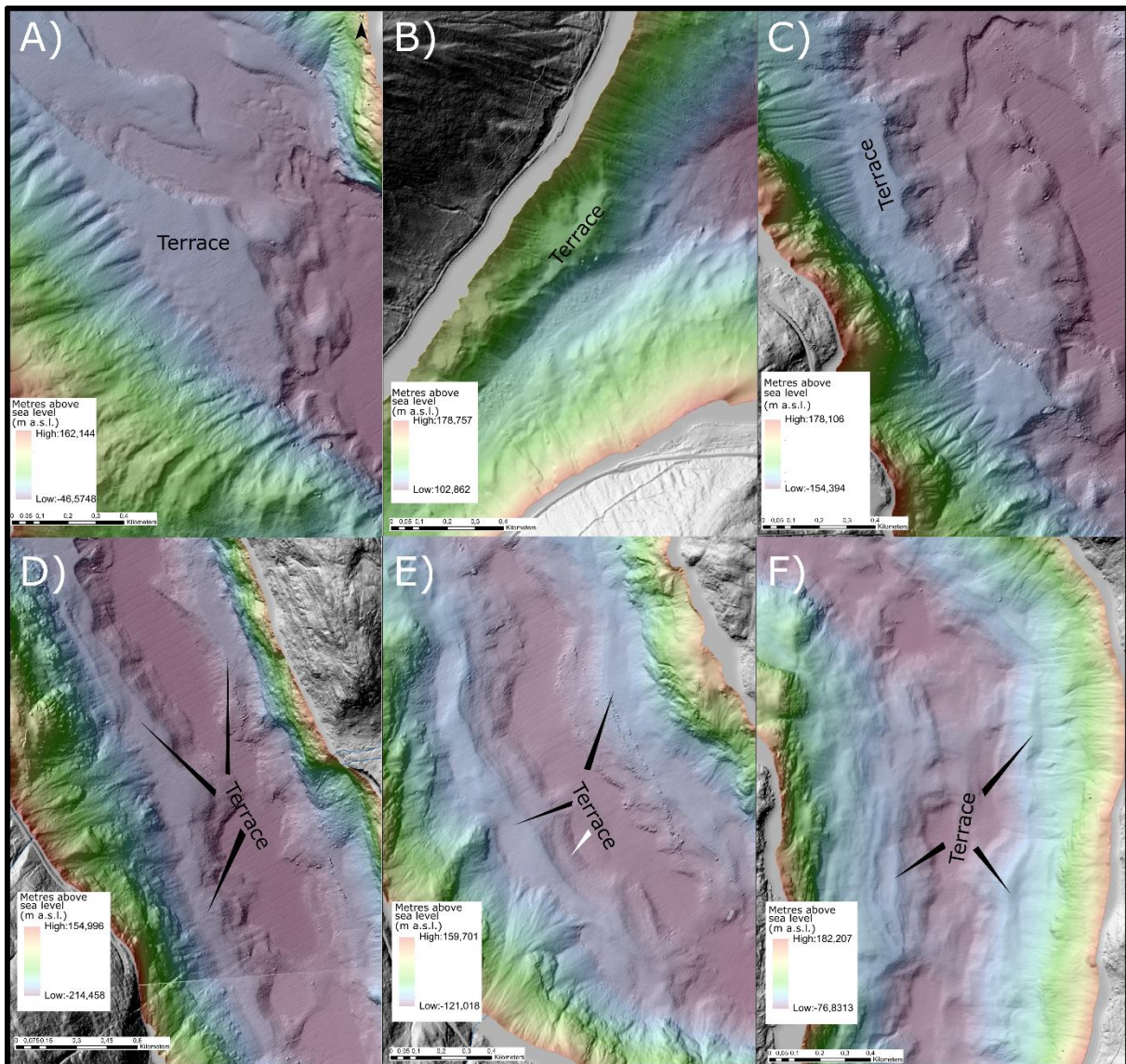


Figure 75: Illustration of mapped terraces in lake Tinnsjø. The white arrow in figure E) represent the terrace located at 350m depth.

### **5.6.5 Landslides**

This section covers a description of the different landslide types occurring in the lake. Following the descriptions is a presentation of the volume estimations performed on the mapped landslide scars, landslide deposits, and fans.

#### **Landslide types**

Three types of landslides occur in lake Tinnsjø. One type occurs in bedrock, is often subaerial, and has mappable displaced mass. This type is interpreted as rockslides. A description of rockslides has been made for the Prestura rockslide in section 5.4 and will not be further described. Another type of landslides occurs alongside the terrace rims, interpreted as soil/debris slides and is further described in section 5.5. The third type of arcuate depressions occur at the basin floor, some measured to have volumes over 5 million m<sup>3</sup> (Appendix G), interpreted as soil/clay slides. An example of this type occurs south of the Austbygdåi delta, having a volume of 6,2 million m<sup>3</sup> and is further described in the following.



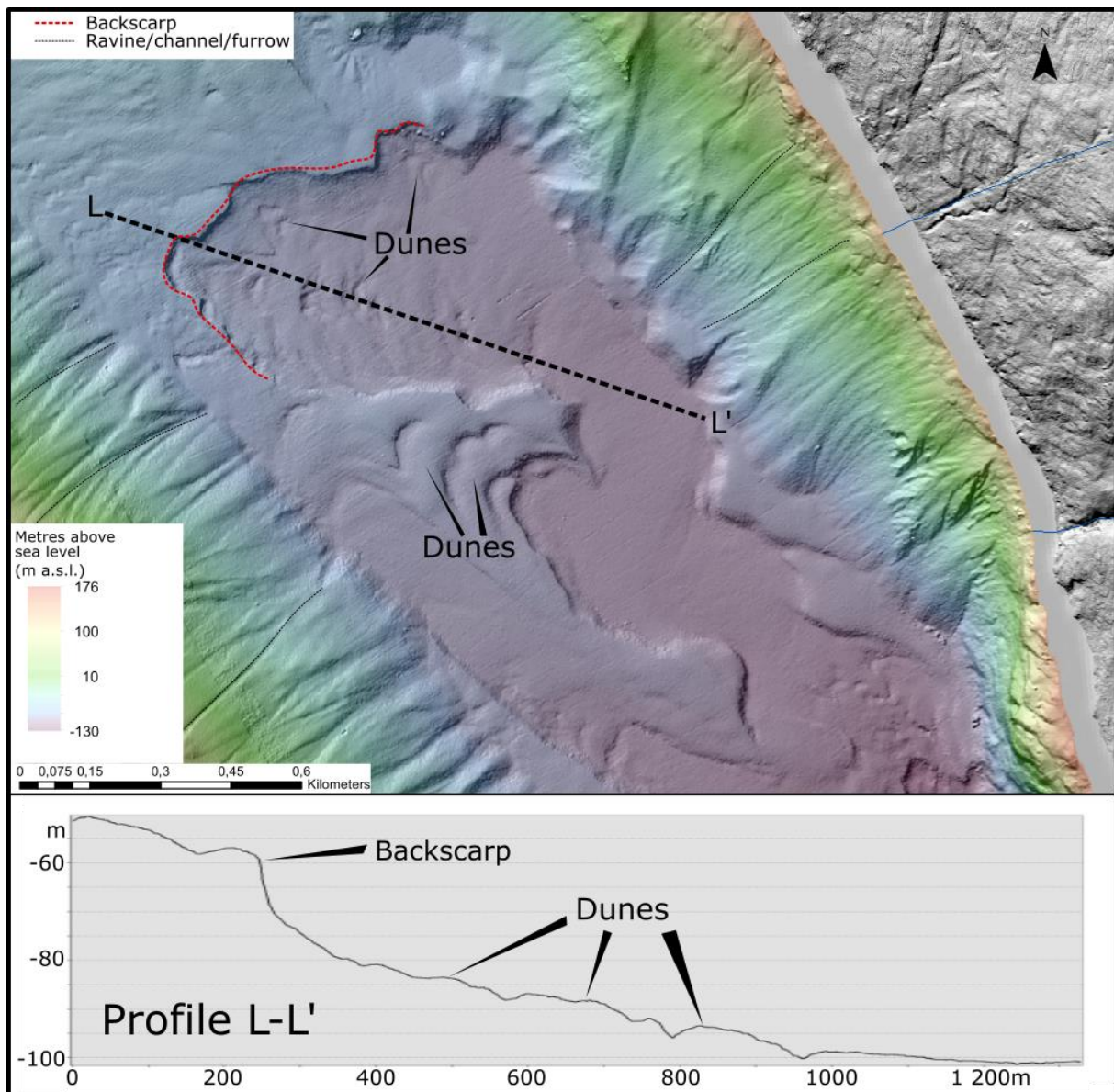


Figure 76: Bathymetry and profile of a large subaquatic landslide, with mapped backscarp and dunes.

A large pear shape depression occurs at the bottomset of the Austbygdåi delta (Figure 76). This landform is interpreted as a landslide failure area, with a NE-SW striking 10m vertical backscarp crossing the basin floor. The length of the failure area is 1 200m. The failure area is at its widest at the backscarp measured to be 700m and is narrowest at the toe of failure zone measured to be 160m. The shape of the failure area is similar to what is normal in quick clay avalanches (L'Heureux *et al.*, 2011a). However, lake Tinnsjø is localized over the marine limit (NGU, 2017), indicating that quick clay is not present. Instead, the sediment cover considered as lacustrine clay or silt. Thus, categorizing the landslide as a clay or silt slide. The backscarp is sharply defined, leading to an interpretation of the landslide as recently active, as according to Turner and Schuster (1996).

## Volume estimations and location of landslide related landforms

Over 200 different landslide scars, landslide deposits and fan deposits have been mapped in the lake. The volume of 107 of these landforms has been calculated using the SLBL and “minimum eroded volume” methods. The result is shown in appendix G and illustrated in Figure 77, Figure 78, and Figure 79.

The calculated volumes have been divided into three landform types (Figure 77, Figure 78, and Figure 79.): Landslide scars, landslide deposits, and fan deposits. The landforms are further divided into three classes based on their volume. These are:

- Over 1 million m<sup>3</sup>.
- Between 100 000 m<sup>3</sup> and 1 million m<sup>3</sup>.
- Between 10 000 m<sup>3</sup> and 100 000m<sup>3</sup>. Landforms with a volume less than 10 000m<sup>3</sup> often has a thickness (height) smaller than 5m, demanding use of high resolution DEMs in the volume estimations. The level of resolution was limited to 5x5m using the SLBL method, because of this, landform smaller than 10 000m<sup>3</sup> was considered inaccurate, and therefore excluded from the data.

The dominating landform in the lake is landslide scars, mainly occurring along the rim of the terraces or at the basin floor. With the highest concentration of scars occurring at the terrace close to the Håkåneset rockslide.

Landforms with visible blocks at its toe, and spatially localized close to a landslide scar (failure area) were interpreted as landslide deposits. Despite the high concentration of landslide scars, there were only four landslide deposits mapped. All of these occurring along the marginal slope, with a minimum of sediments deposited at the basin floor. The lack of visible landslide deposits can be explained either by extremely high sediment supply burying the landslide deposits or the presence of underwater currents moving all the sediments away from the zone of depletion post failure.

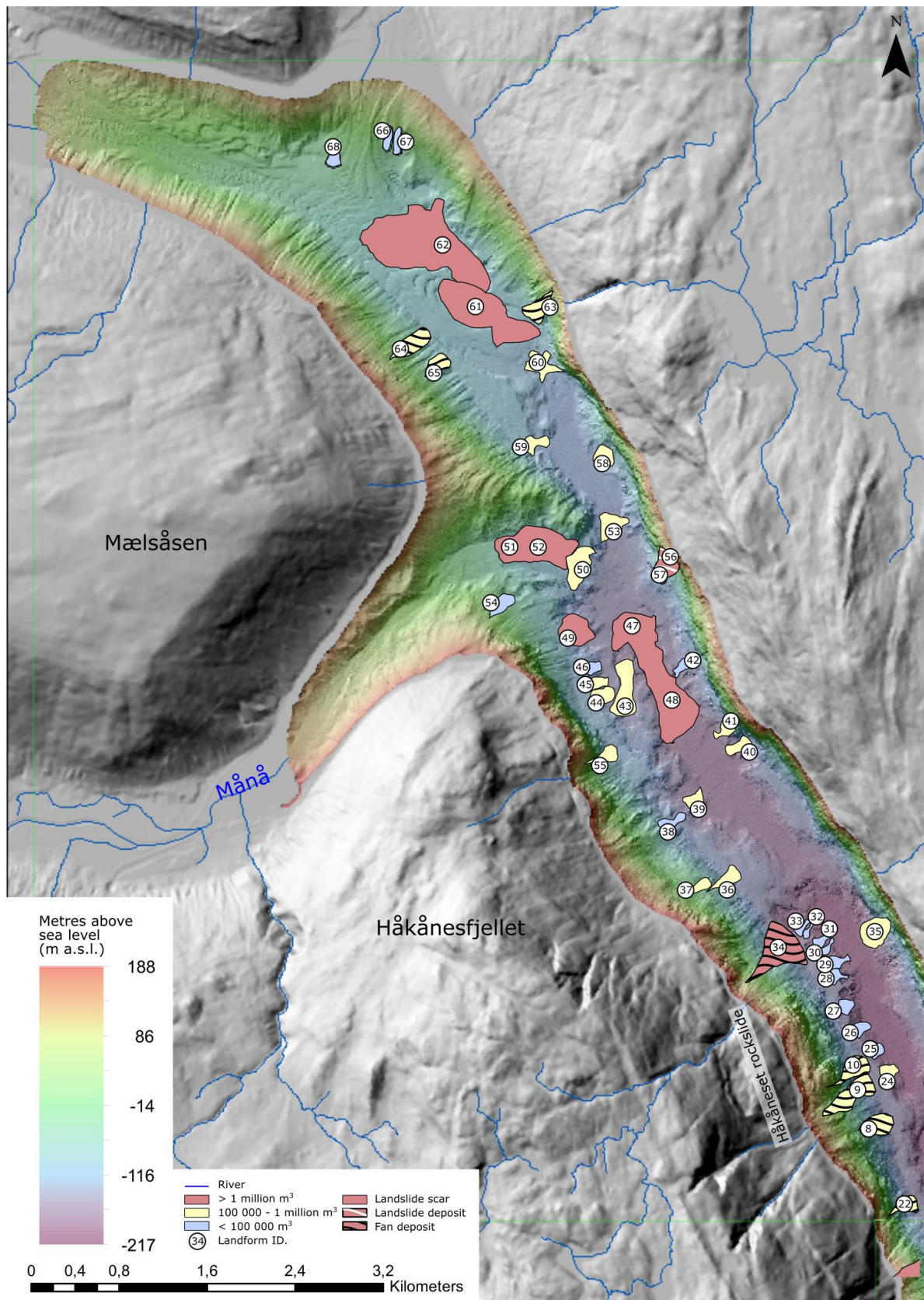


Figure 77: Map of the northern area of lake Tinnsjø. Visualising the calculated landform volumes and its location



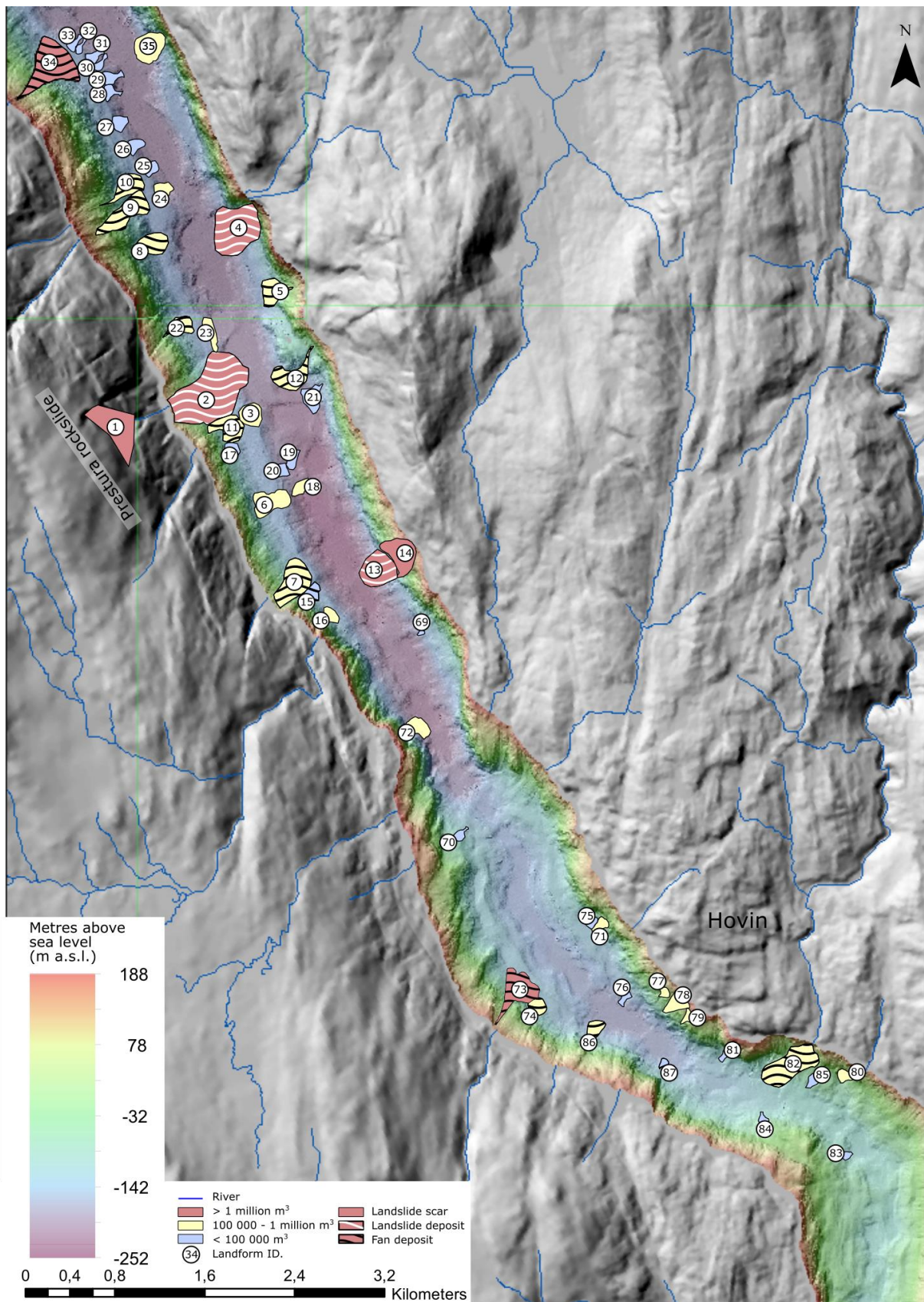


Figure 78: Map of the central area of lake Timmsjø. Visualising the calculated landform volumes and its location



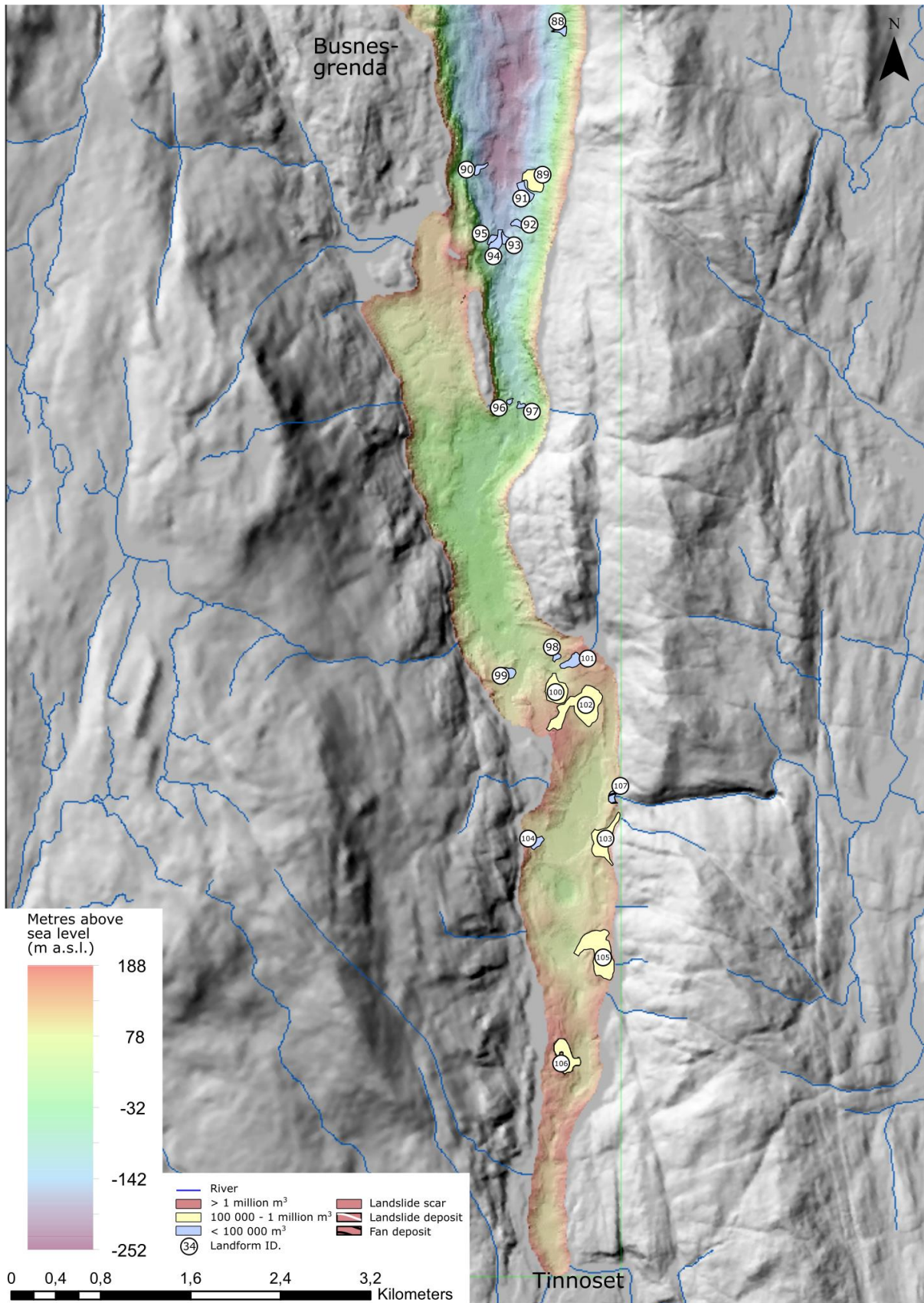


Figure 79: Map of the southern area of lake Timmsjø. Visualising the calculated landform volumes and its location

### 5.6.6 Ravines, channels and furrows

Elongated 1-3m deep and up to 100s meters long landforms occur along the entire marginal slope of lake Tinnsjø. The landforms are interpreted as ravines, channels, or furrows.

Channels occur along delta slopes or fan deposits, interpreted as originating from subaerial rivers and streams. Ravines and furrows occur along the marginal slope, possible to follow upslope reaching elevations over 1000m.a.s.l. Thus, interpreted as created by small landslide, rockfall or snow avalanche events. Ravines and furrows occur at highest concentrations along the western slope of lake Tinnsjø, which correlate well with the historical data presented in Figure 13.

### 5.6.7 Depressions and protuberances

The basin floor is undulating southwards of the Prestura deposits, due to the presence of depressions and protuberances. A typical depression is illustrated in Figure 80A, having a circular shape, divided by 1 – 10m high protuberance ridges. The depressions can be up to 50m deep having diameters varying from 1m to over 60m. These depressions are interpreted as dead ice sinks. Based on their similar features to the landforms mapped in lake Bandak (Eilertsen *et al.*, 2016) 50km southeast of lake Tinnsjø.

Two over 500m long elongated protuberances are mapped in the lake (marked light blue in Figure 64, Figure 65 and Figure 66). These landforms have a longitudinal axis oriented parallel to the lake. The surface of the landforms is angular, while the slopes are dipping over 60°. These landforms are interpreted as bedrock protuberances and illustrated in Figure 80.

A major protuberance occurs between the Kyrsebekk- and Sandvika delta (Profile J-J', in Figure 74). With a height of 50 – 60m covering an area of 525 000 m<sup>2</sup>, dividing the basin

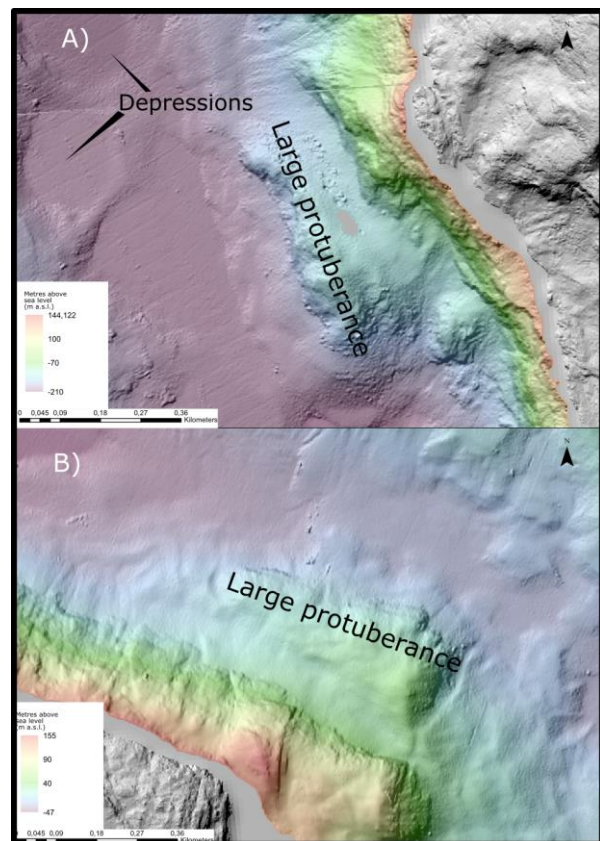


Figure 80: a) N-S oriented bedrock protuberance occurring close to Prestura deposit and circular depressions divided by ridges. b) NW-SE oriented bedrock protuberance south of Skirva delta.

floor in two. At first glance this was interpreted as a delta slope. However, none of the nearby rivers are considered capable of depositing this amount of sediments, having catchment areas less than 2 km<sup>2</sup>. Another reason for this not being a delta is the presence of a 150m diameter depression, occurring southwest of the Sandvika delta plain. Depressions such as these often occur in relation to dead ice terrain (Eilertsen *et al.*, 2016). Because of the above, the surrounding material is considered as silt and the protuberance is interpreted as a bedrock protuberance later covered by sediments such as moraines and sand.

## 6 DISCUSSION

---

Although the entire lake floor of lake Tinnsjø has been mapped within this thesis. It is considered beyond the scope of this master thesis to discuss all the identified landforms. Instead are only those landforms discussed further that are relevant to the Prestura and Håkåneset rockslides.

The discussion starts with the mapped subaquatic landforms surrounding and therefore considered important in the further analysis of the Prestura and Håkåneset rockslides. This is followed by a discussion of the Prestura rockslide leading into a comparison of the Prestura and Håkåneset rockslide. This discussion is focusing on understanding why the Prestura rockslide failed, while the Håkåneset rockslide still is a long-lasting rockslide. The discussion is closed by an evaluation of the potential landslide related hazard in the area and recommendations for further investigations.

### 6.1 SUBAQUATIC MAPPING OF LAKE TINNSJØ

#### 6.1.1 Lake Tinnsjø – a glacially created lake

During the last ice age was the catchment area of lake Tinnsjø covered in ice. The ice met at the intersection of the present rivers Mår, Månå, Austbygdåi and Gøyst, creating a thick ice body. The lake width is narrowing southwards towards the deepest point at a depth of 432m. The gradually narrowing width and deepening basin floor indicate that the ice was forced by the topography to shrink horizontally and expand vertically, being at its thickest south of the Prestura deposits eroding the basin floor and the surrounding slope. This resulted in a steep marginal slope and deep basin floor. Further south lake Tinnsjø is widening again, accompanied by a rapid rise of the basin floor.

At the basin floor depressions are observed, similar to the landforms examined at lake Bandak (Eilertsen *et al.*, 2016). These depressions are interpreted as dead ice sinks and kettle holes, divided by ridges, creating a dead ice terrain. This dead ice terrain may also explain why the basin slope is increasing its depth in a stepwise manner, by interpreting each step as a deglaciation step leaving behind dead ice. A further landform interpreted to be of glacial origin are the terraces observed at the marginal slopes (Figure 81). These terraces have an almost horizontal surface, with steeply dipping slopes (25 - 35°) towards the basin floor and occur on depths of 350m, 300m, 270m, 210m and 90m, often located close to dead ice sinks.



The topography close to the terraces are very similar to the landscape illustrated in Figure 21. Because of this similarity combined with closely occurring dead ice sinks, these terraces are interpreted as kame terraces, representing periods of standstill in the deglaciation of dead ice bodies. They are located deepest at the central parts of lake Tinnsjø, close to Prestura and located closer to the lake surface at Austbygdåi and Hovin. This shows, along with the occurrence of dead ice terrain that a dead ice body was covering the entire lake. The deepest kame terrace is interpreted as being the oldest terraces, explained in Figure 81. This shows that the dead ice cover lasted for the longest time in the central parts of lake Tinnsjø, where the ice cover also was at its thickest. This also explains the stepwise increase in depth towards the centre of the lake.

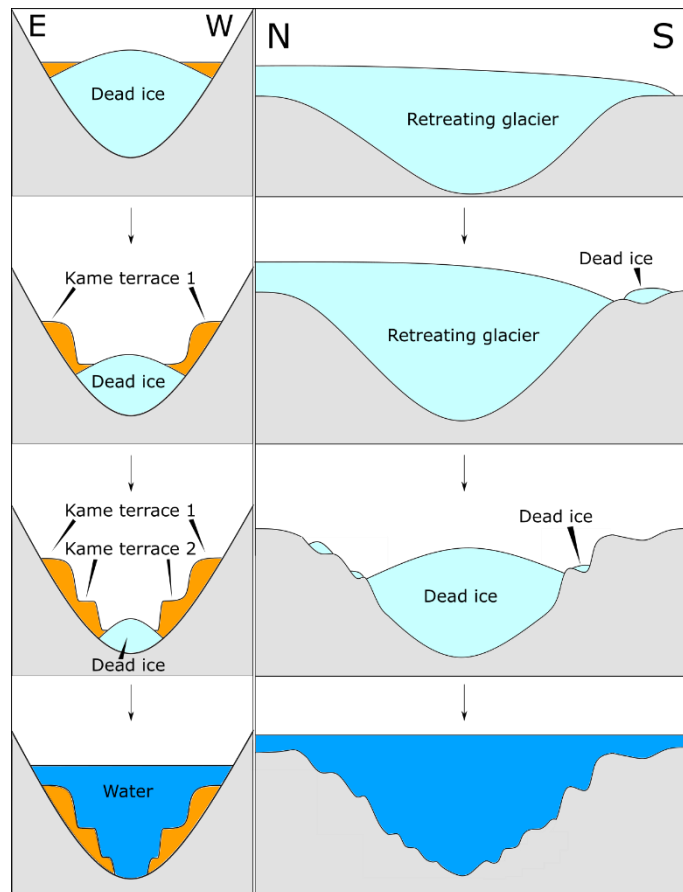


Figure 81: Chronologic evolution of the deglaciation of Tinnsjø (oldest on top). To the left. Transverse profile of the lake, showing the deposition of kame terraces at lake Tinnsjø, showing that the deepest terrace is deposited last. To the right. Longitudinal profile of Tinnsjø, showing a stepwise increase in depth created by dead ice sinks.

Together with these observations and previously mapped glacial deposits close to Mår, Gøyst, Austbygd, Hovin and Tinnoset (NGU, 2017). Is lake Tinnsjø interpreted as a glacial lake, with several dead ice bodies occurring during the deglaciation. According to Stroeven *et al.* (2016) lasted the deglaciation of lake Tinnsjø from 10 600 to 10 300 years ago (Figure 82). This shows that the deglaciation of Tinnsjø happened very fast, increasing the possibility of dead ice bodies at over 200m depth.

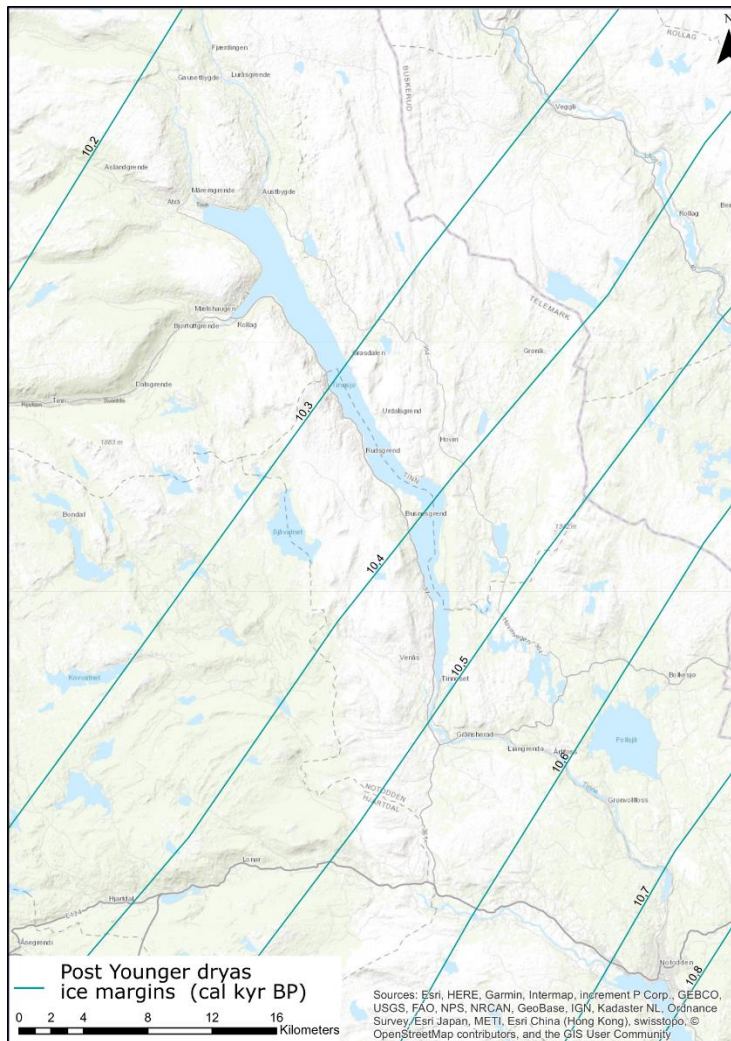


Figure 82: Post Younger Dryas ice margins close to Tinnssjø. Margins collected from (Stroeven *et al.*, 2016).

### 6.1.2 Subaquatic landslides

A total of 200 landslide scars are mapped at the lake floor of lake Tinnssjø. 196 of these landslide scars occur in soil, having a pear-shaped failure area similar to other subaquatic landslides occurring either in quick clay (L’Heureux *et al.*, 2011a, L’Heureux *et al.*, 2011b, Glimsdal *et al.*, 2016) or other fine-grained sediments (Schulten *et al.*, 2018, Casalbore *et al.*, 2018, Turmel *et al.*, 2018) indicating that the failure starts at the narrow toe of rupture surface retrogressing backwards (L’Heureux *et al.*, 2011a).

The potential release surface of the subaquatic landslides have a arcuate shape (Profile L-L in Figure 76) similar to other subaquatic landslides (L’Heureux *et al.*, 2011b) interpreted as a weak clayey sediment layer. However, no seismic mapping or core drilling were performed in this thesis to support such an assumption of materials. This interpretation is therefore not considered as very accurate. More in-depth studies of subaquatic landslides should cover seismic analysis and core drilling.

Most of the landslide scars occur either along the kame terraces or at the foreset of deltas. These landslide scars are often considered small with volumes ranging from 10 000m<sup>3</sup> to 100 000m<sup>3</sup>. The slope at the kame terraces and deltas are varying between 25- 35°, which is roughly the same as the internal angle of friction of most soils (*Soil friction angle*, 2013). Therefore, the variation in slope are considered a possible triggering factor of the smaller landslides. This variation in slope might be created either by undercutting due to turbidity currents or redistribution of the sediment cover by streams. The landslide scars occurring at delta slopes and alluvial fans are according to Prior and Bornhold (1990) common features along delta slopes and triggered by erosion and sediment supply from rivers and streams.

Larger landslide scars (volume over 1 million m<sup>3</sup>) are not as frequent as the smaller landslide scars and occur at the basin floor of lake Tinnsjø only. The occurrence of these landslides can be explained by that the sediments can accumulate for a longer time period at gentler slopes of the basin floor (0 – 10°) , making it possible to generate large-scale landslides (Casalbore *et al.*, 2018). The gentle slope at the basin floor indicate that slope alone is not the only conditioning factor, instead do other conditioning factors such as earthquakes (Schulten *et al.*, 2018), or a high sedimentation rate (Casalbore *et al.*, 2018) lead to the final failure along weak horizons (L'Heureux *et al.*, 2011b).

No evidence of recent high earthquake activity is observed in the area. However, evidence of large sediment supply is visible close to the Gøyst and Austbygdåi delta. This is expressed by 2 – 3 m high symmetrical dunes along the delta slopes (Figure 69, Figure 74) here interpreted as cyclic steps. Therefore, are high sediment rates considered the main triggering factor of the largest landslides (volume over 1 million m<sup>3</sup>). This is further supported by that the large subaquatic landslide scars only occur in the northern area of lake Tinnsjø, close to the large rivers Månå, Mår, Gøyst and Austbygdåi.

### **Where are the landslide deposits?**

Despite of having over 100 landslide scars close to the basin floor, few landslide deposits are mapped at the basin floor. The only mappable landslide deposits at the basin floor originate from large rockslides such as Prestura (Landslide ID: 2, 4 and 13 in Figure 65). The lack of landslide deposits can be explained by the sediment supply being so high that all landslide deposits are covered by sediments. This is supported by the large catchment area of lake Tinnsjø and the presence of 1 – 2m high cyclic steps deposited on the failure surface of young landslides (Figure 76), being evidence of high sedimentation rates. However, if the sediment

supply was big enough to cover landslide deposits with volumes over 1 million m<sup>3</sup>, would it also be big enough to fill the dead ice sinks in the area, creating a much smoother basin floor than observed.

Another explanation is that underwater turbidity currents occur along the basin floor transporting sediments away from the failure area. Cyclic steps are often created by turbidity currents (Cartigny *et al.*, 2011, Clare *et al.*, 2016) which occur in relation to high river discharge or landslide activity (Schulten *et al.*, 2018, Clare *et al.*, 2016). Due to lack of hydrological data in the area is the relation to river discharge not tested, but since trains of cyclic steps follow the orientation of the major rivers Mår and Gøyst (Figure 69) is it assumed that river discharge is high enough to create turbidity currents. However, cyclic steps do also occur in relation to landslides (Figure 74), not occurring close to major rivers. The occurrence of cyclic steps along both the northern and southern areas of the basin floor show that turbidity currents occur along the entire lake floor, capable of spreading huge amount of sediments at the basing floor away from the failure areas.

## **6.2 NEW FINDINGS SHOW SUBAQUEOUS MOVEMENT OF THE HÅKÅNESET ROCKSLIDE**

### **6.2.1 High landslide scar concentration close to the Håkåneset rockslide**

A significant increase in landslide scar concentration occurs on the kame terraces just below Håkåneset. Landslides may according to the limit equilibrium analysis (Nilsen, 2017) occur at slopes dipping steeper than the internal friction angle of the rock mass (soil). The slope dip at the kame terrace rims are varying from 25° to 35° (see appendix C). While the soil cover is assumed to be silty sand or clay (mud), having an internal friction angle of 27 – 34° (clay – silty sand) according to the Unified soil classification system (*Soil friction angle*, 2013). This internal friction angle is not significantly lower than the slope, showing that slope dip alone may not be the only triggering mechanism of the landslides.

A possible explanation might be the presence of underwater turbidity currents at the basin floor undercutting the kame terrace slope. However, no major river catchments occur close to Håkåneset, thus no reasons to believe that this current is any stronger at the kame terrace just below Håkåneset than along other terraces.

Instead can instabilities also be explained by the presence of external loading (named  $F_{\alpha}$  in the limit equilibrium principle (Nilsen, 2017)). This external loading is often created by



earthquakes (Nilsen, 2017). There is no reason that seismic activity in this part of Tinnsjø is higher than elsewhere. A further stress of the sediments below the Håkåneset rock slope is the rockslide itself. The high concentration of landslide scars is therefore interpreted as an evidence of subaqueous rockslide movement at the Håkåneset rockslide

The relative ages of the landslide scars might also show where and when the movement occurred. Various degree of preservation of the scars can be preserved. In Figure 63 we classify them in four groups of scar erosion. Group 1 represents the most pristine scars while those of group 4 are more subtle. These groups are interpreted as representing periods of major movement of the Håkåneset rockslide. However, no significant north south trend is visible, instead the degree of preservation seems rather random, thus suggesting a complex front of the rockslide toe. The new bathymetrical data including the floor of lake Tinnsjø reveal that the Håkåneset rockslide reaches down to the kame terrace. This causes the rockslide indenting into the sediments and pushing them ahead, which can be described as a bulldozer effect. This leads to a local increase of stress, but also to the deformation of the sediments.

### **6.2.2 Longitudinal ridges along terraces indicate movement**

The surface of the terrace located close to the Håkåneset rockslide is disturbed by two longitudinal 6 – 15m high, 33 – 53m wide and 800 – 1000m long ridges, illustrated in Figure 83. No similar ridges occur anywhere else in lake Tinnsjø, thus assumed to be related to the movement of the Håkåneset rockslide. The ridges are thus interpreted to be created by the indentation of the Håkåneset rockslide bulldozing the sediments in front of it creating two parallel bulges in the terrain (Figure 84). This mechanism is interpreted as evidence of movement at a depth of 340m. The presence of two ridges instead of one, can be explained by at least two periods of movement along one single release surface, or because of the complex morphology of the toe of rupture, having several rupture surfaces and internal deformation. The latter is illustrated in Figure 84.

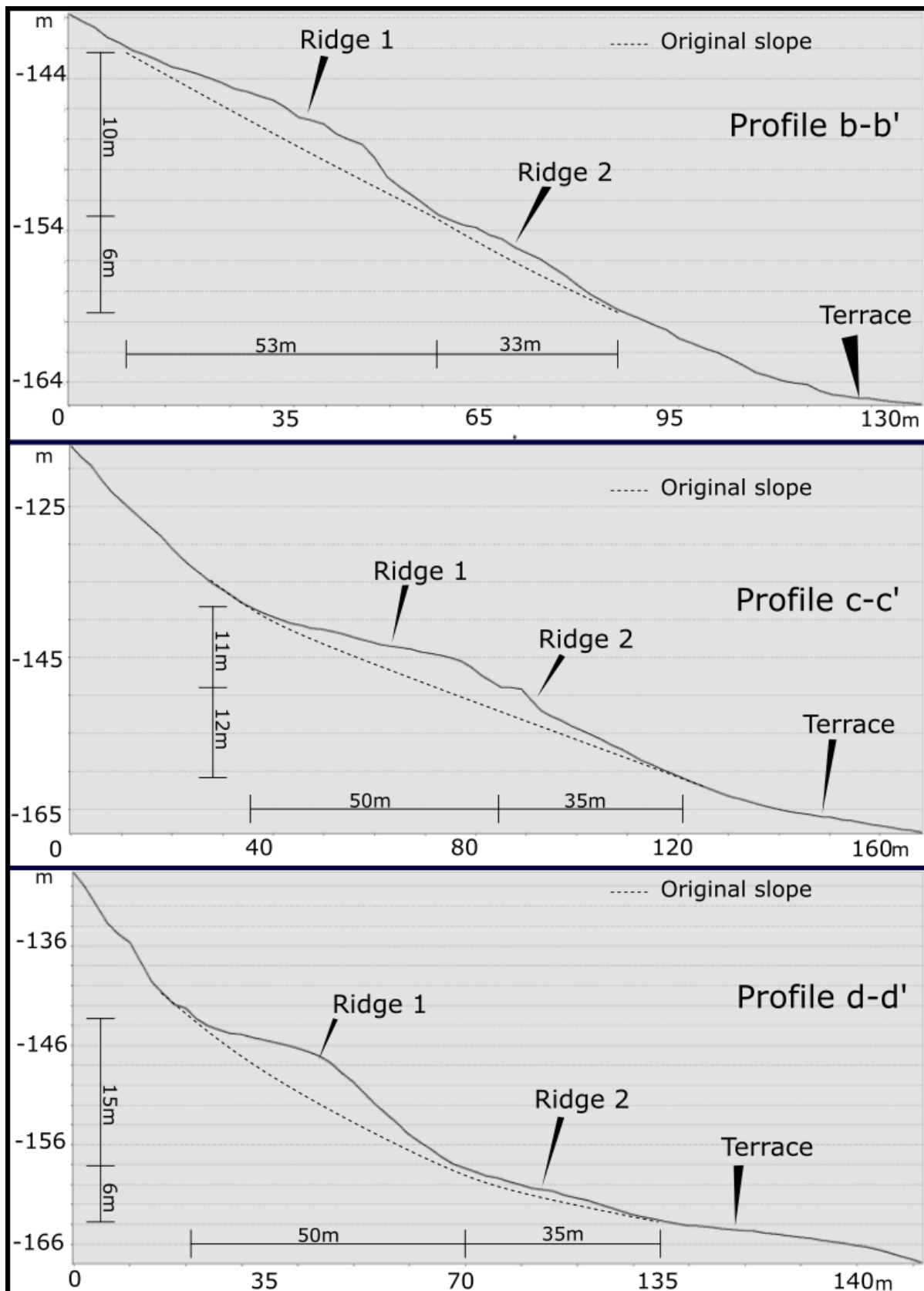


Figure 83: Profile a-a', b-b', and c-c' from Figure 61. Illustrating the dimensions of the ridges occurring at the kame terrace located just below Håkåneset.

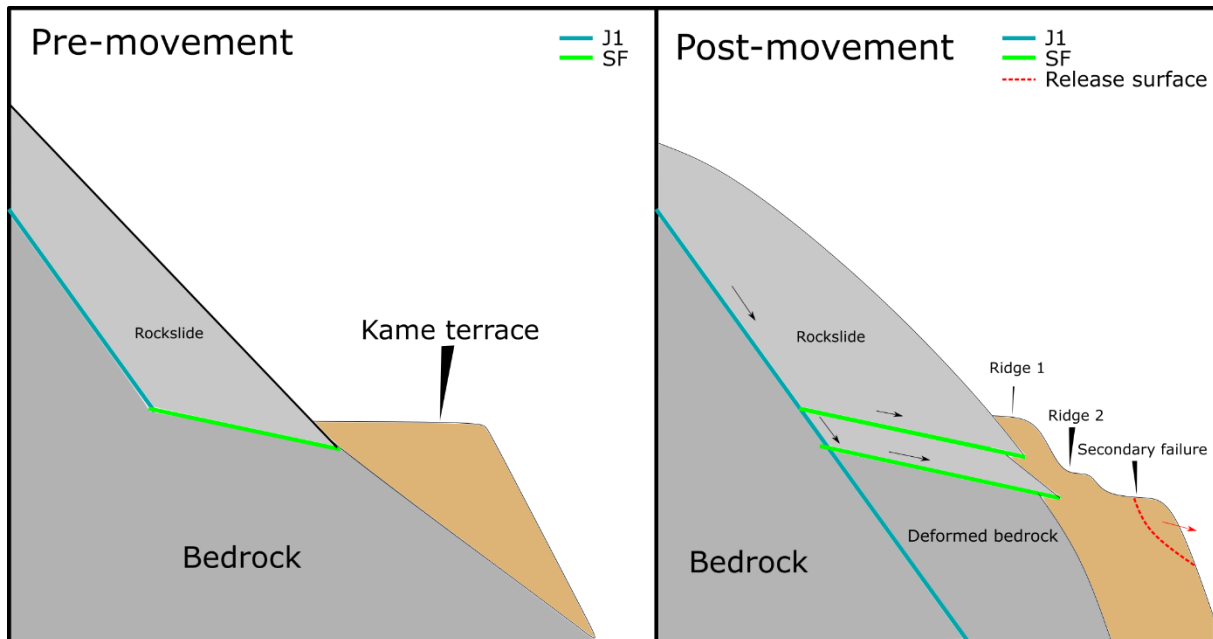


Figure 84: Left: pre-movement topography of the kame terrace localized just below the Håkåneset rockslide. Right: Interpreted creation of two longitudinal ridges and landslides at the kame terrace, due to movement and deformation of the Håkåneset rockslide at the complex toe.

In the following we use simple trigonometry to test if the displacement of the toe of the Håkåneset rockslide equals the offset at the backscarp, by assuming that the combined width of the ridges equals the horizontal offset at the toe. This is a simplification as the toe most likely has a complex form (see above) however it is a valid first order approximation.

Equation (3) is based on the assumption that 100% of the recorded movement at the backscarp is transformed to the toe, will the measured horizontal movement be equal to the calculated movement. The principles in the use of equation 3 is illustrated in Figure 85.

$$\text{Horizontal displacement at toe} = \frac{\text{Vertical offset at backscarp}}{\tan(\text{average dip of surface of rupture})} \quad (3)$$

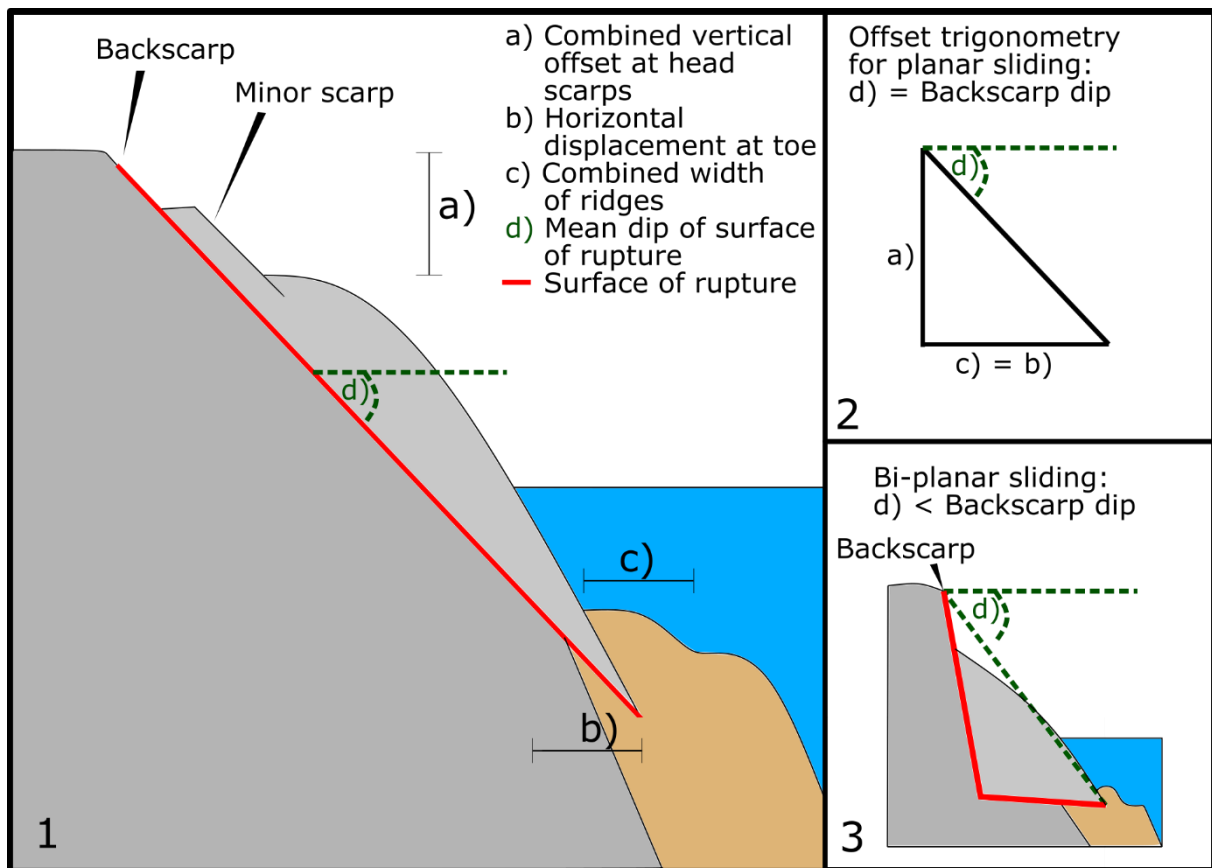


Figure 85: 1) Schematic sketches of offset calculation. 1) Illustration of Håkåneset, with planar sliding set as slide mechanism. 2) Trigonometric sketch illustrating input parameters in equation 3 (the combined width of ridges is assumed equal to the actual horizontal offset at the toe). 3) sketch of Håkåneset, with bi-planar sliding set as failure mode, showing that the surface of rupture has a lower mean dip than the backscarp.

At the head of the Håkåneset rockslide occurs two parallel scarps, dipping  $65^\circ$  along the slope. The height of these scarps is  $\sim 40\text{m}$  and  $60\text{m}$ , having a combined vertical offset of  $100\text{m}$ . Under the assumption of planar sliding as a feasible slide mechanism (Figure 85) would the calculated horizontal displacement at the toe be  $46\text{m}$ . The measured combined width of the ridges is  $85\text{m}$  (Figure 83) showing that over  $100\%$  of the vertical movement measured at the backscarp is transferred to the toe. This suggest that the internal deformation has an expanding behaviour. However, according to Sollie (2014) is bi-planar sliding the most feasible slide mechanism(Figure 85 3)). The average dip of the bi-planar sliding mechanism was considered impossible to map due to the complexity of the rockslope. Thus, assumed to be  $30^\circ$ , giving a calculated horizontal displacement at the toe of  $173\text{m}$ , showing that  $51\%$  of the measured vertical offset at the backscarp is lost in internal deformation of the slope.

This method is a considered as a simplification of a complex process, thus only a first order approximation. However, graben structures mapped by Sollie (2013) within the slope attest for internal deformation, supporting this first order assessment.



## **6.3 ANALYSIS OF THE PRESTURA ROCKSLIDE**

### **6.3.1 One single structural domain**

Five different discontinuities are observed in the area. Four steep and consistent joint sets (J1, J2, J3 and J4) and one almost horizontal and very variable foliation (SF). The SF foliation got high variation due to few measurements (64 poles) and high difficulty in measuring of the orientation with compass, due to its almost horizontal dip and undulating surface. The variation of SF did not have a trend for the area, but rather big difference even between locations only 50 – 100 meters apart. Because of this the entire area is considered one domain for the kinematic analysis.

### **6.3.2 Bi-planar failure mode most feasible**

The kinematic analysis concluded that planar sliding, wedge sliding, and direct toppling is possible release mechanisms at steep slopes. Especially wedge sliding was observed at several locations both at steep slopes around the release surface and at steep road cuts (Figure 38 and Figure 41). By looking at the Prestura release surface on orthophotos and DEMs, it is easy to quickly draw the conclusion that the release mechanism of the Prestura rockslide is wedge sliding, due to the intersection of J2 and J3 release planes (Figure 53). However, by closer examination, no release surface at the intersection of J2 and J3 are observed. Instead it seems that the east dipping J1 joint set represent the sliding plane of the rockslide. J1 does only daylight at slopes dipping steeper than  $60^\circ$ , while the average dip of the slope is  $\sim 46^\circ$ . Therefore, planar sliding along J1 is only possible along very steep slope sections ( $\sim 60^\circ$  dip). Thus, neither planar sliding nor wedge sliding is considered realistic failure mechanisms for the rockslide. Direct toppling is also mainly possible at steep slopes and has only rarely observed releasing rockslides at the size of Prestura (Nichol, S. L. *et al.*, 2002). A more likely scenario is a combination of different joint sets creating a complex failure mechanism. J1 cut the intersection between J2 and J3, making J2 and J3 lateral release surfaces of the rockslide. The steep east dipping J1 does not daylight in the slope, but can with the help of the nearly horizontal SF create bi-planar failure. Such a failure mechanism has been described elsewhere for big rockslides (Glastonbury and Fell, 2010). Thus, the most likely release mechanism is bi-planar failure along J1 and SF with lateral release surfaces created by J2 and J3.

This correspond well to conclusions by Sollie (2014) and is considered similar to other rockslides of similar size, such as the Randa rock slope failure (Sartori *et al.*, 2003). This

similarity is presented in Figure 86 and considered a key observation in the landslide classification in section 6.3.3.

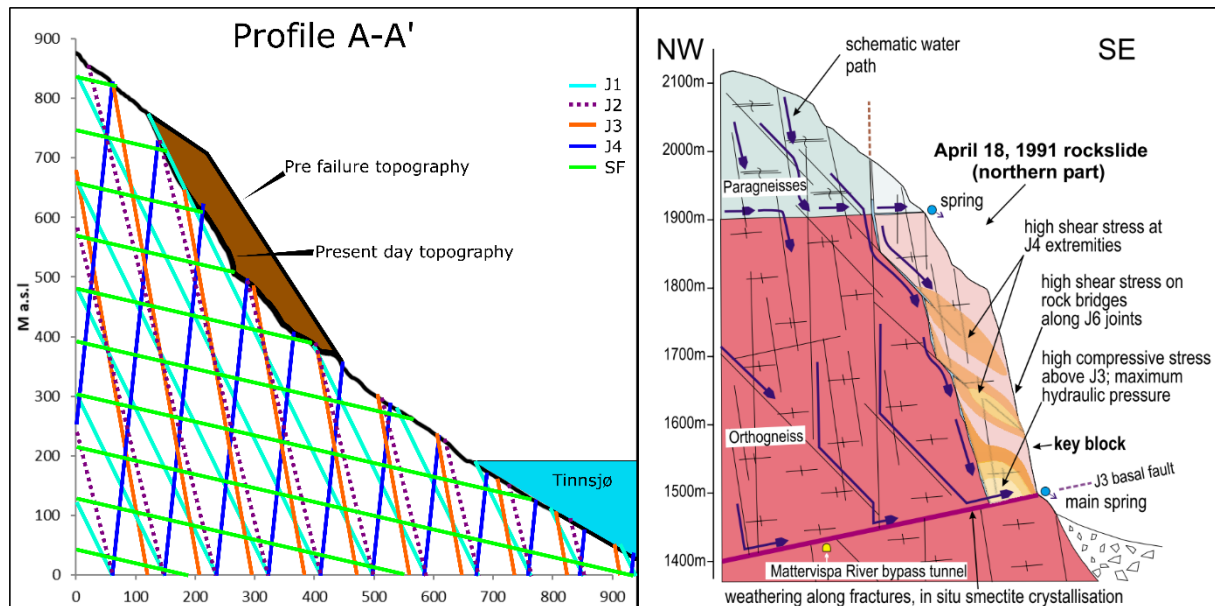


Figure 86: Simplified cross section of the Prestura rock slope (left) and Randa rock slope (right)(Sartori *et al.*, 2003). Both slopes having similar discontinuity orientations. Thus, similar potential failure mode.

### 6.3.3 Landslide classification

Prestura is a rock slope failure that lead to the complete disintegration of the rock mass and relief contrasts are high. The lithology is a competent rhyolitic bedrock (UCS of 98MPa (Sollie, 2014)). Slow rock slope deformation would not result in such a lobate sloped deposit. Therefore, it is possible to conclude that the failure was a catastrophic event. However, despite its large volume (3 – 9 million m<sup>3</sup>), the low run-out is restricted to 1 300m. If the Prestura was considered a rock avalanche, would the run-out be according to the H/L vs volume correlation (Scheidegger, 1973) approximately 2 500m, or even longer since the displaced masses enter a body of water and rock avalanches into liquefiable sediments, rather have a longer run-out as their counterpart on land (Schleier *et al.*, 2017). A rock avalanche would result in the deposition of a landform similar to the deposit below Kassen (Krogh, 2017), covering the entire width of the lake.

The Randa rock slope failure was created by two catastrophic rock slope events occurring in April and May 1991. The volumes of these rockslides were 22 million m<sup>3</sup> (Randa 1) and 7 million m<sup>3</sup> (Randa 2)(Sartori *et al.*, 2003) respectively. The H/L vs volume correlation of both Prestura and the Randa rockslide are plotted in Figure 87 showing almost identical mobility. Other similarities are the presence of strong rock masses in both slopes (rhyolitic bedrock in Prestura and orthogneiss at Randa), and both slopes having bi-planar failure as the most

feasible failure mode (Figure 86). Furthermore, has the deposit rather a debris fan like depositional morphology in the contrary to elongated lobate shaped rock avalanches (e.g. (Schleier *et al.*, 2015, Hermanns and Strecker, 1999). The largest clasts lie in front of this debris fan and the fines closest to the apex. Such depositional features also occur at Randa (Switzerland), as illustrated in Figure 88.

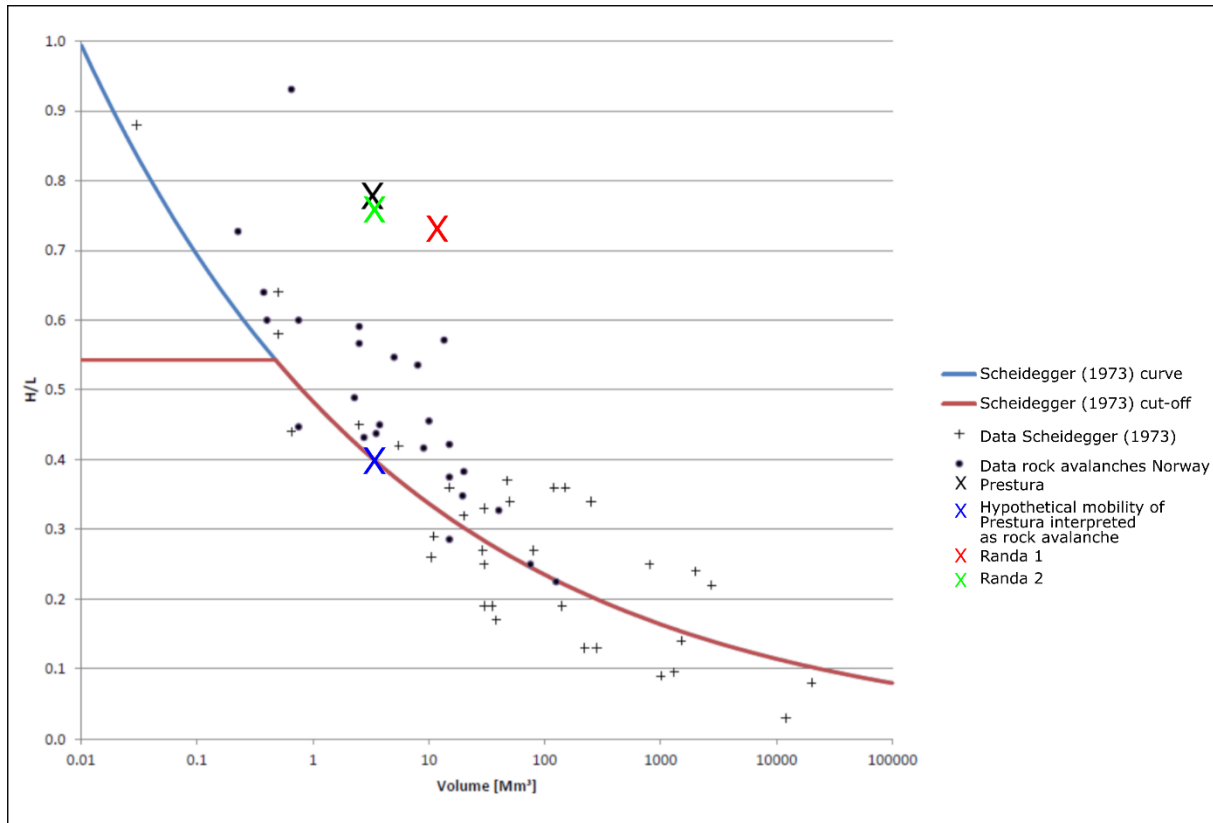


Figure 87: Prestura and Randa rockslides plotted in H/L vs Volume correlation diagram. The data for the Randa event are achieved from (Sartori *et al.*, 2003). Modified from (Hermanns *et al.*, 2012),

According to Sartori *et al.* (2003) were both Randa failures very rapid events, however in contrast to rock avalanches where failure takes place over only a few minutes did both Randa failures occur over a lapse of 3 hours. Because of the strong similarity of depositional features, geometry of the source area and mobility do we conclude that the Prestura was a similar failure event as the Randa rockslope failure and thus a very rapid failure of smaller units not large enough to result in the mobility of a rock avalanche and lasting over several hours. Alternatively, the deposit could be a deposit of several failures separate in time, however depositional features do not allow this interpretation of several events in time.

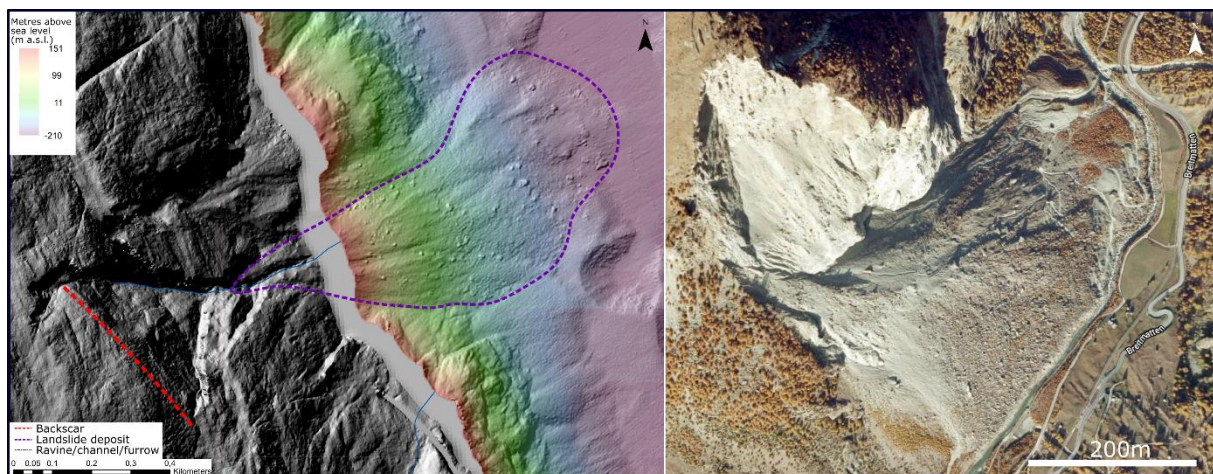


Figure 88: Prestura deposits to the left, having similar morphology as the steep cone of debris deposited by the Randa events (left)(Sartori *et al.*, 2003) The picture of Randa is collected from GoogleMaps.com.

### 6.3.4 One or multiple events?

The Prestura deposits occur on top of a mapped kame terrace occurring at 350m depth (-120 m a.s.l.) Thus, considered younger than the kame terraces in the lake. These terraces were deposited in relation to a dead-ice body. Thus, deposited during the deglaciation of Norway post younger dryas (Stroeven *et al.*, 2016). Since the deposits occur on top of the kame terraces is the Prestura deposit considered younger than the terraces, interpreted as post glacial deposits.

The mean volume of the Prestura deposits is 2,36 million m<sup>3</sup> (Table 12) considered significantly smaller than the mean volume of the failure area (6,33 million m<sup>3</sup>). This is similar to observation in Innfjorddalen (Schleier *et al.*, 2017) and on Ivasnasen (Oppikofer *et al.*, 2017). At both localities the authors concluded that the difference in volume is due to several failure events and that those related to the missing volume, occurred prior to glaciation or deposited on top of a glacier, where the deposits were either eroded or moved downstream by the glacier ice. The sharp lateral flanks of the Prestura slide allow to interpret that the earlier failure was not pre-glacial.

Schleier *et al.* (2017) also discussed the possibility that the rock failure masses at Innfjorddalen fell onto soft soil, subsiding into the soil cover leading to an underestimation of the displaced volume. This alternative explanation for the difference in volume does also count for the Prestura locality.



## 6.4 PRESTURA AND HÅKÅNESET

### 6.4.1 One large unstable complex

The structural data collected from both Prestura and Håkåneset are compared in Table 16. From Table 16 it can be seen that both areas have five distinct discontinuities, showing almost identical orientations. Because of this structural similarity and the closely spatial location of the slopes are both Prestura and Håkåneset considered as part of one large unstable complex (Figure 89).

*Table 16: Results of dip direction/dip measurements from field observations and TLS analysis (Coltop 3D), at Prestura and Håkåneset.*

		J1 (1stdv)	J2 (1stdv)	J3 (1stdv)	J4 (1stdv)	SF (1stdv)
Prestura	Field observations	084/64 (17,5)	354/72 (19,3)	130/86 (19,0)	214/86 (21,5)	269/5 (26,6)
	Coltop 3D	059/68 (13,1)	344/72 (14,7)	113/64 (14,1)	237/66 (14,2)	-
Håkåneset	Field observations	074/59 (20)	358/65 (18)	133/77 (20)	208/76 (16)	237/19 (21)
	Coltop 3D	66/67 (16)	015/60 (19)	122/75 (19)	221/79 (18)	-

The slope is strongest deformed at the Håkåneset instability and deformation reduces towards Prestura. This change in rock slope deformation is visible in Figure 89, where contour lines highlight a highly irregular slope at Håkåneset, indicating deformation, while Prestura appear to have a smooth surface, thus a small degree of deformation of the slope. This is supported by the ridges and landslide scars occurring below Håkåneset within the lake sediments, suggesting ongoing movement and internal deformation at the Håkåneset slope, while the Prestura slope does not show any soft sediment deformation. In combination with no visible active deformation on the Prestura rock slope it is interpreted that this part of the instability is dormant or stabilized today.



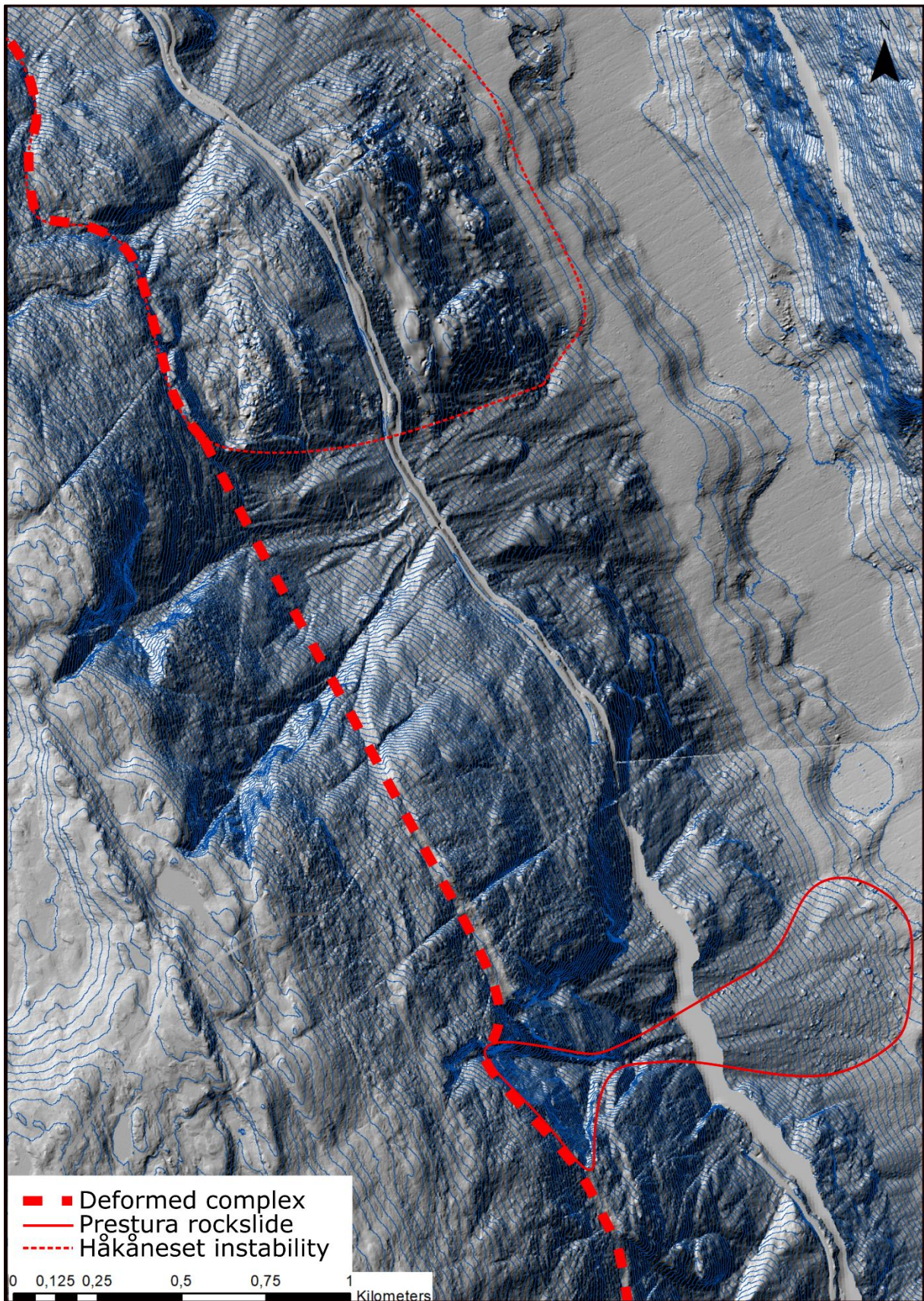


Figure 89: DEM of Håkåneset (north) and Prestura (south) with 10m contour lines (blue line), The thick dashed line represent deformation features, showing that Prestura and Håkåneset are connected by deformation.



#### **6.4.2 Why Prestura?**

Why did the rock slope fail at Prestura and not at Håkåneset? Based on the structural analysis they seem almost identical, they share the same rocks, joint sets, the backscarp is created along the same weakness zone and the kinematic analysis is very similar. However, the mean slope gradient at Prestura (46°) is steeper than the slopes located in Håkåneset (38°). It is also observed both in field and from previous work done by Sollie (2013) that the slope around Prestura and the southern parts of the Håkåneset mapping area is more affected by ice erosion.

A possible reason for the failure of Prestura might then be that Prestura was at the end of the last ice age, more effected by local ice erosion than Håkåneset. This is supported by a change in lake width, showing a significant narrower lake close to Prestura (1 300m) than Håkåneset (1 600m). Thus, creating a steeper slope and a stronger stress release due to deglaciation.

The presence of lake Tinnsjø might also contribute in the stability analysis. According to Sollie (2014) has the presence of lake Tinnsjø a stabilizing effect on the Håkåneset rockslide, due to the presence of hydraulic pressure from the water column stabilizing the slope. In addition, it contributes to less variation in groundwater table oscillation, preventing destabilizing effects due to excessive pore water pressure during ground water table decrease. Prestura is purely subaerial, with no stabilizing water column present and thus a higher variation of the groundwater table, making the stability of the slope more sensitive to sudden variations in precipitation and seepage forces.

Another reason might be that the volume of the failed masses at Prestura is significantly lower (3 - 9 million m<sup>3</sup>) than Håkåneset (17-144 million m<sup>3</sup> based on the old bathymetrical data (Sollie, 2014), now assumed even bigger) making it easier to fail in a complex failure mode such as bi-planar failure. This is especially true due to the low persistence and strong variation in dip direction of the foliation (SF).

#### **6.5 LANDSLIDE THREAT AROUND LAKE TINNSJØ**

Due to the presence of populated areas along the shore of lake Tinnsjø are landslide generated displacement waves by impact of subaerial rockslides into the water body or landslide triggered tsunamis, induced by subaquatic soft sediment failures considered the biggest landslide threat in the area. The potential landslide generated displacement wave threats in lake Tinnsjø are divided into two types: Displacement waves caused by rockslides moving

into a body of water (subaerial) and landslide-triggered tsunamis caused by subaquatic landslides (Hermanns *et al.*, 2013b).

### **6.5.1 Threat from displacement wave caused by rockslides moving into a lake Tinnsjø**

The semi empirical displacement wave analysis show that the Prestura rockslope failure has a potential in creating displacement waves with heights varying from 10m to 20m along the shore of Tinnsjø (Table 13) if the failure would have occurred as a single short-lived failure (lasting seconds to minutes). However, according to Hermanns *et al.* (2013b) do the magnitude of displacement wave generated from a subaerial landslide depend on 1) volume of the moving material (failed mass), and the morphology of the front area, 2) water depth of the water body, and 3) velocity. As discussed above the failure of Prestura was not a short-lived event, but took rather place similar to the Randa failures over several hours. Therefore, is the assumption that the entire failed mass of Prestura entered the lake simultaneously considered an exaggeration of the event.

If the semi empirical displacement wave analysis is used on the Håkåneset rockslide, will the displacement wave height be considerably higher than the results from Prestura. This study has to be carried out by NGU after the volume of the failed scenarios have been defined based on the new bathymetrical data.

### **6.5.2 Threat from subaquatic landslides**

The magnitude of tsunamis triggered by subaquatic landslides depend on 1) volume of the moving material, 2) water depth were the landslide occurs, 3) acceleration and initial velocity of the landslide, 4) rheology of the failed sediments and the dynamics, and 5) distance to shore and seafloor morphology (Hermanns *et al.*, 2013b). The data available and used in this thesis do not cover the acceleration and initial velocity of the landslide (3) or the rheology of the failed masses (4). An empirical relation of volume versus wave run-up height with distance from impact, does not exist for landslide triggered tsunamis. Because of these missing relations and parameters, it is not possible to perform an accurate hazard analysis for the subaquatic landslides in the lake. Instead is the mapped subaquatic landslide compared to similar landslides to get an overview of the potential of generating landslide triggered tsunamis. It is important to note that the following discussion is not considered accurate enough to represent a hazard analysis of the threat of generating landslide triggered tsunamis.



Two subaquatic landslides of similar volume as the mapped landslides in lake Tinnsjø (From 100 000m<sup>3</sup> to 6,2million m<sup>3</sup>, see Figure 77, Figure 78, Figure 79 and appendix G) have occurred along the coast of Trøndelag (L'Heureux *et al.*, 2011b, Glimsdal *et al.*, 2016). Both generating landslide triggered tsunamis with height up to 10m. One of the previously mapped landslides occur at Statland, Namandseid county having a volume of 400 000m<sup>3</sup>, generating a landslide triggered tsunami with a maximum run-up height of 10m. The event damaged an industrial building and destroying 12 boathouses, as well as a section of a road. However, this landslide occurred along the coast at a depth of 1-2m, according to Schulten *et al.* (2018) does displacement generation require an significant volume displacements on the seafloor with increasing depth. In the southern part of lake Tinnsjø occurs five landslide scars of similar volumes as the Statland landslide (volume between 180 000m<sup>3</sup> to 640 000 million m<sup>3</sup>, marked yellow in Figure 79), at depth shallower than 20m. Thus, these landslides are assumed to have potential of generating landslide triggered tsunamis. In the northern parts of Tinnsjø does landslides having similar volumes as the Statland event (volume between 100 000m<sup>3</sup> and 1 million m<sup>3</sup>, marked yellow in Figure 77 and Figure 78), occur at a depth of 150m or deeper. Therefore, only the large subaquatic landslides (volume over 1 million m<sup>3</sup>, marked red in Figure 77, Figure 78, and Figure 79) are considered as having the potential of generating landslide triggered tsunamis in the northern parts of lake Tinnsjø.

The second subaquatic landslide examined in Trøndelag, occurred in 1888. This landslide event generated a landslide triggered tsunami with maximum run-up of 5 – 7m, at the shoreline of Trondheim, killing one person and causing major damage to port facilities (L'Heureux *et al.*, 2011b). According to L'Heureux *et al.* (2011b) was it a W-shaped landslide that generated this landslide triggered tsunami. The W-shaped landslide occurred 2km off shore, at a depth of 80 – 160m, having a volume of 1,45 million m<sup>3</sup>. This shows that subaquatic landslides with volumes over 1 million m<sup>3</sup> can generate landslide triggered tsunamis at depths over 100m. In lake Tinnsjø occur the landslides with volumes over 1 million m<sup>3</sup> (marked red in Figure 77, Figure 78 and Figure 79) at depths of 250 – 350m, 100m deeper than the W-shaped landslide. Thus, is most of the over 1 million m<sup>3</sup> landslides not considered capable of generating landslide triggered tsunamis. An exception is the largest landslide scar mapped in Tinnsjø, occurring south of Austbygdåi delta, at a depth of 250m (Figure 76), having a volume of 6,2 million m<sup>3</sup> (landslide ID.62 in Figure 77 and appendix G). This landslide is considered significantly larger than the W-shaped landslide in Trondheimsfjorden, thus might have been able to generate a landslide triggered tsunami.

However, are the marine sediments in Trondheimsfjorden not necessary comparable to sediments in lake Tinnsjø. In order to do a hazard analysis a better understanding of the lake sediments in lake Tinnsjø is required.

### **6.5.3 Threat from turbidity currents**

According to Schulten *et al.* (2018) have turbidity currents the capability of breaking subaquatic cables. Evidence of turbidity currents occur as cyclic steps, and are visible both at the northern and southern areas at the basin floor of lake Tinnsjø. Therefore, should the damaging potential of turbidity currents be considered if installation of subaquatic cables (such as power cables) in lake Tinnsjø in the future are planned.

## **6.6 RECOMMENDATIONS FOR FURTHER INVESTIGATIONS**

Landform types for the entire lake Tinnsjø are described in the results. However, due to the specific master thesis topic only the landforms associated to the Prestura and Håkåneset rockslide was further discussed. Thus, a thorough discussion of the other landforms mapped in the lake are highly recommended in order, to understand both the depositional environment of lake Tinnsjø and landslide related threats. This mapping should involve discharge measurements of all major rivers flowing into the lake. In addition to geophysical analyses and core sampling of the lake floor, giving more information on the sediment properties and thickness.

The TLS model lack data, especially along the northern lateral flank. Because of this it is suggested to perform a new scan of this area if possible. Two different locations of the scans are suggested in Figure 43, however it is uncertain if it is possible to locate a scanner at those locations.

The new bathymetrical data show a larger unstable area at the Håkåneset rock slope, than the area defined by Sollie (2014). Therefore, it is necessary to redefine and determine the volumes as part of the hazard analysis of the Håkåneset rock slope instability.

## 7 CONCLUSION

---

### 7.1 STRUCTURAL ANALYSIS OF THE PRESTURA ROCKSLIDE

A structural analysis of the Prestura rockslide has been performed followed by a morphologic description, volume estimation, run-out measurements and semi-empirical displacement wave analysis. The key findings are as follows:

- Five different discontinuities occur in the area: joint set J1, J2, J3 J4 and the foliation SF. The orientation of the joint sets correlate well with the joint sets occurring close to the Håkåneset rockslide.
- Planar sliding, wedge sliding and direct toppling are only considered kinematically feasible failure modes at slopes steeper than 60°.
- The complex failure mode bi-planar sliding is considered the most likely failure mode of the Prestura rock slope failure, created by the combination of the steep exfoliation joint sets (J1) and the gently dipping schistose foliation (SF).
- The volume of the potential failed masses of Prestura is considered larger than the displaced masses. Thus, at least one pre-deglaciation event is considered possible.
- The measured run-out of the Prestura rockslide is considered shorter than expected from rock avalanches according to the run-out vs volume correlation presented in Scheidegger (1973) and Hermanns *et al.* (2012). This run-out vs volume correlation of the Prestura deposit is considered similar to the Randa rockslide suggesting that the failure of the rock masses continued over several hours.
- The reason why the slope failed at Prestura and has deformed at Håkåneset over a long time span, can be explained by a combination of the steeper slope gradient and higher degree of glacial erosion of the Prestura slope compared to that of Håkåneset. In addition is Håkåneset covered by lake Tinnsjø which after numerical modelling has a stabilizing effect.
- Semi-empirical displacement wave analysis of the Prestura rockslide indicate a maximum run-up height of 10 – 20m along the shore of lake Tinnsjø. This is however considered very conservative, representing the worst-case scenario. This must have been lower as the Prestura rock slope failure is interpreted to have taken place over several hours.

A mapping of the lake floor was also performed, based on a 2x2m resolution bathymetric map. The results of the bathymetrical mapping are summarized as:

- The lake contains several different types of landforms, such as deltas, landslide scars, depressions, fans, protuberances and terraces.
- The terraces are interpreted as kame terraces and occur at depth of 350m, 300m, 270m and 210m.
- The presence of depressions and terraces is interpreted as the remains of a dead-ice terrain, suggesting that the lake contained several dead ice bodies during the deglaciation after the LGM.
- The most frequently mapped landform are landslide scars and further divided into three different types.
  - o Low angle large landslides (volume over 1 million m<sup>3</sup>) occurring at the basin floor
  - o Pear shaped landslides occurring at the rim of kame terraces, often having volumes ranging from 10 000m<sup>3</sup> to 100 000m<sup>3</sup>.
  - o Large rockslides having a mappable subaerial backscarp often occurring along the margins of lake Tinnsjø.
- The presence of cyclic steps suggest that turbidity currents occur at the basin floor transporting fine grained sediments away from the deltas. This explain why no landslide deposits occur at the basin floor, despite the high frequency of landslide scars. These turbidity currents are also considered of having the potential of breaking subaquatic cables.
- The largest subaquatic landslide scar (volume of 6,2 million m<sup>3</sup>) occur south of Austbygdåi delta. Such failures are considered as having potential of generating landslide triggered tsunamis, however further data acquisition is required to better define the hazard associated with this type of landslide.
- Mapped longitudinal ridges and an increase in landslide scar concentration is considered evidence that movement of the Håkåneset rockslide occur at a depth of 350m.
- Roughly 51% of the movement recorded at the backscarp is transformed into internal deformation of the slope. Since only 49% of the recorded displacement at the backscarp were measured at the toe of rupture surface.



## 8 REFERENCES

---

- Amelan, R. (2005) Norwegian Fjords and Japan's Shiretoko peninsula are among the seven natural sites added to UNESCO's World Heritage List, *Unesco World Heritage centre*, 14.05.2005. Available at: <http://whc.unesco.org/en/news/134/> (Accessed: 30.04.2018).
- Andersen, T. (2005) Terrane analysis, regional nomenclature and crustal evolution in the Southwest Scandinavian Domain of the Fennoscandian Shield, *GFF*, 127, pp. 159-168. doi: 10.1080/11035890501272159.
- Askheim, S. (2017) Norges Dypeste Innsjøer *Store Norske Leksikon*. Available at: [https://snl.no/Norges\\_dypeste\\_innsj%C3%B8er](https://snl.no/Norges_dypeste_innsj%C3%B8er). (Accessed: 15.04.2018).
- Aydin, A. and Basu, A. (2005) The Schmidt hammer in rock material characterization, *Engineering Geology*, 81(1), pp. 1-14. doi: 10.1016/j.enggeo.2005.06.006.
- Blikra, L. H., Braathen, A. and Skurtveit, E. (2002) *Hazard evaluation of rock avalanches : the Baraldsnes - Oterøya area*. (NGU-rapport (trykt utg.) 2001.108). Trondheim: Norges geologiske undersøkelser. Available at: <https://www.ngu.no/en/publikasjon/hazard-evaluation-rock-avalanches-baraldsnes-oter-ya-area> (Accessed: 22.04.2018).
- Boggs, S. (2014) *Principles of sedimentology and stratigraphy*. Pearson new international edition.; Fifth edition. edn. United Kingdom: Pearson.
- Braathen, A., Blikra, L. H., Berg, S. S. and Karlsen, F. (2004) Rock-slope failures in Norway; type, geometry, deformation mechanisms and stability, *Norsk Geologisk Tidsskrift*, 84(1), pp. 67-88. Available at: <http://njg.geologi.no/vol-81-90/details/17/388-388>.
- Brattli, B. (2015) *Kompendium for Ingeniørgeologi løsmasser*. Trondheim: NTNU-Institutt for geologi og bergteknikk.
- Brown, E. T. (1981) *Rock characterization testing & monitoring : ISRM suggested methods*. Oxford: Published for the Commission on Testing Methods, International Society for Rock Mechanics by Pergamon Press.
- Cartigny, M. J. B., Postma, G., van Den Berg, J. H. and Mastbergen, D. R. (2011) A comparative study of sediment waves and cyclic steps based on geometries, internal structures and numerical modeling, *Marine Geology*, 280(1-4), pp. 40-56. doi: 10.1016/j.margeo.2010.11.006.
- Casalbore, D., Martorelli, E., Bosman, A., Morelli, E. and Latino Chiocci, F. (2018) Failure dynamics of landslide scars on the lower continental slope of the Tyrrhenian Calabrian margin: insights from an integrated morpho-bathymetric and seismic analysis, pp. SP477.416. doi: 10.1144/SP477.16.
- Clague, J. J. and Stead, D. (2012) *Landslides : types, mechanisms, and modeling*. New York: Cambridge University Press.
- Clare, M. A., Hughes Clarke, J. E., Talling, P. J., Cartigny, M. J. B. and Pratomo, D. G. (2016) Preconditioning and triggering of offshore slope failures and turbidity currents revealed by most detailed monitoring yet at a fjord-head delta, *Earth and Planetary Science Letters*, 450, pp. 208-220. doi: 10.1016/j.epsl.2016.06.021.
- Cooley, S. W. (2015) *Minimum Eroded Volume*. Available at: <http://gis4geomorphology.com/calculate-basin-volume/> (Accessed: 29.03 2018).
- Corner, G. D. (2006) A transgressive-regressive model of fjord-valley fill: stratigraphy, facies and depositional controls, in Dalrymple, R. W., Leckie, D. and Tilman, R. (ed.) *Incised Valleys in Time and Space*. SEPM Special Publication, pp. 161-178.
- Corominas, J. (1996) The angle of reach as a mobility index for small and large landslides, *Canadian Geotechnical Journal*, 33(2), pp. 260-271. doi: 10.1139/t96-005.
- Dahlgren, S. (1993) Litt om geologien i det sentrale Telemark, *Stein*, 20, pp. 73-79. Available at: <http://www.nags.net/stein/1993/Sentral-Telemark-geologi.pdf>.

- Deere, D. U. and Miller, R. P. (1966) *Engineering classification and index properties for intact rock* (AFWL-TR-65-116). Illinois: University of Illinois Available at: <http://www.dtic.mil/dtic/tr/fulltext/u2/646610.pdf> (Accessed: 18.03.2018).
- Dingman, S. L. (2015) *Physical hydrology*. 3rd ed. edn. Long Grove, Ill: Waveland Press Inc.
- Domaas, U. and Grimstad, E. (2014) Fjell- og steinskred, in Høeg, K., Lied, K. and Karlsrud, K. (ed.) *Skred: skredfare og sikringstiltak*. Oslo: NGI og Universitetsforlaget, pp. 45 - 68.
- Dons, J. A. (1960) *The stratigraphy of supracrustal rocks, granitization and tectonics in the Precambrian Telemark area southern Norway*. Oslo: Norges Geologiske Undersøkelse.
- Dons, J. A. and Jorde, K. (1979) SKIEN Bergrunnskart 1:250 000. Available at: <http://www.ngu.no/upload/Publikasjoner/Kart/B250/Skien.pdf>.
- Eilertsen, R., Bøe, R., Hermanns, R., Longva, O. and Dahlgren, S. (2016) Kettle holes, 'dead-ice topography and eskers on a lake floor in Telemark, southern Norway, in Dowdeswell, J. A., et al. (ed.) *Atlas of Submarine Glacial Landforms: Modern, Quaternary and Ancient*. London: The Geological Society of London, pp. 113-114.
- ESRI (2017a) ArcMap 10.5.
- ESRI (2017b) ArcScene 10.5.
- Fleisher, P. J. (1986) Dead-ice sinks and moats: environments of stagnant ice deposition, *Geology*, 14(1), pp. 39-42. doi: 10.1130/0091-7613(1986)14<153:RBIUCP>2.0.CO2.
- Flint, R. F. (1971) *Glacial and quaternary geology*. New York: John Wiley & Sons.
- Furseth, A. (2006) *Skredulykker i Norge*. Oslo: Tun.
- Glastonbury, J. and Fell, R. (2010) Geotechnical characteristics of large rapid rock slides, *Canadian Geotechnical Journal*, 47(1), pp. 116-132. doi: 10.1139/T09-080.
- Glimsdal, S., L'Heureux, J.-S., Harbitz, C. and Løvholt, F. (2016) The 29th January 2014 submarine landslide at Statland, Norway—landslide dynamics, tsunami generation, and run-up, *Journal of the International Consortium on Landslides*, 13(6), pp. 1435-1444. doi: 10.1007/s10346-016-0758-7.
- Hansen, L., Waldman, N., Stroms, J. E. A., Eilertsen, R. R., Ariztegui, D., Chapron, E. and Nesje, A. (2016) Morphological signatures of mass wasting and delta processes in a fjord-lake system: insights from Lovatnet, western Norway, *Norwegian journal of geology*, vol. 96(no. 3), pp. 1-21. doi: 10.17850/njg96-3-02.
- Hermanns, R., Oppikofer, T., Anda, E., Blikra, L., Böhme, M., Bunkholt, H., . . . Yugsi Molina, F. X. (2012) *Recommended hazard and risk classification system for large unstable rock slopes in Norway*. (2012.029). Trondheim: Norges Geologiske Undersøkelse. Available at: <https://www.ngu.no/en/publikasjon/recommended-hazard-and-risk-classification-system-large-unstable-rock-slopes-norway> (Accessed: 06.12.2017).
- Hermanns, R., Hansen, L., Sletten, K., Böhme, M., Bunkholt, H., Dehls, J., . . . Yugsi Molina, F. X. (2013a) Systematic geological mapping for landslide understanding in the Norwegian context *Landslides and Engineered Slopes: Protecting Society through Improved Understanding*
- Hermanns, R., L'Heureux, J.-S. and Blikra, L. (2013b) Landslide Triggered Tsunami, Displacement Wave, pp. 611-615. doi: 10.1007/978-1-4020-4399-4\_95.
- Hermanns, R. L. and Strecker, M. R. (1999) Structural and lithological controls on large Quaternary rock avalanches (sturzstroms) in arid northwestern Argentina, *GSA Bulletin*, 111(6), pp. 934-948. doi: 10.1130/0016-7606(1999)111<0934:SALCOL>2.3.CO;2.
- Highland, L. M. and Bobrowsky, P. (2008) *The Landslide Handbook—A Guide to Understanding Landslides*. Reston, Virginia: U.S. Geological Survey Circular 135.
- Hoek, E. and Bray, J. (1981) *Rock slope engineering*. Rev. 3rd ed. edn. London: The Institution of Mining and Metallurgy.
- Hoek, E. (2007) *Practical rock engineering*. Rocscience. Available at: <https://www.rocscience.com/documents/hoek/corner/Practical-Rock-Engineering-Full-Text.pdf>.
- Hudson, J. A. and Harrison, J. P. (2000) *Engineering Rock Mechanics: An Introduction to the Principles*. London: Elsevier Science.
- Hungr, O., Leroueil, S. and Picarelli, L. (2014) The Varnes classification of landslide types, an update, *Journal of the International Consortium on Landslides*, 11(2), pp. 167-194. doi: 10.1007/s10346-013-0436-y.

- Innovmetric (2011a) PifEdit.
- Innovmetric (2011b) Polyworks V12.
- Jaboyedoff, M., Baillifard, F., Couture, R., Locat, J. and Locat, P. (2004) Toward preliminary hazard assessment using DEM topographic analysis and simple mechanical modeling by means of sloping local base level, in Lacerda, W., *et al.* (ed.) *Landslides: Evaluation and Stabilization*. London: Taylor & Francis Group, pp. 199-201.
- Jaboyedoff, M., Derron, M.-H., Pazzaglia, F. J. and Dramis, F. (2005) A new method to estimate the infilling of alluvial sediment of glacial valleys using a sloping local base level, 28, pp. 38-39. Available at: [https://www.researchgate.net/publication/257289606\\_A\\_new\\_method\\_to\\_estimate\\_the\\_infilling\\_of\\_alluvial\\_sediment\\_of\\_glacial\\_valleys\\_using\\_a\\_sloping\\_local\\_base\\_level](https://www.researchgate.net/publication/257289606_A_new_method_to_estimate_the_infilling_of_alluvial_sediment_of_glacial_valleys_using_a_sloping_local_base_level).
- Jaboyedoff, M., Metzger, R., Oppikofer, T., Couture, R., Derron, M. H., Locat, J. and Turmel, D. (2007) New insight techniques to analyze rock-slope relief using DEM and 3D-imaging cloud points: COLTOP-3D software, in Eberhardt, E., Stead, D. and Morrison, T. (ed.) *Rock mechanics: Meeting Society's challenges and demands*. Vancouver: Tyler & Francis, pp. 61-68.
- Jaboyedoff, M., Oppikofer, T., Abellán, A., Derron, M.-H., Loye, A., Metzger, R. and Pedrazzini, A. (2012) Use of LIDAR in landslide investigations: a review, *Journal of the International Society for the Prevention and Mitigation of Natural Hazards*, 61(1), pp. 5-28. doi: 10.1007/s11069-010-9634-2.
- Jansen, I. J. (1986) *Kvartærgeologi : jord og landskap i Telemark gjennom 11000 år : beskrivelse til kvartærgeologisk kart i målestokk 1:250000*. Bø: Institutt for naturanalyse.
- Koykka, J. (2010) Lithostratigraphy of the Mesoproterozoic Telemark supracrustal rocks, South Norway: revision of the sub-Heddersvatnet unconformity and geochemistry of basalts in the Heddersvatnet Formation, *Norw. J. Geol.*, 90(1-2), pp. 49-64. Available at: [http://njg.geologi.no/images/NJG\\_articles/NJG\\_1\\_2010\\_Koykka\\_pr.pdf](http://njg.geologi.no/images/NJG_articles/NJG_1_2010_Koykka_pr.pdf).
- Krogh, K. (2017) *The Unstable Rock Slope Kassen - A Hazard, Consequence and Stability Assessment of the Rock Slope*. Master NTNU - Norwegian University of Science and Technology.
- Kvalstad, T. (2014) Undersjøiske skred, in Høeg, K., Lied, K. and Karlsrud, K. (ed.) *Skred: skredfare og sikringstiltak*. Oslo: NGI og Universitetsforlaget, pp. 123 - 136.
- L'Heureux, J. S., Eilertsen, R. S., Hansen, L. and Sletten, K. (2011a) *Morfologi og skredkartlegging i Botn ved Rissa, Sør-Trøndelag*. (2011.037). Trondheim: Norges Geologiske Undersøkelse. Available at: <https://www.ngu.no/publikasjon/morfologi-og-skredkartlegging-i-botn-ved-rissa-s-r-tr-ndelag> (Accessed: 29.04.2018).
- L'Heureux, J. S., Glimsdal, S., Longva, O., Hansen, L. and Harbitz, C. (2011b) The 1888 shoreline landslide and tsunami in Trondheimsfjorden, central Norway, *An International Journal for the Study of the Earth Beneath the Sea*, 32(1), pp. 313-329. doi: 10.1007/s11001-010-9103-z.
- Laajoki, K., Corfu, F. and Andersen, T. (2002) Lithostratigraphy and U-Pb geochronology of the Telemark supracrustals in the Bandak-Sauland area, Telemark, south Norway, *Norsk Geologisk Tidsskrift*, 82(3), pp. 119-138. Available at: [http://njg.geologi.no/images/NJG\\_articles/NGT\\_82\\_3\\_119-138.pdf](http://njg.geologi.no/images/NJG_articles/NGT_82_3_119-138.pdf).
- Lamminen, J. (2011) Provenance and correlation of sediments in Telemark, South Norway; status of the Lifjell Group and implications for early Sveconorwegian fault tectonics, *Norsk Geologisk Tidsskrift, Norwegian Journal of Geology*, 91(1), pp. 57-75. Available at: [http://njg.geologi.no/images/NJG\\_articles/NJG\\_1\\_2\\_2011\\_Lamminen\\_pr.pdf](http://njg.geologi.no/images/NJG_articles/NJG_1_2_2011_Lamminen_pr.pdf).
- Lato, M., Diederichs, M. S., Hutchinson, D. J. and Harrap, R. (2009) Optimization of LiDAR scanning and processing for automated structural evaluation of discontinuities in rockmasses, *International Journal of Rock Mechanics and Mining Sciences*, 46(1), pp. 198. doi: 10.1016/j.ijrmms.2008.04.007.
- Lato, M., Diederichs, M. and Hutchinson, D. (2010) Bias Correction for View-limited Lidar Scanning of Rock Outcrops for Structural Characterization, *Rock Mechanics and Rock Engineering*, 43(5), pp. 625-626. doi: 10.1007/s00603-010-0086-5.
- Lundbo, S. (2017) *Tinnsjø Store Norske Leksikon*. Available at: <https://snl.no/Tinnsjø%C3%A5> (Accessed: 06.11.2017).

- Mangerud, J. (2004) Ice sheet limits on Norway and the Norwegian continental shelf, 2, pp. 1-23. doi: 10.1016/S1571-0866(04)80078-2.
- Mangerud, J. and Vorren, T. O. (2013) Istider kommer og går, in Ramberg, I. B., *et al.* (ed.) *Landet blir til : Norges geologi*. 2. utg. edn. Trondheim: Norsk geologisk forening, pp. 494 - 547.
- Morken, O. A. (2017) *Integrated analysis of past, and potential future rock slope failures of various size from Rombakstøtta, Nordland*. Master, NTNU - Norwegian University of Science and Technology.
- NGI (2015) *Håndbok Bruk av Q-systemet*. Norges Geotekniske Institutt. Available at: <https://www.ngi.no/Publikasjoner-og-bibliotek/Boeker/Q-systemet>.
- NGU (2017) Løsmasser: nasjonal løsmassedatabase: NGU - Norges Geologiske Undersøkelse Available at: <http://geo.ngu.no/kart/losmasse/>.
- Nichol, S., Hungr, O. and Evans, S. G. (2002) Large-scale brittle and ductile toppling of rock slopes, *Can. Geotech. J.*, 39(4), pp. 773-788. doi: 10.1139/T02-027.
- Nichol, S. L., Hungr, O. and Evans, S. G. (2002) Large-scale brittle and ductile toppling of rock slopes, *Canadian Geotechnical Journal*, 39(4), pp. 773-788. doi: 10.1139/t02-027.
- Nichols, G. (2009) *Sedimentology and Stratigraphy* (2). Hoboken: Hoboken, GB: John Wiley & Sons, Incorporated.
- Nicoletti, P. G. and Sorriso-Valvo, M. (1991) Geomorphic controls of the shape and mobility of rock avalanches, *GSA Bulletin*, 103(10), pp. 1365-1373. doi: 10.1130/0016-7606(1991)103<1365:GCOTSA>2.3.CO;2.
- Nilsen, B. (2017) Rock slope stability analysis according to Eurocode 7, discussion of some dilemmas with particular focus on limit equilibrium analysis, *Bulletin of Engineering Geology and the Environment*, 76(4), pp. 1229-1236. doi: 10.1007/s10064-016-0928-9.
- NOAA (2017) *What is bathymetry?* Available at: <https://oceanservice.noaa.gov/about/welcome.html#cite> (Accessed: 06/03 2018).
- NVE (2018) *NVE Atlas*. Available at: <https://atlas.nve.no/Html5Viewer/index.html?viewer=nveatlas#> (Accessed: 17.04 2018).
- NVE (2018a) Nedbørfelt shapefile. Available at: <http://nedlasting.nve.no/gis/> (Accessed: 08.02.2018).
- NVE (2018b) *Historiske data*. Available at: <https://www.nve.no/hydrologi/hydrologiske-data/historiske-data/> (Accessed: 27.04 2018).
- NVE (2018c) *Skredhendelser*. Available at: <https://www.nve.no/flaum-og-skred/kartlegging/skred-og-flaumhendingar/skredhendelser/> (Accessed: 25.04 2018).
- NVE (2018d) *NVE Skredhendelser*. Available at: <https://gis3.nve.no/link/?link=SkredHendelser> (Accessed: 20.04 2018).
- Olsen, L., Fredin, O. and Olesen, O. (2013) *Quaternary geology of Norway*. Trondheim: Geological Survey of Norway.
- Oppikofer, T. (2009) *Detection, analysis and monitoring of slope movements by high-resolution digital elevation models*. Phd, UNIL - Université de Lausanne. Available at: [https://www.researchgate.net/profile/Thierry\\_Oppikofer/publication/265650532\\_Detection\\_and\\_monitoring\\_of\\_slope\\_movements\\_by\\_high-resolution\\_digital\\_elevation\\_models/links/56fd21a408aea3275abb9b1c/Detection-analysis-and-monitoring-of-slope-movements-by-high-resolution-digital-elevation-models.pdf](https://www.researchgate.net/profile/Thierry_Oppikofer/publication/265650532_Detection_and_monitoring_of_slope_movements_by_high-resolution_digital_elevation_models/links/56fd21a408aea3275abb9b1c/Detection-analysis-and-monitoring-of-slope-movements-by-high-resolution-digital-elevation-models.pdf) (Accessed: 13.05.2018).
- Oppikofer, T., Jaboyedoff, M., Blikra, L., Derron, M. and Metzger, R. (2009) Characterization and monitoring of the Aknes rockslide using terrestrial laser scanning, *Nat. Hazards Earth Syst. Sci.*, 9(3), pp. 1004-1006. doi: 10.5194/nhess-9-1003-2009.
- Oppikofer, T., Bunkholt, H., Fischer, L., Saintot, A., Hermanns, R., Carrea, D., . . . Jaboyedoff, M. (2012) Investigation and monitoring of rock slope instabilities in Norway by terrestrial laser scanning, in E., E., *et al.* (ed.) *Landslides and Engineered Slopes: Protecting Society through Improved Understanding – Eberhardt et al. (eds)*. London: Taylor & Francis Group, pp. 1235-1237.
- Oppikofer, T., Böhme, M., Nicolet, P., Penna, I. and Hermanns, R. (2016) *Metodikk for konsekvensanalyse av fjellskred*. (2016.047). Trondheim: Norges Geologiske Undersøkelse. Available at: [http://www.ngu.no/upload/Publikasjoner/Rapporter/2016/2016\\_047.pdf](http://www.ngu.no/upload/Publikasjoner/Rapporter/2016/2016_047.pdf) (Accessed: 20.04.2018).

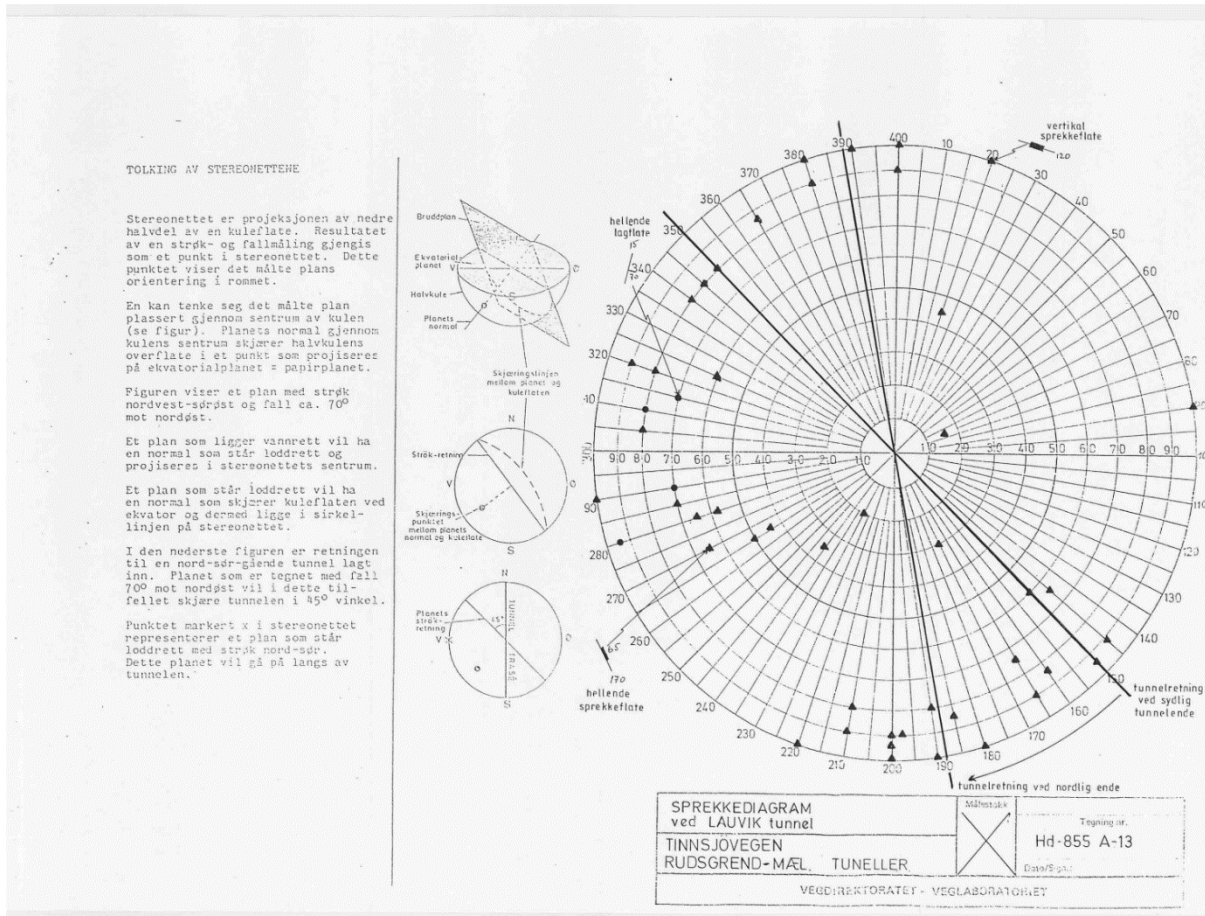


- Oppikofer, T., Saintot, A., Hermanns, R. L., Böhme, M., Scheiber, T., Gosse, J. and Dreiås, G. M. (2017) From incipient slope instability through slope deformation to catastrophic failure — Different stages of failure development on the Ivasnasen and Vollan rock slopes (western Norway), *Geomorphology*, 289, pp. 96-116. doi: 10.1016/j.geomorph.2017.03.015.
- Prior, D. B. and Bornhold, B. D. (1990) The Underwater Development of Holocene Fan Deltas, in Colella, A. and Prior, D. B. (ed.) *Coarse-Grained Deltas*.
- Quanterra (2003) Conefall. Available at: <http://www.quanterra.org/softs.HTM#soft01>.
- Rocscience (2016a) Dips 7.0.
- Rocscience (2016b) Tutorial 4 - Toppling, Planar Sliding and Wedge Sliding. Available at: [https://www.rocscience.com/help/dips/webhelp7/pdf\\_files/tutorials/Tutorial\\_04\\_Toppling\\_Planar\\_and\\_Wedge\\_Sliding.pdf](https://www.rocscience.com/help/dips/webhelp7/pdf_files/tutorials/Tutorial_04_Toppling_Planar_and_Wedge_Sliding.pdf).
- Rocscience (2016c) *Direct toppling*. Available at: [https://www.rocscience.com/help/dips/webhelp/dips/Direct\\_Toppling.htm](https://www.rocscience.com/help/dips/webhelp/dips/Direct_Toppling.htm).
- Romstad, B., Harbitz, C. B. and Domaas, U. (2009) A GIS method for assessment of rock slide tsunami hazard in all Norwegian lakes and reservoirs, *Natural Hazards and Earth System Sciences (NHESS)*, (2), pp. 353-364. doi: 10.5194/nhe5-9-353-2009.
- Rowland, S. M., Duebendorfer, E. M. and Schiefelbein, I. M. (2007) *Structural analysis and synthesis : a laboratory course in structural geology*. 3rd ed. edn. Malden, Mass: Blackwell.
- Sandøy, G. (2012) *Back-analysis of the 1756 Tjellefonna rockslide, Langfjorden*. Master, NTNU - Norwegian University of Science and Technology.
- Sartori, M., Baillifard, F., Jaboyedoff, M. and Rouiller, J. D. (2003) Kinematics of the 1991 Randa rockslides (Valais, Switzerland), *Natural Hazards and Earth System Sciences*, 3(5), pp. 423-433. doi: 10.1007/s40430-014-0141-3.
- Scheidegger, A. E. (1973) On the prediction of the reach and velocity of catastrophic landslides, *Rock mechanics*, 5(4), pp. 231-236. doi: 10.1007/bf01301796.
- Schleier, M., Hermanns, R. L., Rohn, J. and Gosse, J. C. (2015) Diagnostic characteristics and paleodynamics of supraglacial rock avalanches, Innerdalen, Western Norway, *Geomorphology*, 245, pp. 23-39. doi: <https://doi.org/10.1016/j.geomorph.2015.04.033>.
- Schleier, M., Hermanns, R. L., Gosse, J. C., Oppikofer, T., Rohn, J. and Tønnesen, J. F. (2017) Subaqueous rock-avalanche deposits exposed by post-glacial isostatic rebound, Innfjorddalen, Western Norway, *Geomorphology*, 289, pp. 117-133. doi: 10.1016/j.geomorph.2016.08.024.
- Schulten, I., Mosher, D. C., Krastel, S., Piper, D. J. W. and Kienast, M. (2018) Surficial sediment failures due to the 1929 Grand Banks Earthquake, St Pierre Slope, *Geological Society, London, Special publications*, 477. doi: 10.1144/sp477.25.
- SeNorge.no*. Available at: <http://www.senorge.no/?p=klima> (Accessed: 23.02 2018).
- Soil friction angle* (2013). Available at: <http://www.geotechdata.info/parameter/angle-of-friction.html> (Accessed: 25.04 2018).
- Sollie, I. L. (2013) *Håkåneset, Tinnsjø - Geological investigation of potentially rock slide*. Project Assignment, NTNU - Norwegian University of Science and Technology.
- Sollie, I. L. (2014) *The Håkåneset rockslide, Tinnsjø - Stability analysis of a potentially rock slope instability*. Master, NTNU - Norwegian University of Science and Technology.
- Statens Vegvesen (1989) *Hd - 855 A: Tinnsjøvegen, Parsell Rudsgrend - Mæl, Grunnundersøkelser og beskrivelser av tunneler ved Jønjljo og Lauvik*. (Hd - 855 A). Skien: Statens Vegvesen.
- Statens Vegvesen (2013) *Fv 37 Oppgradering av Jønjljo og Prestura tunneler*. (26070-460).
- Stroeven, A. P., Hättestrand, C., Kleman, J., Heyman, J., Fabel, D., Fredin, O., . . . Jansson, K. N. (2016) Deglaciation of Fennoscandia, *Quaternary Science Reviews*, 147, pp. 91-121. doi: <https://doi.org/10.1016/j.quascirev.2015.09.016>.
- Sundal, M. G. (2015) *Vertikal utbredelse av glasielt transportert materiale på Gaustatoppen*. Master, The University of Bergen.
- Terranum (2014) Coltop-3D.
- Travelletti, J., Demand, J., Jaboyedoff, M. and Marillier, F. (2010) Mass movement characterization using a reflexion and refraction seismic survey with the sloping local base level concept, *Geomorphology*, 116(1), pp. 4-5. doi: 10.1016/j.geomorph.2009.10.006.
- Trømborg, D. (2006) *Geologi og landformer i Norge*. Oslo: Landbruksforl.

- Turmel, D., Locat, J., Leblanc, J. and Cauchon-Voyer, G. (2018) Tsunami modelling of the 7250 cal years BP Betsiamites submarine landslide, *Geological Society, London, Special publications*, 477. doi: 10.1144/sp477.9.
- Turner, A. K. and Schuster, R. L. (1996) *Landslides : investigation and mitigation*. Washington: National Academy Press.
- Varnes, D. J. (1978) *Slope movement types and Processes*. Washington, DC: National Academy of Sciences.
- Wille, P. C. (2005) *Sound Images of the Ocean in Research and Monitoring*. Springer Berlin Heidelberg.
- [www.norgebilder.no](https://www.norgebilder.no) (2018). Available at: <https://www.norgebilder.no>.
- Wyllie, D. C. and Mah, C. W. (2004) *Rock slope engineering : civil and mining*. 4th ed. edn. London: Spon Press.
- Ånonsen, K. B. (2010) *Advances in Terrain Aided Navigation for Underwater Vehicles*. Phd, NTNU - Norwegian University of Science and Technology.

# 9 APPENDIX

## 9.1 APPENDIX A: STEREOINET FROM (STATENS VEGVESEN, 1989)

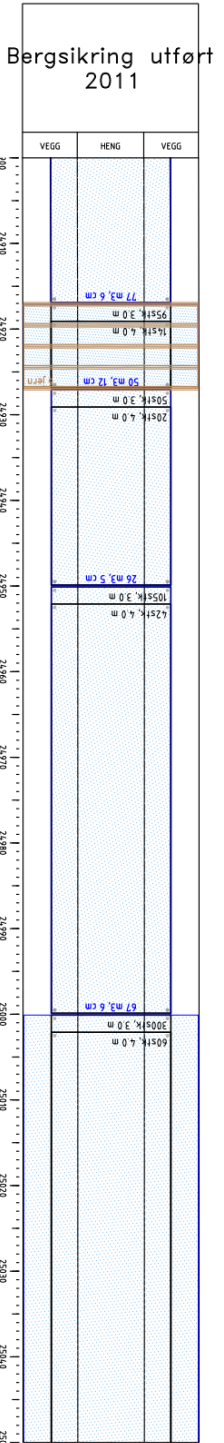
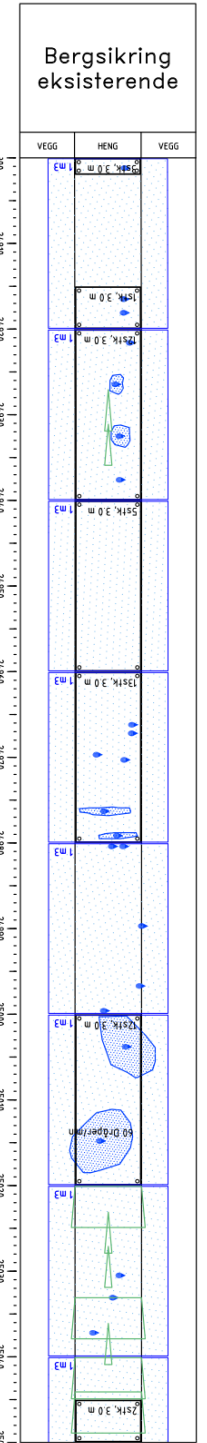
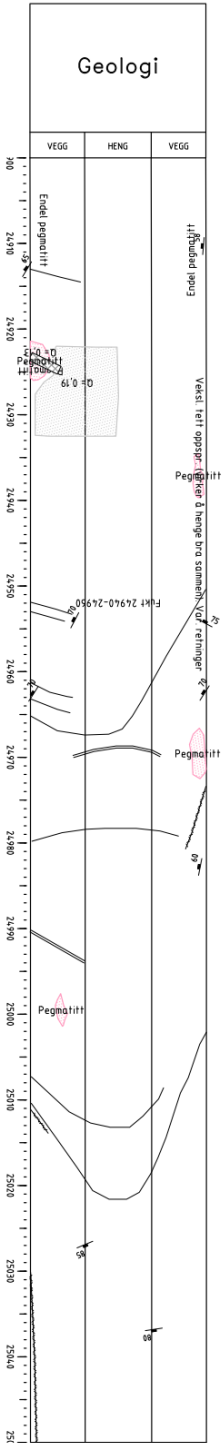








BOI/DN	5074,0	4074,0	5074,0	4074,0	5074,0	4074,0	5074,0	4074,0	5074,0	4074,0
J/100	3,0/2,0	3,0/2,0	3,0/2,0	3,0/2,0	3,0/2,0	3,0/2,0	3,0/2,0	3,0/2,0	3,0/2,0	3,0/2,0
J/1/50	0,66/7,5	1,0/7,5	1,0/7,5	0,66/7,5	0,66/7,5	0,66/7,5	0,66/7,5	0,66/7,5	0,66/7,5	0,66/7,5
Q-Værdi	9,7	6,0	5,0	5,3	6,6	2,7	3,5	3,5	3,5	3,5
Beredelse										
Injektion										



**Beskrivelse**

- Koblingslinjer, mark, vedtak, stift
- Føder, anlegg, vedtak, stift
- Andre botte/typer, vedtak, stift
- Følger
- Sikringsnet
- Sprøyteledning
- Utstøping
- Feltbånd
- Sikringsnett
- Injektion

**Geologiske tegn/fremmer**

- Sprekekne
- Fosasjon
- Sprekk
- Slippe
- Stokkete som anlegg en 1m
- Avstøling etter over 1 time
- SS
- Innsett bergidag

**Beregning**

- Kvartst
- Kvartst
- Lernflett berg
- Pegmatitt

**Vann / -sirkling**

- Lekkasje punkt
- Lekkasje område/interval

**Beredelse**

- A - Svært/ekstrem god (4,0-10,0)
- B - God (10-4,0)
- C - Middels (4-10)
- D - Dårlig (1-4)
- E - Svært dårlig (0,1-1)
- F - Ekstremt dårlig (0,01-0,1)
- G - Eksplosivt dårlig (0,001-0,01)
- Ikke kartlagt med Q-verdi

Region	Regionen gjelder	Utvalgt av	Kontrollert av	Godkjent av	Kontrollert av	Utvalgt av	Kontrollert av	Godkjent av	Kontrollert av	Utvalgt av	Kontrollert av

**Systemet**

Oppgradering jernlinje og Prestura tunnel

Fv 37 hp 06 Kjel - Gryta

**Ingeniørgeslag**

Prestura: Geologi og bergsikring profil 24900 - 25050

Som bygget

Utvalgt av: [ ]









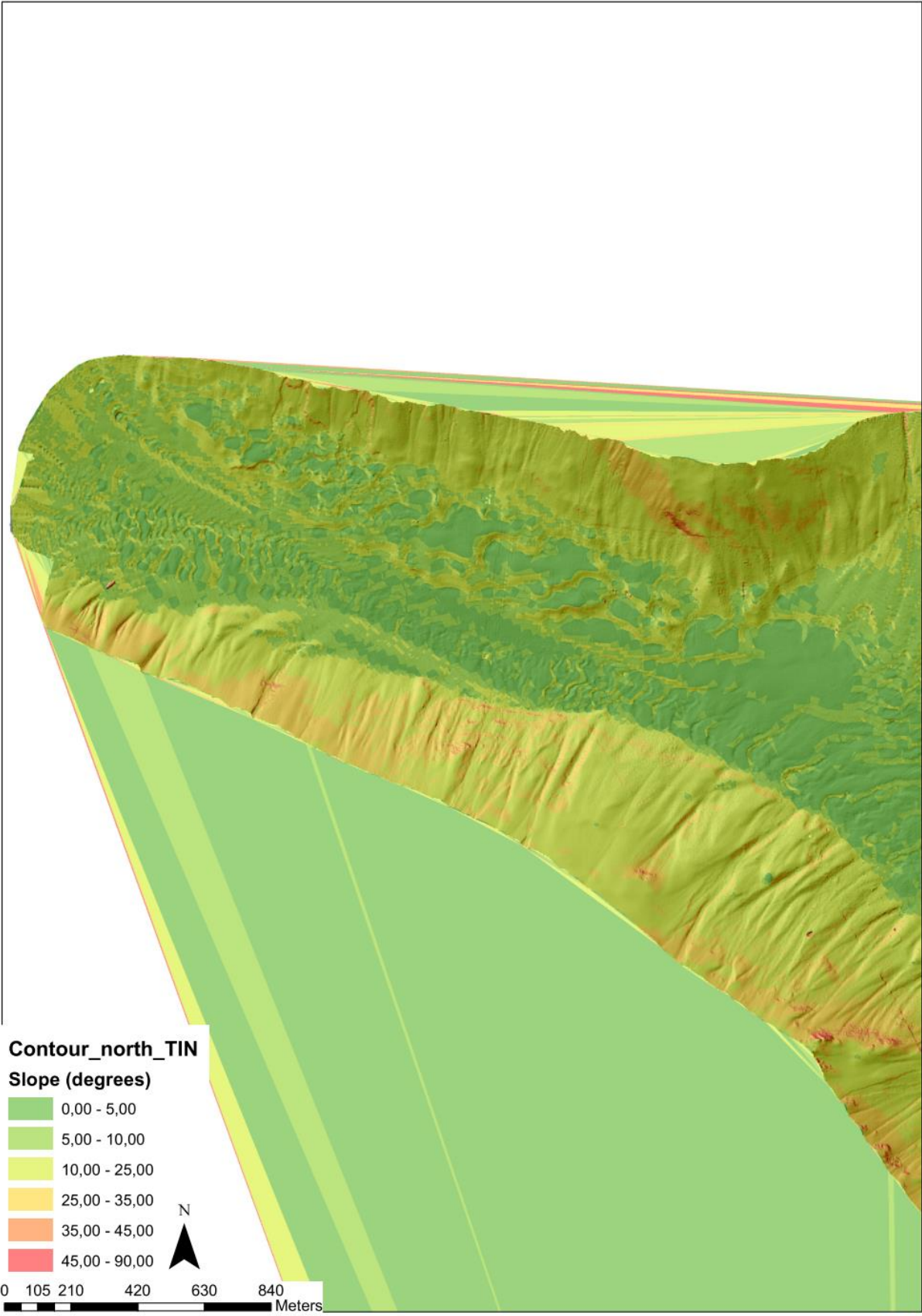


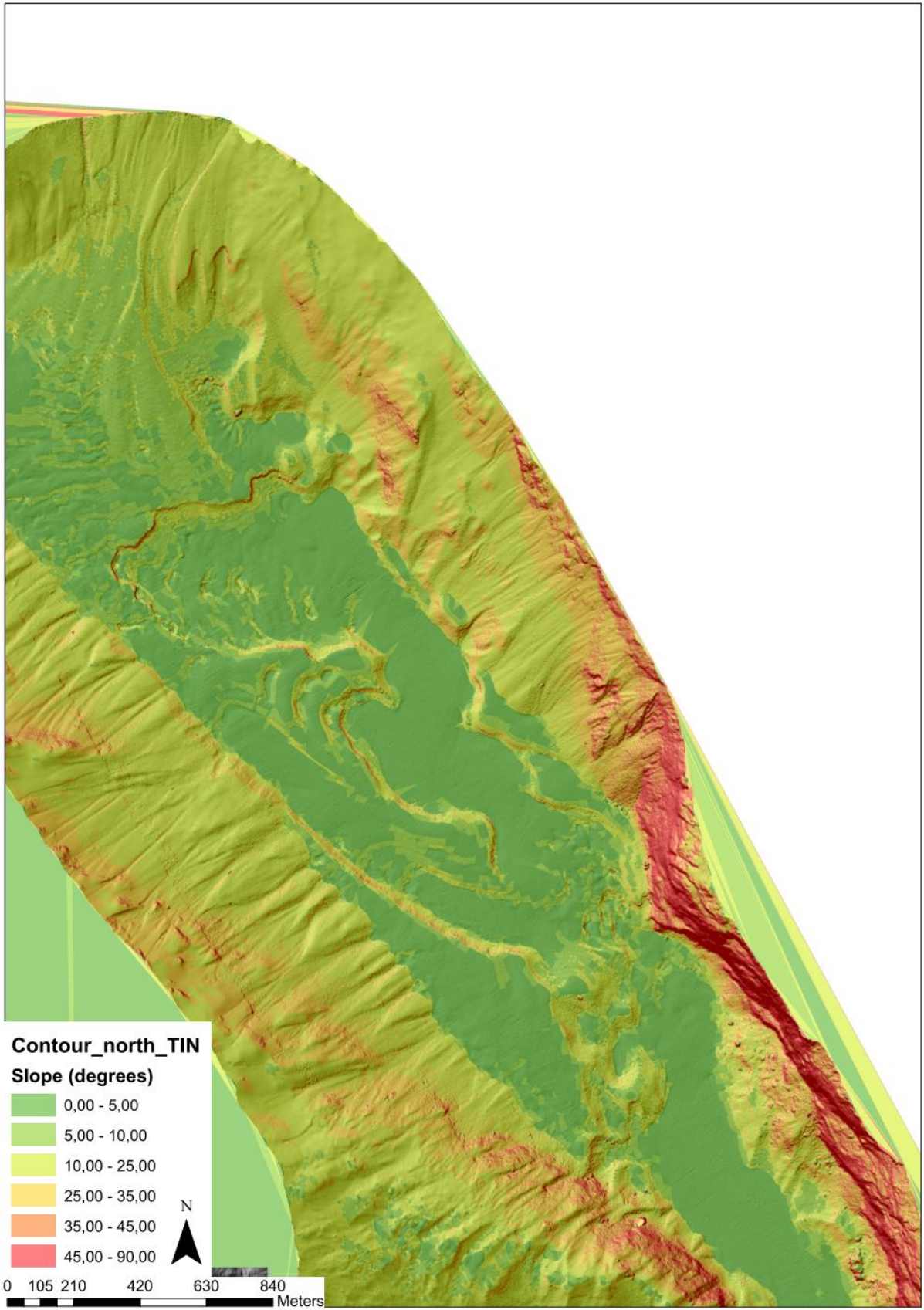




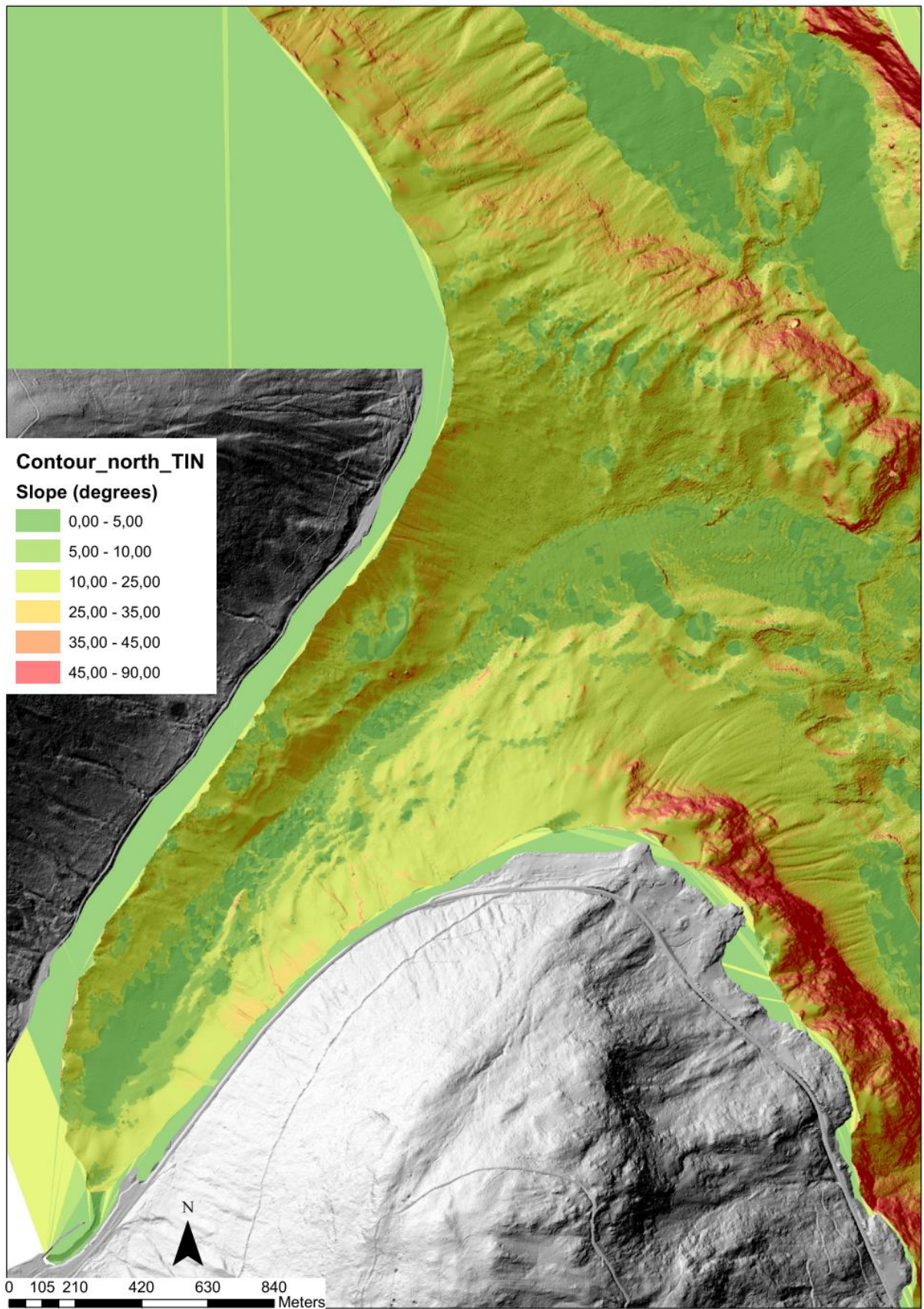


**9.3 APPENDIX C: SLOPE MAP USED DURING THE MAPPING OF LAKE TINNSJØ.  
PRESENTED FROM NORTH TO SOUTH**

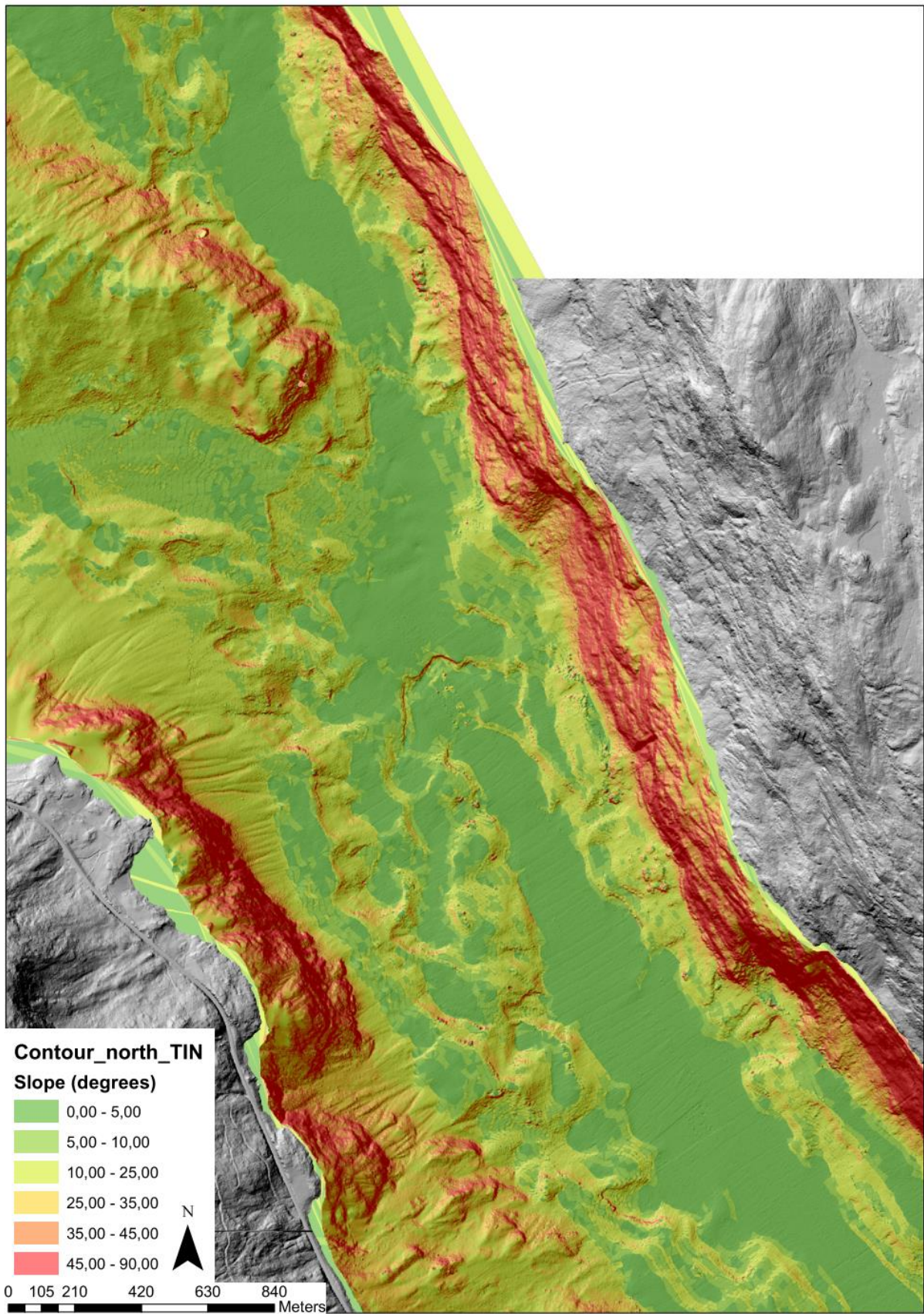




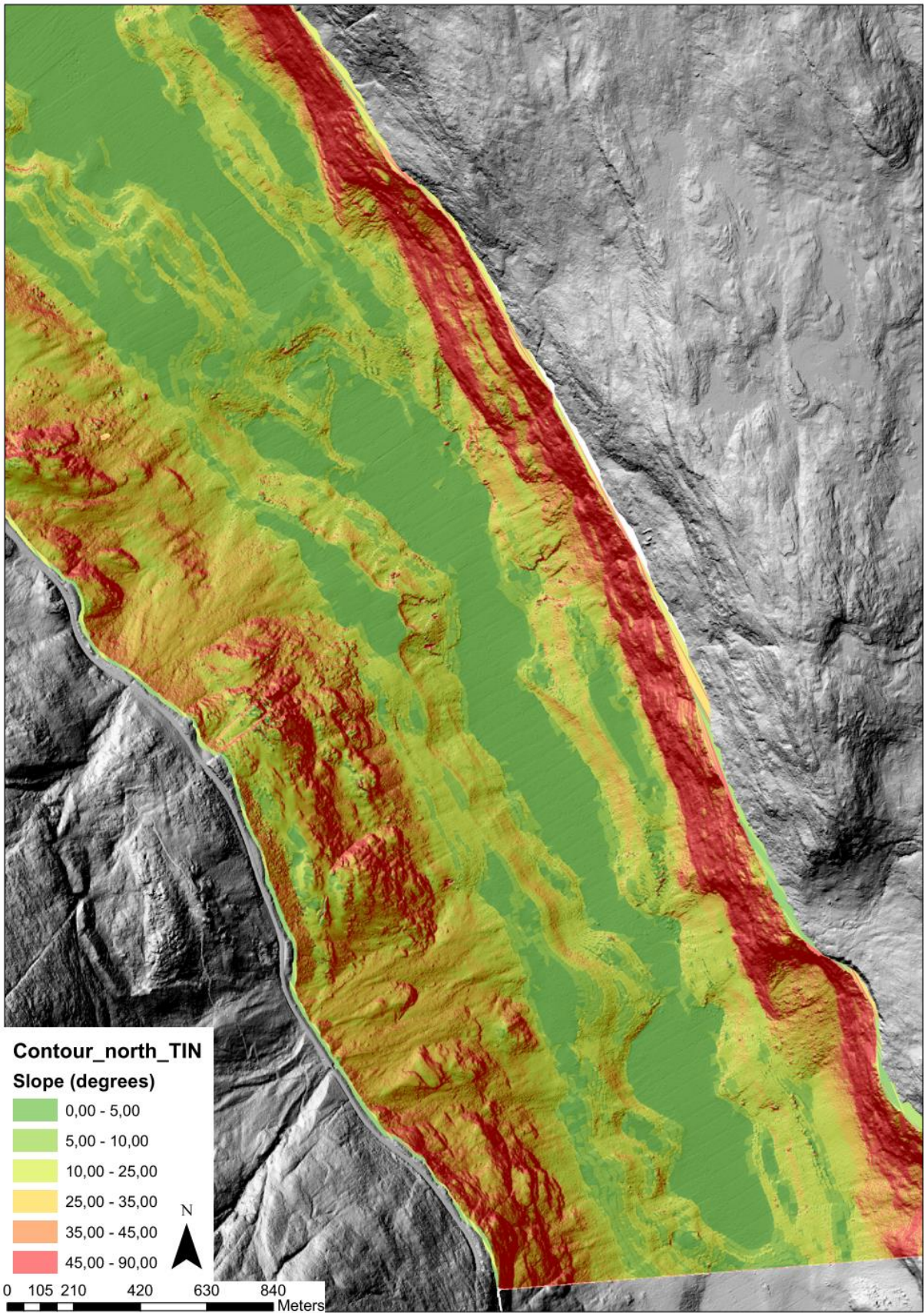




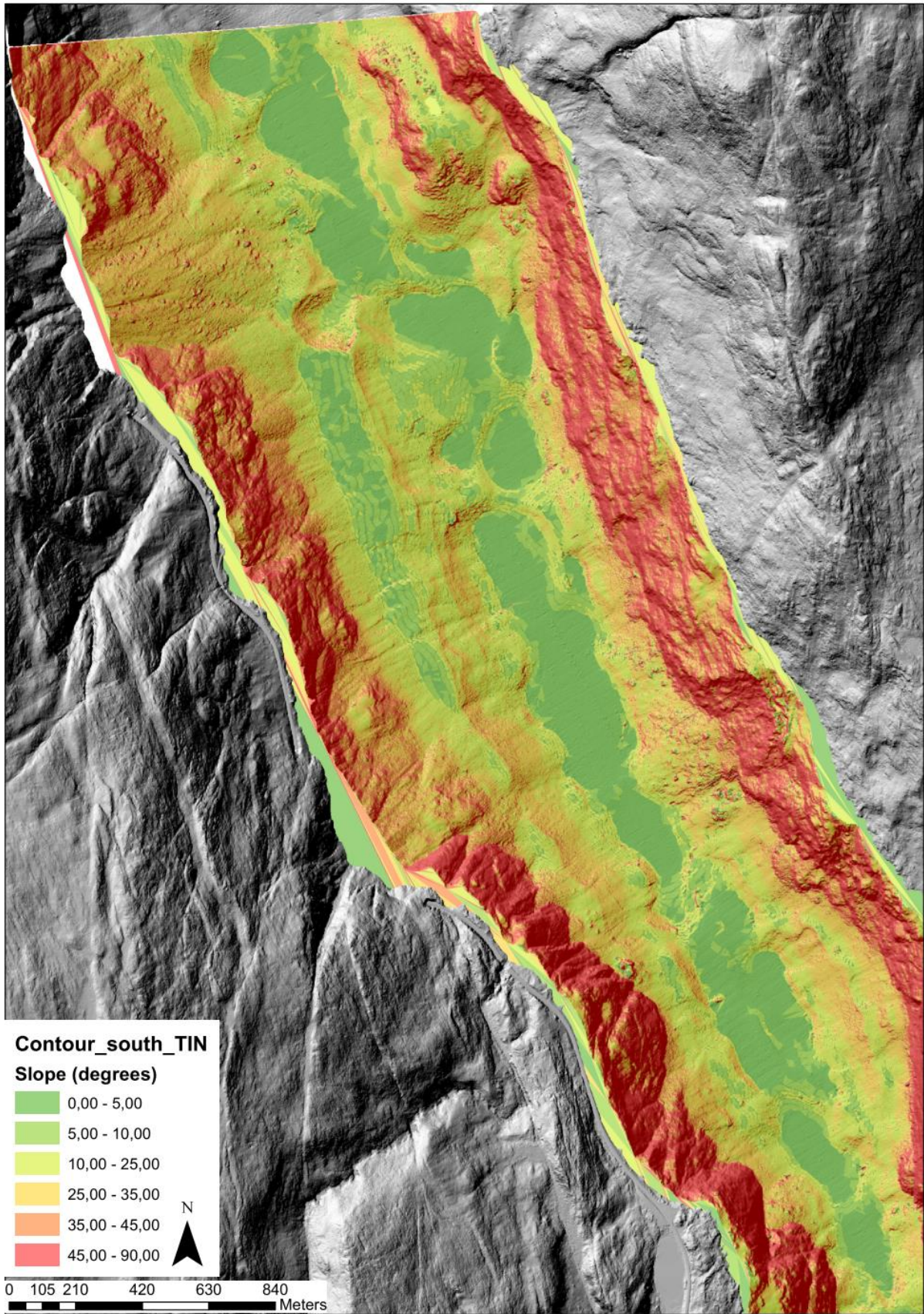




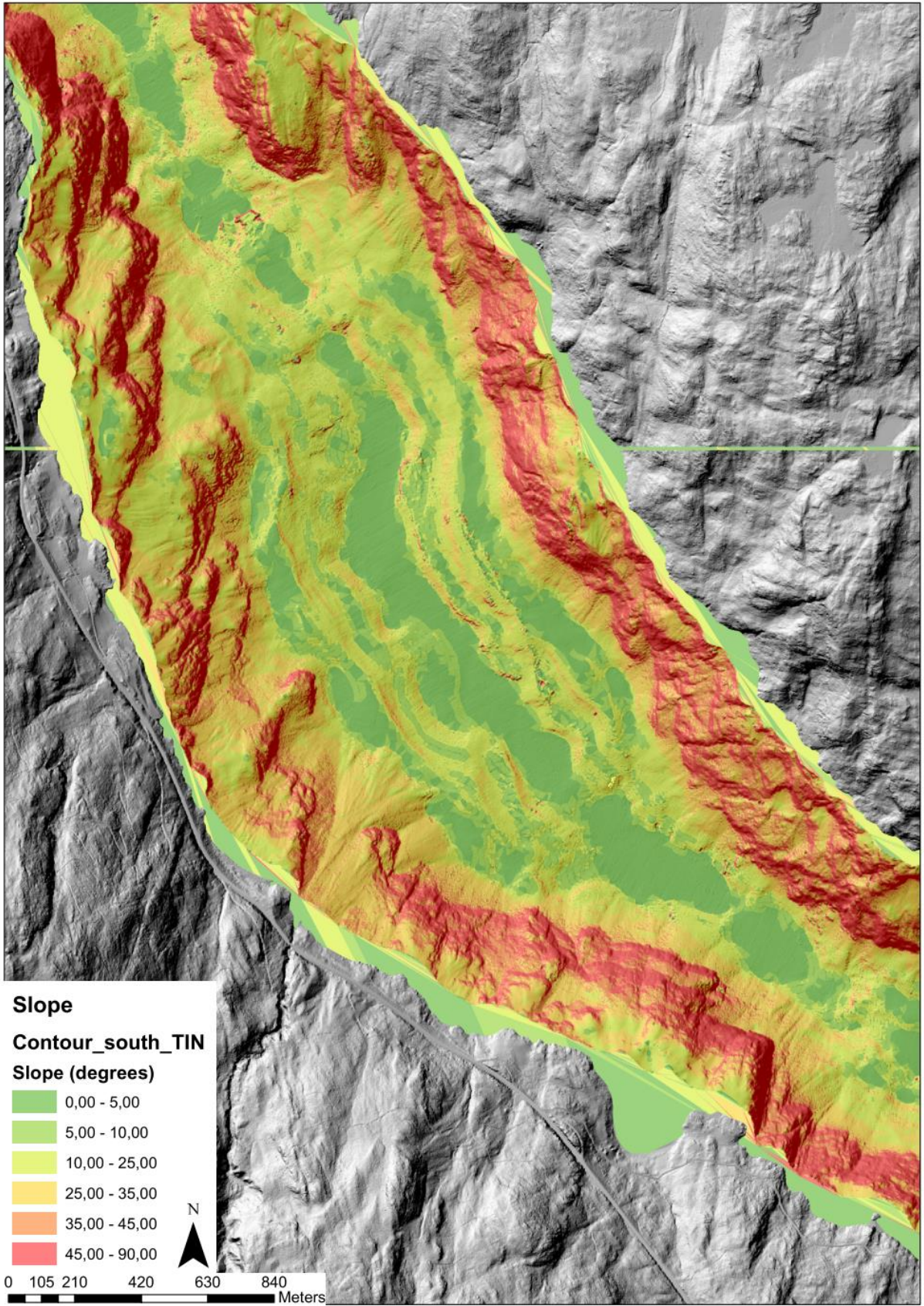




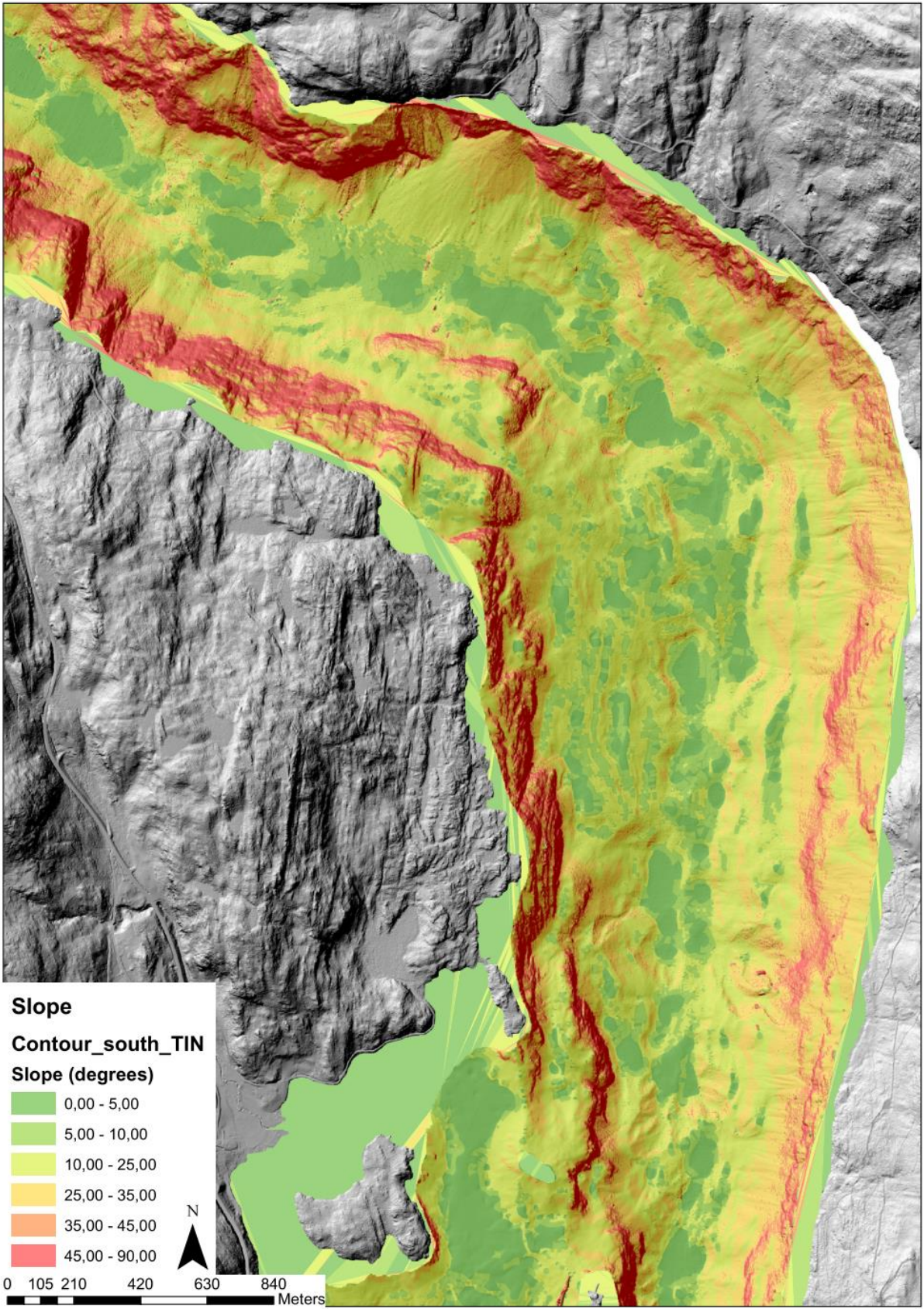




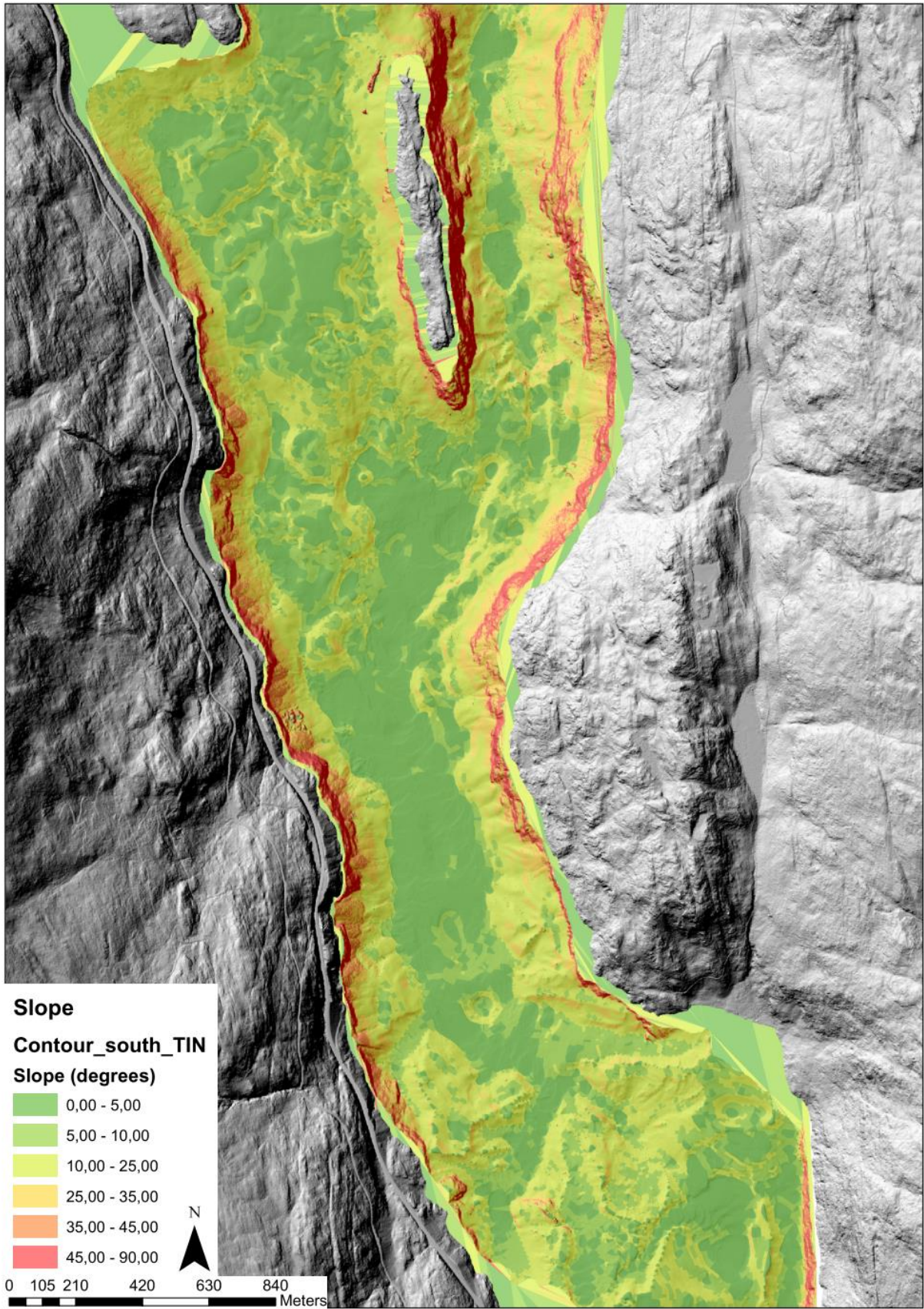




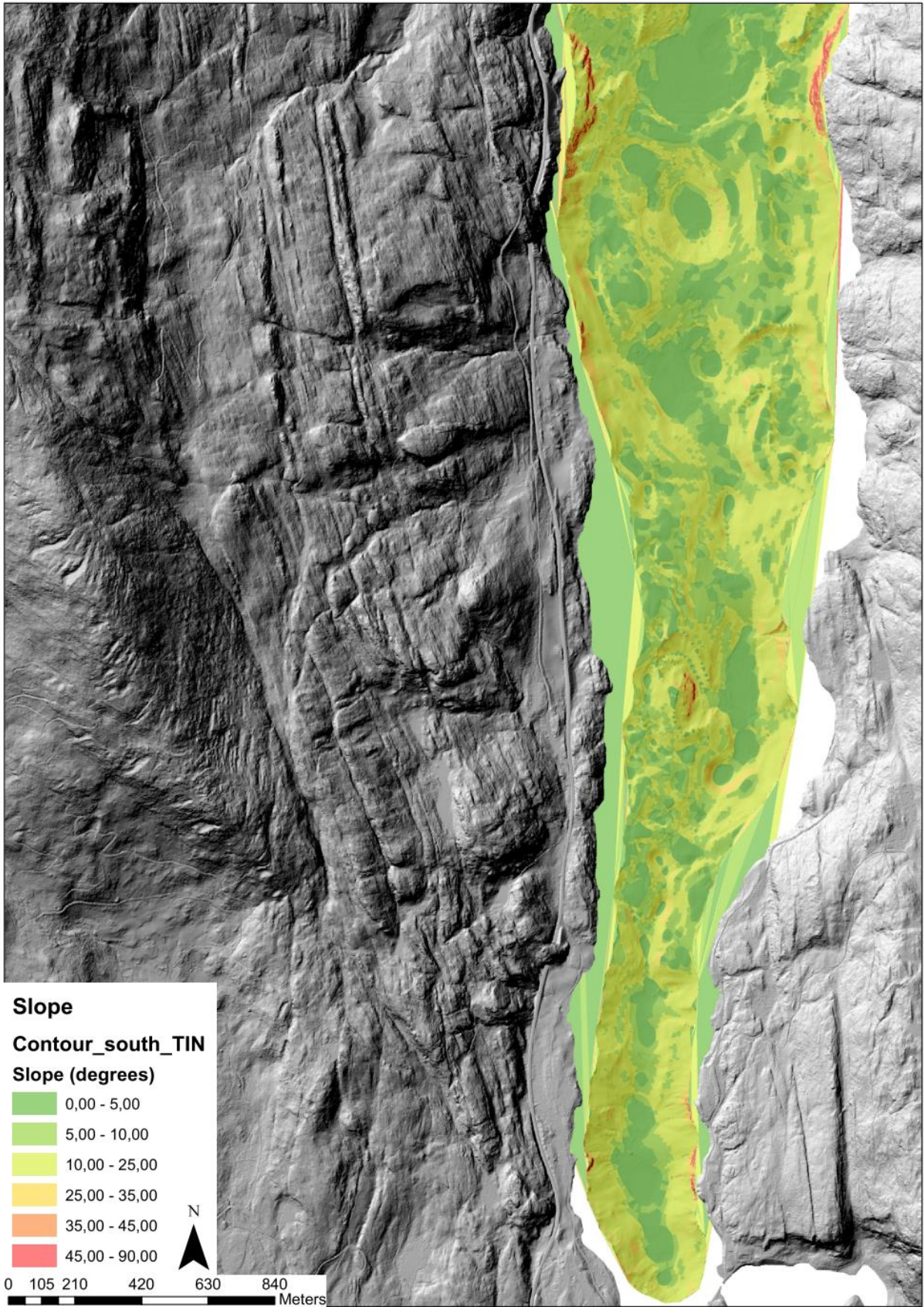












## 9.4 APPENDIX D: SCHMIDT HARDNES

Lokalitet	Sprekkesett	Bergart	Hammer vinkel (°)	Schmidt hardhet	Estimert JCS (MPa)
D1	J1	Rhyolittisk	45	58	325
D1	J1	Rhyolittisk	45	56	310
D1	J1	Rhyolittisk	45	46	180
D1	J1	Rhyolittisk	45	56	310
D1	J1	Rhyolittisk	45	64	400
D1	J1	Rhyolittisk	45	54	275
D1	J1	Rhyolittisk	45	56	310
D1	J4	Rhyolittisk	100	62	400
D1	J4	Rhyolittisk	100	58	350
D1	J4	Rhyolittisk	100	57	340
D1	J4	Rhyolittisk	100	56	320
D1	J4	Rhyolittisk	100	56	320
D1	J4	Rhyolittisk	100	57	340
D1	J4	Rhyolittisk	100	60	380
D1	J2	Rhyolittisk	45	66	380
D1	J2	Rhyolittisk	45	64	380
D1	J2	Rhyolittisk	45	62	380
D1	J2	Rhyolittisk	45	60	380
D1	J2	Rhyolittisk	45	62	380
D1	J2	Rhyolittisk	45	58	325
D1	J2	Rhyolittisk	45	66	380
B1	J1	Rhyolittisk	20	54	275
B1	J1	Rhyolittisk	20	30	85
B1	J1	Rhyolittisk	20	52	270
B1	J1	Rhyolittisk	20	48	210
B1	J1	Rhyolittisk	20	50	240
B1	J1	Rhyolittisk	20	48	210
B1	J1	Rhyolittisk	20	56	310
B1	J1	Rhyolittisk	20	52	270
B1	J3	Rhyolittisk	0	62	360
B1	J3	Rhyolittisk	0	56	270
B1	J3	Rhyolittisk	0	58	310
B1	J3	Rhyolittisk	0	56	270
B1	J3	Rhyolittisk	0	64	360
B1	J3	Rhyolittisk	0	58	310
B1	J3	Rhyolittisk	0	54	250
B1	J3	Rhyolittisk	0	54	250
B1	J2	Rhyolittisk	-70	60	275
B1	J2	Rhyolittisk	-70	64	275
B1	J2	Rhyolittisk	-70	52	210
B1	J2	Rhyolittisk	-70	52	210
B1	J2	Rhyolittisk	-70	58	270
B1	J2	Rhyolittisk	-70	44	135
B1	J2	Rhyolittisk	-70	50	180

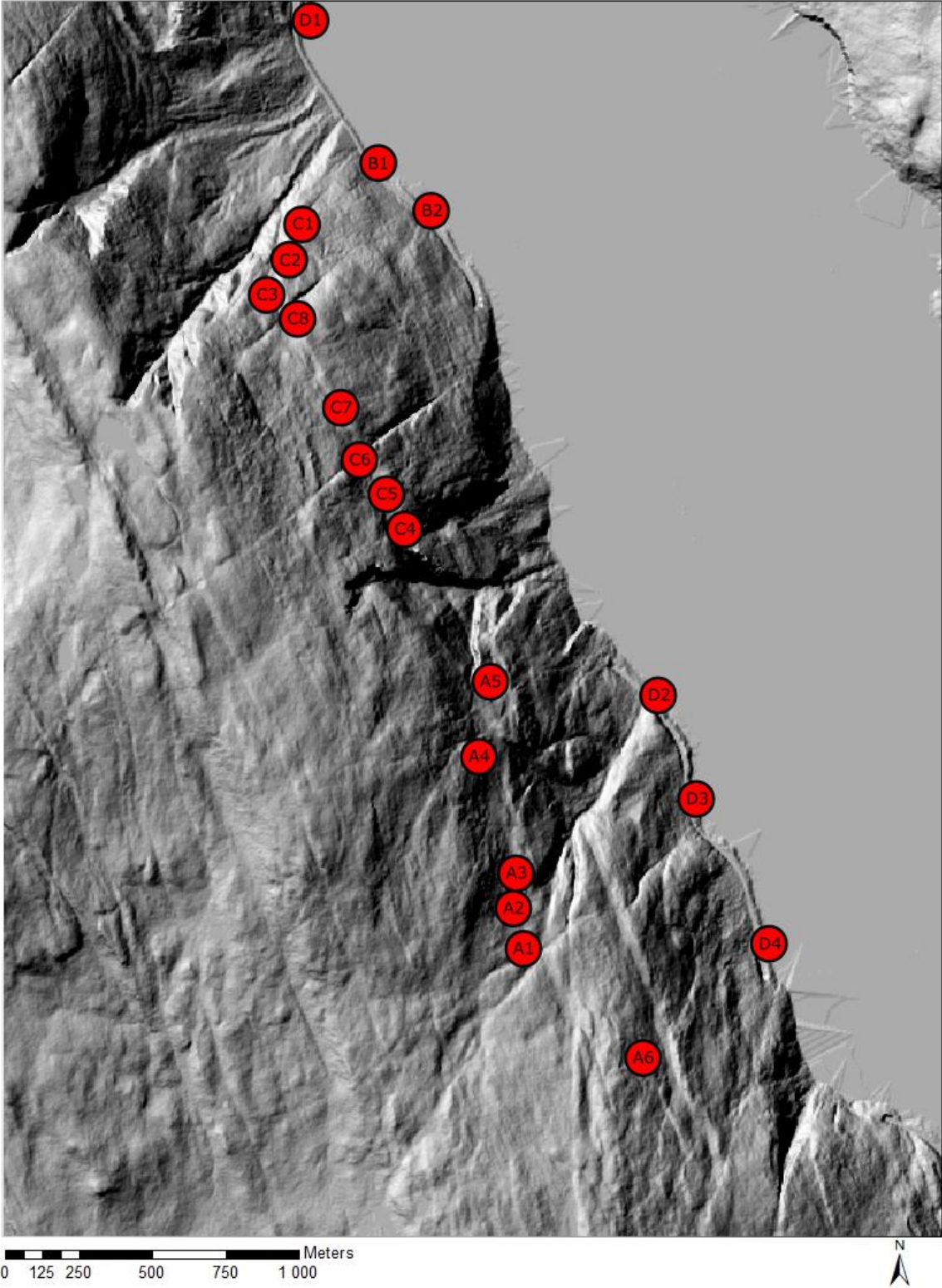
B1	J2	Rhyolittisk	-70	58	270
B1	J2	Rhyolittisk	-70	58	270
B1	J2	Rhyolittisk	-70	48	150
B1	J2	Rhyolittisk	-70	57	260
B1	J2	Rhyolittisk	-70	56	240
B1	J4	Rhyolittisk	-70	62	275
B1	J4	Rhyolittisk	-70	60	275
B1	J4	Rhyolittisk	-70	46	140
B1	J4	Rhyolittisk	-70	60	275
B1	J4	Rhyolittisk	-70	56	240
B1	J4	Rhyolittisk	-70	50	180
B1	J4	Rhyolittisk	-70	56	240
B1	J4	Rhyolittisk	-70	63	275
B1	J4	Rhyolittisk	-70	60	275
B1	J4	Rhyolittisk	-70	63	275
B1	J4	Rhyolittisk	-70	56	240
B1	J4	Rhyolittisk	-70	62	275
B2	J4	Rhyolittisk	-45	54	250
B2	J4	Rhyolittisk	-45	56	270
B2	J4	Rhyolittisk	-45	58	280
B2	J4	Rhyolittisk	-45	54	250
B2	J4	Rhyolittisk	-45	58	280
B2	J4	Rhyolittisk	-45	58	280
B2	J4	Rhyolittisk	-45	52	230
B2	J2	Rhyolittisk	20	51	250
B2	J2	Rhyolittisk	20	54	280
B2	J2	Rhyolittisk	20	51	250
B2	J2	Rhyolittisk	20	53	270
B2	J2	Rhyolittisk	20	50	230
B2	J2	Rhyolittisk	20	62	400
B2	J2	Rhyolittisk	20	56	320
B2	J2	Rhyolittisk	20	50	240
B2	J2	Rhyolittisk	20	59	360
B2	J1	Rhyolittisk	45	50	230
B2	J1	Rhyolittisk	45	62	400
B2	J1	Rhyolittisk	45	56	320
B2	J1	Rhyolittisk	45	54	270
B2	J1	Rhyolittisk	45	60	400
B2	J1	Rhyolittisk	45	52	250
B2	J1	Rhyolittisk	45	54	270
B2	J3	Rhyolittisk	10	66	380
B2	J3	Rhyolittisk	10	62	380
B2	J3	Rhyolittisk	10	58	320
B2	J3	Rhyolittisk	10	60	380
B2	J3	Rhyolittisk	10	60	380
B2	J3	Rhyolittisk	10	56	290
B2	J3	Rhyolittisk	10	58	320

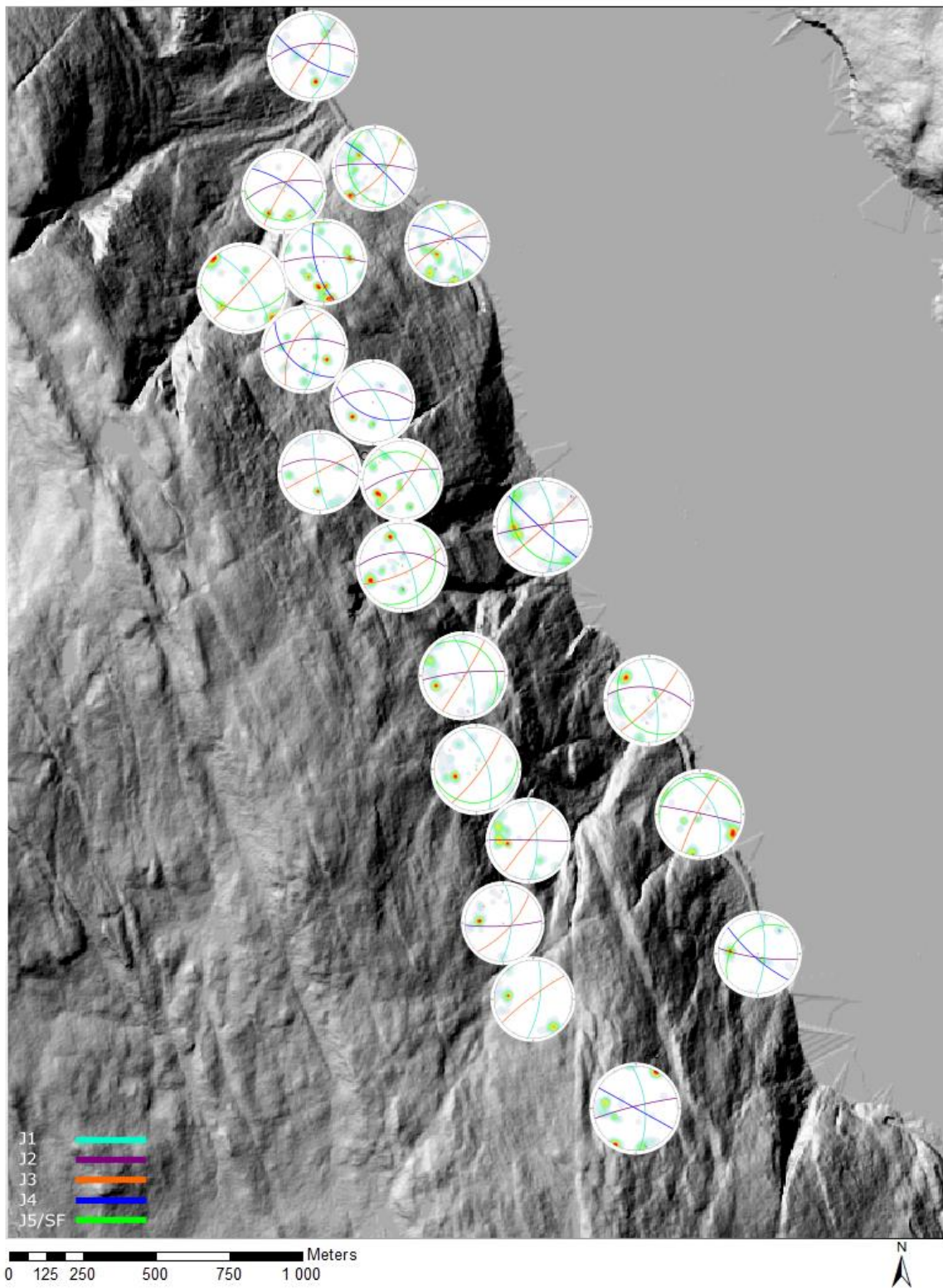


B2	J3	Rhyolittisk	10	59	340
B2	J3	Rhyolittisk	10	60	380
D2	J1	Rhyolittisk	10	42	140
D2	J1	Rhyolittisk	10	38	120
D2	J1	Rhyolittisk	10	46	180
D2	J1	Rhyolittisk	10	45	170
D2	J1	Rhyolittisk	10	38	120
D2	J1	Rhyolittisk	10	46	180
D2	J1	Rhyolittisk	10	38	120
D2	J1	Rhyolittisk	10	46	180
D2	J2	Rhyolittisk	45	38	130
D2	J2	Rhyolittisk	45	42	160
D2	J2	Rhyolittisk	45	40	140
D2	J2	Rhyolittisk	45	44	170
D2	J2	Rhyolittisk	45	46	200
D2	J2	Rhyolittisk	45	40	140
D2	J2	Rhyolittisk	45	44	170
D2	J2	Rhyolittisk	45	38	130
D2	J2	Rhyolittisk	45	45	180
D2	J3	Rhyolittisk	-45	46	180
D2	J3	Rhyolittisk	-45	40	140
D2	J3	Rhyolittisk	-45	43	150
D2	J3	Rhyolittisk	-45	46	180
D2	J3	Rhyolittisk	-45	47	190
D2	J3	Rhyolittisk	-45	38	125
D2	J3	Rhyolittisk	-45	38	125
D2	J3	Rhyolittisk	-45	38	125
D2	J3	Rhyolittisk	-45	40	140
D2	J1	Rhyolittisk	10	48	200
D2	J1	Rhyolittisk	10	46	180
D2	J1	Rhyolittisk	10	44	170
D2	J1	Rhyolittisk	10	43	150
D2	J1	Rhyolittisk	10	52	240
D2	J1	Rhyolittisk	10	50	225
D2	J1	Rhyolittisk	10	46	180
D2	J1	Rhyolittisk	10	44	170
D2	J1	Rhyolittisk	10	48	180
D3	J1	Rhyolittisk	0	50	225
D3	J1	Rhyolittisk	0	48	180
D3	J1	Rhyolittisk	0	54	260
D3	J1	Rhyolittisk	0	56	300
D3	J1	Rhyolittisk	0	48	180
D3	J1	Rhyolittisk	0	44	170
D3	J1	Rhyolittisk	0	48	180
D3	J3	Rhyolittisk	0	59	340
D3	J3	Rhyolittisk	0	64	380
D3	J3	Rhyolittisk	0	64	380

D3	J3	Rhyolittisk	0	58	320
D3	J3	Rhyolittisk	0	60	380
D3	J3	Rhyolittisk	0	54	250
D3	J3	Rhyolittisk	0	52	240
D3	J3	Rhyolittisk	0	62	380
D3	J3	Rhyolittisk	0	60	380
D3	J3	Rhyolittisk	0	64	380
D3	J2	Rhyolittisk	45	51	250
D3	J2	Rhyolittisk	45	50	230
D3	J2	Rhyolittisk	45	42	160
D3	J2	Rhyolittisk	45	52	260
D3	J2	Rhyolittisk	45	50	230
D3	J2	Rhyolittisk	45	60	400
D3	J2	Rhyolittisk	45	62	400
D3	J2	Rhyolittisk	45	52	260
D3	J2	Rhyolittisk	45	54	270
D3	J2	Rhyolittisk	45	48	200
C1	J1	Rhyolittisk	45	44	160
C1	J1	Rhyolittisk	45	50	220
C1	J1	Rhyolittisk	45	42	140
C1	J1	Rhyolittisk	45	50	220
C1	J1	Rhyolittisk	45	52	240
C1	J1	Rhyolittisk	-10	57	310
C1	J1	Rhyolittisk	-10	54	260
C1	J1	Rhyolittisk	-10	52	240
C1	J1	Rhyolittisk	-10	48	180
C1	J1	Rhyolittisk	-10	54	260
C7	J1	Rhyolittisk	45	40	140
C7	J1	Rhyolittisk	45	50	230
C7	J1	Rhyolittisk	45	41	150
C7	J1	Rhyolittisk	45	36	130
C7	J1	Rhyolittisk	45	40	140
C7	J1	Rhyolittisk	45	35	125
C7	J1	Rhyolittisk	45	25	65
C7	J1	Rhyolittisk	45	22	55

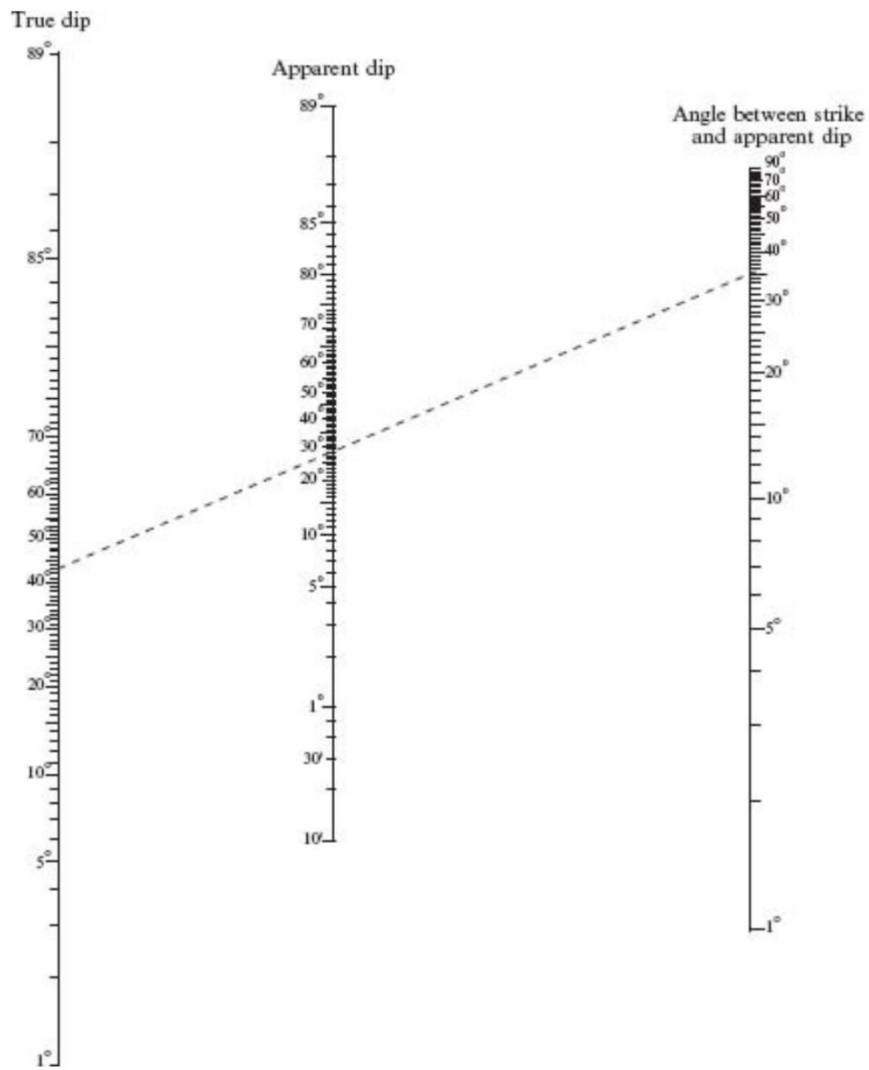
**9.5 APPENDIX E: MAP WITH LOCALITIES, AND MAP WITH STEREOONETS OF THE STUDIED AREA OF THE PRESTURA ROCKSLIDE**







## 9.6 APPENDIX F: ALIGNMENT DIAGRAM (FROM (ROWLAND *ET AL.*, 2007))



## 9.7 APPENDIX G: TABLE OF ALL VOLUME CALCULATIONS OF LANDFORMS MAPPED IN LAKE TINNSJØ

Id	Landside name	Deposit/initial	Hmax	Hmin	L	C min	C interm.	C max	SLBL	SLBL	SLBL	SLBL		Min. eroded Volume
			(ma.s.l)	(ma.s.l)	(m)				V min (Mm <sup>3</sup> )	interm. (Mm <sup>3</sup> )	V max (Mm <sup>3</sup> )	V mean	stdv	
1	Prestura_1	Landslide scar	877	438	350	0	0.03098	0.14844	3.54	4.81	8.87	5.74	3.13	3.70
2	Prestura_2	Landslide deposit	140	-180	750	0	-0.00805	-0.01606	1.41	1.68	3.99	2.36	1.63	2.23
3	MB1	Landslide scar	-160	-200	220	0	0.00659	0.03423	0.405	0.46	0.663	0.51	0.15	0.42
4	MB2	Fan deposit	160	-200	530	0	-0.01394	-0.03309	1.28	1.3	3.26	1.95	1.31	0.00
5	MB4	Landslide deposit	160	-160	380	0	-0.08558	-0.12179	0.39	0.47	0.85	0.57	0.28	0.00
6	MB5	Landslide scar	-70	-220	390	0	0.01081	0.04085	0.33	0.468	0.855	0.55	0.30	0.00
7	MB6	Fan deposit	160	-150	440	0	-0.01575	-0.03311	0.24	0.75	1.19	0.73	0.46	0.33
8	MB7	Fan deposit	-30	-160	300	0	-0.05983	-0.081	0.42	0.66	0.99	0.69	0.30	0.00
9	MB8	Fan deposit	160	-160	720	0	-0.0123	-0.02557	0.23	0.27	0.52	0.34	0.18	0.11
10	MB9	Fan deposit	160	-160	740	0	-0.0484	-0.0242	0.22	0.3	0.44	0.32	0.12	0.00
11	MB10	Fan deposit	10	-150	420	0	-0.081	-0.03757	0.16	0.2	0.46	0.27	0.19	0.18
12	MB11	Fan deposit	160	-160	490	0	-0.01254	-0.05521	0.18	0.22	0.46	0.29	0.17	0.13
13	MB12	Landslide deposit	-110	-240	340	0	-0.01896	-0.04658	0.61	0.81	2.44	1.29	1.15	0.53
14	MB13	Landslide scar	110	-110	220	0	0.07632	0.18828	0.7	1.59	3.09	1.79	1.30	0.00
15	MB14	Fan deposit	-20	-160	248	0	-0.01654	-0.09429	0.048	0.052	0.094	0.06	0.03	0.00
16	MB15	Fan deposit	-20	-160	190	0	-0.01847	-0.16064	0.085	0.113	0.17	0.12	0.05	0.00
17	MB16	Fan deposit	-20	-160	200	0	-0.01561	-0.04832	0.019	0.04	0.089	0.05	0.04	0.07
18	MB17	Landslide scar	-210	-250	140	0	0.01493	0.03423	0.077	0.091	0.11	0.09	0.02	0.00
19	MB18	Landslide scar	-220	-235	120	0	0.01907	0.04315	0.044	0.055	0.072	0.06	0.02	0.00
20	MB19	Landslide scar	-160	-210	160	0	0.03459	0.0809	0.037	0.078	0.132	0.08	0.05	0.03
21	MB20	Fan deposit	-110	-220	400	0	-0.12	-0.1424	0.044	0.049	0.058	0.05	0.01	0.00
22	MB21	Fan deposit	-50	-160	259	0	-0.00378	-0.0674	0.104	0.116	0.249	0.16	0.09	0.00
23	MB22	Landslide scar	-170	-210	290	0	0.01293	0.0197	0.092	0.108	0.117	0.11	0.01	0.15
24	MB23	Landslide scar	-170	-210	160	0	0.01717	0.06472	0.088	0.12	0.205	0.14	0.07	0.00
25	MB24	Landslide scar	-170	-210	170	0	0.01675	0.05733	0.027	0.038	0.062	0.04	0.02	0.00

			Hmax	Hmin										
			(ma.s	(ma.s		C								Min.
MC			.l)	.l)	L (m)	min	C interm.	C max	Vmin	Vinter	Vmax	Vmea	stdv	eroded
												n		Volume
26	MB25	Landslide scar	-170	-210	180	0	0.01635	0.05114	0.056	0.075	0.11	0.08	0.03	0.03
27	MC2	Landslide scar	-170	-210	150	0	0.01761	0.07364	0.05	0.087	0.17	0.10	0.07	0
28	MC3	Landslide scar	-170	-210	170	0	0.01675	0.05733	0.04	0.097	0.156	0.10	0.06	0
29	MC4	Landslide scar	-170	-210	190	0	0.01598	0.0459	0.069	0.08	0.108	0.09	0.02	0.064
30	MC5	Landslide scar	-170	-210	175	0	0.01655	0.0541	0.023	0.026	0.032	0.03	0.01	0
31	MC6	Landslide scar	-170	-210	175	0	0.01655	0.0541	0.022	0.027	0.037	0.03	0.01	0.023
32	MC7	Landslide scar	-170	-210	160	0	0.01717	0.06472	0.01	0.012	0.019	0.01	0.005	0
33	MC8	Landslide scar	-170	-210	170	0	0.01675	0.05733	0.014	0.017	0.022	0.02	0.00	0
34	MC9	Fan deposit	160	-160	625	0	-0.01428	-0.03393	0.835	0.858	1.781	1.16	0.62	0.25
35	MC10	Fan deposit	-80	-210	310	0	-0.02799	-0.05603	0.343	0.5	1.055	0.63	0.42	0
36	MC11	Fan deposit	20	-150	350	0	-0.00559	-0.05748	0.044	0.076	0.2126	0.11	0.10	0
37	MC12	Landslide deposit	130	-50	330	0	-0.00793	-0.0466	0.063	0.075	0.253	0.13	0.12	0
38	MC13	Landslide scar	-60	-150	250	0	0.01401	0.05965	0.059	0.142	0.26	0.15	0.11	0
39	MC14	Landslide scar	-170	-190	150	0	0.01761	0.03682	0.146	0.197	0.237	0.19	0.04	0
40	MC15	Landslide scar	-150	-190	240	0	0.0143	0.02876	0.154	0.193	0.237	0.19	0.04	0.13
41	MC16	Landslide scar	-150	-180	140	0	0.03734	0.0634	0.155	0.192	0.219	0.19	0.03	0
42	MC17	Landslide scar	-150	-190	170	0	0.00707	0.05733	0.045	0.049	0.08	0.06	0.02	0
NA			Hmax	Hmin		C								Min.
			(ma.s	(ma.s	L (m)	min	C interm.	C max	Vmin	Vinter	Vmax	Vmea	stdv	eroded
			.l)	.l)								n		Volume
43	NA1	Landslide scar	-140	-180	500	0	0.00476	0.00663	0.4377	0.538	0.575	0.52	0.06	0
44	NA2	Landslide scar	-120	-150	250	0	0.01401	0.01988	0.2171	0.283	0.31	0.27	0.04	0
45	NA3	Landslide scar	-120	-160	270	0	0.01345	0.02773	0.1088	0.143	0.165	0.14	0.03	0.04
46	NA4	Landslide scar	-120	-160	160	0	0.01717	0.06472	0.0655	0.091	0.152	0.10	0.05	0
47	NA5	Landslide scar	-180	-190	300	0	0.00199	0.0046	0.3843	0.427	0.483	0.43	0.05	0.34
48	NA5_2	Landslide scar	-180	-190	1220	0	0.00008	0.00028	1.8148	1.828	1.862	1.83	0.03	1.69
49	NA6	Landslide scar	-90	-170	340	0	0.01178	0.02867	0.7215	1.075	1.524	1.11	0.42	0

50	NA7	Landslide scar	-130	-150	200	0	0.01561	0.02071	0.1838	0.357	0.412	0.32	0.09	0
51	NA8	Landslide scar	-40	-70	300	0	0.00894	0.01381	0.2311	0.549	0.689	0.49	0.20	0.325
52	NA8_2	Landslide scar	-40	-130	710	0	0.00538	0.0074	1.2955	2.099	2.33	1.91	0.42	1.046
53	NA9	Landslide scar	-150	-160	220	0	0.00393	0.00856	0.1951	0.218	0.245	0.22	0.03	0
54	NA10	Fan deposit	60	0	350	0	-0.01996	-0.02029	0.0102	0.113	0.1138	0.08	0.03	0
55	NA11	Fan deposit	10	-120	300	0	-0.03602	-0.05983	0.0773	0.0999	0.16889	0.12	0.05	0.03
56	NA12	Landslide deposit	-20	-130	150	0	-0.11432	-0.2025	0.2124	0.2303	0.6008	0.35	0.25	0
57	NA13	Landslide scar	-120	150	240	0	0.06936	0.19416	1.387	1.922	2.95	2.09	0.86	0
			Hmax	Hmin		C						Vmea		Min.
			(m.a.	(ma.s		min	C interm.	C max	Vmin	Vinter	Vmax	n	stdv	eroded
			s.l)	.l)	L (m)									Volume
NB														
58	NB1	Landslide scar	-100	-140	200	0	0.01058	0.04142	0.135	0.174	0.273	0.19	0.08	0.12
59	NB2	Landslide scar	-90	-140	290	0	0.01293	0.02463	0.136	0.163	0.186	0.16	0.02	0
60	NB3	Landslide scar	-120	-130	400	0	0.00032	0.00259	0.271	0.272	0.286	0.28	0.01	0
61	NB4	Landslide scar	-90	-115	900	0	0.00075	0.00128	1.298	1.391	1.454	1.38	0.07	1.26
62	NB5	Landslide scar	-60	-100	1150	0	0.0007	0.00125	5.5945	6.29	6.75	6.21	0.54	5.72
63	NB6	Fan deposit	50	-95	220	0	-0.048	-0.12409	0.139	0.2068	0.5655	0.30	0.26	0
64	NB7	Fan deposit	10	-80	270	0	-0.0398	-0.05114	0.02294	0.1702	0.321	0.17	0.15	0
65	NB8	Fan deposit	70	-80	400	0	-0.00772	-0.03883	0.03934	0.2187	0.4786	0.25	0.23	0
			Hmax	Hmin		C						Vmea		Min.
			(m.a.	(ma.s		min	C interm.	C max	Vmin	Vinter	Vmax	n	stdv	eroded
			s.l)	.l)	L (m)									Volume
NC														
66	NC1	Landslide scar	40	-10	210	0	0.02145	0.04696	0.0286	0.055	0.0752	0.05	0.02	0
67	NC2	Landslide scar	40	-20	250	0	0.01983	0.04315	0.03003	0.058	0.072	0.05	0.019	0.0251
68	NC3	Landslide scar	-10	-20	150	0	0.00728	0.01841	0.0216	0.028	0.035	0.03	0.01	0
			Hmax	Hmin		C						Vmea		Min.
			(m.a.	(ma.s		min	C interm.	C max	Vmin	Vinter	Vmax	n	stdv	eroded
			s.l)	.l)	L (m)									Volume
MA														
69	MA1	Landslide scar	-160	-190	70	0	0.05128	0.2536	0.006	0.008	0.014	0.01	0.005	0
70	MA2	Landslide scar	-60	-100	150	0	0.03592	0.07364	0.019	0.033	0.049	0.03	0.02	0.031



71	MA3	Landslide scar	-30	-120	170	0	0.0598	0.12899	0.101	0.134	0.172	0.14	0.04	0
72	MA4	Fan deposit	-70	-220	180	0	-0.05705	-0.15533	0.082	0.284	0.714	0.36	0.35	0
73	MA5	Fan deposit	60	-130	320	0	-0.03384	-0.07686	0.21	0.911	1.774	0.97	0.81	0.184
74	MA6	Fan deposit	0	-120	220	0	-0.048	-0.1027	0.025	0.158	0.312	0.17	0.15	0
75	MA7	Fan deposit	-70	-130	110	0	-0.08324	-0.2054	0.015	0.0266	0.066	0.04	0.03	0.004
SD			Hmax (m.a. s.l)	Hmin (ma.s .l)	L (m)	C			Vmin	Vinter	Vmax	Vmea		Min. eroded Volume
76	SD1	Landslide scar	-150	-180	140	0	0.01807	0.0634	0.015	0.021	0.036	0.02	0.01	0
77	SD2	Landslide scar	70	-20	110	0	0.15484	0.30809	0.084	0.132	0.17	0.13	0.04	0.072
78	SD3	Landslide scar	150	-70	230	0	0.0727	0.17226	0.444	0.645	0.906	0.67	0.24	0
79	SD4	Landslide scar	120	-40	160	0	0.10702	0.25888	0.109	0.166	0.227	0.17	0.06	0.104
80	SD5	Landslide scar	20	-40	130	0	0.07378	0.14706	0.076	0.134	0.178	0.13	0.05	0
81	SD6	Landslide scar	-70	-120	100	0	0.08885	0.20711	0.022	0.031	0.043	0.03	0.01	0.01
82	SD7	Fan deposit	100	-100	500	0	-0.0147	-0.03314	0.229	0.581	1.442	0.75	0.69	0.32
83	SD8	Delta slope	-50	-80	110	0	0.02922	0.1027	0.022	0.028	0.0399	0.03	0.01	0
84	SD9	Landslide scar	-10	-80	120	0	0.02822	0.20135	0.009	0.015	0.056	0.03	0.03	0.008
85	SD10	Landslide scar	-20	-60	180	0	0.01635	0.05114	0.044	0.061	0.087	0.06	0.02	0
86	SD11	Fan deposit	-30	-180	230	0	-0.05828	-0.11745	0.13	0.149	0.252	0.18	0.08	0
87	SD12	Fan deposit	-130	-170	100	0	-0.04427	-0.16569	0.005	0.011	0.024	0.01	0.01	0
SC			Hmax (m.a. s.l)	Hmin (ma.s .l)	L (m)	C			Vmin	Vinter	Vmax	Vmea		Min. eroded Volume
88	SC1	Landslide scar	50	30	120	0	0.01907	0.05753	0.015	0.018	0.023	0.02	0.00	0
89	SC2	Landslide scar	20	-50	240	0	0.0143	0.05034	0.193	0.257	0.416	0.29	0.13	0.19
90	SC3	Landslide scar	0	-60	150	0	0.01761	0.11046	0.024	0.027	0.041	0.03	0.01	0
91	SC4	Landslide scar	0	-50	200	0	0.01561	0.05178	0.073	0.087	0.117	0.09	0.02	0.07
92	SC5	Landslide scar	0	-30	120	0	0.01907	0.08629	0.014	0.019	0.036	0.02	0.01	0
93	SC6	Landslide scar	-10	-30	110	0	0.01961	0.06847	0.009	0.012	0.018	0.01	0.01	0
94	SC7	Landslide scar	30	-30	200	0	0.01561	0.06213	0.053	0.064	0.092	0.07	0.02	0.04

			Hmax	Hmin										
			(m.a.	(ma.s										Min.
SB			s.l)	.l)	L (m)	min	C interm.	C max	Vmin	Vinter	Vmax	Vmea	stdv	eroded
												n		Volume
95	SC8	Landslide scar	30	-30	120	0	0.01907	0.17259	0.01	0.012	0.032	0.02	0.01	0
96	SB1	Landslide scar	70	40	70	0	0.02209	0.2536	0.004	0.005	0.011	0.01	0.00	0
97	SB2	Landslide scar	60	40	80	0	0.02141	0.12944	0.006	0.007	0.011	0.01	0.00	0
98	SB3	Landslide scar	140	110	90	0	0.02078	0.15241	0.005	0.008	0.019	0.01	0.01	0
99	SB4	Landslide scar	140	120	170	0	0.01675	0.02867	0.053	0.084	0.101	0.08	0.02	0.05
100	SB5	Landslide scar	160	110	280	0	0.00609	0.02642	0.085	0.128	0.314	0.18	0.14	0
101	SB6	Landslide scar	170	110	205	0	0.01049	0.05914	0.023	0.039	0.096	0.05	0.04	0.028
102	SB7	Landslide scar	170	150	600	0	0.00168	0.0023	0.364	0.399	0.412	0.39	0.02	0.25
SA			(m.a.	(ma.s										Min.
			s.l)	.l)	L (m)	min	C interm.	C max	Vmin	Vinter	Vmax	Vmea	stdv	eroded
												n		Volume
103	SA1	Landslide scar	180	130	420	0	0.0103	0.01174	0.354	0.41	0.418	0.39	0.02	0.25
104	SA2	Landslide scar	160	130	140	0	0.01807	0.0634	0.03	0.036	0.051	0.04	0.01	0
105	SA3	Landslide scar	170	130	650	0	0.00163	0.00392	0.61	0.637	0.676	0.64	0.04	0.52
106	SA4	Landslide scar	170	140	340	0	0.00841	0.01075	0.204	0.229	0.236	0.22	0.01	0
107	SA5	Fan deposit	180	150	50	0	-0.19925	-0.49706	0.006	0.031	0.075	0.04	0.04	0.006